Designing a Tightly Coupled Ultra-wideband Millimeter-wave Phased Array Antenna

by

Nazanin Rahmati

A thesis
presented to the University of Waterloo
in fulfillment of the
thesis requirement for the degree of
Doctor of Philosophy
in
Electrical and Computer Engineering

Waterloo, Ontario, Canada, 2024

© Nazanin Rahmati 2024

Examining Committee Membership

The following served on the Examining Committee for this thesis. The decision of the Examining Committee is by majority vote.

External Examiner:	Lotfollah Shafai Professor, Dept. of Electrical and Computer Engineering, University of Manitoba
Supervisor(s):	Amir Hamed Majedi Professor, Dept. of Electrical and Computer Engineering, University of Waterloo Amir Borji Research Assistant Professor, Dept. of Electrical and Computer Engineering, University of Waterloo
Internal Member:	Raafat Mansour Professor, Dept. of Electrical and Computer Engineering, University of Waterloo
Internal Member:	Slim Boumaiza Professor, Dept. of Electrical and Computer Engineering, University of Waterloo

Internal-External Member:	Jim Martin Associate Professor, Dept. of Physics and Astronomy, University of Waterloo
Defence Chair:	Michael Mayer Associate Professor, Dept. of Mechanical and Mechatronics Engineering, University of Waterloo

Author's Declaration

I hereby declare that I am the sole author of this thesis. This is a true copy of the thesis, including any required final revisions, as accepted by my examiners.

I understand that my thesis may be made electronically available to the public.

Abstract

The advent of 5G and 6G wireless communication networks has significantly increased interest in Ultra-Wideband (UWB) phased array antennas operating in the millimeter-wave (mm-wave) spectrum, particularly within the 24-71 GHz range. Tightly Coupled Arrays (TCAs) have emerged as a promising candidate for planar, low-profile UWB phased array implementations.

Despite the wideband capabilities of Tightly Coupled Dipole Arrays (TCDA), a primary challenge remains designing compact, low-profile baluns suitable for integration within small unit cells at high mm-wave frequencies. This thesis addresses this challenge by introducing a novel, planar Marchand balun-based antenna element that achieves an acceptable Voltage Standing Wave Ratio (VSWR) across the 22.6 to 72.6 GHz band while maintaining a thin profile suitable for mobile devices. In addition, a wideband bowtie element, utilizing the planar Marchand balun, is developed to cover two key 5G mm-wave frequency bands (24-29 GHz and 37-43 GHz). The performance of these elements is evaluated through the design, fabrication, and measurement of a small 2×2 antenna array.

In this project, in order to provide more space for accommodating the complex feeding network and reduce the cost of the array by reducing the number of required transceiver (T/R) modules, a thinned 8×8 TCDA is proposed in which only 22 elements are excited. By strategically terminating a part of unexcited elements (20 elements) and leaving the rest as open-circuit (22 elements), the array leverages mutual coupling to induce appropriate currents and maintain acceptable radiation characteristics. The scheme of excitation is obtained by investigating the current distribution among elements and with the help of optimization. Genetic Algorithm (GA) optimization is employed to determine the optimal excitation voltages and terminating impedances for broadside radiation and scanning up to 45 degrees in the E-plane.

An innovative, low-profile distributed circuit, comprising a cascade of striplines terminated to a resistance, is designed to realize the required terminating impedances. Additionally, a wideband matching network is developed for each excited port using the Real Frequency Technique (RFT) to ensure impedance matching across the operating frequency range and steering angles. The thinned 8×8 TCA, including the antenna array, terminating impedances, matching networks, and feedlines, is simulated using Ansys High Frequency Structure Simulator (HFSS). Simulation results demonstrate the effectiveness of the thinned TCDA concept, achieving acceptable input reflection coefficients at all excited ports and maintaining desired Side Lobe Level (SLL) and directivity across the entire frequency range and steering angles.

Acknowledgements

I would like to thank my supervisor, Prof. Amir Hamed Majedi for his huge support after the sudden passing of Professor Safieddin Safavi-Naeini. I would like to specially thank my supervisor, Professor Amir Borji for his patience, kindness, guidance, enormous support and deep knowledge which made this work possible. I would also like to thank my late supervisor Professor Safieddin Safavi-Naeini for the original idea and his significant contribution and support in all aspects of my professional and personal life.

I would like to thank my thesis committee members, Professor Slim Boumaiza who helped me to do my antenna measurements in his own Labratory, Prof. Raafat Mansour, Prof. Jim Martin, and Prof. Lotfollah Shafai for the time they put on reviewing my thesis and their helpful suggestions and comments on this work.

I would like to thank my dear husband, Kamyar Tahmasebpour for his great help, understanding, support, and motivation during this journey.

I would like to thank all my friends and colleagues at University of Waterloo specially, Dr. Naimeh Ghaffarian who was always like my sister, Dr. Aidin Taeb and Mohammad Chalaki who helped me a lot for my measurements, Dr. Amir Raeesi, Ardeshir Palizban whose experiences helped me a lot.

At the end, I would like to thank Huawei Technologies, canada for financially supporting this research.

Dedication

This is dedicated to my beloved family and to the memory of my dear supervisor, professor Safieddin Safavi-Naeini.

Table of Contents

Examining Committee ii

Author's Declaration iv

Abstract v

Acknowledgements vi

Dedication vii

List of Figures xi

List of Tables xxiii

List of Abbreviations xxiv

1 Introduction 1

1.1 Motivation 1

1.2 Contribution 3

1.3 Thesis Outline 6

2 Literature Review 7

2.1 Ultra-Wideband Antenna Arrays 7

2.2 Basic Concept of Tightly Coupled Arrays 8
2.3 Tightly Coupled Array's Feeding Challenges 13
2.4 Tightly Coupled Array's Bandwidth Improvement 17
2.5 Thinned Tightly Coupled Antenna Array 19
2.6 Conclusion 21

3 Design of a Wideband Tightly Coupled Bowtie Array 22
3.1 Design of a Thin, Planar UWB Bowtie Element for Tightly Coupled mm-Wave Phased Arrays 23
3.1.1 Design Requirements 23
3.1.2 Bowtie Element Design with Modified Planar Marchand Balun . . . 23
3.1.3 Simulation Results 28
3.2 Design of a Small 2 × 2 Wideband, Tightly Coupled Bowtie Array for mm-Wave 5G Applications 33
3.2.1 Bowtie Element Design 34
3.2.2 Design and Simulation of the 2 × 2 Array 38
3.2.3 Fabrication and Measurement of the 2 × 2 Array 43
3.3 Design of a 8 × 8 Tightly Coupled Bowtie Array 48
3.4 Conclusion 53

4 Thinned Tightly Coupled Bowtie Array 54
4.1 Thinned Array Excitation Scheme 55
4.2 Ideal Terminating Impedances 57
4.3 Optimization Procedure 59
4.4 The thinned Array Pattern Calculation 63
4.5 50Ω Terminating Loads 65
4.6 Optimization Results of the Thinned Tightly Coupled Bowtie Array 66
4.7 Thinned Array Stackup 72
4.8 Realization of Terminating Impedances 72
4.9 Conclusion 78

5 Design of a Wideband Antenna Matching Network **88**
5.1 Matching Network Optimization Using Real Frequency Technique 89
5.2 Circuit Level Optimization of the Matching Network 95
5.3 Full Wave Optimization of the Matching Network 100
5.4 Design of the Feeding Network 104
5.5 Thinned 8 × 8 Tightly Coupled Bowtie Array 106
5.6 Feed Network Calibration 109
5.7 Simulation Results 110
5.8 Conclusion 112

6 Concluding Remarks and Future Works **122**
6.1 Summary and Contribution 122
6.2 Future Work 124

References **130**

APPENDICES **136**

A **137**
A.1 Thinned 32 × 13 TCDA Design 137
A.2 Thinned TCDA Optimization 138

B **140**
B.1 Calculation of Zeros 142

C **143**
C.1 Designing a Lossless Distributed Matching Network 143
C.1.1 Synthesis Procedure 145
C.2 Modified Real Frequency Technique for Lossy Circuits 145
C.2.1 Synthesis Procedure 148

List of Figures

2.1 a hypothetical rectangular waveguide supporting TEM mode (a) Waveguide of small height and antenna of equal height [21]. (b) Waveguide of substantial height and antenna of lesser effective height [21]. (c) Equivalent transformer coupling the antenna with the waveguide [21]. 10

2.2 Munk's equivalent transmission line model for an infinite periodic array of short dipoles [24]. 12

2.3 (a) Transmission line model of a TCDA above ground plane [24]. (b) Smithchart showing the impedance Z_{1+}, $2R_{A0}||Z_{1+}$, and $2R_{A0}||Z_{1+} + jX_A$ [24]. 13

2.4 Wideband Marchand balun presented in [30] (a) The balun configuration [30]. (b) The input impedance of the balanced line (phase and magnitude) [30]. (c) The balun's lumped equivalent circuit model [30]. (d) The balun's transmission line circuit model [30]. 15

2.5 (a) Unit cell of TCDA-IB [29]. (b) TCDA-IB equivalent circuit fed by a Marchand balun [29]. 16

2.6 A unit cell design sampled from a periodic array with roughly $\lambda/2$ spacing in both directions [3]. 17

2.7 (a) Electric field distribution at the common mode resonance frequency in an unbalanced fed TCDA [28]. (b) Top view of a PUMA unit cell with shorting vias [28]. 18

2.8 (a) Transmission model of a TCDA with a superstrate on top and backed by a ground plane [24]. (b) Smithchart showing the impedance Z_{1+}, $Z_{1-}||Z_{1+}$, and $Z_{1-}||Z_{1+} + jX_A$ [24]. 19

3.1 (a) Transmission line model of a TCDA and its feeding network including the wideband Marchand balun [3]. (b) Edge view of the unit-cell design shown in Fig. 3.2 with tuning elements of the balun labeled. A microstrip excitation is assumed (bottom left) [3]. 24

3.2 (a) a unit cell design sampled from a periodic array with roughly $\lambda/2$ spacing in both directions [3] (b) Upper layer [3] (c) side view of the unit cell [3](d) Bottom layer [3] 25

3.3 Infinite array VSWR of the element shown in Fig. 3.2 at broadside and $\pm 45^o$ scanning in E and H planes. The 5G and Industrial, Scientific, and Medical (ISM) bands are highlighted and are observed to fall in the passband of the array [3] 27

3.4 Designed unit cell [2] (a) 3D view. (b) side view. (c) Upper layer. (d) Bottom layer 27

3.5 Key limiting parameters for PCB fabrication labeled and provided in Table 3.3 [3] 28

3.6 Simulation results of the optimized element design shown in Fig. 3.4 in an infinite periodic array environment [2] (a) active VSWR for broadside radiation and when steering up to 30^o in E and H planes (b) Realized gain and directivity (co- and cross-polarization) for broadside radiation (c) Realized co- and cross-polarized gain at 27 GHz, 40 GHz, and 64 GHz in E-Plane. (d) Realized co- and cross-polarized gain at 27 GHz, 40 GHz, and 64 GHz in H-Plane. (e) Realized co- and cross-polarized gain at 27 GHz in $\phi = 223^o, 43^o$ where cross-polarization is maximized at this frequency. (f) Realized co- and cross-polarized gain at 40 GHz in $\phi = 334^o, 154^o$ where cross-polarization is maximized at this frequency. (g) Realized co- and cross-polarized gain at 64 GHz in $\phi = 190^o, 10^o$ where cross-polarization is maximized at this frequency. 30

3.7 The simulation results of the design shown in Fig. 3.4 for different S_2 parameter and when $D_3 = 0.3mm$. The rest of the parameters shown in Fig. 3.4 are the same as Table 3.2 (a) The real part of active input impedance. (b) The imaginary part of active input impedance. (c) The active input reflection coefficient (S_{11}). 32

3.8 (a) The 3D design of the unit cell with PEC wall. (b) The active input reflection coefficient (S_{11}) for the design with PEC wall and by using via fence. (c) The real part of active input impedance for the design with PEC wall and by using via fence. (d) The imaginary part of active input impedance for the design with PEC wall and by using via fence. 33

3.9 Bowtie element (a) 3D view. (b) Top view. (c) Side view. 35

3.10 simulation results of the designed bowtie element shown in Fig. 3.9 (a) VSWR versus frequency when the beam is steering in E-Plane. (b) VSWR versus frequency when the beam is steering in E-Plane. (c) Simulated realized gain (dBi) for broadside radiation. (d) Simulated realized gain at 27 GHz, 40 GHz in E-Plane. (e) Simulated realized gain at 27 GHz, 40 GHz in H-Plane. (f) Simulated realized gain at 27 GHz in $\phi = 24^o, 204^o$ plane where cross-polarization in maximized. (g) Simulated realized gain at 40 GHz in $\phi = 22^o, 202^o$ plane where cross-polarization in maximized. 37

3.11 Designed 2×2 tightly coupled bowtie array [4] (a) 3D view. (b) side view. (c) Top view. (d) Bottom view. (e) bottom view zoomed in feedlines . . . 40

3.12 simulation results of the designed 2×2 tightly coupled bowtie array shown in Fig. 3.11a [4] (a) Active input reflection coefficient (S_{11}) at all connector ports for broadside radiation. (b) Realized co- and cross-polarization gain for broadside radiation. (c) Realized co- and cross-polarized gain at 27 GHz, 40 GHz in E-Plane. (d) Realized co- and cross-polarized gain at 27 GHz, 40 GHz in H-Plane. (e) Realized co- and cross-polarized gain at 27 GHz in $\phi = 241^o, 61^o$ Plane where cross-polarization is maximized. (f) Realized co- and cross-polarized gain at 40 GHz in $\phi = 117^o, -63^o$ Plane where cross-polarization is maximized. (g) Antenna array efficiency for two different board sizes. 42

3.13 Fabricated 2×2 tightly coupled bowtie array (a) Top view (b) bottom view 43

3.14 (a) Measurement set up for measuring the antenna's scattering parameters (b) The measured and simulated results of the active reflection coefficient when all elements are excited with the same phase and amplitude at all four ports 44

3.15 (a) Far-field measurement setup for measuring the 2×2 antenna pattern (b) Simulated and measured E-Plane pattern at 27 GHz, 40 GHz. (c) Simulated and measured H-Plane pattern at 27 GHz, 40 GHz. (d) The input reflection coefficient of the splitter connected to the antenna 46

3.16 (a) The measurement setup for measuring the insertion loss of the splitter and cables. (b) The magnitude of the transmission coefficient measured for all 4 cables connected to the splitter. (c) The phase of the transmission coefficient measured for all 4 cables connected to the splitter. 47

3.17 Measured active input reflection coefficient of the 2×2 array by calibrating the insertion loss of the splitter and cables (black curve) and by measuring the scattering parameters and using the equation (3.1) (blue curve). 48

3.18 8×8 tightly coupled array (a) 3D view. (b) side view 50

3.19 The simulation results of the designed 8×8 antenna array shown in Fig. 3.18 excited with 50Ω waveports (a) Active S_{11} at port numbers 1, 4, 9, 13, 17, 21, 28. (b) Realized gain versus frequency for broadside radiation. (c) Antenna pattern in E-Plane at 27 GHz, 35 GHz, 40 GHz. (d) Antenna pattern in H-Plane at 27 GHz, 35 GHz, 40 GHz Bottom layer 51

3.20 Steering the pattern of the designed 8×8 TCA shown in Fig. 3.18 (a) In E-Plane at 27 GHz. (b) In H-Plane at 27 GHz. (c) In E-Plane at 40 GHz. (d) In H-Plane at 40 GHz. 52

3.21 The magnitude of mutual scattering parameter in dB between the element numbers 28,29 (mutual coupling in H-Plane), between the element numbers 28,36 (mutual coupling in E-Plane), and between the element numbers 28,37 (mutual coupling in Diagonal plane). 53

4.1 The initially designed periodic thinned array with 50% thinning factor . . 55

4.2 The non-periodic thinned array configuration with 66% thinning factor . . 56

4.3 The radiation result of the thinned 8×8 array shown in Fig. 4.2 at 43 GHz when the beam is steered to 45^o in E-Plane if *all* 42 unexcited ports were left open (a) Radiation pattern. (b) Thinned array directivity in E-Plane in compare with the directivity of a fully excited array. 57

4.4 *Ideal* terminating impedances at 40GHz when the beam is steered to $\theta = 30^o, \phi = 0^o$ (a) Real part. (b) Imaginary part. 59

4.5 Defined mask compared with the pattern of a fully excited array at 40 GHz for broadside radiation (a) E-Plane. (b) H-Plane 61

4.6 Flowchart showing the optimization procedure 62

4.7 Optimization results at 43 GHz when the 20 terminated ports shown in Fig. 4.2 are loaded with 50Ω resistance and the beam is steered to $\theta = 45^o, \phi = 0^o$ (a) optimized 3D pattern of the thinned TCDA. (b) optimized and desired directivity in E-plane. 66

4.8 Optimization results of the thinned TCDA at 43 GHz (a) Optimized 3D pattern for broadside radiation. (b) Optimized and desired directivity in E-Plane for broadside radiation. (c) Optimized 3D pattern scanned to $\theta = 15^o$ in E-Plane. (d) Optimized and desired directivity in E-Plane scanned to $\theta = 15^o$. (e) Optimized 3D pattern scanned to $\theta = 30^o$ in E-Plane. (f) Optimized and desired directivity in E-Plane scanned to $\theta = 30^o$. (g) Optimized 3D pattern scanned to $\theta = 45^o$ in E-Plane. (h) Optimized and desired directivity in E-Plane scanned to $\theta = 45^o$. 68

4.9 Optimization results of the thinned TCDA at 37 GHz (a) Optimized 3D pattern for broadside radiation. (b) Optimized and desired directivity in E-Plane for broadside radiation. (c) Optimized 3D pattern scanned to $\theta = 15^o$ in E-Plane. (d) Optimized and desired directivity in E-Plane scanned to $\theta = 15^o$. (e) Optimized 3D pattern scanned to $\theta = 30^o$ in E-Plane. (f) Optimized and desired directivity in E-Plane scanned to $\theta = 30^o$. (g) Optimized 3D pattern scanned to $\theta = 45^o$ in E-Plane. (h) Optimized and desired directivity in E-Plane scanned to $\theta = 45^o$. 69

4.10 Optimization results of the thinned TCDA at 29 GHz (a) Optimized 3D pattern for broadside radiation. (b) Optimized and desired directivity in E-Plane for broadside radiation. (c) Optimized 3D pattern scanned to $\theta = 15^o$ in E-Plane. (d) Optimized and desired directivity in E-Plane scanned to $\theta = 15^o$. (e) Optimized 3D pattern scanned to $\theta = 30^o$ in E-Plane. (f) Optimized and desired directivity in E-Plane scanned to $\theta = 30^o$. (g) Optimized 3D pattern scanned to $\theta = 45^o$ in E-Plane. (h) Optimized and desired directivity in E-Plane scanned to $\theta = 45^o$. 70

4.11 Optimization results of the thinned TCDA at 25 GHz (a) Optimized 3D pattern for broadside radiation. (b) Optimized and desired directivity in E-Plane for broadside radiation. (c) Optimized 3D pattern scanned to $\theta = 15^o$ in E-Plane. (d) Optimized and desired directivity in E-Plane scanned to $\theta = 15^o$. (e) Optimized 3D pattern scanned to $\theta = 30^o$ in E-Plane. (f) Optimized and desired directivity in E-Plane scanned to $\theta = 30^o$. (g) Optimized 3D pattern scanned to $\theta = 45^o$ in E-Plane. (h) Optimized and desired directivity in E-Plane scanned to $\theta = 45^o$. 71

4.12 The stack up of the optimized thinned 8×8 tightly coupled bowtie array 72

4.13 Optimized Terminating impedances at port numbers (a) 4, Imaginary part ($X\Omega$). (b) 4, real part ($R\Omega$). (c) 27, Imaginary part ($X\Omega$). (d) 27, real part ($R\Omega$). (e) 36, Imaginary part ($X\Omega$). (f) 36, real part ($R\Omega$). (g) 54, Imaginary part ($X\Omega$). (h) 54, real part ($R\Omega$). 73

4.14 The RLC circuit synthesizing the rational function in equation (4.9) 74

4.15 Resistor CH02016 from VISHAY company. (a) 3D view. (b) Side view. (c) Top view. 77

4.16 The ADS optimization result for realization of the terminating impedance at port NO. 4 (a) The optimized circuit. (b) The reactive part of the optimized circuit's input impedance in compare with the required GA optimized reactance. (c) The resistive part of the optimized circuit's input impedance in compare with the required GA optimized resistance. 79

4.17 The ADS optimization result for realization of the terminating impedance at port NO. 22 (a) The optimized circuit. (b) The reactive part of the optimized circuit's input impedance in compare with the required GA optimized reactance. (c) The resistive part of the optimized circuit's input impedance in compare with the required GA optimized resistance. 80

4.18 The ADS optimization result for realization of the terminating impedance at port NO. 47 (a) The optimized circuit. (b) The reactive part of the optimized circuit's input impedance compared with the required GA optimized reactance. (c) The resistive part of the optimized circuit's input impedance in compare with the required GA optimized resistance. 81

4.19 The ADS optimization result for realization of the terminating impedance at port NO. 61 (a) The optimized circuit. (b) The reactive part of the optimized circuit's input impedance in compare with the required GA optimized reactance. (c) The resistive part of the optimized circuit's input impedance in compare with the required GA optimized resistance. 82

4.20 Distributed circuit optimized using Ansys HFSS to realize the required terminating impedances at all 20 terminated ports. (a) 3D view. (b) Top view showing the optimized variables of the design. (c) Bottom view. (d) Side view. 83

4.21 Full wave optimization result for the realization of the required terminating impedance at port NO. 4 (a) The optimized distributed circuit with $w_1 = 0.12mm, w_2 = 1.3mm, w_3 = 0.7mm, w_4 = 0.5mm, w_5 = 0.3mm, w_6 = 0.12mm, l_1 = 0.6mm, l_2 = 0.4mm, l_3 = 1mm, l_4 = 0.5mm, l_5 = 0.2mm, l_6 = 0.4mm, R = 75\Omega$. (b) The reactive part of the optimized circuit's input impedance in compare with the required GA optimized reactance. (c) The resistive part of the optimized circuit's input impedance in compare with the required GA optimized resistance. 84

4.22 Full wave optimization result for the realization of the required terminating impedance at port NO. 22 (a) The optimized distributed circuit with $w_1 = 0.12mm, w_2 = 1.3mm, w_3 = w_4 = w_5 = 1.1mm, w_6 = 0.16mm, l_1 = 0.6mm, l_2 = 0.4mm, l_3 = 0.95mm, l_4 = 0.5mm, l_5 = 0.2mm, l_6 = 0.5mm, R = 100\Omega$. (b) The reactive part of the optimized circuit's input impedance in compare with the required GA optimized reactance. (c) The resistive part of the optimized circuit's input impedance in compare with the required GA optimized resistance. 85

4.23 Full wave optimization result for the realization of the required terminating impedance at port NO. 47 (a) The optimized distributed circuit with $w_1 = 0.12mm, w_2 = 1.3mm, w_3 = w_4 = 1mm, w_5 = 0.3mm, w_6 = 0.3mm, l_1 = 0.5mm, l_2 = 0.4mm, l_3 = 0.8mm, l_4 = 0.5mm, l_5 = 0.3mm, l_6 = 0.4mm, R = 100\Omega$. (b) The reactive part of the optimized circuit's input impedance in compare with the required GA optimized reactance. (c) The resistive part of the optimized circuit's input impedance in compare with the required GA optimized resistance. 86

4.24 Full wave optimization result for the realization of the required terminating impedance at port NO. 61 (a) The optimized distributed circuit with $w_1 = 0.12mm, w_2 = 1.3mm, w_3 = w_4 = w_5 = 1mm, w_6 = 0.12mm, l_1 = 0.6mm, l_2 = 0.45mm, l_3 = 0.8mm, l_4 = 0.5mm, l_5 = 0.2mm, l_6 = 0.5mm, R = 100\Omega$. (b) The reactive part of the optimized circuit's input impedance in compare with the required GA optimized reactance. (c) The resistive part of the optimized circuit's input impedance in compare with the required GA optimized resistance. 87

5.1 The structure of the optimized matching network using modified real frequency technique 90

5.2 The optimized input reflection coefficient of 4 and 8 stage lossless distributed equalizers at excited port number 53 using real frequency technique. 91

5.3 The optimization result of the 3 stages distributed matching network with lossy junctions using Real Frequency Technique at excited port number 3 with optimized parameters: $R_1 = 956.28\Omega, R_2 = 791.89\Omega, R_3 = 205.25\Omega, Z_{o1} = 76.64\Omega, Z_{o2} = 103.09\Omega$ shown in Fig. 5.1 (a) The input reflection coefficient (dB). (b) The transmission coefficient (dB). (c) The smith chart comparing the input reflection coefficient of the antenna (L_{11}) with the input reflection coefficient of the matched network (S_{11}) for different steering angles. 92

5.4 The optimization result of the 3 stages distributed matching network with lossy junctions using Real Frequency Technique at excited port number 28 with optimized parameters: $R_1 = 4392\Omega, R_2 = 730.7\Omega, R_3 = 143.8\Omega, Z_{o1} = 67.14\Omega, Z_{o2} = 95.12\Omega$ shown in Fig. 5.1 (a) The input reflection coefficient (dB). (b) The transmission coefficient (dB). (c) The smith chart comparing the input reflection coefficient of the antenna (L_{11}) with the input reflection coefficient of the matched network (S_{11}) for different steering angles. 93

5.5 The optimization result of the 3 stages distributed matching network with lossy junctions using Real Frequency Technique at excited port number 44 with optimized parameters: $R_1 = 3586\Omega, R_2 = 725\Omega, R_3 = 161.3\Omega, Z_{o1} = 78.86\Omega, Z_{o2} = 100.44\Omega$ shown in Fig. 5.1 (a) The input reflection coefficient (dB). (b) The transmission coefficient (dB). (c) The smith chart comparing the input reflection coefficient of the antenna (L_{11}) with the input reflection coefficient of the matched network (S_{11}) for different steering angles. 94

5.6 The Full wave simulation design extracting the scattering parameter model of the via connecting the 3rd layer to the 6th layer (a) 3D view. (b) Side view showing the layers and the via connecting the antenna port on 3rd layer to the 6th layer. 96

5.7 The circuit design of the three stage distributed matching network with 3 resistant junctions connected to the antenna when beam is steered to broadside 96

5.8 The result of the circuit level optimization of the 3 stage matching network with lossy junctions at excited port number 3 with optimized parameters: $R_1 = 2024\Omega, R_2 = 257.5\Omega, R_3 = 128\Omega, L_1 = 1.63mm, L_2 = 1.52mm, W_1 = 0.318mm, W_2 = 0.437mm, G = 0.2mm$ shown in Fig. 5.7 (a) The input reflection coefficient of the matched network. (b) The transmission coefficient of the optimized matching network defined in equation C.1. (c) The smith chart comparing the input reflection coefficient of the antenna (L_{11}) with the input reflection coefficient of the matched network (S_{11}) for different steering angles. 97

5.9 The result of the circuit level optimization of the 3 stage matching network with lossy junctions at excited port number 28 with optimized parameters: $R_1 = 396\Omega, R_2 = 453.5\Omega, R_3 = 117.5\Omega, L_1 = 0.915mm, L_2 = 0.936mm, W_1 = 0.241mm, W_2 = 0.156mm, G = 0.2mm$ shown in Fig. 5.7 (a) The input reflection coefficient of the matched network. (b) The transmission coefficient of the optimized matching network defined in equation C.1. (c) The smith chart comparing the input reflection coefficient of the antenna (L_{11}) with the input reflection coefficient of the matched network (S_{11}) for different steering angles. 98

5.10 The result of the circuit level optimization of the 3 stage matching network with lossy junctions at excited port number 44 with optimized parameters: $R_1 = 1705.5\Omega, R_2 = 163.5\Omega, R_3 = 124.5\Omega, L_1 = 1.77mm, L_2 = 1.35mm, W_1 = 0.34mm, W_2 = 0.46mm, G = 0.2mm$ shown in Fig. 5.7 (a) The input reflection coefficient of the matched network. (b) The transmission coefficient of the optimized matching network defined in equation C.1. (c) The smith chart comparing the input reflection coefficient of the antenna (L_{11}) with the input reflection coefficient of the matched network (S_{11}) for different steering angles. 99

5.11 The result of the full wave optimization of the 3 stage matching network with lossy junctions at excited port number 3 with optimized parameters: $R_1 = OC, R_2 = 250\Omega, R_3 = 100\Omega, L_1 = 1.63mm, L_2 = 1.63mm, W_1 = 0.32mm, W_2 = 0.43mm, G = 0.2mm$ (a) The structure of the matching network (b) The input reflection coefficient of the matched network. (c) The transmission coefficient of the optimized matching network defined in equation C.1. (d) The smith chart comparing the input reflection coefficient of the antenna (L_{11}) with the input reflection coefficient of the matched network (S_{11}) for different steering angles. 101

5.12 The result of the full wave optimization of the 3 stage matching network with lossy junctions at excited port number 28 with optimized parameters: $R_1 = 500\Omega, R_2 = 500\Omega, R_3 = 100\Omega, L_1 = 0.86mm, L_2 = 1mm, W_1 = 0.24mm, W_2 = 0.24mm, G = 0.2mm$ (a) The structure of the matching network (b) The input reflection coefficient of the matched network. (c) The transmission coefficient of the optimized matching network defined in equation C.1. (d) The smith chart comparing the input reflection coefficient of the antenna (L_{11}) with the input reflection coefficient of the matched network (S_{11}) for different steering angles. 102

5.13 The full wave optimization results of the 3 stage distributed matching network with lossy junctions at excited port number 44 with optimized parameters: $R_1 = 500\Omega, R_2 = 500\Omega, R_3 = 100\Omega, L_1 = 1.77mm, L_2 = 1.77mm, W_1 = 0.37mm, W_2 = 0.37mm, G = 0.2mm$ (a) The structure of the matching network (b) The input reflection coefficient of the matched network. (c) The transmission coefficient of the optimized matching network defined in equation C.1. (d) The smith chart comparing the input reflection coefficient of the antenna (L_{11}) with the input reflection coefficient of the matched network (S_{11}) for different steering angles. 103

5.14 A preview of the whole thinned array structure showing the 22 feedlines connected to 22 edge connectors 104

5.15 Feeding line design (a) 3D view. (b) Side view. (c) Bottomn view showing the GCPW feed lines (d) Top view showing the 22 antenna ports on 3^{rd} layer. 105

5.16 The input reflection coefficient of the feeding network design shown in Fig. 5.15 which is connected to the 8×8 thinned antenna array with known optimized voltages and currents on 22 excited ports for the whole frequency bands and steering range (a) at Exited port number 3 (Exc_3 shown in Fig. 5.15a). (b) at Exited port number 23 (Exc_7 shown in Fig. 5.15a). (c) at Exited port number 28 (Exc_9 shown in Fig. 5.15a). (d) at Exited port number 39 (Exc_{14} shown in Fig. 5.15a). (e) at Exited port number 44 (Exc_{16} shown in Fig. 5.15a). (f) at Exited port number 62 (Exc_{22} shown in Fig. 5.15a). . . . 106

5.17 Thinned tightly coupled bowtie array structure (a) 3D view. (b) Top Layer 1. (c) Layer 2. (d) Layer 4. (e) stack up showing all layers. (f) Bottom Layer 6. 109

5.18 The input reflection coefficient of the simulated 8×8 thinned array shown in Fig. 5.17 at two frequency bands (25-29 GHz, 37-43 GHz) and for steering angles broadside, $15^o, 30^o, 45^o$ in E-Plane at exited port numbers (a) 3. (b) 23. (c) 28. (d) 39. (e) 44. (f) 62. 114

5.19 Simulated radiation pattern of the thinned array at 43 GHz for (a) broadside radiation. (c) scanned to $\theta = 15^o$ in E-Plane. (e) scanned to $\theta = 30^o$ in E-Plane. (g) scanned to $\theta = 45^o$ in E-Plane. Simulated Directivity of the thinned and fully excited array at 43 GHz for (b) broadside radiation. (d) scanned to $\theta = 15^o$ in E-Plane. (f) scanned to $\theta = 30^o$ in E-Plane. (h) scanned to $\theta = 45^o$ in E-Plane. 115

5.20 Simulated radiation pattern of the thinned array at 40 GHz for (a) broadside radiation. (c) scanned to $\theta = 15^o$ in E-Plane. (e) scanned to $\theta = 30^o$ in E-Plane. (g) scanned to $\theta = 45^o$ in E-Plane. Simulated Directivity of the thinned and fully excited array at 40 GHz for (b) broadside radiation. (d) scanned to $\theta = 15^o$ in E-Plane. (f) scanned to $\theta = 30^o$ in E-Plane. (h) scanned to $\theta = 45^o$ in E-Plane. 116

5.21 Simulated radiation pattern of the thinned array at 37 GHz for (a) broadside radiation. (c) scanned to $\theta = 15^o$ in E-Plane. (e) scanned to $\theta = 30^o$ in E-Plane. (g) scanned to $\theta = 45^o$ in E-Plane. Simulated Directivity of the thinned and fully excited array at 37 GHz for (b) broadside radiation. (d) scanned to $\theta = 15^o$ in E-Plane. (f) scanned to $\theta = 30^o$ in E-Plane. (h) scanned to $\theta = 45^o$ in E-Plane. 117

5.22 Simulated radiation pattern of the thinned array at 25 GHz for (a) broadside radiation. (c) scanned to $\theta = 15^o$ in E-Plane. (e) scanned to $\theta = 30^o$ in E-Plane. (g) scanned to $\theta = 45^o$ in E-Plane. Simulated Directivity of the thinned and fully excited array at 25 GHz for (b) broadside radiation. (d) scanned to $\theta = 15^o$ in E-Plane. (f) scanned to $\theta = 30^o$ in E-Plane. (h) scanned to $\theta = 45^o$ in E-Plane. 118

5.23 Simulated radiation pattern of the thinned array at 27 GHz for (a) broadside radiation. (c) scanned to $\theta = 15^o$ in E-Plane. (e) scanned to $\theta = 30^o$ in E-Plane. (g) scanned to $\theta = 45^o$ in E-Plane. Simulated Directivity of the thinned and fully excited array at 27 GHz for (b) broadside radiation. (d) scanned to $\theta = 15^o$ in E-Plane. (f) scanned to $\theta = 30^o$ in E-Plane. (h) scanned to $\theta = 45^o$ in E-Plane. 119

5.24 Simulated radiation pattern of the thinned array at 29 GHz for (a) broadside radiation. (c) scanned to $\theta = 15^o$ in E-Plane. (e) scanned to $\theta = 30^o$ in E-Plane. (g) scanned to $\theta = 45^o$ in E-Plane. Simulated Directivity of the thinned and fully excited array at 29 GHz for (b) broadside radiation. (d) scanned to $\theta = 15^o$ in E-Plane. (f) scanned to $\theta = 30^o$ in E-Plane. (h) scanned to $\theta = 45^o$ in E-Plane. 120

5.25 The efficiency of the designed thinned array shown in Fig. 5.17 (a) The simulated radiation efficiency and the simulated total efficiency including VSWR mismatch. (b) Simulated and calculated total efficiency. (C) Calculated total efficiency in compare with calculated matching network efficiency. 121

6.1 The stackup of the structure including 4450T bondply layers. 125

6.2 The building block of beamformer Eval board ADMV4928 from Analog Device. 126

6.3 The dual-polarized, triple-band antenna element [6]. (a) 3D view (b) side view (c) layer 1 showing the antenna element (d) layer 2 showing the resonant patch 128

A.1 (a) 13×32 tightly coupled dipole array. (b) Thinned array configuration. . 138

A.2 optimized directivity in E-Plane when unexcited ports are terminated to complex impedances (R+jX) and the beam is steered up to broadside, 15^o, 30^o, 45^o at 20 GHz, 50 GHz, and 70 GHz (a) at 20 GHz, broadside (b) at 20 GHz steering to $\theta = 15^o$, $\phi = 0^o$. (c) at 20 GHz steering to $\theta = 30^o$, $\phi = 0^o$. (d) at 20 GHz steering to $\theta = 45^o$, $\phi = 0^o$. (e) at 50 GHz for broadside (f) at 50 GHz steering to $\theta = 15^o$, $\phi = 0^o$. (g) at 50 GHz steering to $\theta = 30^o$, $\phi = 0^o$. (h) at 50 GHz steering to $\theta = 45^o$, $\phi = 0^o$. (i) at 70GHz for broadside. (j) at 70 GHz steering to $\theta = 15^o$, $\phi = 0^o$. (k) at 70 GHz steering to $\theta = 30^o$, $\phi = 0^o$. (l) at 70 GHz steering to $\theta = 45^o$, $\phi = 0^o$. . . . 139

C.1 the building block of the lossless, reciprocal equalizer connected to the antenna load 146

C.2 Multistage lossless distributed equalizer 146

C.3 The real network (N) of the multistage distributed equalizer with lossy junctions [56] 148

C.4 The image network ($\overline{N}$) of the multistage distributed equalizer with lossy junctions [56] 148

List of Tables

1.1 Desired Antenna Array Characteristics 2

3.1 Desired Requirements 23
3.2 Optimized Parameters' values (mm) shown in Fig. 3.4 [2] 28
3.3 Minimum achievable dimensions of the key parameters shown in Fig. 3.5 [3][54]. 28
3.4 Optimized Parameters' values (mm) shown in Fig. 3.9. 36
3.5 Optimized Parameters' values (mm) shown in Fig. 3.11. 41

4.1 Dimensions (mm) of the resistor shown in Fig. 4.15 78
4.2 Electrical specification of the resistor shown in Fig. 4.15 78

List of Abbreviations

ADS Advanced Design System 76

BAVA Balanced Antipodal Vivaldi Array 7, 8

BOR Body of Revolution 7

BT Bismaleimide Triazine 26, 137

BTA Banyan Tree Antenna 7, 8

CPW Coplanar Waveguide 95

CSA Current Sheet Antenna 9

DM-BAVA Doubly Mirrored Balanced Antipodal Vivaldi Array 7, 8

DVGA Digital Variable Gain Amplifier 124, 125

ECal Electronic Calibration 43

EmRG Emerging Radio System Group 3, 44

ETI Electromagnetic Technology industries 44

FSS Frequency Selective Surface 18

GA Genetic Algorithm 4, 6, 20, 21, 53, 54, 59–61, 65, 66, 75, 76, 78, 109, 110, 129

GCPW Grounded Coplanar Waveguide 3, 5, 26, 34, 38, 72, 76, 78, 95, 104, 107, 110–112

HFSS High Frequency structure simulator 5, 6, 26, 34, 38, 57, 63, 76, 77, 95, 100, 104, 106, 112

LTE Long Term Evolution 1

MEMS Micro Electronic Mechanical Systems 126, 127

mm-Wave Millimeter Wave 1–4, 6, 8, 14, 16, 19, 21–24, 33, 34, 53, 127

PCB Printed Circuit Board 3, 7, 24, 26, 38, 43, 53, 95

PEC Perfect Electric Conductor 9, 31

PMC Perfect Magnetic Conductor 9

PNA Power Network Analyzer 43, 44

PSO Particle Swarm Optimization 20

PUMA Planar Ultra-wideband Modular Antenna 17

RF Radio Frequency 38, 126

RFT Real Frequency Technique 5, 6, 91, 112

SA Simulated Anealing 20

SLL Side Lobe Level 2, 4–6, 20, 50, 53, 54, 56, 58–60, 65–67, 78, 111, 113, 128, 138

SoC System on Chip 2, 3, 16, 22, 23, 39

SRFT Simplified Real Frequency Technique 89, 144

T/R Transceiver 2, 3, 15, 19, 20, 54, 124

TCA Tightly Coupled Array 2–4, 6, 8, 9, 13, 14, 17–19, 21, 22, 34, 49, 56, 59, 124

TCDA Tightly Coupled Dipole Array 3, 5, 12–15, 18, 20, 22, 34, 54, 60

TCDA-IB Tightly Coupled Dipole with Integrated Balun 14

TEM Transverse Electromagnetic Mode 9, 10

TPG Transducer Power Gain 143

UWB Ultra-Wideband 1, 3, 6–8, 20–22, 34, 127

VM Vector Modulator 124, 125

VSWR Voltage Standing Wave Ratio 2, 3, 6–9, 11, 13, 14, 17–20, 24, 28, 34, 35, 38, 39, 111

WSA Wavelength Scaled Array 20

Chapter 1

Introduction

1.1 Motivation

The impending advent of 5G mobile network technology, provides higher data transfer rate (tens of Gbit/s) with lower latency (a few millisecond) compared to previous generations of cellular networks. In order to achieve such high data rates, the 5G frequency band is extended to Millimeter Wave (mm-Wave) frequencies above 24 GHz up to around 80 GHz. Basically the 5G frequency spectrum is divided into two categories: 1- The sub-6 GHz used by the 5G base station and the previous generations of communication system such as 4G and Long Term Evolution (LTE). 2- The mm-Wave frequencies above 24 GHz which are used in 5G cell-phone devices as well as automative radars, satellite communications, and imaging. The exact standard 5G mm-Wave frequency bands vary from country to country. Therefore, devices that are targeted for global market, must be able to cover all different frequency bands. The commonly used 5G mm-Wave frequencies are the three frequency bands 24-29 GHz, 37-41 GHz, and 57-71 GHz. Consequently, in recent years, multi-band or Ultra-Wideband (UWB) phased array antennas capable of covering these three frequency bands have attracted a lot of attentions.

Furthermore, any other multi-functional multi-band communication system, can also benefit from an UWB array by consolidating multiple antennas into one single radiating aperture that can simultaneously accommodate multiple frequency bands, multiple beams, and multiple polarizations. This greatly reduces the size and cost of the system. Basically, there is a high path loss and penetration loss at mm-Wave frequencies above 20 GHz; so, an UWB phased array antenna with high directivity and adaptive beam scanning capability both in base station and mobile terminal is required.

This thesis presents a low profile, wideband thinned phased array antenna which can cover the two commonly used mm-Wave frequency bands (25-29 GHz and 37-43 GHz) required for the fifth and sixth generation of communication system. Table 1.1 shows the the desired antenna characteristics. The antenna array must be small enough to be used in 5G System on Chip (SoC) devices. So, the overall size of the array must not exceed $25mm \times 25mm$ and the total available thickness is less than 1.5 mm. Since the size is limited, the required gain is not high and it is acceptable to be above 10 dB for broadside radiation and for the whole frequency of operation. The proposed antenna array must be capable of steering the beam up to $\pm 45^o$ with acceptable side lobe levels shown in Table 1.1. The required Side Lobe Level (SLL) is better than -13 dB for broadside radiation and it can decrease up to -8 dB when the beam is scanned out to $\pm 45^o$.

Table 1.1: Desired Antenna Array Characteristics

Antenna Characteristics	Desired Performance
Frequency	25-29 GHz, 37-43 GHz
Antenna Array Gain	$>$ 10 dBi for broadside radiation
Beam Scanning Range	$\pm 45^o$
Side Lobe Level	< -10 dB for Broadside < -8 dB steering upto $\pm 45^o$
Dimension	$25mm \times 25mm$
Total Antenna Thickness	$< 1.5mm$

Considering the aforementioned specifications, Tightly Coupled Antenna Arrays (TCAs) are a good candidate since they are low profile, planar antenna arrays that can provide ultra-wideband Voltage Standing Wave Ratio (VSWR) bandwidth with large beam scanning capability. Structurally, Tightly Coupled Array (TCA)s are similar to ordinary arrays except that the radiating elements are closely spaced or *tightly coupled* instead of being separated by roughly half a wavelength. Strong mutual coupling among neighboring elements enables TCA to operate over an extremely wide VSWR bandwidth while being a low profile structure.

Although the TCAs can work over a wide frequency bandwidth, the small separation between elements makes small room to fit all the Transceiver (T/R) modules including phase shifters, matching networks and feedlines for each antenna element. Additionally, in Tightly Coupled Dipole Arrays (TCDAs), any dipole element needs a balun to prevent from the common mode resonances that can decrease the VSWR bandwidth and may results in unwanted radiations from the vertical feedlines. On the other hand, wide band

baluns are either narrowband or large and expensive. One of the wideband baluns used in Tightly Coupled Dipole Array (TCDA)s is Marchand balun; however, the vertical through plane assembly of the Marchand balun makes the planar structure of the TCDAs large in thickness which is not suitable for applications where the available area is limited. Also, the implementation of those long through plane integrated Marchand baluns would practically be challenging at high mm-Wave frequencies due to the fabrication constraints. So, there are only a few of studies that have focused on TCAs' operation above 20 GHz. In the next section, the contribution of this thesis in mitigating these problems will be explained.

1.2 Contribution

As mentioned in previous section, TCDAs can provide UWB VSWR bandwidth while having low profile structure in 2D plane. However, planar TCDAs generally have a relatively high profile in depth (large thickness) due to the need for wideband baluns for each dipole to provide a balanced feedline and prevent the common mode resonance.

In this project, the planar version of the Marchand balun [1] is modified to design a thin (0.71mm), UWB antenna element covering the whole frequency range of 24 GHz-71 GHz which includes the three high mm-Wave frequency bands (24 GHz-29 GHz, 37 GHz-43 GHz, and 57 GHz-71 GHz) for 5G applications [2]. For this purpose, the Marchand balun's open circuit transmission line is implemented by a Grounded Coplanar Waveguide (GCPW) line to decrease its characteristic impedance and obtain the same wide bandwidth as in [1] but with a smaller antenna thickness which is of significant importance for SoC devices.

Also, the planar Marchand balun [3] is used to design and fabricate a small ($6mm \times 6mm$), 2×2 fully excited tightly coupled bowtie array working from 24 GHz up to 45 GHz which covers continously the two commonly used 5G mm-Wave frequency bands [4](24 GHz-29 GHz and 37 GHz-43 GHz). The designed TCA has return loss below -10 dB for broadside radiation and gain between 3-7 dBi for the entire range of frequency. The designed antenna array is fabricated using the Printed Circuit Board (PCB) manufacturing method. The antenna pattern and scattering parameters are measured in Emerging Radio System Group (EmRG) Labratory and the measurement results agree well with the simulation results.

Furthermore, in order to facilitate the feeding structure and provide more room for each element's excitation and much importantly in order to significantly reduce the cost of the array by reducing the number of required T/R modules, a 8×8 thinned TCA is

designed using the proposed bowtie element to fully cover the two commonly used 5G mm-Wave frequency bands (25-29 GHz and 37-43 GHz). In this designed thinned array with 64 elements, only 22 elements (34% of the whole array) are excited, 20 elements are terminated to properly optimized complex impedances (R+jX) and the rest are kept open but are not removed from the aperture not to disturb the element lattice. The scheme of excitation is obtained by optimization and investigating the current distribution among elements. In traditional array thinning, the inactive elements are terminated to a matched load, or dummy loads (open circuited). Also, in these cases, the array needs to be large enough not to disturb the array pattern.

Reducing the number of excited ports simplifies the feeding network and reduces the cost; however, it increases the distance between two consecutive excited elements which may result in grating lobe appearance or large side lobe levels specially at high frequencies and large steering angles if no current passes through the unexcited ports that lay in between the excited ones. Non-periodic arrays can mitigate the appearance of grating lobes but it disperses the energy of the grating lobes into the sidelobe region, resulting in an overall increase in the SLL [5]. In the proposed thinned TCA, by terminating a part of the unexcited elements to proper complex impedances and by taking advantage of the strong mutual coupling between adjacent elements, proper currents are induced on the terminated elements to mimic the current distribution of an ideal fully excited array. The excitation voltages and terminating loads are optimized using Genetic Algorithm (GA) in order to obtain the radiation pattern that closely resembles the desired pattern with satisfying radiation characteristics such as gain and SLL [6].

The error function is defined based on the difference between the thinned array pattern with a predefined mask in 2 principal planes (E-plane, H-plane) instead of point by point matching of the pattern with the desired pattern of a fully excited array in the whole space. This approach significantly speeds up the optimization and also increases the chance of survival to get more reasonable solutions by relaxing the condition of the cost function.

Ideally, at each frequency and for each steering angle, a different set of optimized excitation voltages and terminating impedances are required; however, controlling the terminating impedances by both steering angle and frequency is practically impossible; so, the terminating impedances are kept fixed to their optimized values for the worst case scenario which is when the beam is steered to the highest angle (here 45^o in E-Plane) and only the excitation voltages are re-optimized for each steering angle. By this technique, the optimized terminating impedances are only a function of frequency and do not change by scanning the beam; however, a different set of optimized excitation voltages are required for each frequency and each steering angle.

The frequency behaviour of the terminating impedances and also the input impedance at excited ports can have sharp fluctuations if the initial values are randomly chosen and there is no limitations on the values that optimization can select. This makes the realization of terminating impedances and matching networks almost impossible; so, in order to smooth out their frequency behaviour, the optimization starts from the highest frequency (43 GHz) when the beam is scanned to 45^o in E-Plane and the optimized values at each frequency is used as the initial point for the next frequency which is 1 GHz lower. By this approach, the optimization was run down to 25 GHz with 1 GHz steps. In addition, the terminating impedances (both real and imaginary parts) are limited to vary *within* 10% *of their initial values*.

The optimization is done on all excitation voltages and termination impedances for the two commonly used 5G frequency bands 25 GHz-29 GHz and 37 GHz-43 GHz with 1 GHz step frequency and for steering angles broadside, $15^o, 30^o$, and 45^o in E-plane. The promising results show that the strong mutual coupling among the elements in the thinned TCDA can maintain the required radiation characteristics in a wide frequency range (25 GHz-29 GHz and 37 GHz-43 GHz) and steering angles up to $\pm 45^o$ while reducing the number of excitation to around 34% of the whole elements in array.

The optimized terminating impedances are realized with a cascade of striplines terminated with a proper resistance. This circuit is optimized for all 20 terminated ports. Also, the modified Real Frequency Technique (RFT) is used to design the wideband matching network for the 22 excited ports implemented by a 3 stage cascaded GCPW transmission lines with lossy junctions.

At the end, the whole thinned array including all feeding networks and terminating impedances is simulated in Ansys High Frequency structure simulator (HFSS) software. The feeding network calibration is done to find the required excitation voltages at all 22 waveports around the edges of the board. The simulated antenna showed good input reflection coefficient ($S_{11} < -8dB$) at all 22 excited ports over the two frequency bands and for the whole required steering range. The simulated SLL is below -13dB, -8.6dB at higher frequency band for broadside radiation and steering up to 45^0 in E-Plane respectively. At lower frequency band, the SLL increases to -10.5 dB, -6 dB for broadside radiation and when steering upto 45^o in E-Plane. The maximum directivity is dropping between 2-3.5 dB and 2.5-5 dB compared with a fully excited array at higher and lower frequency bands respectively. The simulated total radiation efficiency is between 0.06-0.21 at the two frequency bands and for required steering range. The low efficiency is shown to be almost exclusively due to the losses introduced in the designed wideband matching networks.

1.3 Thesis Outline

This thesis is comprised of six chapters. The contents of the remainder of this document is as follows. Chapter 2 starts with a background on UWB phased arrays, introduces the TCAs and explains how they can provide wide VSWR bandwidth. Then the challenges on their feedline's design and the approaches used to improve their bandwidth is thoroughly explained. Finally, it ends with a literature review on the traditional thinning of phased array antennas.

In chapter 3, a modified version of planar Marchand balun is used to design and simulate a thin, planar, UWB antenna element covering the three 5G mm-Wave frequency bands. Also, a small 2×2 tightly coupled bowtie array working from 25 GHz-45 GHz is designed, simulated and fabricated. Furthermore, a wideband 8×8 tightly coupled bowtie array is designed for the first two 5G mm-Wave frequency bands (25 GHz-29GHz, 37 GHz-43 GHz).

In chapter 4, the designed 8×8 tightly coupled bowtie array in chapter 2 is thinned with selectively exciting only 22 elements. The unexcited elements of the array are partly terminated with proper loads and the rest are left as open circuited. The 8×8 thinned tightly coupled bowtie array is optimized using GA optimization in order to get an acceptable radiation characteristics such as gain and SLL at the two desired frequency bands (25 GHz-29 GHz, 37 GHz-43 GHz) for steering up to 45^o in E-Plane. At the end, a distributed circuit realizing the optimized terminating impedances are designed and simulated for all terminated ports.

In chapter 5, the modified RFT is used to design a distributed matching network circuit which is optimized for all 22 excited ports of the thinned array. The twenty two 50Ω feed lines are designed to connect the matching networks to the twenty two 2.4mm, 50Ω edge connectors mounted all around the board. The 6 layer structure of the thinned array including all terminating impedances and feeding networks are simulated using Ansys HFSS software. The simulation results are reported and investigated in this chapter. In chapter 6, a summary of the thesis contributions are given and the research areas that can be addressed more in future will be discussed.

Chapter 2

Literature Review

2.1 Ultra-Wideband Antenna Arrays

One of the popular wideband antennas is the Vivaldi antenna which is extensively used in UWB systems providing more than 12:1 VSWR bandwidth [7]. Despite their wideband capability, Vivaldi arrays are typically bulky (more than $4\lambda_{Hi}$ in height [8]) which is not suitable for applications where available space is limited like cell-phone devices. These arrays also suffer from high cross-polarization when scanned in diagonal planes. Furthermore, Vivaldi arrays are not suitable for modular construction because they require electrical connection between their adjacent elements which raises the fabrication cost and complexity to be repaired or renewed [9]. A modular Vivaldi type was proposed as Body of Revolution (BOR) Vivaldi array [10]; however, it requires special machining and is difficult to fabricate at high frequencies (above X-band). Moreover, this antenna is still not low profile.

Several low profile, modular types of Vivaldi arrays are proposed by removing the electrical connection between neighbouring elements. Similar to an ordinary Vivaldi array they consist of vertically integrated PCB cards backed by a ground plane but the height of these vertically oriented PCBs are reduced to half of the wavelength at highest frequency (λ_H). The Bunny-ear [11], Balanced Antipodal Vivaldi Array (BAVA) [12], Doubly Mirrored Balanced Antipodal Vivaldi Array (DM-BAVA) [13], and Banyan Tree Antenna (BTA)[14] are a few examples of these class of antennas.

The bunny-ear can provide 5:1 VSWR bandwidth in a dual-polarized array without electrical connection between adjacent elements; however, it requires film resistors to be connected in the gap between antenna arms and the ground plane to suppress resonances

caused by the gap [11]. Furthermore, it requires an external balun which makes the overall height of the element more than one wavelength at highest frequency of operation. DM-BAVA introduced by Elsallal and Schaubert in [13, 15]. This dual-polarized DM-BAVA works over 5.4:1 VSWR bandwidth with wide scan volume ($\pm 60^o$). By double mirroring in E and H planes, it alleviates impedance anomalies caused when BAVA element is placed in an array environment. However, it creates the need for 180^o hybrids to maintain beam collimation. The dual-polarized BTA array shows 3.75:1 VSWR bandwidth ($VSWR < 2.8$) while scanning up to $\pm 45^o$ [14]. The polarization purity is better than 14 dB out to 45^o in D-plane. This antenna resembles BAVA and bunny-ear design but the most important advantage over those antennas is that it uses metallic shorting posts between fins and ground plane to suppress the mid-band common-mode resonance which alleviates the need for external baluns or hybrids.

Basically, phased arrays with vertically integrated radiating elements are difficult to integrate at mm-Wave frequencies and they require a lot of space. TCA are planar UWB arrays which are good candidates for wideband applications where the available space for the antenna is limited. TCAs have the potential to operate over an extremely wide VSWR bandwidth while being low profile enough to be used in applications like handheld devices. Moreover, TCAs are capable of steering the beam in a relatively wide scanning volume with low cross-polarization level. TCAs have been previously demonstrated to achieve up to 21:1 bandwidth and more than 60^o scanning capability[16, 17]; However, only a few of studies have focused on TCAs' operation above 20 GHz [18, 19, 20, 3, 1].

In the next sections, the basic concept of TCAs is explained and the prior arts on design and development of these antennas are reviewed.

2.2 Basic Concept of Tightly Coupled Arrays

Conventionally, in a planar narrow band phased array antenna, the elements are first designed according to the required bandwidth and radiation characteristics and then they are integrated in an array with roughly half a wavelength spacing between adjacent elements. The mutual coupling between adjacent elements in such array is not strong enough to fundamentally alter the radiating element's characteristics such as its current distribution, input impedance, or radiation pattern. Moreover, the size of the unit cell is large enough for integrating the active and passive circuitry required for operation of the phased array.

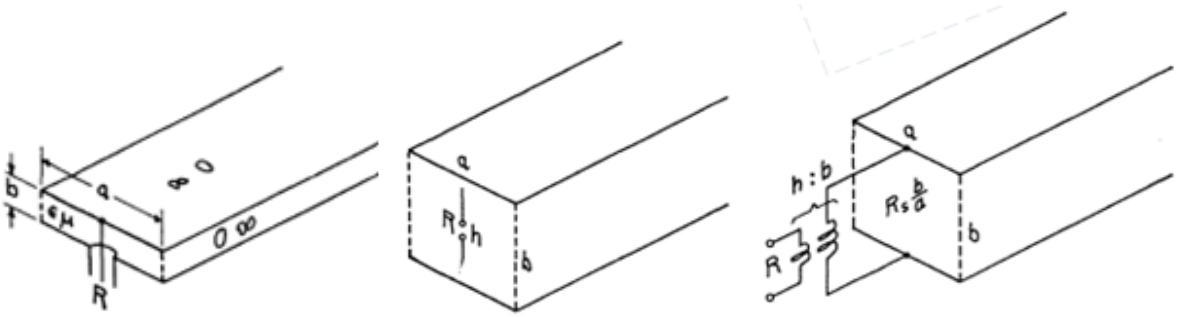
In TCAs the spacing between the adjacent elements is very small. Typically it is chosen to be half of the wavelength at the highest frequency of operation. Therefore, for

example in 10:1 ratio bandwidth, the spacing is in around 0.05 wavelength at the lower end of the band. In a 4:1 ratio bandwidth, the spacing is about 0.125 wavelength at the lowest frequency. This small separation between elements leads to significant increase in the mutual couplings specially at lower frequencies and substantially disturbs the current distribution and thus radiation characteristics of the elements, however, as we shall see, the same strong mutual coupling can be exploited to achieve ultra wide bandwidth of operation.

The concept of TCA was first originated from Wheeler's Current Sheet Antenna (CSA) concept [21]. Wheeler showed that an ideal continuous current sheet without ground plane has an input impedance with infinite VSWR bandwidth. The input impedance of such ideal radiator has no reactance when there is no ground plane and its radiation resistance is independent of frequency but depends on scan angle. The current sheet is considered as a limiting case of many small electric dipoles, closely spaced, and backed by an open circuit boundary. For practical emulation of the infinite array, Wheeler used the so-called *waveguide simulator* concept. In this method, the space above the array antenna is divided into infinitely many waveguides or tubes of radiation, one for each unit cell of the array. By enforcing proper boundary conditions on the walls of these imaginary waveguides, array scanning to any angle can be simulated. Note that such waveguide supports pure Transverse Electromagnetic Mode (TEM) propagation. Wheeler was able to derive simple but intuitive equations for the input impedance of an infinite array using this method. The waveguide simulator and current sheet concept are discussed in more details in the following.

Using the image theory, a rectangular unit-cell in an infinite periodic array can be modeled by applying Perfect Electric Conductor (PEC) (infinite electric permittivity and zero magnetic permeability) and Perfect Magnetic Conductor (PMC) (zero permittivity and infinite permeability) boundary condition on the unit cell boundaries as shown in Fig. 2.1a where a and b are the unit cell dimensions. The intervening space has nominal values of permittivity ϵ and permeability μ of the surrounding medium. The PEC and PMC boundary conditions shown in Fig. 2.1a ensure the TEM mode propagation in the waveguide. The wave impedance of such a line transmitting only TEM mode is purely resistive $R = R_s b/a$ where $R_s = \sqrt{\mu/\epsilon}$ is the plane wave impedance of the medium. If the antenna length (b) is much shorter than the radian length, it has uniform current over its length. Therefore, its effective length is equal to its physical length b and the radiation resistance of this antenna in Fig. 2.1a is equal to the wave impedance of the rectangular line $R_r = R_s b/a$

If any configuration of antenna is located in the end plane of the rectangular line, its coupling with the line is proportional to its effective length (h) in the direction of the



(a) (b) (c)

Figure 2.1: a hypothetical rectangular waveguide supporting TEM mode (a) Waveguide of small height and antenna of equal height [21]. (b) Waveguide of substantial height and antenna of lesser effective height [21]. (c) Equivalent transformer coupling the antenna with the waveguide [21].

electric field (vertical). This is understood if a plane wave is being received from the line by the antenna; the induced voltage is proportional to the effective height. By the law of reciprocity, the same rule applies to the coupling of transmission from the antenna to the line. Fig. 2.1b shows a vertical dipole antenna in the end plane of the waveguide simulator. It has a certain effective length h. The power radiated from the antenna through the line determines the radiation resistance of the antenna, by definition of the latter:

$$R_r = R_s \frac{b}{a} \left(\frac{h}{b}\right)^2 \tag{2.1}$$

This represents only the power radiated in the simple plane wave (TEM) which is the only mode of vertical polarization if both of the transverse dimensions are less than one wavelength, hence, no grating lobes. A series-resonant antenna in the end plane of the rectangular line has an impedance equal to its radiation resistance, free of reactance. At its wavelength of resonance, it may be regarded as an ideal transformer coupling the antenna terminals to the line. This is illustrated in Fig. 2.1c, the voltage ratio of the transformer being $h : b$. In tightly coupled arrays as the distance between elements decreases, the current distribution over the elements becomes more stable (uniform) and the effective length h in equation (2.1) tends to the total length of the antenna and becomes frequency independent.

Wheeler derived the radiation resistance of an antenna element in an infinite periodic array intuitively. The rigorous mathematical derivation of the input impedance was done

by Stark and Munk as well. In 1965, Stark [22] mathematically derived the input impedance of a dipole in an infinite array above ground plane and scanned for any angle of radiation by means of plane wave expansions and the Floquet mode theory. Stark showed that the radiation resistance of the antenna is the product of the radiation resistance for broadside, R_{bs}, times a scanning factor which is identified as below:

$$\begin{aligned} R &= R_{bs} \times SF \\ SF &= \frac{|EF_n(\theta_s, \phi_s)|^2}{cos(\theta_s)} \end{aligned} \tag{2.2}$$

where $EF_n(\theta_s, \phi_s)$ is the normalized element pattern at steering angle θ_s, ϕ_s. SF denotes the scanning factor. Also, Munk [23] calculated the input impedance of an infinite periodic dipole array in a more general multilayered medium using Floquet mode theory. Both derivations given by Munk and Stark agree well with the results previously obtained by Wheeler in equation (2.1) for an infinite periodic array elements without ground plane having an effective length (h) and for broadside radiation.

The electrical distance of the planar array to the ground plane, the effective length of the antenna element and the scanning factor shown in equation (2.2) makes the input impedance frequency dependent. Note that the effect of ground plane is embedded in R_{bs} and the element pattern EF_n which in turn determines the effective length. The current distribution on antenna elements approaches uniform distribution as the elements become tightly coupled; hence, the effective antenna length tends to the physical length and becomes frequency independent; However, usually planar array needs a ground plane to remove the backward radiation which makes the input impedance frequency dependent and limits the VSWR bandwidth.

Munk proposed a simplified circuit model for the input impedance of an infinite dipole array embedded in a multilayer medium [24] shown in Fig. 2.2. As mentioned earlier, Munk derived the formula for the input impedance of such infinite dipole array by using the Floquet mode theory and created a transmission line model shown in Fig. 2.2 using the only radiating term in that Floquet series. In this model $R_{A1} + jX_{A1}$,R_{A0} are the input impedance and radiation resistance of the infinite dipole array without ground plane located in a medium with intrinsic impedance Z_1 and Z_0 respectively. In this figure r_{1y} represents the phase constant in Y-direction in each media and it depends on the steering angle and is given by:

$$r_{1y} = \sqrt{1 - (S_x + \frac{k\lambda}{D_x})^2 - (S_z + \frac{n\lambda}{D_z})^2} \tag{2.3}$$

In equation (2.3), D_x, D_z are the unit cell dimensions in x, z directions, respectively. The

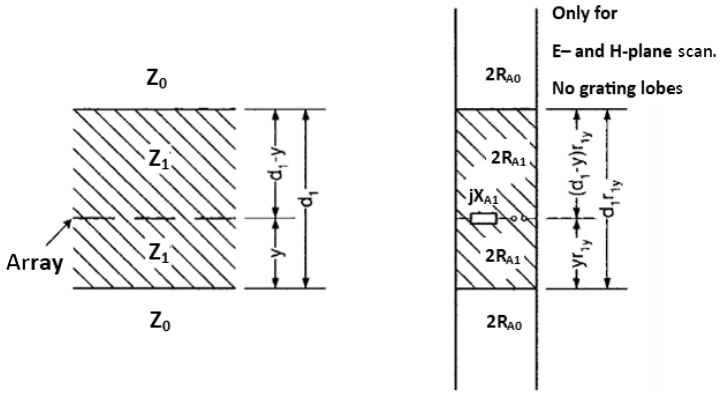
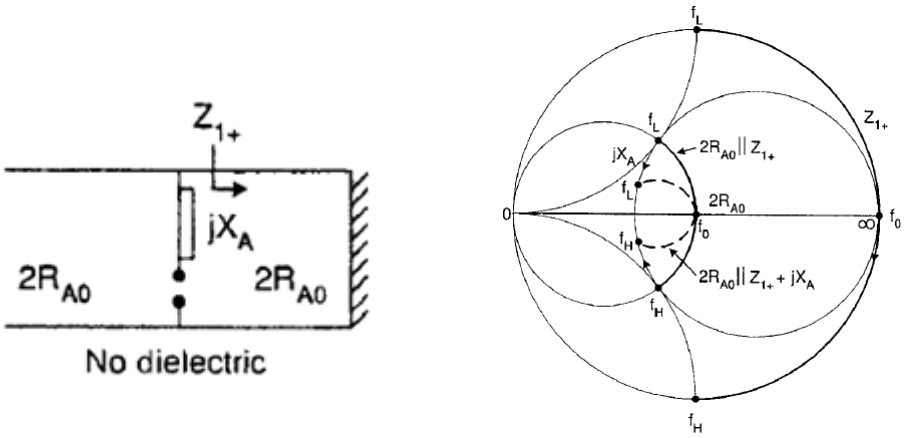


Figure 2.2: Munk's equivalent transmission line model for an infinite periodic array of short dipoles [24].

infinite periodic array is placed in X-Z plane. k and n are integer numbers and generate the Floquet modes. S_x and S_z together show the direction of the propagation of the fundamental mode (main beam of the array) in each medium which contain the steering angle. This model is based on three simplifying assumptions (1) the distance between elements is small enough that no grating lobe appears in our frequency range thus only one mode is propagating all others are evanescent (2) the element length is small such that the effective antenna length is independent of medium impedance and (3) the scanning angles are limited to principal E and H planes.

By using the Munk transmission line model which is basically the modified and enhanced version of the original Wheeler's current sheet model, a TCDA located above the ground plane can be characterized as shown in Fig. 2.3a. The impedance seen towards the ground plane (Z_{1+}) is purely reactive as shown in Fig. 2.3b. The reactance jX_A acts like a series inductance representing the current through wire dipole and a series capacitance representing the coupling among neighboring elements. At low frequencies where the distance between elements are small in terms of wavelength and the couplings are strong, the series capacitance C is the dominant part in jX_A. On the other hand, at low frequencies where the distance to ground is less than a quarter of wavelength, the impedance Z_{1+} becomes purely inductive; So, the capacitive jX_A compensates for the inductive effect of ground plane and increases the input impedance bandwidth [25].

The smith chart shown in Fig. 2.3b represents the total input impedance variation of the TCDA above ground plane ($Z_{1+}||2R_{A0}+jX_A$) versus frequency when the distance to ground is a quarter of wavelength at center frequency. The frequency behaviour of jX_A which



(a) (b)

Figure 2.3: (a) Transmission line model of a TCDA above ground plane [24]. (b) Smithchart showing the impedance Z_{1+}, $2R_{A0}||Z_{1+}$, and $2R_{A0}||Z_{1+} + jX_A$ [24].

is typically inductive at frequencies below the center frequency f_o drags the impedance $2R_{A0}||Z_{1+}$ downward towards capacitive region. Similarly, the impedances $2R_{A0}||Z_{1+}$ will be pushed upward when the frequency is above the center frequency (f_o). The net result is that the frequency behaviour of jX_A provides a total impedance that is clustered in a smaller area than the impedances of the various impedance components individually. This shows how the mutual coupling among the elements in TCDA helps in decreasing the input impedance variation by frequency and improving the VSWR bandwidth.

It is also worth mentioning that since in TCAs, the unit cell dimension is smaller than half of the wavelength at highest frequency of operation, the grating lobes do not appear for steering angles up to 90^o in the whole frequency range although array blindness may occur due to propagating surface waves in the multilayer structure. In [26], a comprehensive review is done on TCA antennas.

2.3 Tightly Coupled Array's Feeding Challenges

In 2003, B. Munk designed a TCDA as the first practical implementation of Wheeler's theoretical current sheet concept with a ground plane below the array [27]. The most challenging part in TCDA designs are their feeding structure. The small spacing between elements leaves us with a very small space for accommodating the feed circuitry and on

the other hand the TCDA feed must include a balun or 180^o hybrid for each element to provide the same current on both arms of the dipole at all frequencies in order to prevent the so-called common mode resonances and unwanted radiations from the vertical feed lines. Common mode resonance occurs whenever the currents on the vertical feed lines are not balanced producing a net current and , thus, net radiation from feed lines [28]. Additionally, baluns must be wide band enough not to ruin the wide band capability of TCAs and at the same time small in size to fit within each unit cell which can be as small as $\lambda/10$ at lowest frequency. The available volume for each balun is more limited for the arrays operating at high frequencies which is one of the biggest challenges in TCA designs at mm-Wave frequency range.

Commercially available passive baluns are either narrowband or large and expensive. Also, active baluns are limited to receive only applications. In 1944, Marchand proposed a wideband balun shown in Fig. 2.4a. This balun can convert the unbalanced coaxial line to a balanced two wire line ($I_{B1} = I_{B2}$) within a wide frequency range of 3:1 as shown in Fig. 2.4b. In order to provide wideband VSWR with this balun, the characteristic impedance of the shorted transmission line (Z_{OT}) must be large enough and also the characteristic impedance of the open transmission line (Z_{OE}) must be chosen as $Z_{OE} = \frac{Z_{OC}^2}{2Z_{OT}}$ where the impedance Z_{OC} is the impedance looking into the loaded coaxial line. Fig. 2.4c, and 2.4d show the equivalent circuit of the balun shown in Fig. 2.4a. In this Balun, two shorted transmission lines with equal length and characteristic impedances (Z_{OT}) are connected in series to ensure that there is no current flowing into balanced line shield ($I_{3B} = 0$). The open circuit transmission line with characteristic impedance Z_{OE} makes the input impedance's phase variation smoother when the frequency shifts away from the center frequency which leads into a wide band balun. The impedance Z_{OC} shown in Fig. 2.4d is the impedance looking into the loaded coaxial line.

In [29] a Marchand balun [30] is used as part of a matching network for each array element. This reduces the size and cost of the array by integrating the balun as part of the matching network. The aforementioned Tightly Coupled Dipole with Integrated Balun (TCDA-IB) achieves 7.35:1 bandwidth (0.68 GHz-5 GHz) while scanning to $\pm 45^o$ in all directions subject to $VSWR < 2.65$. Fig. 2.5 shows the TCDA-IB unit cell and the proposed equivalent circuit for the matching network. The TCDA-IB has low cross-polarization of $< -20dB$. It is important to note that the dipole element of each unit cell is splitted into two small dipoles along E-plane in order to reduce the input impedance by a factor of two and simplify the matching circuit by using a 1:2 wilkinson power divider of 50Ω to two 100Ω ports plus two baluns for each half element.

When the mutual couplings are strong enough that make the current distribution almost

uniform, we can replace the effective length (h) in (2.1) with the unit cell dimension in E-plane (d_E). In this case, the input impedance of the unit cell is $R_{in} = R_s \frac{d_E}{d_H}$ which is proportional to the aspect ratio $\frac{d_E}{d_H}$. d_E and d_H are the unit cell dimensions in E- and H-plane, respectively. By splitting the cell into two halves along E plane, the impedance of each half is correspondingly reduced by a factor of two. The input impedance of a TCDA with a square unit cell is typically around 200Ω thus, a wideband 50Ω to 200Ω transformer is also required, further increasing the size and complexity of the feed. To eliminate the need for the impedance transformer, we may reduce the E-plane dimension of the unit cell by a factor of 2, which correspondingly reduces the input impedance to 100Ω. The square unit cell then contains two "half" elements, each comprised of a dipole and a balun. However, rather than feeding each half-element individually (which would double the number of phase shifters and T/R modules), the pair can be combined in parallel to provide a single 50Ω feed. Therefore, the effective element count and unit cell size remains the same, and no impedance transformers are required. The idea of "double balun" is also used in [31] to excite the TCDA and achieve 4:1 impedance bandwidth. The "double balun" technique has also been shown to reduce cross-polarization by eliminating the common mode resonance occurring when total length of dipole and feed line is electrically long. [32].

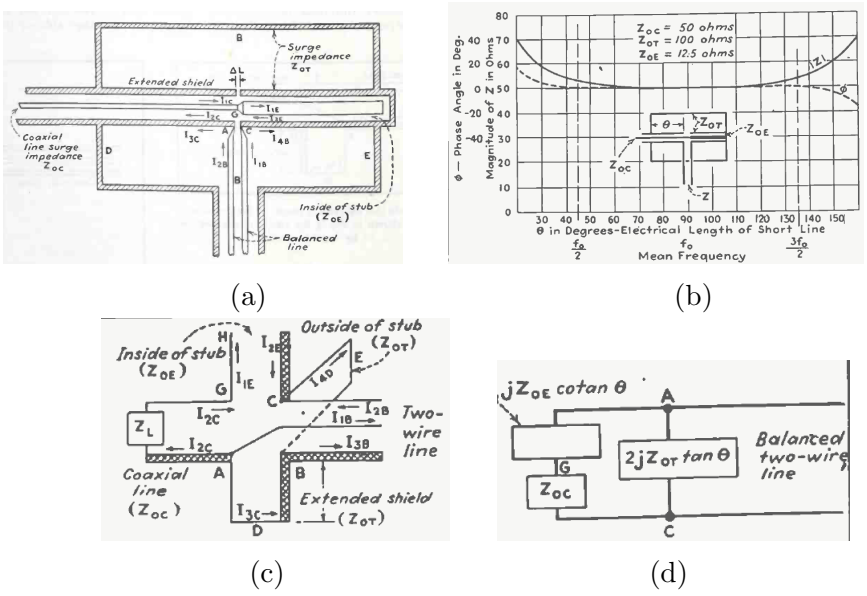


Figure 2.4: Wideband Marchand balun presented in [30] (a) The balun configuration [30]. (b) The input impedance of the balanced line (phase and magnitude) [30]. (c) The balun's lumped equivalent circuit model [30]. (d) The balun's transmission line circuit model [30].

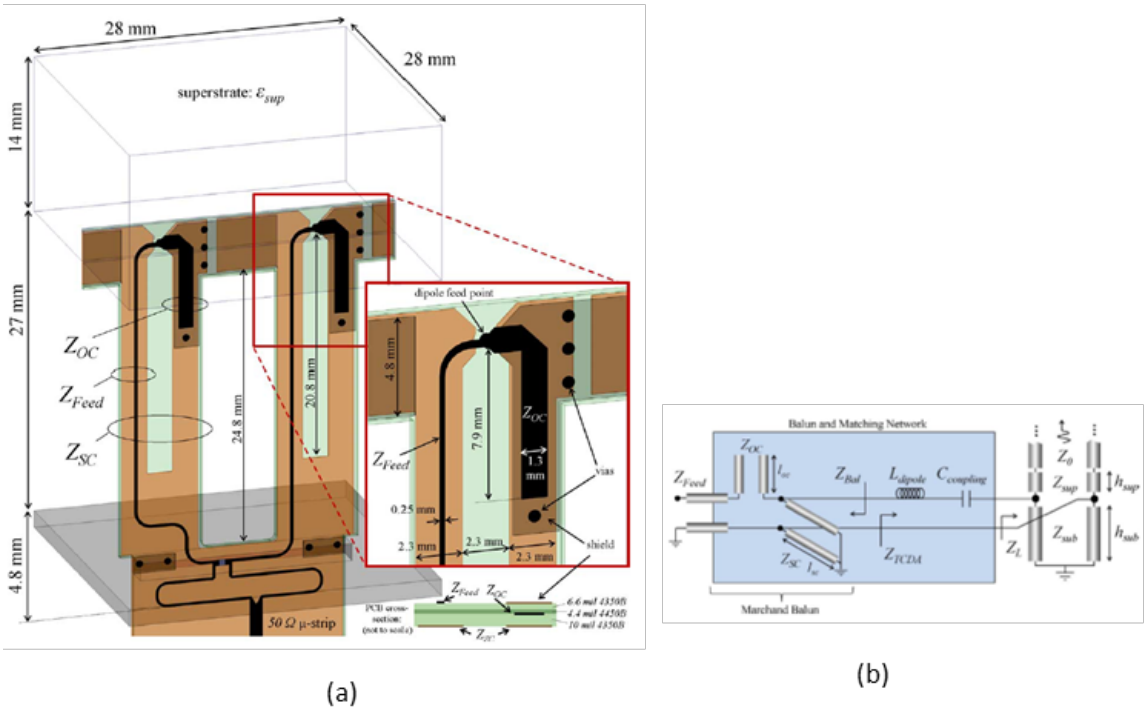


Figure 2.5: (a) Unit cell of TCDA-IB [29]. (b) TCDA-IB equivalent circuit fed by a Marchand balun [29].

The wideband Marchand balun used in [29] requires complex through plane assembly whose implementation is extremely challenging at high mm-Wave frequencies above 20 GHz. In order to overcome the fabrication challenges, a planar Marchand balun was proposed in [1, 3] using 3 vias and 2 metalized layers shown in Fig. 2.6; however, the antenna thickness is large (more than 1.3mm) for most SoC devices. As shown in Fig. 2.6, the Marchand balun's high impedance, short and the low impedance, open transmission lines are realized by a shorted twin wire line and a patch over a dipole's arm (as its ground) respectively.

Another feeding structure for tightly coupled horizontal dipoles was proposed in [28] which eliminates the need for bulky feed organizers or external baluns while maintaining good broadband and scan performance. Basically, when the two arms of a dipole are driven with unbalanced feeds, the net vertical current on the feed lines produces a resonance that results in a short circuit in the input impedance of the elements. This resonance is called *common mode resonance* which mostly occurs near mid-band when the *diagonal distance* between elements (vertical feed lines) is integer multiple of half wavelength. Observing the

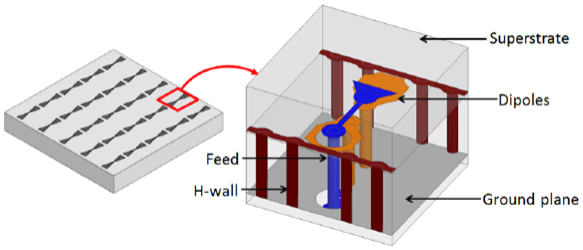


Figure 2.6: A unit cell design sampled from a periodic array with roughly $\lambda/2$ spacing in both directions [3].

vertical field distribution at common mode resonance frequency reveals a strong vertical electric field distribution with a cosine amplitude variation along the diagonal feed to feed direction with nulls at the grounded half of each feed as shown in Fig. 2.7a. The proposed Planar Ultra-wideband Modular Antenna (PUMA) shifts the frequency of the common mode resonance to higher frequencies by reducing the diagonal distance between feed lines using shorting vias on dipole arms at a specific distance from feeding lines. Fig. 2.7b shows the shorting vias at distance s from the feed point which reduce the diagonal distance L and shift the common mode resonance frequency to:

$$f_{cm_{(PUMA)}} \approx \frac{nc_0}{2\sqrt{\epsilon_r}\sqrt{D_y^2 + (D_x - 2s)^2}} \tag{2.4}$$

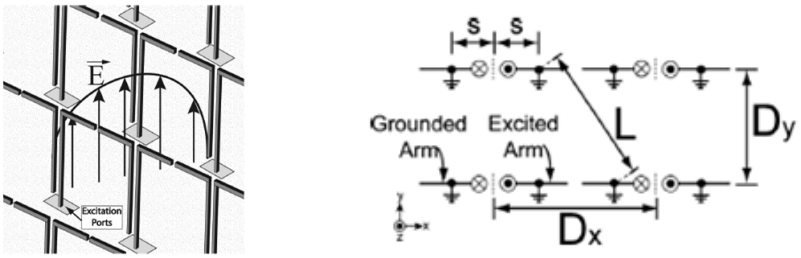
However, if the shorting vias were not used the resonance frequency would be:

$$f_{cm} \approx \frac{nc_0}{2\sqrt{\epsilon_r}\sqrt{D_y^2 + D_x^2}} \tag{2.5}$$

where n is an integer, D_x, D_y are the unit cell dimensions, c_0 is the light speed in free space, and ϵ_r is the substrate permittivity. The dual-polarized PUMA design achieves 5:1 bandwidth for $VSWR < 2.1$ at broadside and cross-polarization is around -15 dB out to $\theta = \pm 45^o$ in diagonal planes.

2.4 Tightly Coupled Array's Bandwidth Improvement

A lot of research has focused on further increasing the TCA bandwidth and scanning capability. By adding a magnetic or lossy substrate between the array and the ground

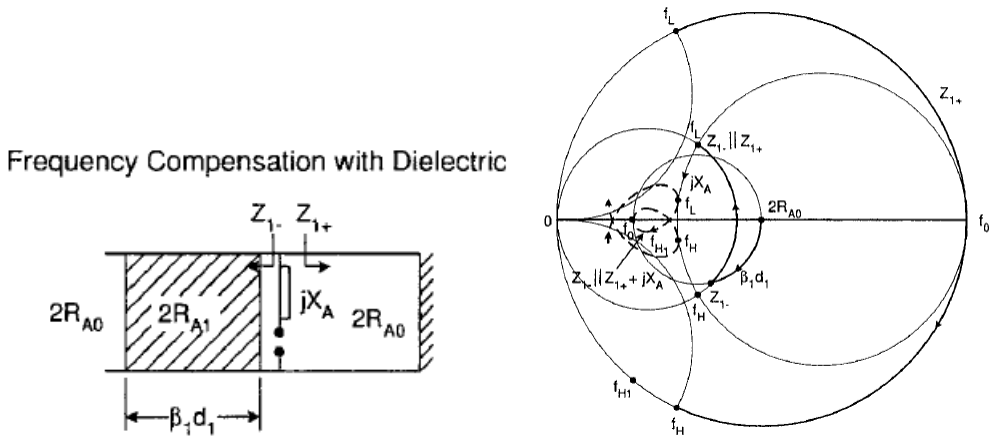


(a) (b)

Figure 2.7: (a) Electric field distribution at the common mode resonance frequency in an unbalanced fed TCDA [28]. (b) Top view of a PUMA unit cell with shorting vias [28].

plane or applying a dielectric superstrate on top of the array, the VSWR bandwidth and scan volume of TCAs can be further increased [24]. One approach in order to increase the bandwidth is to keep the level of impedance seen towards the ground plane (Z_{1+} in Fig. 2.8a) high for the whole frequency range. Filling the space between the dipole array and the ground plane with a material having a higher intrinsic impedance than that of free space leads to a higher ground plane impedance (Z_{1+}) and thereby a potential for larger bandwidth. Unfortunately, materials with a higher relative permeability (μ_r) than their relative permittivity (ϵ_r) are rare; and if encountered at all, they are usually synthetic and narrow band and very lossy. Another approach is to lower the impedance Z_{1-} shown in Fig. 2.8a relative to Z_{1+}, where Z_{1-} denotes the input impedance of the equivalent transmission line looking to the left. Fig. 2.8b shows the input impedance variation vs frequency for a TCDA backed by a ground plane and having a superstrate on top as shown in Fig. 2.8a. The reason for getting a wider bandwidth by adding a dielectric superstrate is that the ground plane impedance Z1+ is partly canceled by the reactive part of Z_{1-} at higher as well as lower frequencies. In contrast to the nondielectric case in Fig.2.3, the Z_{1-} impedance remains equal to $2R_{A0}$ without any reactive part at any frequency and will consequently not reduce the effect of the variation of Z_{1+} as a function of frequency.

In [16] a resistive Frequency Selective Surface (FSS) is used as a substrate to increase the impedance bandwidth and a dielectric superstrate is used to alleviate losses due to the resistive FSS and improve the radiation efficiency. The proposed array of dual-polarized tightly coupled bowtie elements achieves 21:1 bandwidth ($VSWR < 3$) and radiation efficiency greater than 73% across the frequency band of 0.28 GHz-5.91 GHz. In [33] the bulky dielectric layer is replaced with a periodic array of printed elements and still achieves wide angle and wideband impedance matching. In [17] a new non-symmetric TCDAis used in order to generate more degrees of freedom to control the capacitance



(a) (b)

Figure 2.8: (a) Transmission model of a TCDA with a superstrate on top and backed by a ground plane [24]. (b) Smithchart showing the impedance Z_{1+}, $Z_{1-}||Z_{1+}$, and $Z_{1-}||Z_{1+} + jX_A$ [24].

canceling the ground inductive effect and, thus, increase the bandwidth as a result. A circularly polarized interwoven spiral array achieves 10:1 bandwidth for $VSWR < 2$ while having a wide scan capability [34]. The self-complementary spiral elements have their arms interwoven to enhance capacitive coupling and mitigate the inductive effect of the ground plane in order to increase VSWR bandwidth.

2.5 Thinned Tightly Coupled Antenna Array

As thoroughly discussed in this chapter, the TCA can provide wide VSWR bandwidth due to the strong mutual coupling among the elements. However, as mentioned earlier, the most challenging issue with TCA design is their feeding structure and the difficulties to accommodate the bulky feeding network including a large wideband balun, matching network, phase shifter, and amplifier in each small unit cell area specially at high mm-Wave frequencies above 20 GHz.

Reducing the number of excited elements can help to accommodate the bulky feeding networks and reduce the cost by reducing the number of required T/R modules. Basically, in a thinned array, only a subset of elements are excited in a uniformly spaced or periodic array to create a desired amplitude density across the aperture. In traditional

array thinning, the inactive elements are terminated to a matched load[35], dummy loads (open circuited) or even completely removed from the array [36],[37][38]; so, they wouldn't contribute to the total array pattern. In addition to thinned arrays, there are other array architectures that can reduce the number of required excited elements. The wideband Wavelength Scaled Array (WSA) use multiple elements scaled in size from the base high-frequency element, so, they can use 6.4-times fewer elements[39]. Furthermore, irregular arrangement of polyomino[40], polygon[41], or domino-shaped tiles [42, 43] are optimized to reduce the number of T/R modules while keeping acceptable radiation performance in each direction. Also, the number of excited elements can be reduced by only 13.4 % by arranging the elements in a pattern of equilateral triangles rather than in a square pattern [39].

Thinned arrays are typically optimized to get the desired antenna pattern with desired radiation characteristics like low SLL, high aperture efficiency or even shaping the pattern for some applications. The thinning of an N element array with 2^N possible choices for selecting the location of active elements would be exhaustive specially when N is large and symmetry is not enforced. The optimization has been done on the location of the active elements, excitation voltages or a combination of both in the literature. Statistical density tapering [44] is a simple thinning technique using a desired amplitude taper as a probability density function to realize an approximation of that aperture distribution [45]. However, this approach works effectively when N is sufficiently large. Global optimization methods such as the GA[46], Particle Swarm Optimization (PSO) [47, 48], and Simulated Anealing (SA) [49] are proven to be useful for array thinning.

Although there are a lot of studies using different optimization techniques on thinning the phased array antennas, there are only a few addressing array thinning on tightly coupled antenna arrays [42, 35]. Based on the discussion in [42], the non-uniform inter element spacing in a thinned array can disturb the uniform current distribution of TCDAs causing in-band resonances or scan blindness which can disturb the wide VSWR bandwidth. In [35], A GA based optimization is used to demonstrate the feasibility of thinning this UWB connected Vivaldi array. It is assumed that the thinning factor is 0.5 meaning half of the elements are inactive and terminated to matched 50Ω loads in this optimization; so, the location of the active elements are optimized in such a way to minimize loss at lowest frequency of operation (10 GHz) and the SLL at the highest frequency (35 GHz) to consider the worst case scenario.

The optimization result showed that the half excited elements are clustered around the center of the array to maintain the quality of the main beam and good impedance match and the rest are closer to the edge to create a spatial amplitude taper reducing the SLL in E- and H-planes. In this optimization, For the array pattern calculation, the

embedded element pattern (considering all mutual couplings) is multiplied by the array factor. For array factor calculation, the current on inactive elements are assumed zero in spite of the mutual coupling among elements. However, this agrees with the fact that the loss is minimized on 50Ω resistive loads. So, since the loads are purely resistive, the current on inactive elements are minimized to minimize the loss. However, the strong mutual coupling in TCAs can help us induce proper currents on inactive elements by their proper terminations. This induced current can also contribute to the far field pattern and improve the radiation characteristic by a good optimization procedure.

2.6 Conclusion

So far, a literature review is given on the tightly coupled antenna arrays and their desirable characteristics which makes them a good candidate where a low profile, UWB antenna array is required for applications like 5G cell-phone devices. The challenges in the design of their feedlines are thoroughly explained and the array thinning is proposed as a viable solution. A background on the traditional array thinning is provided. In the next chapter, the steps through the design of a wideband, 8×8 fully excited tightly coupled bowtie array working in 25 GHz-43 GHz frequency band that covers the two commonly used 5G mm-Wave frequency bands (25-29 GHz, 37-43 GHz) is explained. Then, the designed 8×8 array is thinned and the GA optimization is used in chapter 4 to optimize all excitation voltages on excited ports and all terminating impedances on unexcited elements. By this approach, the mutual coupling among elements are used to engineer the current distribution over the array and make the pattern as closely as possible to the pattern of a fully excited array with much fewer number of excited elements.

Chapter 3

Design of a Wideband Tightly Coupled Bowtie Array

As discussed in chapter 2, the strong capacitive coupling among the elements in TCAs compensates for the inductive effect of the ground plane and, consequently, the resulting array can have a very wide bandwidth. Numerous studies have been published on the design of UWB TCDAs; however, only a few of them have focused on TCAs operation above 20 GHz [50, 3, 51]. The reason is that the TCA's feeding network including through plane integrated baluns [29] cannot be implemented practically at these high mm-Wave frequencies due to the fabrication constraints. To overcome the fabrication challenges, a planar Marchand balun is proposed in [50],[3] using 3 vias and 2 metalized layers; however, the antenna thickness is still large (more than 1.3mm) for most SoC devices. In this chapter, the planar balun's design [3] is modified in such a way as to decrease the antenna thickness while maintaining the antenna bandwidth to cover the whole 24 GHz to 71 GHz required for 5G application [2]. Also, the planar Marchand balun is used to design and fabricate a small 2×2 tightly coupled bowtie array working from 24 GHz to 45 GHz which can cover the two mm-Wave frequency bands (24 GHz-29 GHz and 37 GHz-43 GHz) used for most of the 5G applications [4]. At the end, the proposed bowtie element working from 24 GHz-45 GHz is used in a 8×8 TCA for thinning purpose in the following chapters.

3.1 Design of a Thin, Planar UWB Bowtie Element for Tightly Coupled mm-Wave Phased Arrays

3.1.1 Design Requirements

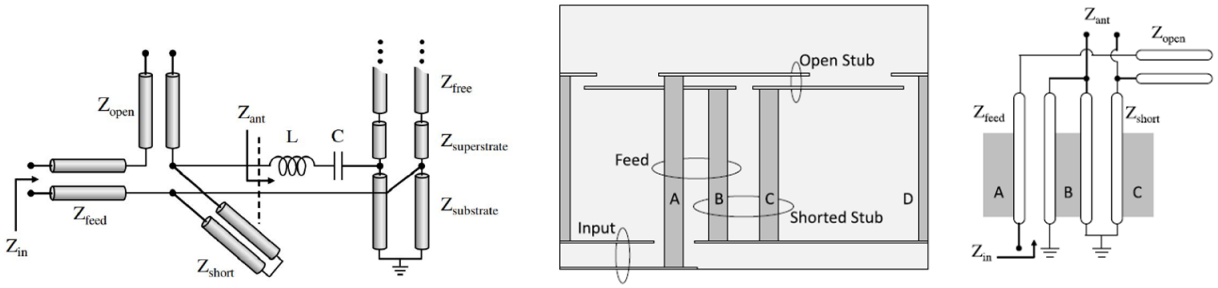
It is well known that in printed circuit antennas, the antenna bandwidth increases by increasing the distance to the ground plane; however, the antenna thickness is limited for SoC applications where size is of great importance. In this section, the antenna thickness is limited to 0.9mm as shown in Table 3.1which is suitable for applications like cell-phone devices. Allocating a part of this thickness for feeding network, the available thickness for the radiating element is about 0.4mm-0.7mm. Existing antennas are either narrowband [18],[52] or have a high profile [3] or/and require complex fabrication methods [53][29]. In this section, the goal is to design a thin ($\leq 0.9mm$), antenna element having low input reflection coefficient (S_{11} below -10 dB) that can cover the three designated mm-Wave bands for 5G wireless standard, namely 24GHz-29GHz, 37GHz-43GHz, and 57GHz-71GHz. Table 3.1 shows the antenna element design requirements.

Table 3.1: Desired Requirements

Antenna Characteristics	Desired Performance
Frequency	24-29 GHz, 37-43 GHz, 57-71 GHz
Total Antenna Thickness	$< 0.9mm$
Input Reflection Coefficient (S_{11})	< -10 dB

3.1.2 Bowtie Element Design with Modified Planar Marchand Balun

When the two arms of dipoles are driven with unbalanced feeds, the net vertical current distribution couples into a resonance that results in a short circuit in the input impedance of the elements as well as unwanted radiations from the feed lines. This resonance happens when the distance between the two neighboring grounded vias is half of the wavelength in substrate media. So, as mentioned earlier, a wideband Marchand balun is required for each dipole element to ensure balanced feeding; however, the wideband Marchand balun used in [29] requires complex through plane assembly whose implementation is extremely challenging at these high mm-Wave frequencies. Fig. 3.1a shows the transmission line model of a wideband Marchand balun that was used in [29].



(a) (b)

Figure 3.1: (a) Transmission line model of a TCDA and its feeding network including the wideband Marchand balun [3]. (b) Edge view of the unit-cell design shown in Fig. 3.2 with tuning elements of the balun labeled. A microstrip excitation is assumed (bottom left) [3].

Basically, a wideband Marchand balun includes short and open circuit transmission lines with extreme impedance ratios ($Zshort >> Zopen$) for wideband operation [30]. In order to overcome the fabrication constraints dealt with designing a wideband Marchand balun at mm-Wave frequencies, a planar form of the balun designed in [29] is used in [3] (shown in Fig. 3.2) to cover the whole frequency bands from 24 GHz to 71 GHz.

As shown in Fig. 3.2, the high impedance short and the low impedance open transmission lines are realized by a shorted twin wire line and a patch over a dipole's arm (acting as the return conductor) respectively. The low surface area and relatively large separation of the two twin-wire conductors results in a high characteristic impedance which is required for the short-circuited stub ($> 100\Omega$ characteristic impedance); however, this becomes problematic for the open-circuit element (ideally $< 20\Omega$). For the open transmission line, it is necessary to produce a strong capacitance between the feed and the return trace to lower the impedance. In [3], this is provided by means of a patch placed directly above the opposite arm of the dipole. In addition to the feeding network, a conducting wall (H-wall shown in Fig. 3.2a) is inserted along the edge of the unit cell to shield each unit cell from back scatter occurring between the feeds of neighboring elements [1].

Fig. 3.3 shows the VSWR of the element in an *infinite array structure* shown in Fig. 3.2. The proposed design in [3] achieves VSWR< 2.2 for the whole frequency range of 24GHz-71GHz for broadside radiation and $VSWR < 2$ and VSWR< 3 when the beam is steered to $\pm 45°$ in E- and H-plane, respectively. This design is good in terms of the bandwidth. Furthermore, the sizes and spacings accounts for the fabrication constraints of large scale, low cost PCB technology in contrast to most of the previous works in literature. However, the superstrate which is used to further increase the bandwidth has made the antenna

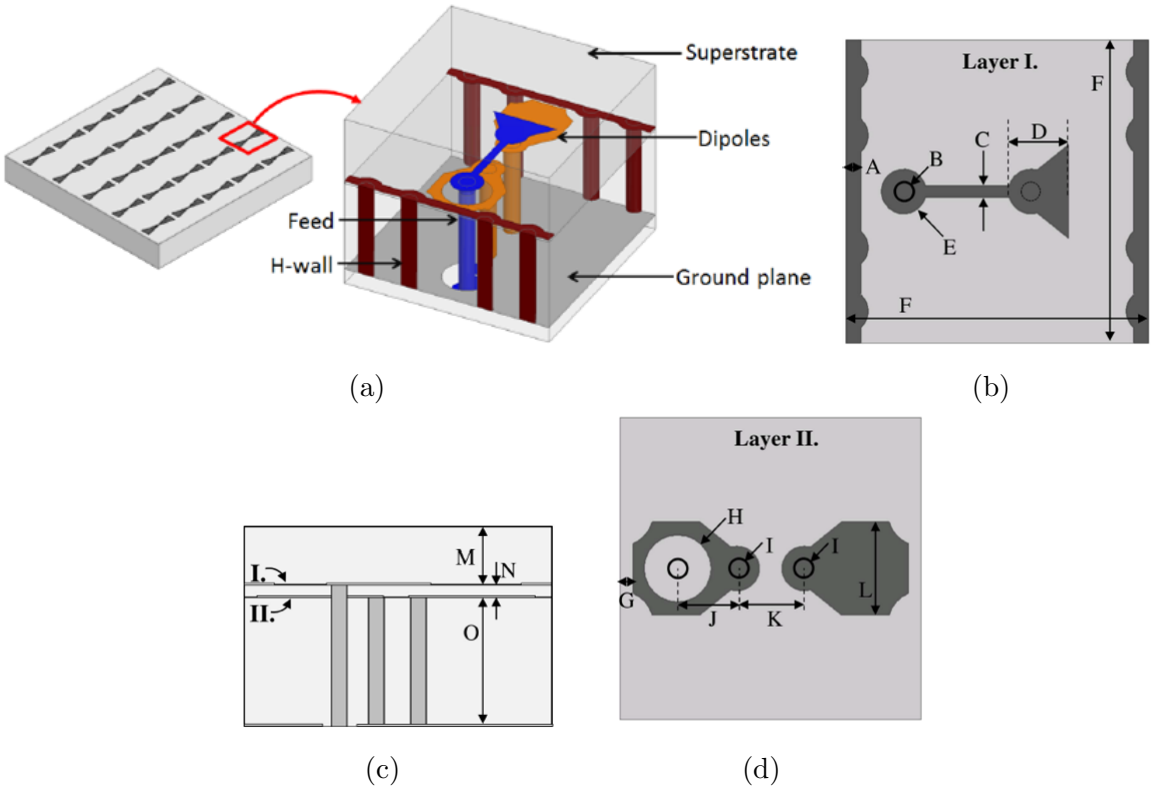


Figure 3.2: (a) a unit cell design sampled from a periodic array with roughly $\lambda/2$ spacing in both directions [3] (b) Upper layer [3] (c) side view of the unit cell [3](d) Bottom layer [3]

high profile in terms of thickness for applications where available antenna height is at a premium. The core substrate is a 0.9mm Rogers Duroid 5880 and the superstrate is a 0.6mm Rogers 2929 which results in a 1.6mm thickness including the layer between the open stub and the dipole. This thickness is not still including the feeding lines' layer which is required underneath the element for excitation. Since the antenna thickness must not exceed 0.9mm in our targeted application, the design shown in Fig. 3.2 must be modified in such a way to decrease the antenna thickness while maintaining acceptable bandwidth for our purpose.

In order to further decrease the open line characteristic impedance, in our proposed design, the open transmission line is realized by a GCPW [2]. The revised design is shown in Fig. 3.4. The capacitance between the feed and the ground is increased by adding two ground planes on both sides of the feed line and connecting both to the dipole's arm underneath (acting as the ground for the GCPW line). Due to the fabrication constraints, as shown in Fig. 3.4d, two via pads with diameter D_1 are attached on both sides of the dipole. A conducting H-wall used in [3][50] is also placed along the H-Plane edge of the unit cell to shield the vertical feed lines from the neighboring elements and to eliminate the common mode resonance. The shorting vias can produce cross-polarization if the symmetry of the structure is disturbed; so, the structure and vias are designed symmetrical as shown in Fig. 3.4.

The design shown in Fig. 3.4 is simulated in an infinite periodic structure to include the effect of mutual couplings between elements. All parameters shown in Table 3.2 are optimized using Ansys HFSS optimization tool considering the minimum achievable feature sizes for PCB fabrication. The limiting size values may vary by different vendors but Table 3.3 shows a set of minimum values for the dimensions shown in Fig. 3.5 provided by Candor PCB shop [3] [54]. The substrate used is a Bismaleimide Triazine (BT)-material with relative permittivity of 3.6 and a dielectric loss tangent of 0.015. The distance to ground is 0.52 mm and the overall antenna thickness is 0.715 mm including the open stub layer. The remaining 0.2mm is reserved for the microstrip feed line underneath the ground plane.

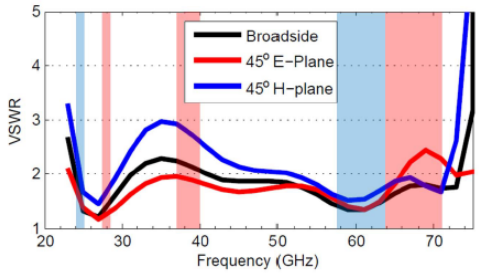


Figure 3.3: Infinite array VSWR of the element shown in Fig. 3.2 at broadside and $\pm 45^o$ scanning in E and H planes. The 5G and Industrial, Scientific, and Medical (ISM) bands are highlighted and are observed to fall in the passband of the array [3]

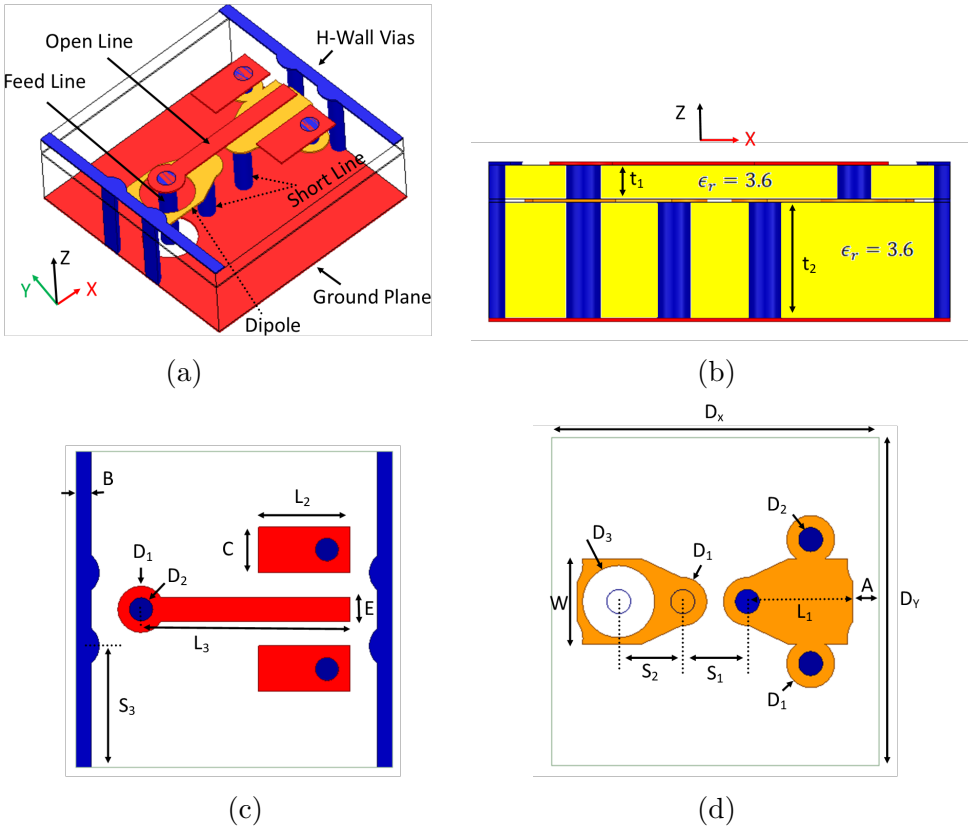


Figure 3.4: Designed unit cell [2] (a) 3D view. (b) side view. (c) Upper layer. (d) Bottom layer

Table 3.2: Optimized Parameters' values (mm) shown in Fig. 3.4 [2]

Parameter	Value	Parameter	Value	Parameter	Value
A	0.1625	E	0.16	S_3	0.7975
B	0.1	S_1	0.41	L_3	1.37
C	0.3	S_2	0.406	D_x	2.075
D_1	0.305	L_1	0.67	D_y	2.075
D_2	0.152	L_2	0.6	W	0.54
t_1	0.15	t_2	0.52		

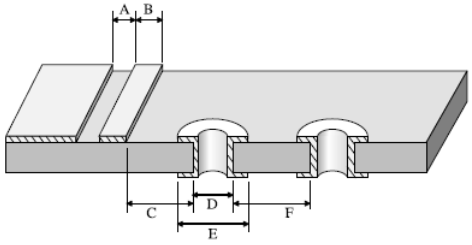


Figure 3.5: Key limiting parameters for PCB fabrication labeled and provided in Table 3.3 [3]

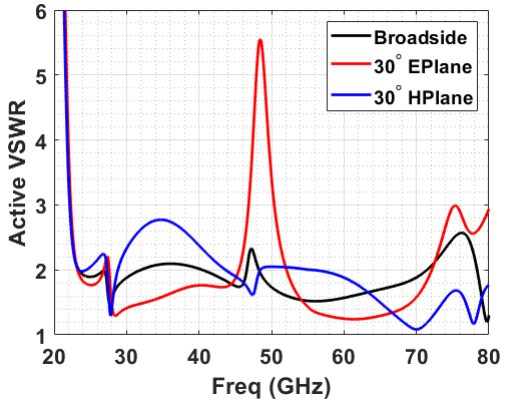
Table 3.3: Minimum achievable dimensions of the key parameters shown in Fig. 3.5 [3][54].

Dimensions	A	B	C	D	E	F
minimum values (μm)	76.2	76.2	152.4	152.4	304.8	254

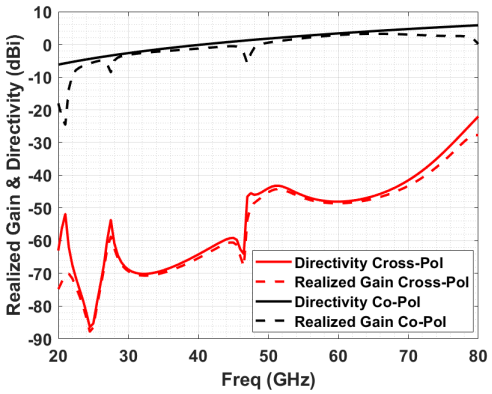
3.1.3 Simulation Results

The simulated active VSWR is shown in Fig. 3.6a. As can be seen, the VSWR is below 2.24 across the frequency range 22.6 GHz-72.6 GHz for broadside radiation and below 2.8 when the beam is steered to $\pm 30^\circ$ in E and H planes except for a narrow bandwidth between 46.7GHz to 50.6GHz when steering the beam in E-Plane which is not located in our desired frequency ranges. There are two narrow band resonances around 27.5GHz and 47GHz which increase the VSWR specially when beam is steered in E-plane. Fig. 3.6b shows the simulated realized gain and directivity for the proposed element design shown in Fig. 3.4 in an infinite periodic array for broadside radiation. The two narrowband resonances around

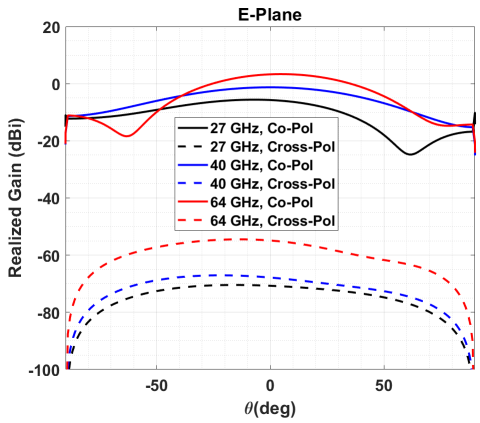
27.5GHz and 47GHz also create a small dip (about 4 dBi) in Co-polarized realized gain for a narrow bandwidth around those frequencies. Although there is no dip shown in directivity curve which confirms that the reason for those dips in gain is merely the input mismatch. Fig. 3.6c,3.6d shows the co- and cross-polarized realized gain in E and H planes. The asymmetry seen in the pattern in E-plane is due to the asymmetry in the location of the excitation port in this plane. The maximum of the cross-polarization is found to occur in $\phi = 43^o, 154^o$, and 10^o planes at 27GHz, 40GHz, and 64GHz respectively. Fig. 3.6e,3.6f, 3.6g show that the cross-polarized gain can even goes beyond the co-polarization at some specific angles in these planes; however, for broadside radiation the cross-polarization is more than 40 dBi below the co-polarization in the whole frequency band (24 GHz-71 GHz) as shown in Fig. 3.6b.



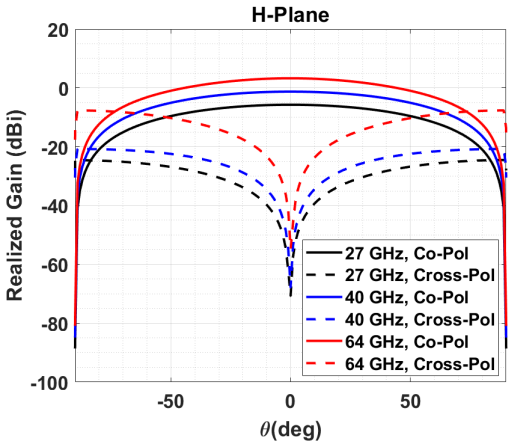
(a)



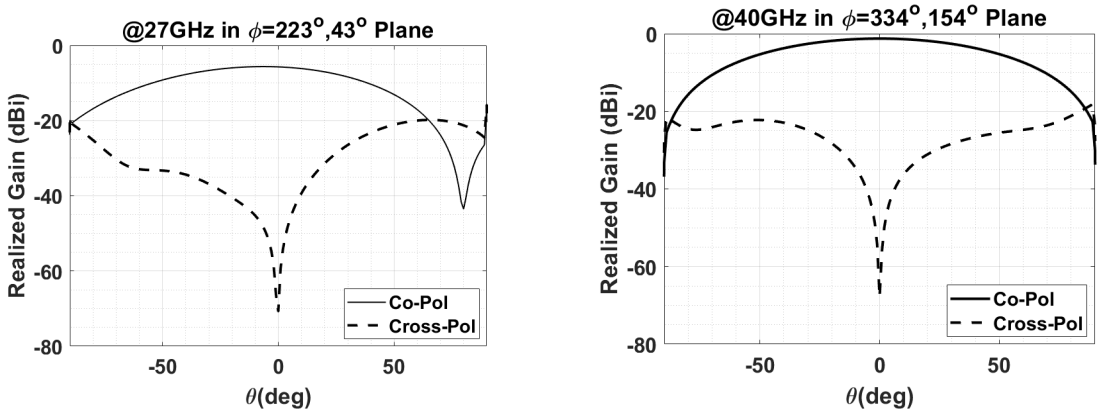
(b)



(c)

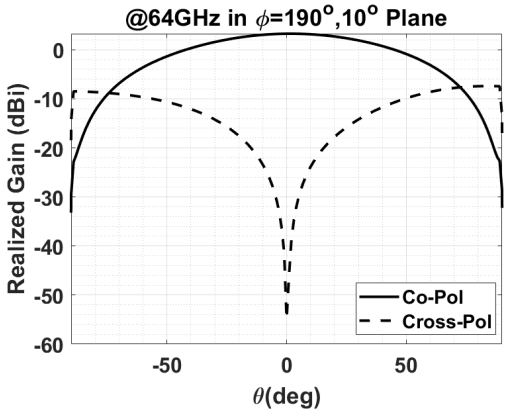


(d)



(e)

(f)



(g)

Figure 3.6: Simulation results of the optimized element design shown in Fig. 3.4 in an infinite periodic array environment [2] (a) active VSWR for broadside radiation and when steering up to 30^o in E and H planes (b) Realized gain and directivity (co- and cross-polarization) for broadside radiation (c) Realized co- and cross-polarized gain at 27 GHz, 40 GHz, and 64 GHz in E-Plane. (d) Realized co- and cross-polarized gain at 27 GHz, 40 GHz, and 64 GHz in H-Plane. (e) Realized co- and cross-polarized gain at 27 GHz in $\phi = 223^o, 43^o$ where cross-polarization is maximized at this frequency. (f) Realized co- and cross-polarized gain at 40 GHz in $\phi = 334^o, 154^o$ where cross-polarization is maximized at this frequency. (g) Realized co- and cross-polarized gain at 64 GHz in $\phi = 190^o, 10^o$ where cross-polarization is maximized at this frequency.

The lower resonance at 27.5GHz can be removed by decreasing the distance between

the feed line and its neighboring grounded via (parameter S_2 shown in Fig. 3.4d); however, the minimum edge-to-edge pitch for mechanically drilled vias is commonly 10 mil ($254\mu m$) and the minimum via diameter is 6 mil ($152.4\mu m$). Laser drilled holes can reach beyond this limit while they are limited to very thin layers. The comparatively thick core substrate must be mechanically drilled, resulting in a minimum diameter of 6 mil (152.4 μm) as shown in table 3.3. Fig. 3.7 shows the real and imaginary parts of the active input impedance for different distance S_2 shown in Fig. 3.4d. Except for the parameter D_3 which is reduced to 0.3mm, all other parameters are kept as shown in table 3.2. The parameter D_3 is reduced to prevent reshaping the dipole when distance S_2 is decreased. As can be seen in Fig. 3.7a, as the distance S_2 is decreased, the resonance around 27.5 GHz is suppressed and finally removed when $S_2 = 0.25mm$. However, the active input reflection coefficient is increased to -4 dB at around 24 GHz as seen in Fig. 3.7c. Furthermore, the dimension $S_2 = 0.25mm$ is not practically possible since there would not be enough space for via pads on both ends.

The resonance around 47GHz can be removed by replacing the via fence H-wall with a solid PEC wall as shown in Fig. 3.8a. Figs. 3.8b,3.8c,3.8d show the simulation result for the design shown in Fig. 3.8a in an infinite periodic array. In this design, the parameters S_2, D_3 are reduced to $0.25mm, 0.3mm$ to remove the resonance around 27.5 GHz. All other parameters are the same as the optimized values shown in table 3.2. However, the sharp resonance around 78GHz which was out of our band of interest moves to 70GHz and increases the active input reflection coefficient (S_{11}) in the end of the third band of interest as shown in Fig. 3.8b. Furthermore, implementing a PEC wall as shown in Fig. 3.8a is very hard to do and the via fence wall provides the best practical solution.

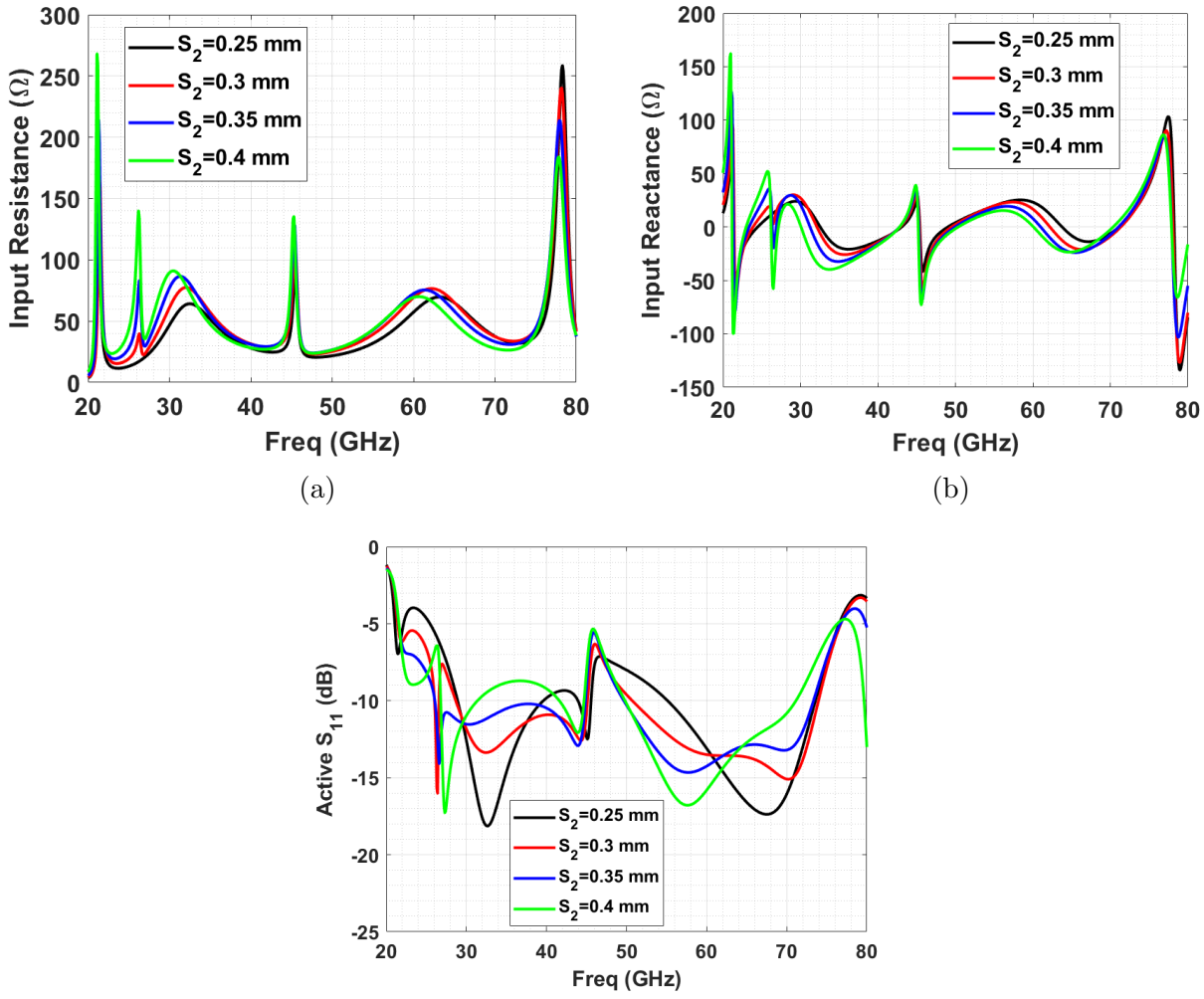
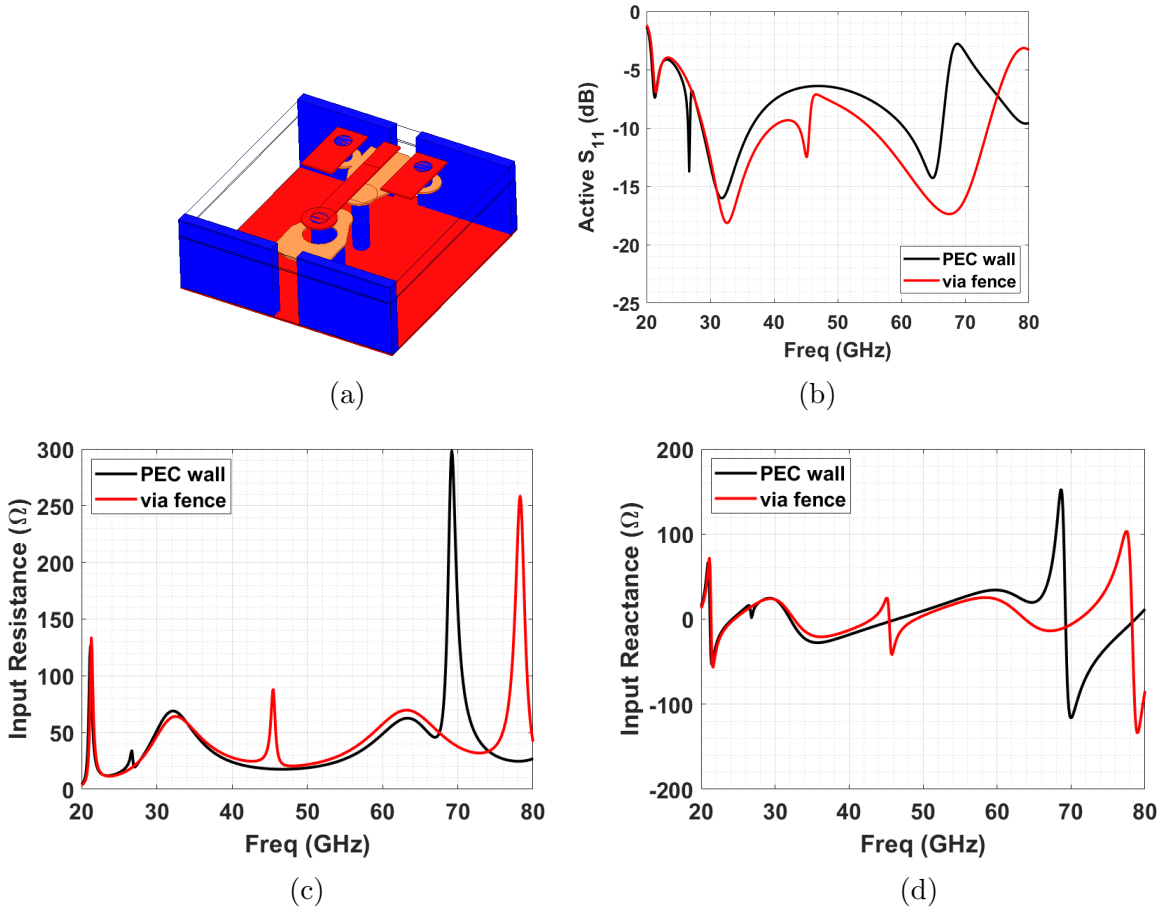


Figure 3.7: The simulation results of the design shown in Fig. 3.4 for different S_2 parameter and when $D_3 = 0.3mm$. The rest of the parameters shown in Fig. 3.4 are the same as Table 3.2 (a) The real part of active input impedance. (b) The imaginary part of active input impedance. (c) The active input reflection coefficient (S_{11}).



(a) (b) (c) (d)

Figure 3.8: (a) The 3D design of the unit cell with PEC wall. (b) The active input reflection coefficient (S_{11}) for the design with PEC wall and by using via fence. (c) The real part of active input impedance for the design with PEC wall and by using via fence. (d) The imaginary part of active input impedance for the design with PEC wall and by using via fence.

3.2 Design of a Small 2 × 2 Wideband, Tightly Coupled Bowtie Array for mm-Wave 5G Applications

In this section, a small 2 × 2 antenna array is designed for the first two 5G mm-Wave frequency bands (24 GHz-43 GHz). The goal is to design and fabricate a small, version of

the 8×8 array which is going to be used for proofing the thinned TCDA concept in chapter 4. The first step in designing an antenna array is designing a single antenna element with required gain and VSWR bandwidth. An antenna array with wide VSWR bandwidth needs a wide band antenna element as well. So, designing a thinned TCA working from 24 GHz-43 GHz starts by focusing on the design of an antenna element working in this frequency range. In this section, the antenna element design is first explained and then the design of a small 2×2 array of this element is addressed. In the following, the 2×2 array is fabricated and measured to confirm the simulation results.

3.2.1 Bowtie Element Design

So far, a modified version of planar Marchand balun is used in section 3.1.2 to design a thin, UWB antenna element covering the three 5G mm-Wave frequency bands from 24 GHz-71 GHz. In this section, our target frequency range is limited to the first two 5G mm-Wave frequency bands (25 GHz-43 GHz); so, by proper choice of unit cell dimension (see equation (2.5)) the common mode resonance frequency would be out of our desired frequency range without the need for H-wall vias used in the antenna element design in section 3.1.2. Also, in this section, we don't have a strict limitation on the antenna thickness. The more important requirement is to get acceptable VSWR in the whole desired frequency range (25 GHz-43 GHz) and for steering up to 45^o. So, the Marchand balun's open stub is kept as a simple microstrip line instead of using GCPW line used in section 3.1.2. Also, it would be preferred to keep the antenna structure as simple as possible because this antenna element is going to be used in a large 8×8 array for proofing the idea of thinned TCDA.

So, the bowtie element design shown in Fig. 3.9a is excited by a waveport on bottom layer shown in green and is simulated in an infinite periodic array setup using Ansys HFSS software. The parametric values shown in Fig. 3.9b is optimized in order to achieve S_{11} better than -10dB for the entire frequency range (24 GHz-43 GHz). Simulating the antenna element in an infinite periodic array accounts for the strong mutual couplings among elements. Table 3.4 shows the optimized parameters in the design of the bowtie element. Basically in phased arrays the unit cell dimensions are chosen below $\lambda/2$ at the highest frequency of operation to keep the pattern free from grating lobe appearance for the whole frequency range and steering up to 90^o. Additionally, having unit cells smaller than $\lambda/2$ at highest frequency ensures strong mutual couplings at lower frequencies in TCAs with large bandwidth ratio. This strong couplings compensate for the inductive effect of the ground plane at low frequencies and increases the VSWR bandwidth. Furthermore, the size of the 8×8 array is limited to $25mm \times 25mm$. So, in this design, the unit cell size is set to be $D_X = D_Y = 3mm$, which is 0.43 of the wavelength at highest frequency

(43GHz). With this choice of D_X, D_Y, the common mode resonance frequency is calculated to occur at 18.48 GHz by using the equation (2.5) which is far enough from our frequency band and there is no need for the H-wall vias as mentioned earlier.

As can be seen in Fig. 3.10a, 3.10b, the VSWR is below 2 ($S_{11} < -10dB$) for the entire frequency range 24.2 GHz-43.4 GHz; Furthermore, VSWR is below 2.6, 2.8 in the whole frequency range 24 GHz-43 GHz when the beam is steered up to 45^o in E and H plane respectively. As shown in Fig. 3.10c, the total broadside realized gain of the antenna element is varying from -2.9 dBi to 3.34 dBi as the frequency increases from 24 GHz to 43 GHz. Fig. 3.10d,3.10e show the antenna pattern in E and H planes at 27 GHz and 40 GHz. There is an asymmetry seen in the antenna pattern in E-Plane which is due to the asymmetric location of the excitation feed in E-Plane. Fig. 3.10f,3.10g show the co- and cross-polarized realized gain in $\phi = 204^o, 202^o$ planes where cross-polarization is maximized at 27 GHz, 40 GHz respectively.

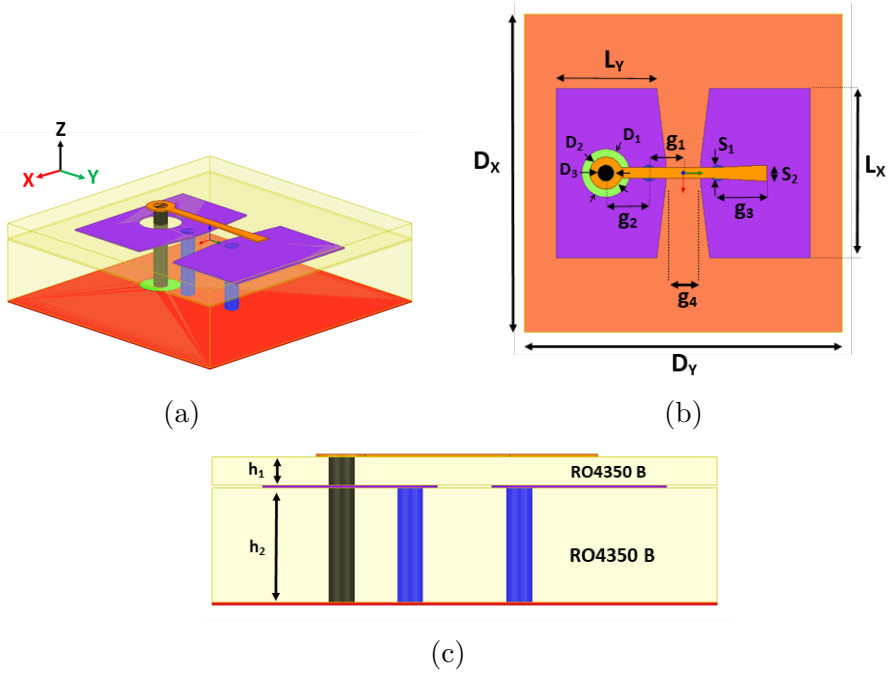
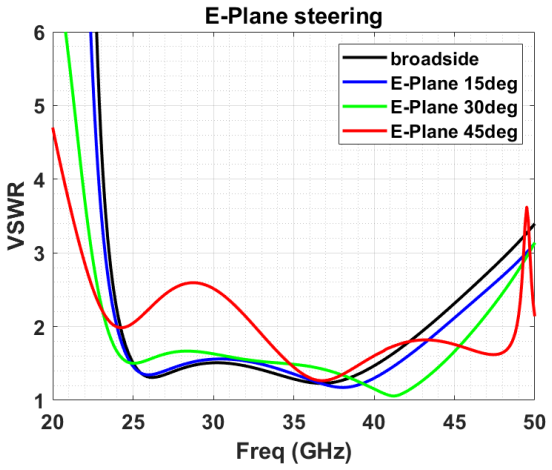


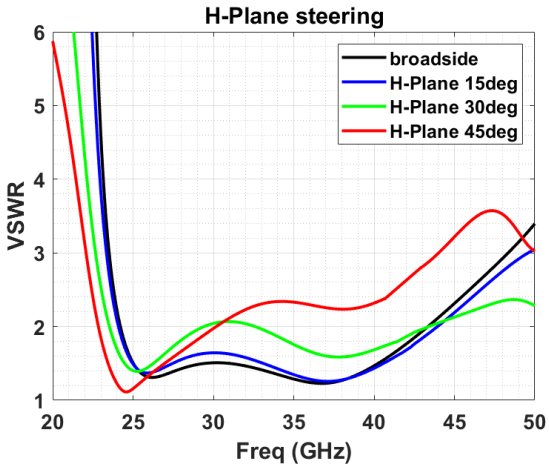
Figure 3.9: Bowtie element (a) 3D view. (b) Top view. (c) Side view.

Table 3.4: Optimized Parameters' values (mm) shown in Fig. 3.9.

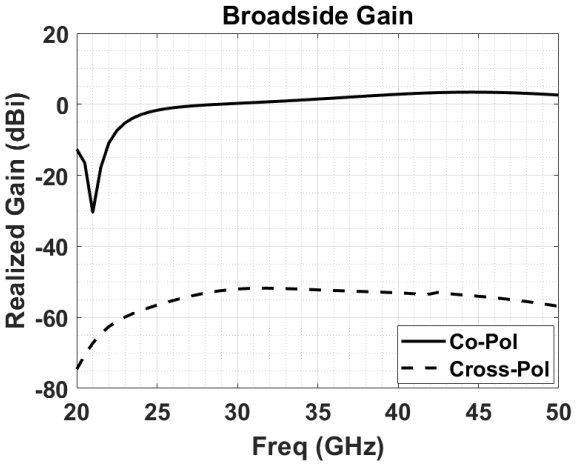
Parameter	Value	Parameter	Value	Parameter	Value
$D_X = D_Y$	3	L_X	1.6	L_Y	0.95
S_1	0.1	S_2	0.15	g_1	0.325
g_2	0.406	g_3	0.5	g_4	0.325
D_1	0.457	D_2	0.305	D_3	0.152
h_1	0.168	h_2	0.676		



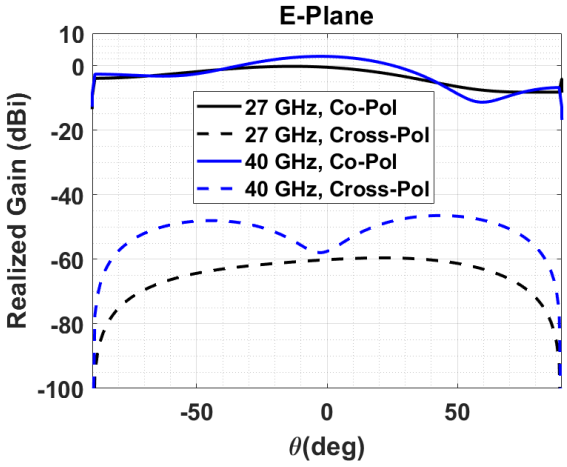
(a)



(b)



(c)



(d)

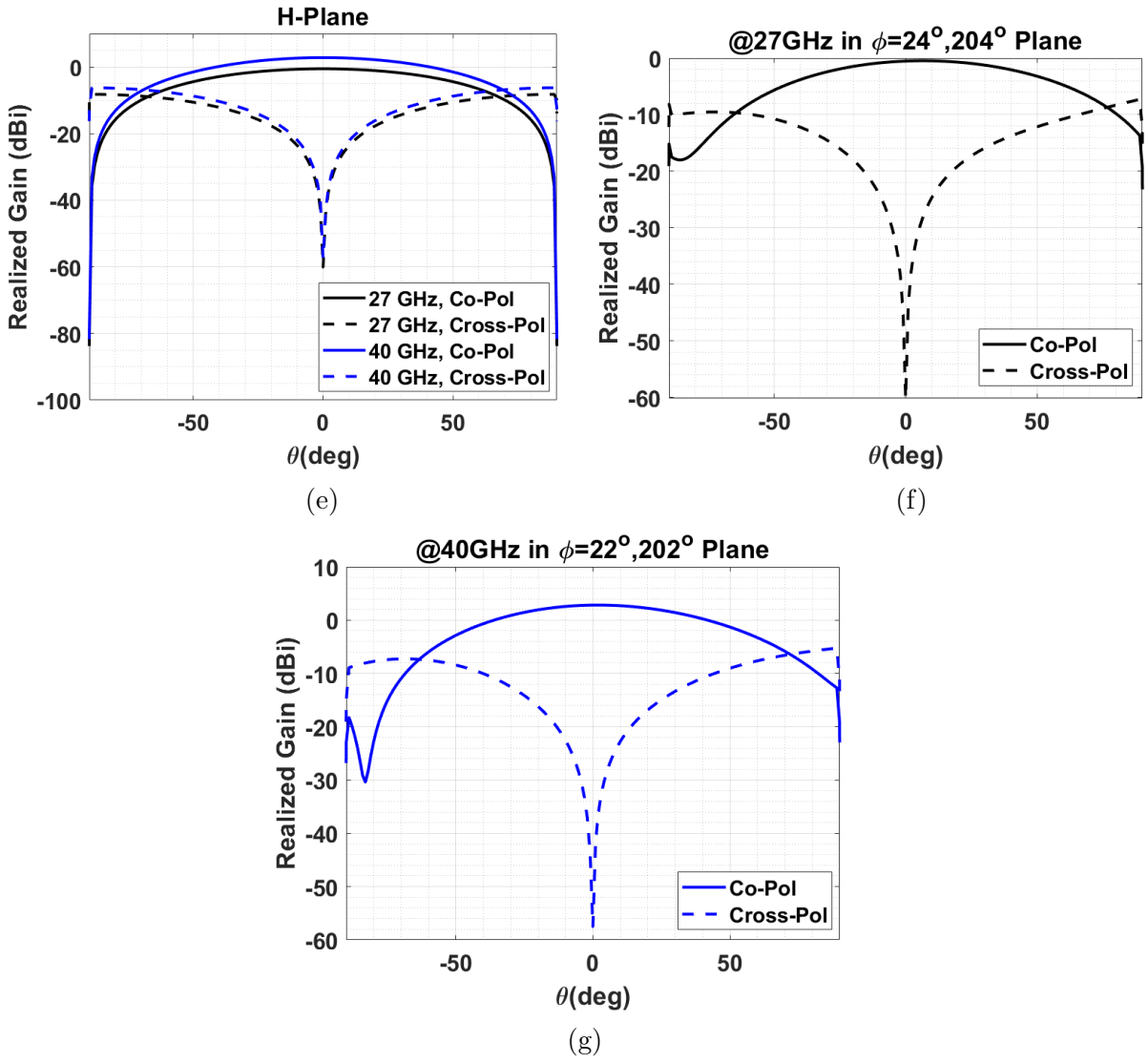


Figure 3.10: simulation results of the designed bowtie element shown in Fig. 3.9 (a) VSWR versus frequency when the beam is steering in E-Plane. (b) VSWR versus frequency when the beam is steering in E-Plane. (c) Simulated realized gain (dBi) for broadside radiation. (d) Simulated realized gain at 27 GHz, 40 GHz in E-Plane. (e) Simulated realized gain at 27 GHz, 40 GHz in H-Plane. (f) Simulated realized gain at 27 GHz in $\phi = 24^o, 204^o$ plane where cross-polarization in maximized. (g) Simulated realized gain at 40 GHz in $\phi = 22^o, 202^o$ plane where cross-polarization in maximized.

3.2.2 Design and Simulation of the 2 × 2 Array

The design of the 2 × 2 tightly coupled array, starts by arranging the optimized bowtie elements (described in section 3.2.1) in a 2 × 2 configuration. Since in the 2 × 2 array all four elements are on the corners, the return loss at each port of the 2 × 2 array is different from the return loss of the optimized element in the infinite periodic setup. Hence, starting with the optimized values in Table 3.4 for all four elements, the whole 2 × 2 array shown in Fig. 3.11 is re-optimized using Ansys HFSS in order to get acceptable S_{11} at all four ports in the entire frequency range 24 GHz-43 GHz [4]. The design parameters are first optimized by exciting the four elements by four 50Ω waveports as like we did for the bowtie element in the previous section (shown in green in Fig. 3.9a).

As seen in Fig. 3.11, the balun causes the relative location of the excitation port be different for half of the elements. Thus the two elements on the right in Fig. 3.11c are taking different parameters from the two on the left to compensate for the unsymmetric excitation and to achieve return loss above $10dB$ at all four ports. Once the parametric values of the elements are optimized to get matched input impedances at all 4 ports, the antenna ports are connected to four 50Ω GCPW transmission line underneath the antenna ground plane. The transition feed lines connecting the antenna ports to 50Ω GCPW lines are designed and optimized using $\lambda/4$ impedance matching and tapering methods to get acceptable return loss on four waveports exciting the 50Ω GCPW transmission lines on the four edges of the antenna board. At the end, the 50Ω waveports are replaced with four 50Ω, 2.4mm, Radio Frequency (RF) edge connectors from Samtec Inc. In order to maintain the low VSWR, the GCPW lines must be tapered close to the location of the connector's center pin as shown in Fig. 3.11d. The antenna array simulation is done using the 3D model of the connectors provided by the manufacture and the results are shown in Fig. 3.12.

The optimized values of all parameters shown in Fig. 3.11 can be found in Table 3.5. The sizes and spacings are chosen considering the fabrication constraints of large scale, low cost PCB method. The substrate used is RO4350B with relative permittivity of 3.66 and the dielectric loss tangent of 0.004. Fig. 3.11b shows the stackup of the design. The total antenna thickness including the feeding lines' layer and all metal thicknesses is 1.2mm. Fig. 3.12a shows the simulated active return loss at all 4 ports when all elements are excited with the same phase and amplitude. The active return loss at two ports is slightly different from the other two which is because of the asymmetry of the excitation probe's location as stated before. However, the return loss at all four ports is above 10dB for the whole frequency range of 25GHz-45GHz.

As shown in Fig. 3.12b the Co-polarized realized gain of the 2 × 2 array increases with

a small fluctuation from 3dBi to 6.7 dBi as we increase the frequency from 25 GHz to 45 GHz which is acceptable for a small, 2×2 ($6mm \times 6mm$) array. Fig. 3.12c,3.12d show the simulated realized gain at 27 GHz, 40 GHz in E and H Planes respectively. Also the co- and cross-polarized realized gain are plotted in Fig. 3.12e,3.12f in $\phi = 61^o, -63^o$ planes where cross-polarization is maximized at 27 GHz, 40 GHz respectively. The simulated total and radiation efficiency of the antenna array is shown in Fig. 3.12g for different lengths of feed lines equivalent to board sizes of ($B_X = B_Y$) 13.462mm and 97.462mm. As shown in this figure the total efficiency for the shorter feedlines ($B_X = B_Y = 13.462mm$) is very large (above 0.85) for the entire frequency range (25 GHz-43 GHz) while the efficiency has dropped to above 0.55 by increasing the length of feed lines. The total efficiency in Fig. 3.12g includes all the losses in the system as well as the VSWR mismatch; however, the radiation efficiency excludes VSWR mismatch. In this design, the board size is selected $B_X = B_Y = 97.462mm$ to accommodate the connectors, facilitate cables connections, and provide enough space for mounting the antenna to the holding panel; however, in practice, there is no need for long feedlines in SoC application.

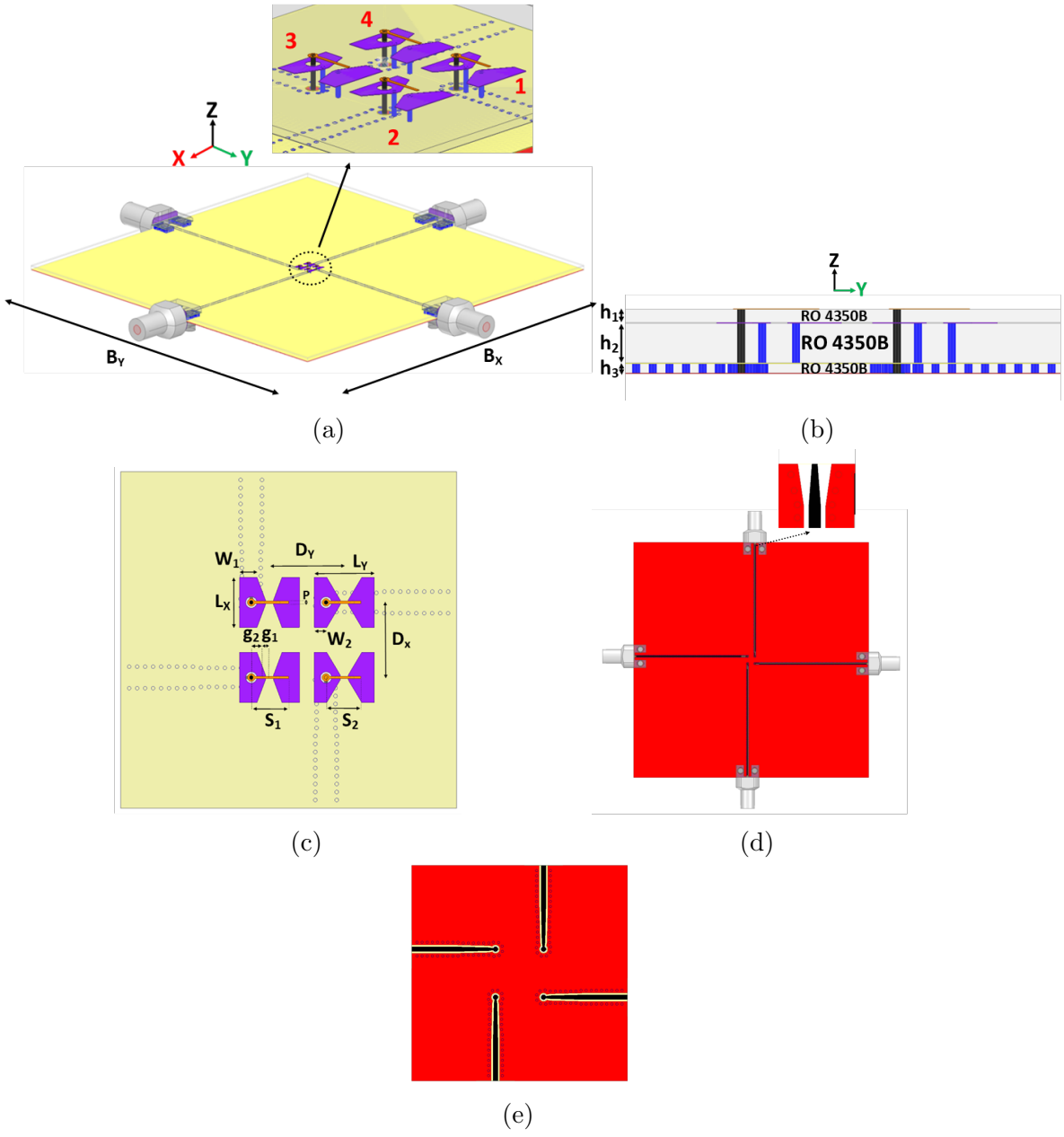
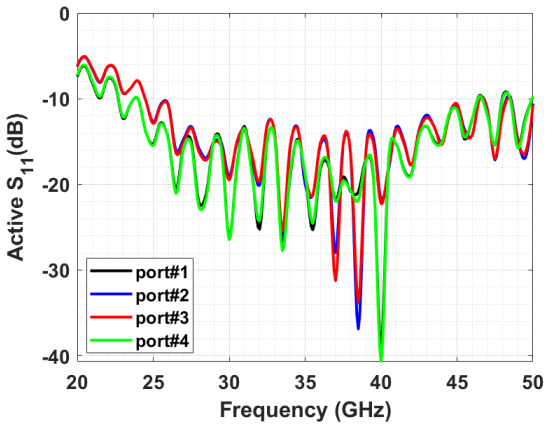


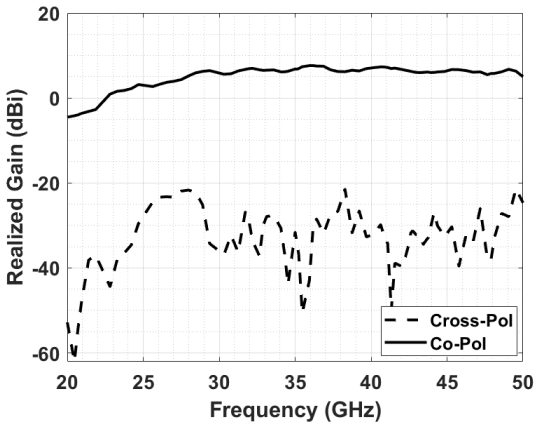
Figure 3.11: Designed 2 × 2 tightly coupled bowtie array [4] (a) 3D view. (b) side view. (c) Top view. (d) Bottom view. (e) bottom view zoomed in feedlines

Table 3.5: Optimized Parameters' values (mm) shown in Fig. 3.11.

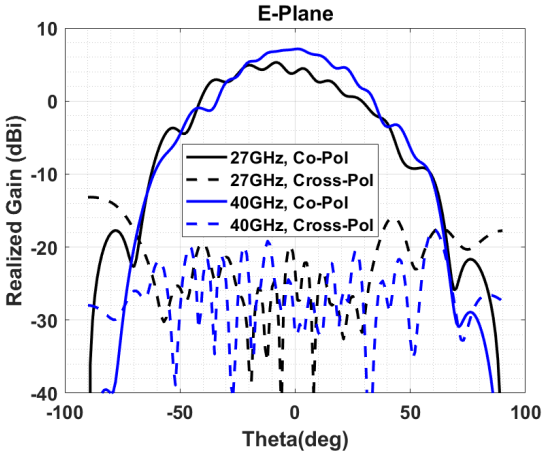
Parameter	Value	Parameter	Value	Parameter	Value	Parameter	Value
W_1	0.7	W_2	0.5	g_1	0.325	g_2	0.406
$D_X = D_Y$	3	S_1	1.5	S_2	1.4	L_X	2
L_Y	2.4	h_1	0.25	h_2	0.762	h_3	0.17
P	0.1	$B_X = B_Y$	97.462				



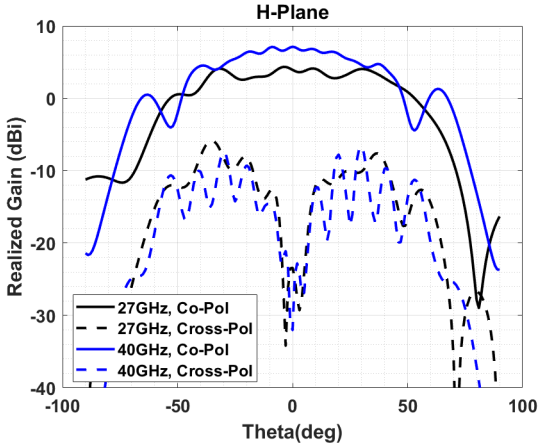
(a)



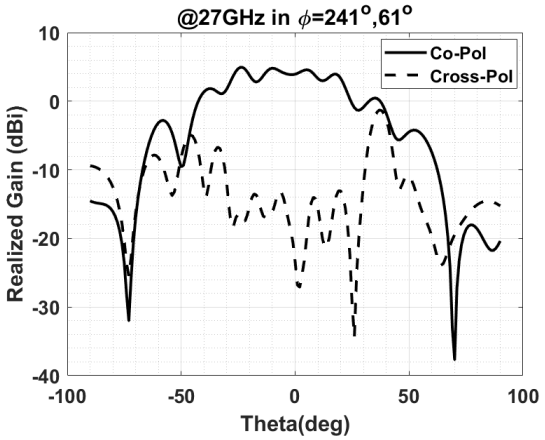
(b)



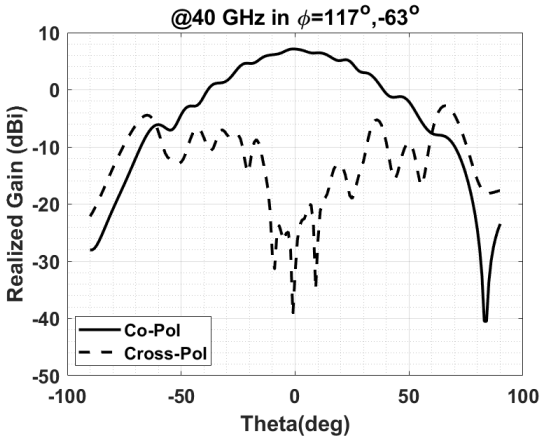
(c)



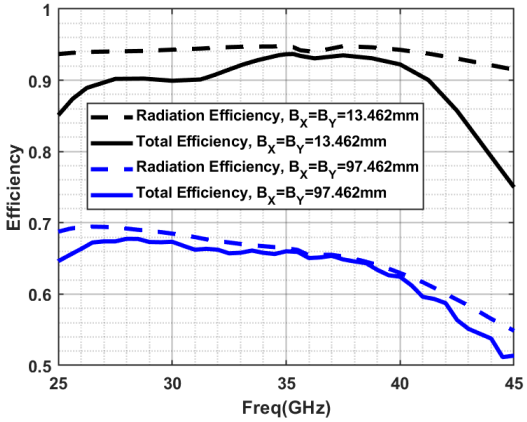
(d)



(e)



(f)



(g)

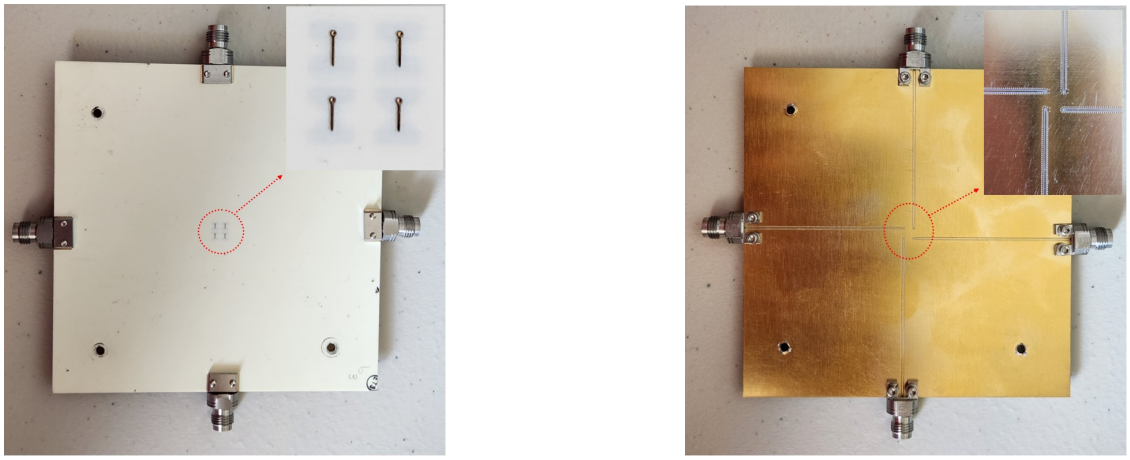
Figure 3.12: simulation results of the designed 2×2 tightly coupled bowtie array shown in Fig. 3.11a [4] (a) Active input reflection coefficient (S_{11}) at all connector ports for broadside radiation. (b) Realized co- and cross-polarization gain for broadside radiation. (c) Realized co- and cross-polarized gain at 27 GHz, 40 GHz in E-Plane. (d) Realized co- and cross-polarized gain at 27 GHz, 40 GHz in H-Plane. (e) Realized co- and cross-polarized gain at 27 GHz in $\phi = 241^o, 61^o$ Plane where cross-polarization is maximized. (f) Realized co- and cross-polarized gain at 40 GHz in $\phi = 117^o, -63^o$ Plane where cross-polarization is maximized. (g) Antenna array efficiency for two different board sizes.

3.2.3 Fabrication and Measurement of the 2 × 2 Array

The designed 2×2 tightly coupled bowtie array shown in Fig. 3.11 is fabricated using PCB manufacturing method. Fig. 3.13 shows the fabricated board with four 2.4mm connectors connected on four sides of the board. The scattering parameters of the 4 port antenna array are measured using the two port Keysight 50GHz Power Network Analyzer (PNA)-X (N5245B). The PNA is calibrated to the end of the connected cables using the Electronic Calibration (ECal) module. In order to measure the mutual scattering parameters (S_{ij}), i'th and j'th ports are connected to the two calibrated ports of PNA and the other ports are terminated to 50Ω loads using 2.4M-2.9M adaptors. The measurement setup for measuring the scattering parameters between two different ports can be seen in Fig. 3.14a. Once all the scattering parameters are measured, The active input reflection coefficients at all four ports are calculated using the equation below:

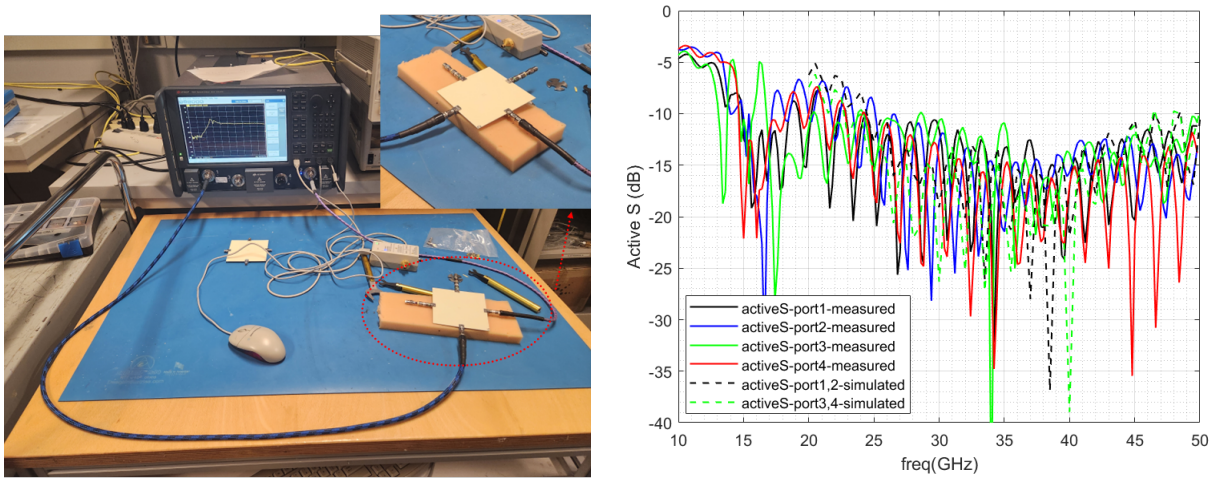
$$S_j^{Active} = \sum_{i=1}^{4} S_{ji} \frac{a_i}{a_j} \tag{3.1}$$

where a_i, a_j are the excitation coefficients of the i'th and j'th elements which are both one for broadside radiation. The calculated active $[S]$ parameters based on the measurement of the scattering parameters agrees well with the simulated results for broadside radiation as shown in Fig. 3.14b.



(a) (b)

Figure 3.13: Fabricated 2×2 tightly coupled bowtie array (a) Top view (b) bottom view



(a) (b)

Figure 3.14: (a) Measurement set up for measuring the antenna's scattering parameters (b) The measured and simulated results of the active reflection coefficient when all elements are excited with the same phase and amplitude at all four ports

The small difference between the plots could be due to the fact that the measurement errors for each scattering parameter is accumulated by using the equation 3.1. The antenna pattern is also measured in a far field set up as shown in Fig. 3.15a at EmRG Labratory. A 1:8 power divider (P8D640-8) from Electromagnetic Technology industries (ETI) working from 6 GHz to 40 GHz is used to excite the four input ports with same phase and amplitudes. Four 2.4mm cables with same lengths are connecting four of the splitter outputs to the antenna input ports. The other four ports of the splitter are matched loaded with 50Ω loads. Standard horn antennas, WR28 (NSI-RF-SG28, 26.5-40 GHz), WR22 (RAYTECH ANHP-Q02400, 33-50 GHz) are used to measure the antenna pattern at 27 GHz and 40 GHz respectively.

Fig. 3.15b, 3.15c shows the simulated and measured co-polarized realized gain of the antenna array at 27 GHz, 40 GHz. The gain has been offset by the measured insertion loss of the splitter and cables. As shown in Fig. 3.16a, in order to measure the insertion loss of the splitter and cable, one port of the PNA is connected to the input of the splitter and the other ports are connected to the end of a cable connected to one output of the splitter while the other outputs of the splitter are terminated. The S_{21} of this system is measured for all four outputs of the splitter that are going to be connected to the antenna. Fig. 3.16b shows that the difference between the magnitude of the transmission coefficients

at all four ports are below 1 dB for the whole frequency range (25 GHz-43 GHz). The difference between the phase of the transmission coefficients at four ports varies between -34^o to 40^o in our frequency of operation as shown in Fig. 3.16c. Assuming that $S_{21_{Sp,Cablei}}$ (i=1 to 4), represent the insertion loss of the splitter and cables at four output ports, based on the friis equation, the received power in dB could be calculated by the equation below when the horn antenna is receiving the power radiated by the fabricated antenna and vice versa:

$$P_r^{[dB]} = P_t^{[dB]} + \Sigma_{i=1}^{i=4} 20log_{10}(|S_{21_{Sp,Cablei}}|) + G_{Ant}^{[dBi]} + 20log_{10}(\frac{\lambda_0}{4\pi d}) + G_{Horn}^{[dBi]} \tag{3.2}$$

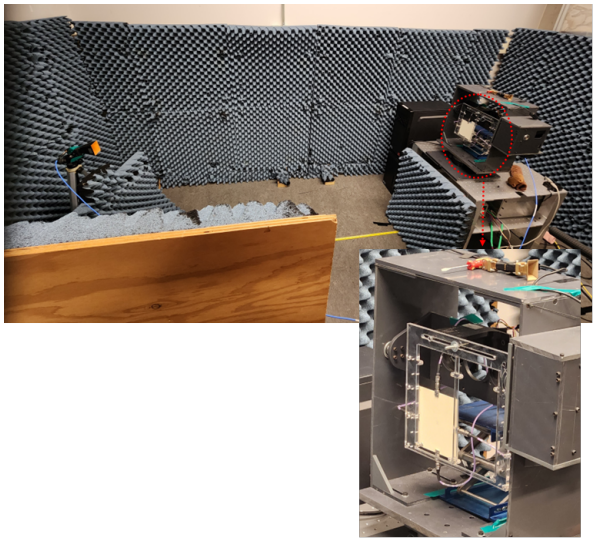
where G_{Horn} is the gain of the standard Horn, G_{Ant} is the Gain of our antenna and d is the distance between the two antennas. Since the magnitude of the $S_{21_{Sp,Cablei}}$ for i=1,2,3,4 are pretty much similar as shown in Fig. 3.16b, we could have only measured one of them and add it by 6 dB for the four antenna elements instead the four parameters and summing up all together.

Fig. 3.15d shows the input reflection coefficient at the input of the splitter whose four outputs are connected to the antenna with four equi-length cables. This return loss is artificially low since the reflected power is absorbed by the splitter. Basically the reflection coefficient at the input of splitter can be derived by using the equation 3.3.

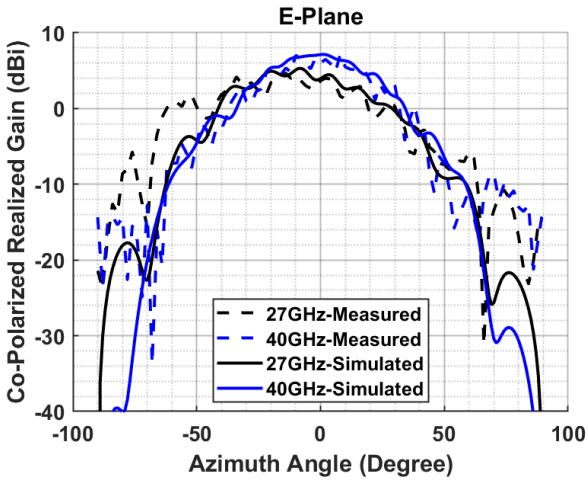
$$S_{11}^{Sp+Cable+Ant} = S_{11}^{Sp} + \Sigma_{i=1}^{i=4} S_{21_{Sp,Cablei}}^2 S_i^{Active} \tag{3.3}$$

where S_{11}^{Sp} is the input reflection coefficient of the splitter and S_i^{Active} is the active reflection coefficient at i'th port of the antenna. Since the excitation port of the antenna is not located symmetric, the active reflection coefficient of the two ports 1,3 are different from the other two (ports 2,4); however, if we assume they are the same, we can find the active input reflection coefficients by using the equation 3.3 and having the measured $S_{21_{Sp,Cablei}}$ (shown in Fig. 3.16c, 3.16b) for four splitter's outputs which are going to be connected to the antenna.

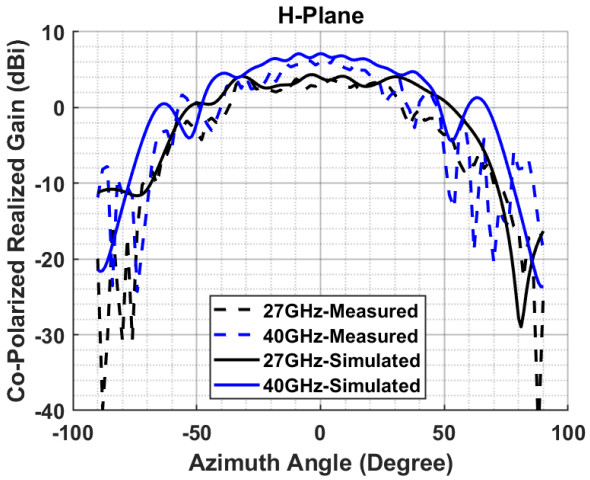
Fig. 3.17 shows the active S_{11} calculated by compensating the round trip insertion loss of the splitter and cables using equation 3.3 and compares it with the active S_{11} calculated at port number 1 by measuring the scattering parameters of the antenna and using the equation 3.1. The two figures start to deviate at frequencies above 40 GHz where is beyond the splitter's frequency of operation. For the frequencies below 40 GHz the two figures match and small deviations are due to the fact that as shown in Fig. 3.16c,3.16b, all four port of the antenna are not provided by exactly the same magnitude and phase and also in this calculation there is an assumption that all ports have identical active S_{11} which is not exactly the case.



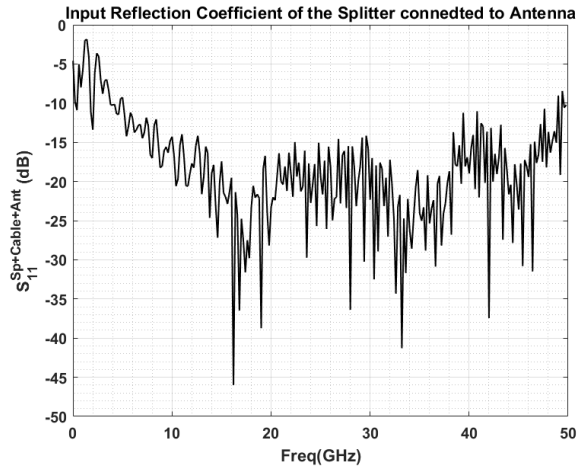
(a)



(b)

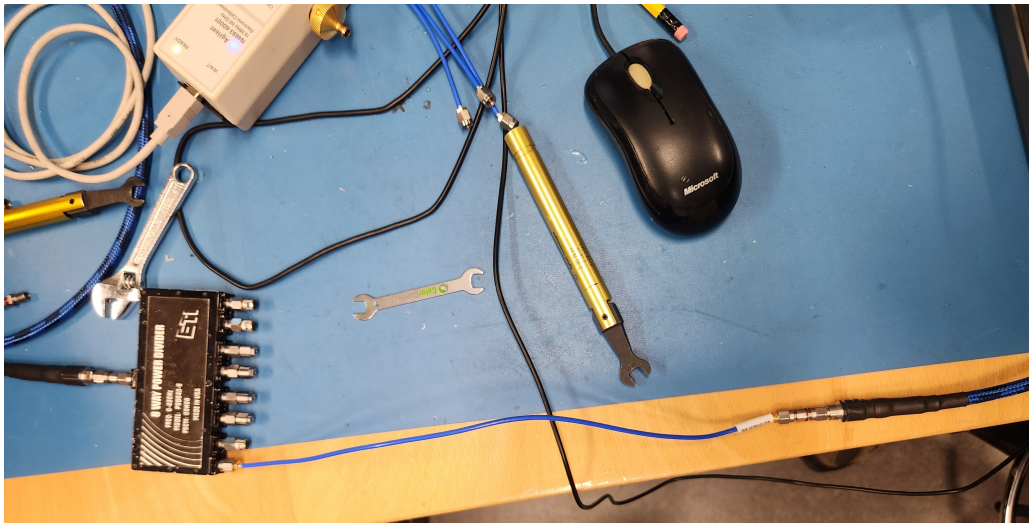


(c)

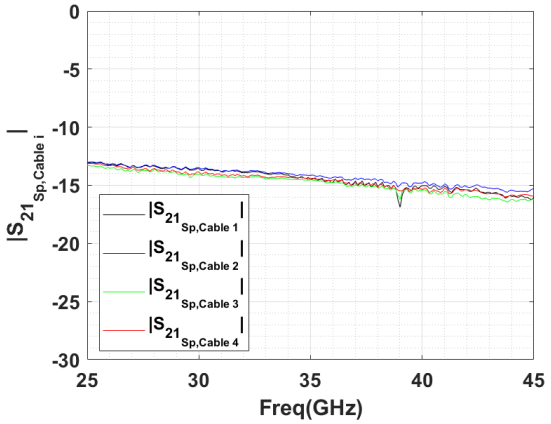


(d)

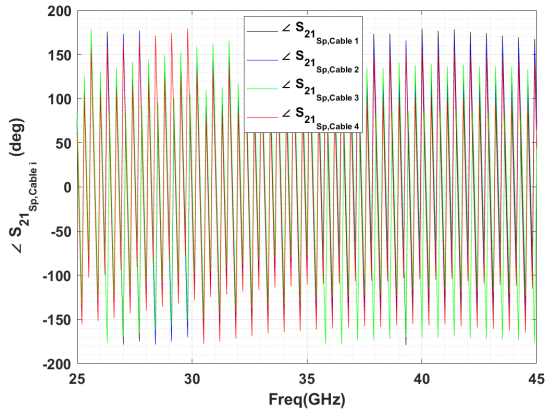
Figure 3.15: (a) Far-field measurement setup for measuring the 2×2 antenna pattern (b) Simulated and measured E-Plane pattern at 27 GHz, 40 GHz. (c) Simulated and measured H-Plane pattern at 27 GHz, 40 GHz. (d) The input reflection coefficient of the splitter connected to the antenna



(a)



(b)



(c)

Figure 3.16: (a) The measurement setup for measuring the insertion loss of the splitter and cables. (b) The magnitude of the transmission coefficient measured for all 4 cables connected to the splitter. (c) The phase of the transmission coefficient measured for all 4 cables connected to the splitter.

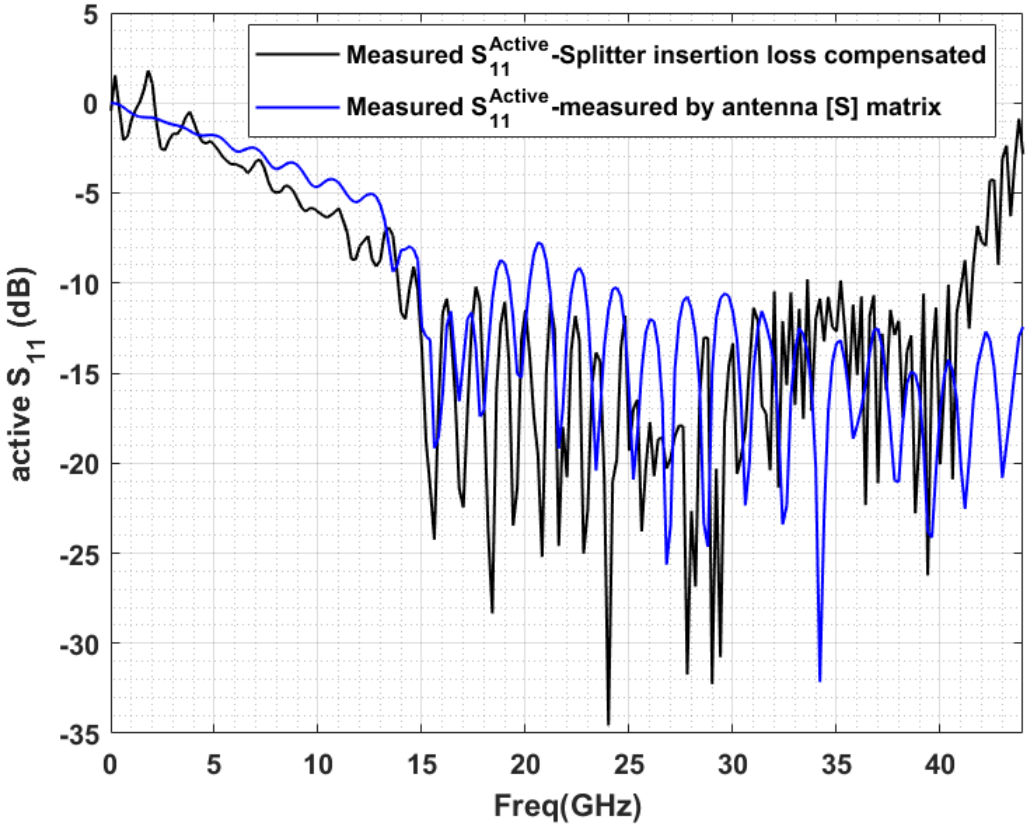


Figure 3.17: Measured active input reflection coefficient of the 2×2 array by calibrating the insertion loss of the splitter and cables (black curve) and by measuring the scattering parameters and using the equation (3.1) (blue curve).

3.3 Design of a 8×8 Tightly Coupled Bowtie Array

The wideband antenna element designed in section 3.2.1 is used to design an 8×8 tightly coupled bowtie array working in the frequency range 25 GHz-45 GHz. Sixty four antenna elements are located in a square lattice configuration as shown in Fig. 3.18. As mentioned in section 3.2.1, the unit cell size is 0.43 of the wavelength at the highest frequency (43 GHz) in each direction ($D_X = D_Y = 3mm$) to ensure there is no grating lobe in the whole frequency range and at the same time there is strong mutual couplings among elements. The designed array is excited with sixty four 50Ω waveports on the ground layer (shown

in green in Fig. 3.18a) and the simulation results are shown in Fig. 3.19.

In the next chapter, this array with 64 elements is used to design the thinned TCA in which only 22 elements are excited. Degrees of freedom play a significant role in the optimization of the thinned array which cannot be provided by small arrays. The number of variables must be large enough in order to obtain satisfactory optimization results. Also, when it comes to steering the beam, using a small array with small gain and wide pattern, makes the comparison of the fully and partially excited patterns difficult. On the other hand, the optimization of a very large array is time consuming and is not a good choice for proofing the idea at first stage. So, in this section, an 8×8 array is designed with the Co-polarized realized gain ranging from 16.5 dBi to 21.6 dBi in the frequency range 25 GHz-45 GHz as shown in Fig. 3.19b. These numbers are sensible since the Co-polarized realized gain of the antenna element is varying from -1.67dBi to 3.41dBi in this frequency range as seen in Fig. 3.10c. The array gain can be roughly calculated using the equation 3.4 which gives us approximately the same numbers for the array gain. In this equation, N represents for the total number of antenna elements in the array. The equation 3.4 assumes there is no mutual coupling among elements; however, the mutual couplings are already considered in the gain of antenna element since the unit cell is simulated in a periodic boundary condition.

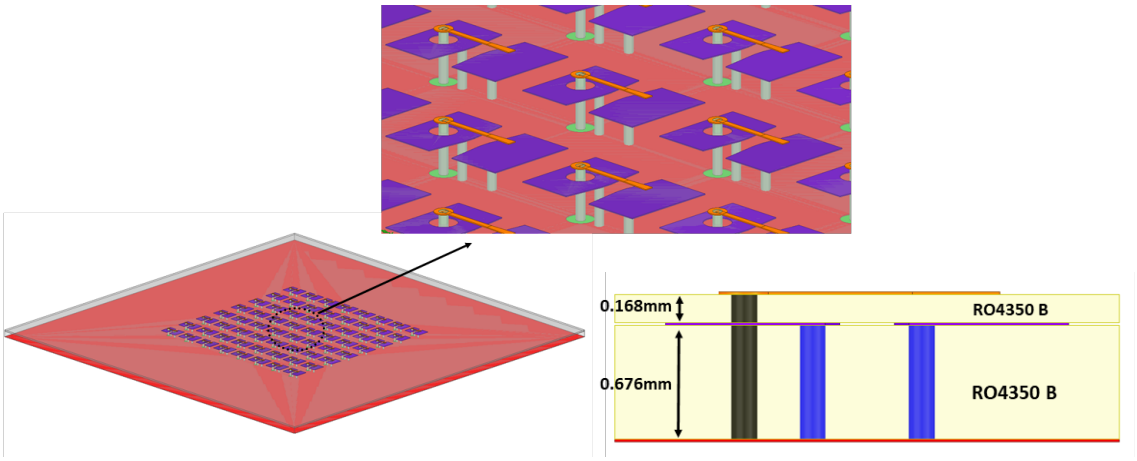
$$G_{Array} = G_{Antenna-Element} + 10log_{10}(N) \tag{3.4}$$

Fig. 3.19a shows the active reflection coefficient at a few ports located at the center (port number 28), around the edges (port numbers 1,4,9,17) and in between (port numbers 13,21) for broadside radiation. Active S_{11} is the reflection coefficient at a specified port when all other ports are also excited. As can be seen in this figure, S_{11} is below -10 dB for the central element (port number 28) for the whole frequency range 25 GHz-45 GHz which makes sense since the antenna element is optimized in an infinite periodic boundary condition. However, for the elements on the edges which are located in a new environment, the S_{11} is increased up to -6 dB. Fig. 3.19b shows the co- and cross-polarized realized gain for broadside radiation.

In Fig. 3.20, it is tried to steer the beam of the 8×8 array to $\theta = 15^o, 30^o, 45^o$ in E and H planes at two frequencies 27 GHz, 40 GHz; so, the proper phase shifts are used by using the equation 3.5 and the results are shown in Fig. 3.20. In this equation, θ_s, ϕ_s represents the desired steering angle and D_x, D_y are the antenna element spacing in x and y directions. As shown in Fig. 3.20, the beam is deviated a bit from the aimed angles which is due to the mutual couplings among the elements.

$$\begin{aligned} \Delta\phi_y &= 2n\pi - kD_y sin(\theta_s) sin(\phi_s) \\ \Delta\phi_x &= 2m\pi - kD_x sin(\theta_s) cos(\phi_s) \end{aligned} \tag{3.5}$$

Fig. 3.21 shows the mutual scattering parameter between the element numbers 28 (central element) and 29 which is a representative of the mutual coupling in H-Plane, also, between element numbers 28 and 36 referring to the mutual coupling in E plane and between element numbers 28 and 37 which represents the mutual coupling in diagonal plane. The mutual coupling in E and H plane is between -12dB and -19dB (mostly between -12dB and -17 dB) in the whole frequency range (25 GHz-43 GHz) which is quite high. However, the mutual coupling in diagonal plane is the lowest compared to the E and H planes. Comparing the three figures, the mutual coupling at higher frequencies in E plane is increased up to -12 dB which helps us in the optimization of the thinned array since at high frequencies the distance between two consecutive excited elements may exceed half of the wavelength which can cause grating lobe or large SLL.



(a) (b)

Figure 3.18: 8×8 tightly coupled array (a) 3D view. (b) side view

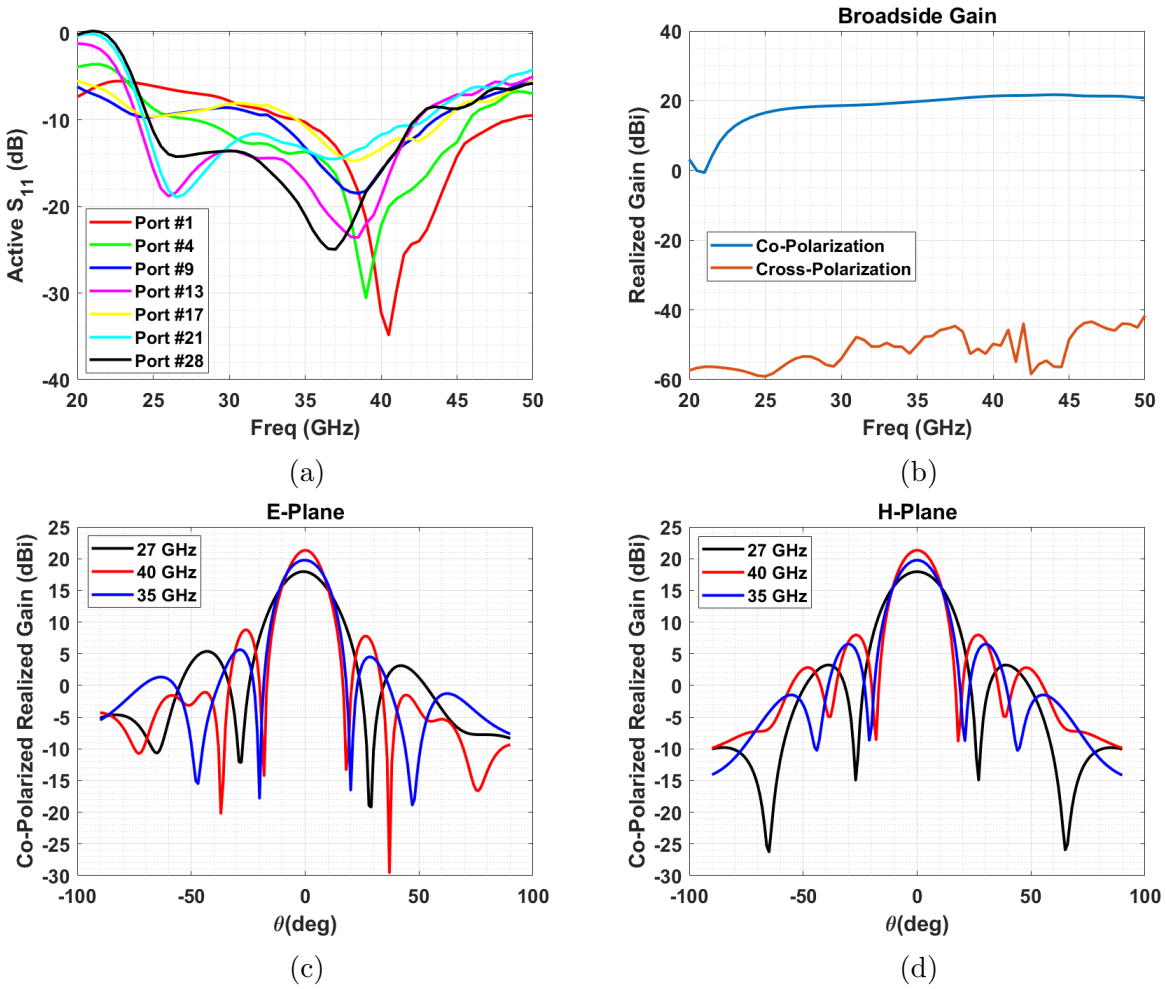


Figure 3.19: The simulation results of the designed 8×8 antenna array shown in Fig. 3.18 excited with 50Ω waveports (a) Active S_{11} at port numbers 1, 4, 9, 13, 17, 21, 28. (b) Realized gain versus frequency for broadside radiation. (c) Antenna pattern in E-Plane at 27 GHz, 35 GHz, 40 GHz. (d) Antenna pattern in H-Plane at 27 GHz, 35 GHz, 40 GHz Bottom layer

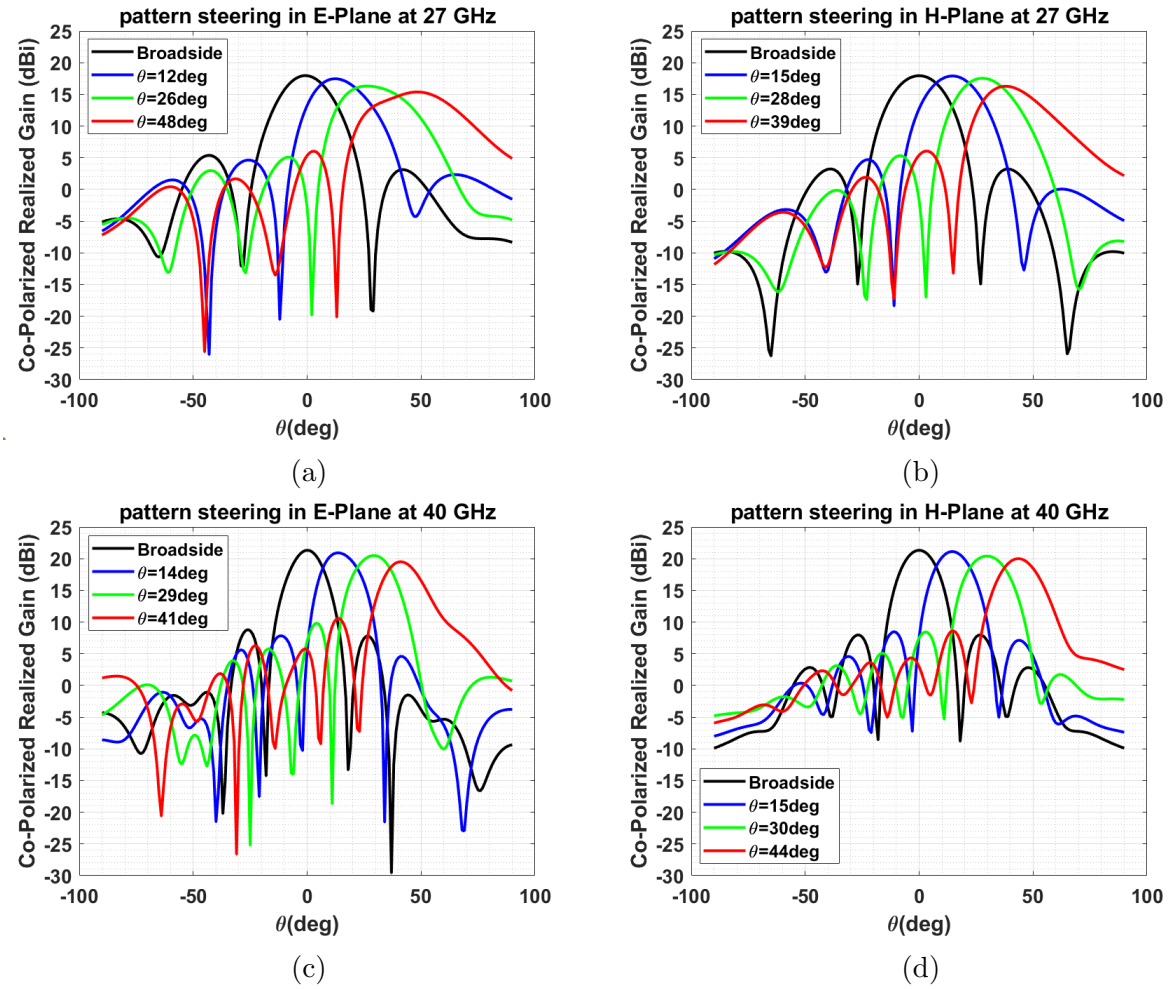


Figure 3.20: Steering the pattern of the designed 8×8 TCA shown in Fig. 3.18 (a) In E-Plane at 27 GHz. (b) In H-Plane at 27 GHz. (c) In E-Plane at 40 GHz. (d) In H-Plane at 40 GHz.

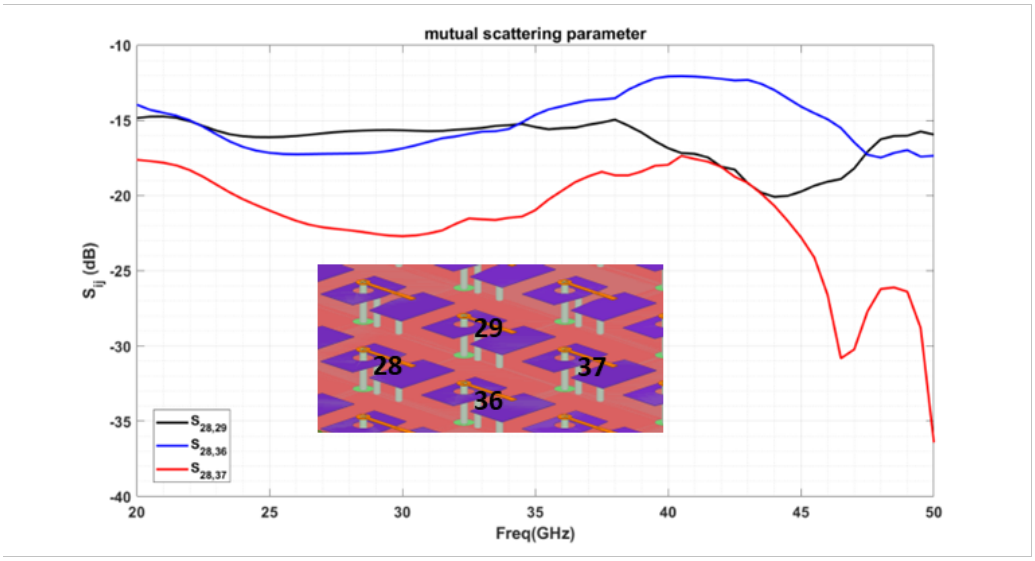


Figure 3.21: The magnitude of mutual scattering parameter in dB between the element numbers 28,29 (mutual coupling in H-Plane), between the element numbers 28,36 (mutual coupling in E-Plane), and between the element numbers 28,37 (mutual coupling in Diagonal plane).

3.4 Conclusion

In this chapter, a thin, planar antenna element that covers the 5G mm-Wave frequency bands (25-29 GHz, 37-43 GHz, 57-71 GHz) required for 5G cell phone devices is designed. Also, an antenna element is designed for the two commonly used 5G frequency bands (25-29 GHz, 37-43 GHz). A 2×2 array of this element is designed, simulated, fabricated and measured using low cost, large scale PCB method. The simulation and measurement results agrees well and confirm the functionality of the antenna element. Then, the designed antenna element is used to design a large 8×8 array. In the next chapter, the designed 8×8 array is thinned with an optimized configuration in which only 22 elements are excited, 20 elements are terminated to proper impedances and the rest are left as open circuit. The GA optimization is used in the next chapter to achieve an acceptable thinned array pattern with satisfying gain and SLL which is comparable with the pattern of a fully excited array.

Chapter 4

Thinned Tightly Coupled Bowtie Array

An array of 8×8 tightly coupled bowtie array was designed in section 3.3 with active S_{11} better than -10 dB for the entire frequency range 25 GHz-43 GHz. In this chapter, in order to facilitate the feeding structure of the TCDAs and reduce the cost of the array by reducing the number of required T/R modules, the designed 8×8 array is thinned such that only a subset of the array elements (22 elements) is excited, a number of unexcited ports (20 elements) are terminated by proper passive impedances ($R_i + jX_i$) and the rest, 22 elements, are left as open. All the 22 excitation voltages and 20 terminating impedances in the designed thinned array are optimized using GA algorithm in such a way that the radiation pattern satisfies a given gain and SLL characteristics which is comparable with the fully excited array's. Since the cell dimension in both directions (D_X, D_Y) is chosen 0.43 of the wavelength at 43 GHz, no grating lobe would appear in the whole desired frequency range 25 GHz-43 GHz if all elements were excited. However, in the case of thinned array, in which unexcited elements lay in between active elements, grating lobes can appear at some frequencies and for a range of steering angles if the distance between two consecutive *excited* elements exceeds $\lambda/2$ and no current is induced on the unexcited element that lays in between. Disturbing the periodicity of the array by thinning the array in a non periodic fashion can avoid from the appearance of grating lobe; however, large sidelobes will still appear which disturb the pattern. In the following section, a non-periodic thinned array configuration is introduced to prevent the appearance of grating lobes the partially excited array and minimize the SLL by optimizing the terminating loads on unexcited or passive elements as well as the excitation voltages of the active elements.

4.1 Thinned Array Excitation Scheme

The first step in optimization of the thinned array is selecting a proper scheme of excitation. For this purpose, half of the elements were initially excited in a triangle lattice and the other 32 elements were terminated to proper impedances. Fig. 4.1 shows the configuration of the initially designed partially excited array with 50% thinning factor. The thinning factor is defined as the ratio of the inactive elements to the whole number of elements. For further thinning the array and disturbing the periodicity of excitation, The optimization is done on all excitation voltages and terminating impedances at the highest frequency of operation (at 43 GHz) and for the largest steering angle (steering to $\theta = 45^o$ in E-Plane) as the worst case scenario. The optimization procedure and the cost function used is going to be thoroughly discussed in the following sections. Once the optimization is done, the currents on all 64 elements are calculated by having the impedance matrix of the array. The current distribution on the array is observed and the elements with relatively small current magnitude (smaller than 0.01 of the largest current magnitude) were left open and the optimization is done again on the remaining elements considering that some of the elements are left open (terminated to a very large impedance). Again, the currents are calculated and the ones with small relative values were left open. This process continues until there is no relatively small current magnitude. At the end, the configuration shown in Fig. 4.2 with 22 excited elements (66% thinning factor) is obtained.

As shown in Fig. 4.2. the 22 elements shown with a voltage source, are active (excited), the 20 elements shown with an impedance Z, are terminated to proper impedances and the rest of 22 elements that are empty are left as open circuit. As can be seen in this Figure, most of the open circuited elements are located around edges where currents have less impact on the antenna pattern.

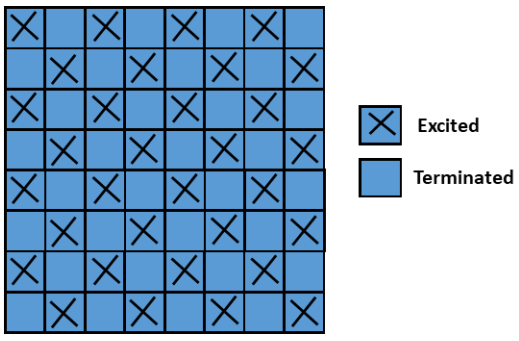


Figure 4.1: The initially designed periodic thinned array with 50% thinning factor

As mentioned earlier in section 3.2.1, since the antenna array must be smaller than $25mm \times 25mm$, the unit cell dimension in this designed TCA are chosen 3mm in both directions (D_X, D_Y) which is smaller than half of the wavelength at highest frequency (0.43 of the wavelength at 43 GHz). Therefore, no grating lobe would appear at 25 GHz-43 GHz frequency range if all elements were excited. However, by thinning the array as shown in Fig. 4.2, the distance between two consecutive excited elements is increased. By disturbing the periodicity of the array grating lobes are not occurring in the required frequency ranges (25 GHz-29 GHz and 37 GHz-43 GHz) and steering angles up to 45^o; however, there will still be large SLL if *all* unexcited ports were left open and their port currents were zero. Fig. 4.3 shows the radiation pattern and directivity of the antenna array if *all* unexcited ports were left open at 43 GHz when the beam is steered to 45^o in E-Plane. As shown in Fig. 4.3, the directivity is reduced by 4.2dBi and the SLL is increased to only 5.14 dB at $\theta = -18^o$ in E-Plane.

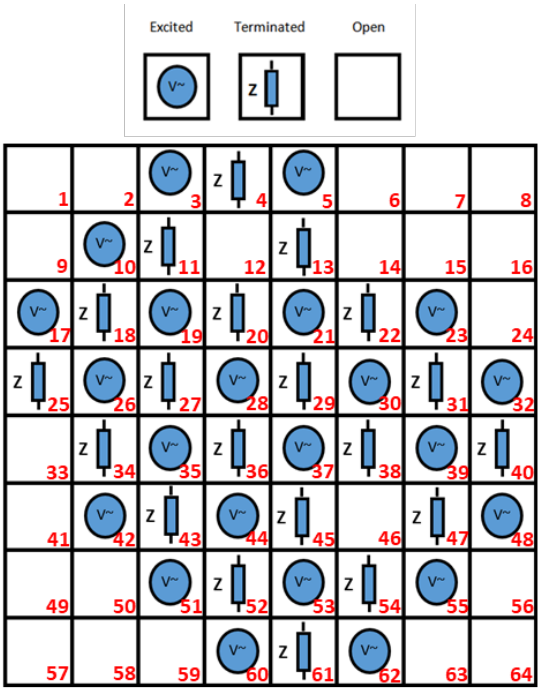
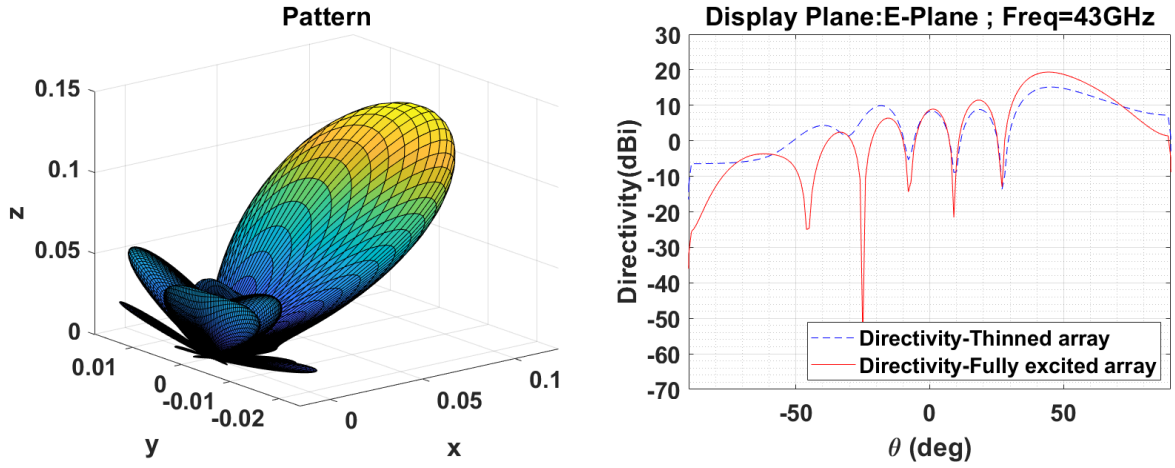


Figure 4.2: The non-periodic thinned array configuration with 66% thinning factor

In order to reduce the SLL and make the pattern as close as possible to the pattern of a fully excited array, proper currents must be induced on the terminated elements by proper excitation of active elements as well as appropriate termination of passive elements. In the

next section, the ideal terminating impedances on all unexcited elements (20 terminated ports + 22 open circuited elements shown in Fig. 4.2) are calculated that will result in exactly the same current distribution on the aperture as in a fully excited array. However, we shall see that this solution is not feasible in practice.



(a) (b)

Figure 4.3: The radiation result of the thinned 8×8 array shown in Fig. 4.2 at 43 GHz when the beam is steered to 45^o in E-Plane if *all* 42 unexcited ports were left open (a) Radiation pattern. (b) Thinned array directivity in E-Plane in compare with the directivity of a fully excited array.

4.2 Ideal Terminating Impedances

Theoretically, using the impedance matrix of the entire array, we can calculate what impedances should ideally terminate the unexcited ports in order for the array pattern to remain unchanged from the fully excited array. The impedance matrix of the designed 8×8 array is obtained by simulating the whole array shown in Fig. 3.18 excited with sixty four 50Ω waveports using ansys HFSS software. For any unexcited port (i'th element) terminated into a passive load impedance Z_{L_i} in Fig. 4.2 , equation (4.1) must be satisfied:

$$-Z_{L_i} I_i = Z_{i,1} I_1 + Z_{i,2} I_2 + ...Z_{i,64} I_{64} \tag{4.1}$$

where Z_{L_i} is the load impedance on the i'th element which must be calculated. I_i is the desired current *into* the i'th element and $Z_{i,j}$ is the element of the array impedance matrix

which represents the mutual impedance between i'th and j'th ports. In order to generate the *same current distribution* as in the fully excited array when the beam is steered to θ_s, ϕ_s, the currents I_i in equation 4.1, must be replaced by currents with the same magnitudes (uniform distribution) and with proper phase shifts which are given by (4.2) depending on the steering angle:

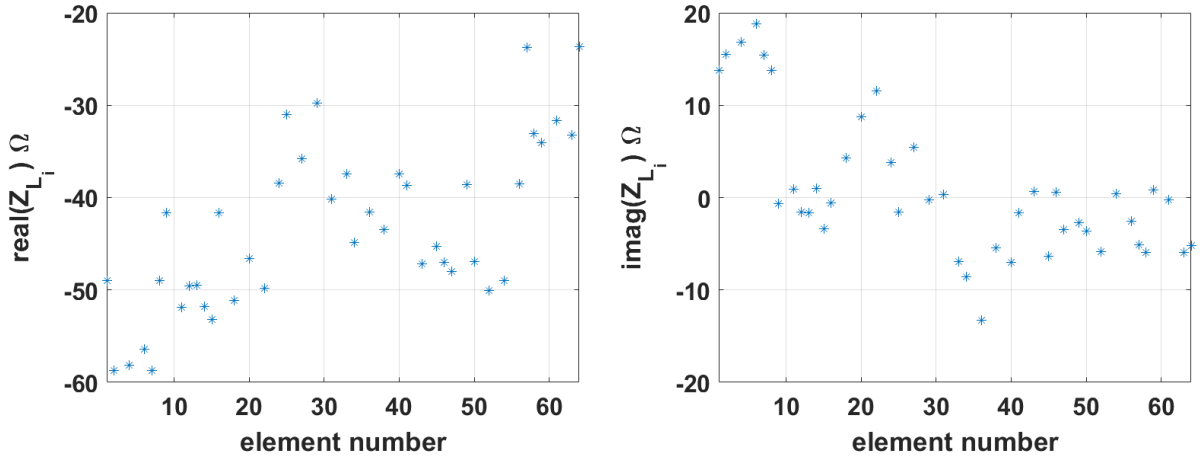
$$\begin{aligned} \alpha_x &= 2n\pi - kD_x \sin(\theta_s)\cos(\phi_s) \\ \alpha_y &= 2m\pi - kD_y \sin(\theta_s)\sin(\phi_s) \end{aligned} \tag{4.2}$$

Where α_x, α_y are the required phase shifts in excitation currents along X and Y direction, respectively. $k = 2\pi/\lambda$ is the wave number, D_x, D_y are the cell dimensions in X and Y direction.

By using equation 4.1 for each unexcited port, the required terminating impedances Z_{L_i} on all unexcited ports are calculated at a desired frequency and steering angle. Fig. 4.4 shows the real and imaginary parts of the calculated ideal terminating impedances at 40GHz when the beam is steered to $\theta = 30^o$ in E-Plane. As expected, these calculated terminating impedances show negative resistive part, *i.e.* they cannot be passive impedances. In order to create exactly the same currents and, consequently, the same output power on the aperture with fewer number of excitations, additional power needs to be generated somewhere which is represented by these negative resistances.

Obviously these loading impedances cannot be realized in practice with purely passive circuits which is our goal. Basically, generating these negative resistances require resonant structures which are extremely narrow band spoiling the wideband capability of the designed array. Hence, in the following sections, instead of synthesizing the exact current distribution of a fully excited array, the excitation voltages and complex terminating impedances (R+jX) are *optimized* in order to obtain a radiation pattern that still satisfies the given gain and SLL conditions.

Practically, realizing purely reactive loads is challenging because each inductor or capacitor has a finite quality factor and the interconnecting transmission lines also add their own loss. Moreover, if we only consider purely reactive loads, the optimized terminating reactances turn out to have *descending* frequency behaviour which theoretically cannot be realized by a lossless circuit based on Foster's reactance theorem. So, in this project, the unexcited ports are terminated to complex impedances $(R_i + jX_i)$ and all R_i, X_i, and excitation voltages (both real and imaginary parts) are optimized.



(a) (b)

Figure 4.4: *Ideal* terminating impedances at 40GHz when the beam is steered to $\theta = 30^o, \phi = 0^o$ (a) Real part. (b) Imaginary part.

4.3 Optimization Procedure

In section 4.2, we observed that the ideal terminating impedances which provide the same current distribution as in a fully excited array turned out to have negative real parts. On the other hand, the thing that matters to us is the total radiation characteristic of the array not the current distribution on the aperture. So, in this section, the excitation voltages and terminating impedances of the thinned 8×8 TCA shown in Fig. 4.2 are optimized to obtain a total radiation pattern that shows satisfying radiation characteristics with acceptable gain and SLL. The optimization procedure for optimizing the thinned array is fully described in this section.

The 22 excitation voltages (complex values) and 20 terminating impedances (complex numbers), contain 84 variables which must be optimized at each frequency. Genetic Algorithm, which has been successfully applied for optimizing systems with large number of variables, was selected for optimization since it can search simultaneously from a large sampling set, does not require the derivative information, and is effective for multiobjective scenarios[46]. Matlab is used to implement the GA algorithm.

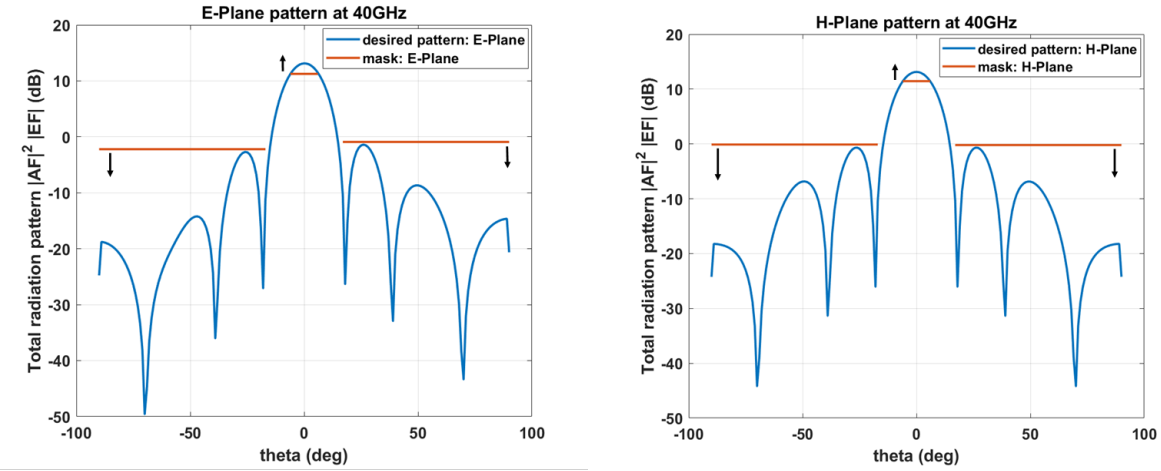
Ideally, for the error function calculation, the patterns of the thinned and fully excited arrays must be compared point by point in the whole space; however, it would be time

consuming since these calculations must be done in each iteration and could be repeated thousands if not millions of times during the optimization process. Furthermore, applying strict conditions on the cost function lowers the chance of survival in the optimization process. So, in order to speed up the optimization process and also allow more populations to survive in each step of the GA and, thus, providing a better chance to obtain reasonable solutions, the total radiation pattern of the 8×8 thinned array ($EF \times |AF|^2$) is compared with a predefined mask in only 2 principal planes (E-Plane and H-Plane) which forces the gain to be higher and the SLL to be lower than a certain level defined based on the pattern of the fully excited array at each frequency and steering angle.

The cost function, at a given frequency and steering angle, is shown in equation 4.3 where b_m is equal to -1, 1, 0 if the pattern at point θ_m must be below, above, or exactly on the mask, respectively. M determines the number of points (θ_m) for which the cost function is calculated. Fig. 4.5 shows the defined mask in 2 principal planes at 40 GHz for broadside radiation. The direction of the black arrows in Fig. 4.5 determines if the pattern of the thinned array must be below or above the mask levels plotted by orange lines. As can be seen in equation 4.3, for the angles where the total pattern of the thinned array violates the mask, the difference between the pattern and the mask (in dB) is added to the cost function. This error is calculated in each of 2 planes from $\theta = -90^o$ to 90^o with 1^o resolution and they will be summed up at the end to form the error function.

$$\text{Cost function} = \sum_{m=1}^{M} \frac{1}{|b_m| + 1} [|\text{pattern}_{dB}(\theta_m) - \text{mask}_{dB}(\theta_m)| - b_m(\text{pattern}_{dB}(\theta_m) - \text{mask}_{dB}(\theta_m))] \tag{4.3}$$

Ideally, the GA optimization must be done for each steering angle and at each frequency which leads to terminating impedances that are not only frequency dependent, they also depend on the steering angle. Practical realization of such impedances that are function of both frequency and scan angle is very complicated if not impossible and certainly defeats the purpose of simplifying the design of TCDA in first place. Therefore, we first carry out the optimization on all excitation voltages and terminating impedances at each frequency when the beam is steered to $\theta = 45^o$ in E-Plane and then the optimized terminating impedances are kept fixed and only the excitation voltages are optimized for different steering angles at each frequency. Since 45^o is the extreme steering angle and presents a worse case scenario, it is better to keep the terminating impedance values for that extreme case and work backward to make sure the mask conditions are better met over the whole space. By using this two steps approach, the terminating impedances will only be a function of frequency. However, the optimized excitation voltages vary by both steering angle and frequency which is normal in all phased array antennas.



(a) (b)

Figure 4.5: Defined mask compared with the pattern of a fully excited array at 40 GHz for broadside radiation (a) E-Plane. (b) H-Plane

In order to realize the 22 optimized terminating impedances, and also match the input impedances of the 20 excited ports to 50Ω, it is necessary that these impedances have a smooth frequency behaviour. However, if the optimization starts from a random value and there is no limiting criteria for selecting the variables in the optimization process, they could have extremely sharp variations with frequency which makes their realization impossible. So, in order to smooth out the frequency bahaviour of the optimized terminating impedances, the optimization starts from the highest frequency (43 GHz) when the beam is steered to $\theta = 45^o$ in E-Plane. All 84 variables including 44 for excitation voltages (real and imaginary parts) and 40 for terminating impedances (real and imaginary parts) are optimized using GA algorithm. Then the optimized variables at each frequency is used as the initial point for the next frequency which is 1 GHz lower. The optimization on all 84 variables is repeated down the lowest frequency (25 GHz) and for steering angle of $\theta = 45^o$ in E-Plane. Furthermore, The real and imaginary parts of terminating impedances are limited to only vary with 10% of their initial values at 1 GHz higher frequency. The real part of terminating impedances are kept below 50Ω to avoid additional losses.

Once the optimization on all variables are done at each frequency for steering the beam to $\theta = 45^o$ in E-Plane, the optimized terminating impedances are kept fixed and only excitation voltages (44 variables) are re-optimized for different steering angles at the given frequency including steering to $\theta = 30^o, 15^o$ in E-Plane and for broadside radiation. The

flowchart shown in Fig. 4.6 shows the optimization steps.

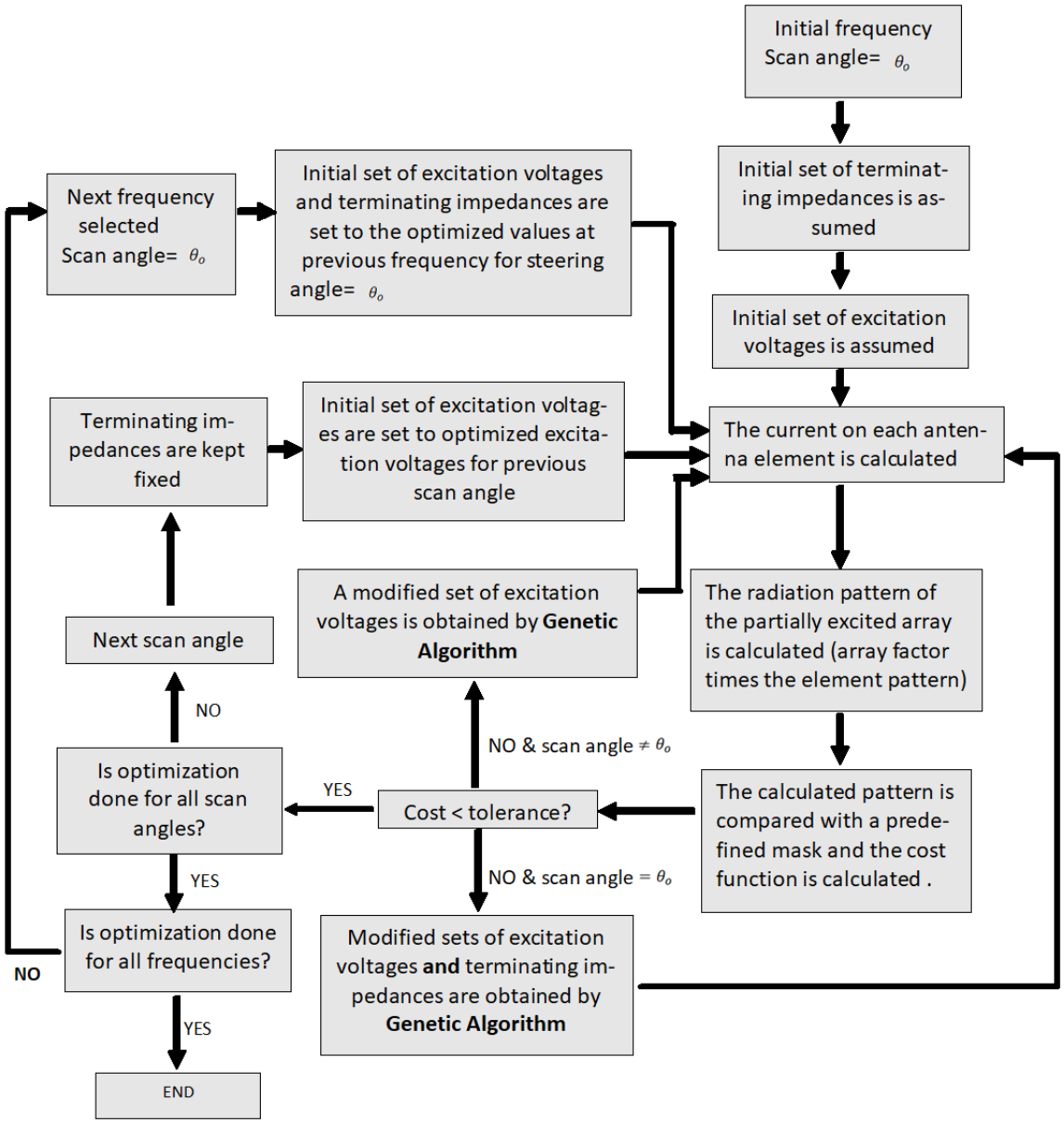


Figure 4.6: Flowchart showing the optimization procedure

In each iteration of the optimization process, having a set of values for excitation voltages and terminating impedances, considering the excitation scheme as shown in Fig. 4.2,

and having the pattern of a single antenna element, the radiation pattern of the thinned antenna array is calculated and compared with defined masks in E and H planes and the error function is calculated, If the stopping criteria defined by the optimization is satisfied, the optimization for that frequency and steering angle is terminated; otherwise, a different set of variables are obtained by Genetic Algorithm implemented in Matlab.

The algorithm stops if the average relative change in the best error function value over *MaxStallGenerations* generations (set to 50) is less than or equal to $FunctionTolerance$ (set to 1e-6). Maximum number of iterations before the algorithm halts is set to 8400 which is 100 times the total number of variables. The optimization starts from an initial population which is defined as a 20*84 matrix including 20 sets of 84 variables around the initial set of variables. The initial excitation voltages are set as the values used for a fully excited array at the specific frequency and steering angle where the optimization is being done. Also, as mentioned before, the initial terminating impedances are set as the optimized values at the previous frequency (1 GHz higher). Furthermore, a lower and upper bound is defined and applied on the terminating impedances that forces them (both resistive and reactive part) to vary within 10% of their initial point and their resistive part to be positive and less than 50Ω.

In the next section, it is thoroughly explained how to calculate the pattern of the thinned array by knowing all excitation voltages and terminating impedances.

4.4 The thinned Array Pattern Calculation

The pattern of the thinned array needs to be calculated in each iteration of the optimization in order to be compared with a predefined mask and calculate the error function. In this section, it will be shown how to calculate the current distribution on the aperture and finally calculate the pattern of the array by knowing the 22 excitation voltages at excited ports and the 20 terminating impedances on unexcited ports located as shown in Fig. 4.2.

The 8×8 antenna array is excited with sixty four 50Ω waveports on ground plane (shown in green in Fig. 3.18). The full wave simulation of the array is done using Ansys HFSS software and the impedance matrix ($[Z]_{64\times64}$) of the array is extracted. If the 20 terminated elements shown in Fig. 4.2 are loaded with impedance Z_{L_i} (i refers to the terminated element's port number), the 22 excited elements shown in Fig. 4.2 are excited with voltage $V_{exc,i}$(i refers to the excited element's port number) and the open circuited elements shown in Fig. 4.2 are modeled by terminating the port to a very large resistance Z_∞. The current on each element can be calculated using the equations 4.4,4.5,4.6

$$\left[I\right]_{64\times1} = \left[Z_P\right]^{-1}_{64\times64} \times \left[V_P\right]_{64\times1} \tag{4.4}$$

$$[Z_P] = \begin{bmatrix} Z_{1,1}+Z_\infty & Z_{1,2} & Z_{1,3} & Z_{1,4} & \cdots & \cdots & Z_{1,64} \\ Z_{2,1} & Z_{2,2}+Z_\infty & Z_{2,3} & Z_{2,4} & \cdots & \cdots & Z_{2,64} \\ Z_{3,1} & Z_{3,2} & Z_{3,3} & Z_{3,4} & \cdots & \cdots & Z_{3,416} \\ Z_{4,1} & Z_{4,2} & Z_{4,3} & Z_{4,4}+Z_{L_4} & \cdots & \cdots & Z_{4,416} \\ \vdots & \vdots & \vdots & \ddots & & \vdots & \vdots \\ Z_{61,1} & \cdots & \cdots & \cdots & Z_{61,61}+Z_{L_{61}} & \cdots & Z_{61,64} \\ \vdots & \cdots & \cdots & \cdots & \cdots & \ddots & \vdots \\ Z_{64,1} & \cdots & \cdots & \cdots & \cdots & \cdots & Z_{64,64}+Z_\infty \end{bmatrix} \tag{4.5}$$

$$\left[V_P\right] = \begin{bmatrix} 0 & 0 & V_{exc,3} & 0 & \cdots & V_{exc,60} & 0 & V_{exc,62} & 0 & 0 \end{bmatrix}^T \tag{4.6}$$

The diagonal elements in the impedance matrix ($[Z]_{64\times64}$) are supplemented by either the load impedances (Z_{L_i}) for terminated ports or a very large resistance Z_∞ for open circuited elements to generate $[Z_P]$ matrix. Also, the elements corresponding to the unexcited ports in $[V_P]$ are replaced by zero. By having Z_{L_i} on terminated ports and $V_{exc,i}$ on excited elements and replacing Z_∞ with a very large impedance like $100k\Omega$, the current vector $[I]_{64\times1}$ can be calculated. By having the current distribution on all antenna ports, the array factor and the total radiation pattern of the array can be calculated by using the equations 4.7,4.8. Equation 4.7 calculates the array factor of a $N \times M$ planar array which has N rows and M columns along Y and X axes, respectively. The current I_{nm} in equation 4.7 is the current on (n,m)'th element, k is the wave number, D_X and D_Y are elements spacings along X and Y axes, respectively, and θ and ϕ refer to the observation point at which the array factor is calculated.

$$\mathrm{AF}(\theta,\phi) = \sum_{n=1}^{N}\sum_{m=1}^{M} I_{nm} e^{jk(m-1)D_X sin(\theta)cos(\phi)} e^{jk(n-1)D_Y sin(\theta)sin(\phi)} \tag{4.7}$$

$$\text{Array Pattern} = AF^2 \times EF \tag{4.8}$$

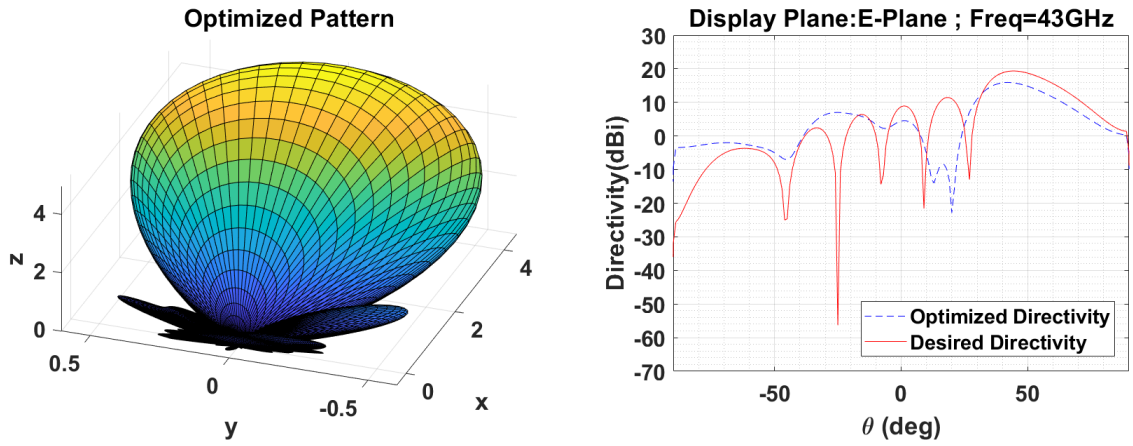
The antenna element shown in Fig. 3.9 is simulated using CST microwave studio in order to extract the pattern of the antenna element (Element Factor EF). Because of strong mutual couplings in this tightly coupled structure, the single element cannot be simulated in isolation; otherwise, the field data will be too erroneous. Therefore, the antenna element

is simulated in an infinite periodic array in order to take the mutual coupling effects into consideration. Fig. 3.10d,3.10e show the realized gain of the bowtie element at 27GHz, 40 GHz in E and H planes. Once the array factor and the element factor is calculated, the total pattern of the array can be calculated by using equation 4.8.

4.5 50Ω Terminating Loads

Before starting the full optimization of the array including all excitation voltages and terminating impedances, it would be interesting to see how the array would perform if all 20 terminated ports shown in Fig. 4.2 were simply terminated to standard 50Ω loads. In this part, the GA optimization is only performed on the 22 excitation voltages and the 20 terminated elements shown in Fig. 4.2 are loaded with 50Ω resistances. The goal is to minimize the cost function defined in equation 4.3 in E and H planes. During the optimization process, by substituting Z_{L_i} with 50Ω for terminated ports in equation 4.5, the current vector ($[I]_{64\times1}$) is calculated for each set of excitation voltages using equation 4.4. Having the current distribution on the aperture, the array factor and finally the antenna array pattern is calculated by using equations 4.7,4.8 and compared with the predefined masks in each planes.

The optimization of excitation voltages is carried out at 43 GHz when the beam is steered to $\theta = 45^o, \phi = 0^o$ to see if the optimized pattern could meet the required radiation characteristics. Once the GA optimization is done on excitation voltages, the radiation pattern and directivity of the array are calculated and compared with the desired (ideal) patterns of a fully excited array as shown in Fig. 4.7. It is clear in Fig. 4.7 that the maximum directivity is reduced by about 3.43 dBi and the SLL is increased to 6.1 dB at $\theta = 30.74^o, \phi = -42^o$. This means that by loading the 20 terminated ports (shown in Fig. 4.2) to 50Ω and allowing the current to pass through the elements, the maximum directivity is increased by 0.77dB and the SLL is reduced by around 1 dB compared to the case where the unexcited elements were all left open as shown in Fig. 4.3. In next section, we replace the terminating loads with unknown impedances that must be optimized and we will see that the SLL can be further suppressed and the gain would be increased by engineering the current distribution on the aperture.



(a) (b)

Figure 4.7: Optimization results at 43 GHz when the 20 terminated ports shown in Fig. 4.2 are loaded with 50Ω resistance and the beam is steered to $\theta = 45^o, \phi = 0^o$ (a) optimized 3D pattern of the thinned TCDA. (b) optimized and desired directivity in E-plane.

4.6 Optimization Results of the Thinned Tightly Coupled Bowtie Array

In this section, all the 22 excitation voltages and the 20 terminating impedances are optimized at each frequency and steering angle using GA algorithm. As explained in section 4.3, the optimization is carried out for the the two frequency bands 25 GHz-29 GHz, 37 GHz-43 GHz with 1 GHz steps when the beam is steered to $\theta = 45^o$ in E-Plane. When the optimization is done at each frequency, in order to steer the beam, the terminating impedances are kept fixed to the optimized values and only the excitation voltages are re-optimized for different steering angles including $\theta = 30^o, 15^o$ in E-Plane and for broadside radiation.

Fig. 4.11, 4.10, 4.9, 4.8 show the pattern and directivity of the optimized thinned array and compare its directivity with the desired directivity of a fully excited array at 25 GHz, 29 GHz, 37 GHz, and 43 GHz for broadside and beam scanned to $\theta = 15^o, \theta = 30^o, \theta = 45^o$ in E-Plane. The desired directivity of a fully excited array is calculated by having the simulated element pattern of the antenna and also calculating the array factor by using the ideal current distribution on array elements at each frequency and steering angles (equation 3.5). It is clear in Fig. 4.8g,4.8h that the SLL is reduced to 8.7 dB at 43 GHz when steering to 45^o in E-Plane which is even 0.8 dB better than the fully excited array

and the maximum directivity is reduced by 2.85 dB compared to the fully excited array. For the whole frequency range, when the beam is steered to 45^o, the SLL is better than 8.7 and the directivity is decreased by less than 2.85 dB. Both extremes happen at the highest frequency of 43 GHz; for example, at 37 GHz when the beam is steered to 45^o, the SLL for the optimized thinned array is 9.84dB and the directivity is reduced by 2.3 dB. For broadside radiation, the SLL is better than 14 dB and the gain is decreased by less than 2 dB in the whole frequency range for the optimized thinned array.

With stronger mutual couplings among the radiating elements and with larger arrays, more significant results can be achieved. For example, Appendix A shows the results of the same optimization for a 32×13 closely spaced dipoles at 20 GHz, 50 GHz, 70 GHz. Considering the fully periodic excitation scheme used in this thinned array (shown in Fig. A.1b), if no currents are induced on unexcited ports, grating lobes would appear at 70 GHz for steering the beam to more than 9^o and at 50 GHz when the beam is steered to more than 37^o. However, as can be seen in Fig. A.2, by the optimization of the thinned array, the grating lobes at these frequencies and steering angles are completely removed.

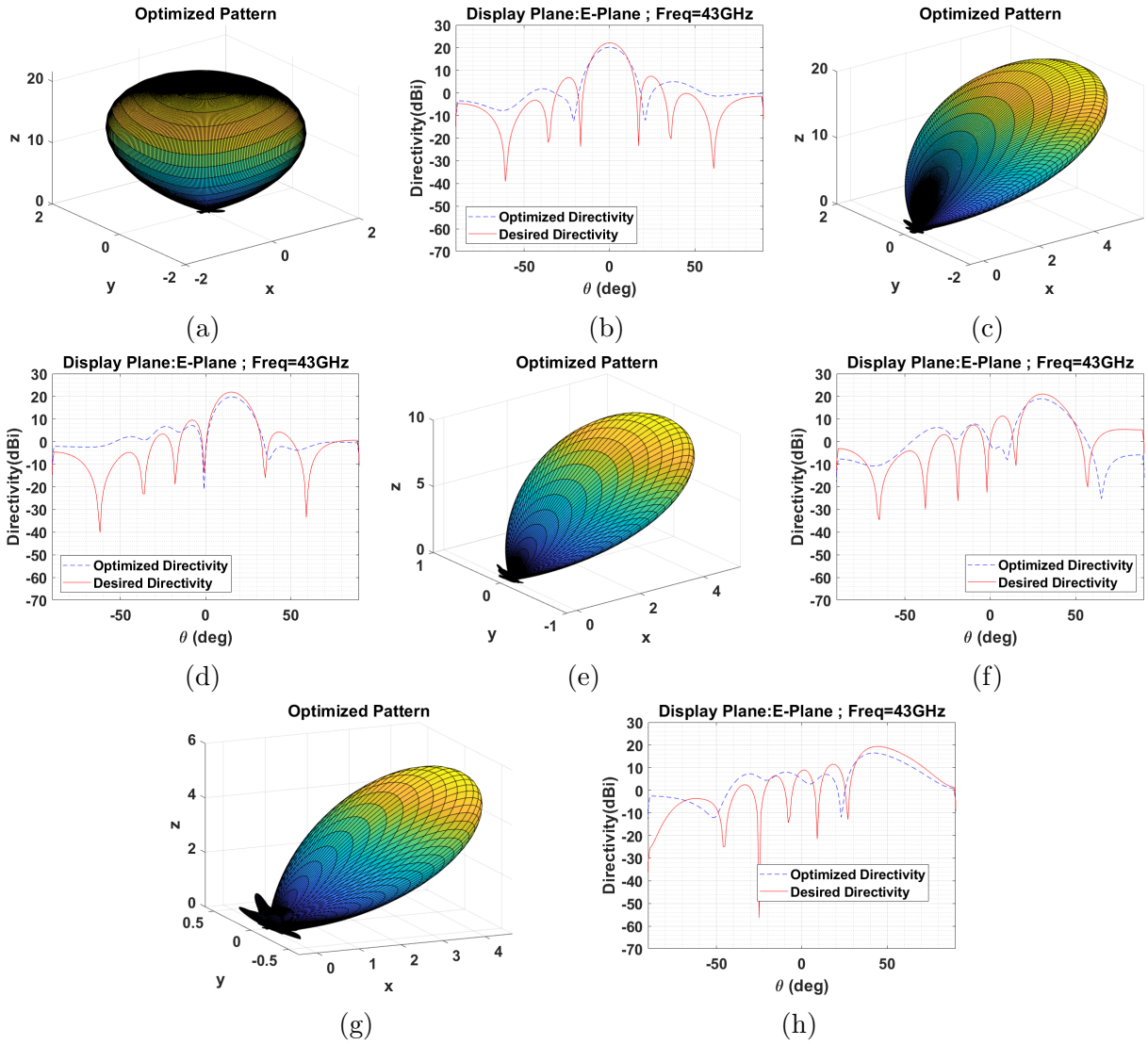


Figure 4.8: Optimization results of the thinned TCDA at 43 GHz (a) Optimized 3D pattern for broadside radiation. (b) Optimized and desired directivity in E-Plane for broadside radiation. (c) Optimized 3D pattern scanned to $\theta = 15^o$ in E-Plane. (d) Optimized and desired directivity in E-Plane scanned to $\theta = 15^o$. (e) Optimized 3D pattern scanned to $\theta = 30^o$ in E-Plane. (f) Optimized and desired directivity in E-Plane scanned to $\theta = 30^o$. (g) Optimized 3D pattern scanned to $\theta = 45^o$ in E-Plane. (h) Optimized and desired directivity in E-Plane scanned to $\theta = 45^o$.

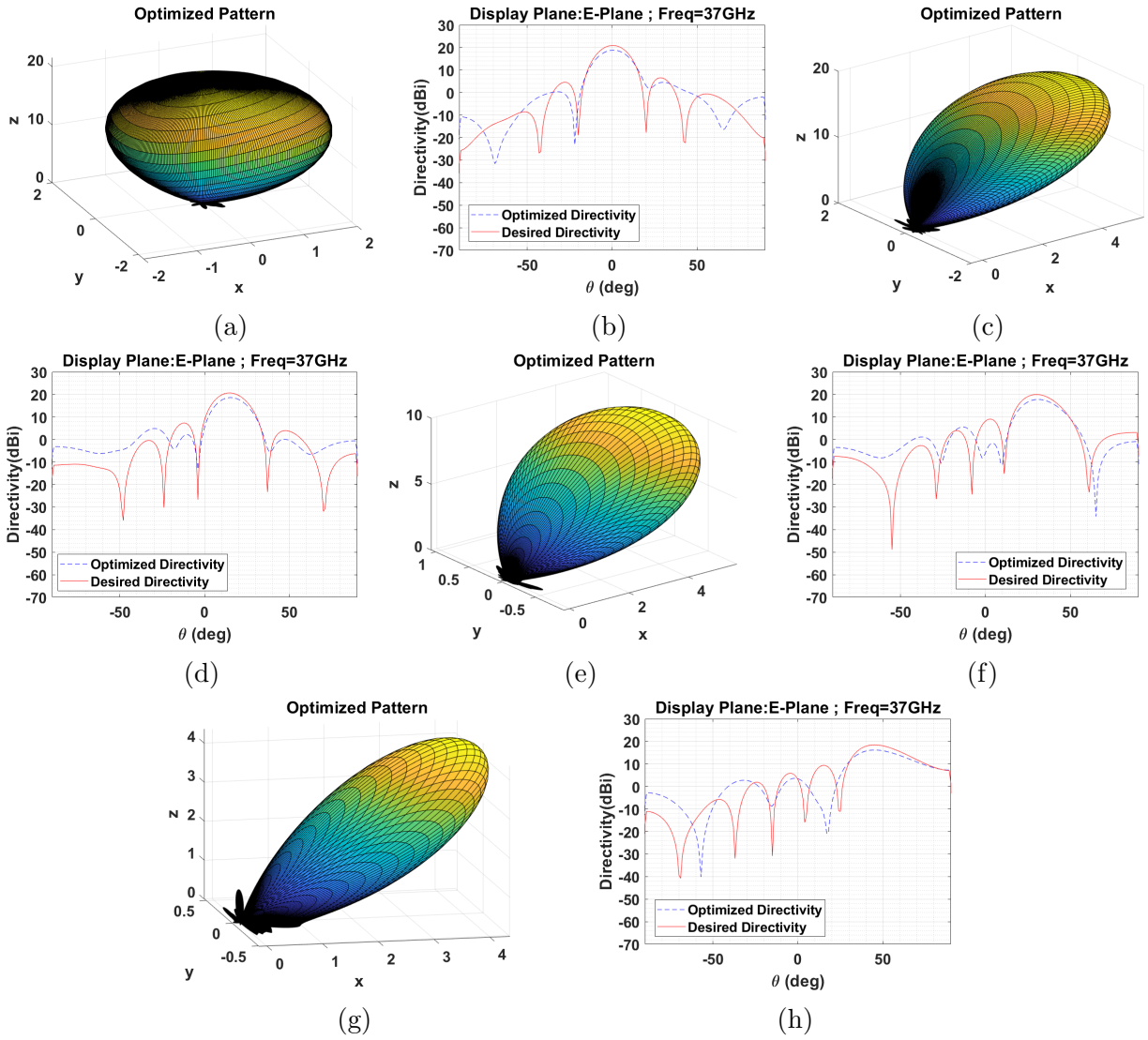


Figure 4.9: Optimization results of the thinned TCDA at 37 GHz (a) Optimized 3D pattern for broadside radiation. (b) Optimized and desired directivity in E-Plane for broadside radiation. (c) Optimized 3D pattern scanned to $\theta = 15^o$ in E-Plane. (d) Optimized and desired directivity in E-Plane scanned to $\theta = 15^o$. (e) Optimized 3D pattern scanned to $\theta = 30^o$ in E-Plane. (f) Optimized and desired directivity in E-Plane scanned to $\theta = 30^o$. (g) Optimized 3D pattern scanned to $\theta = 45^o$ in E-Plane. (h) Optimized and desired directivity in E-Plane scanned to $\theta = 45^o$.

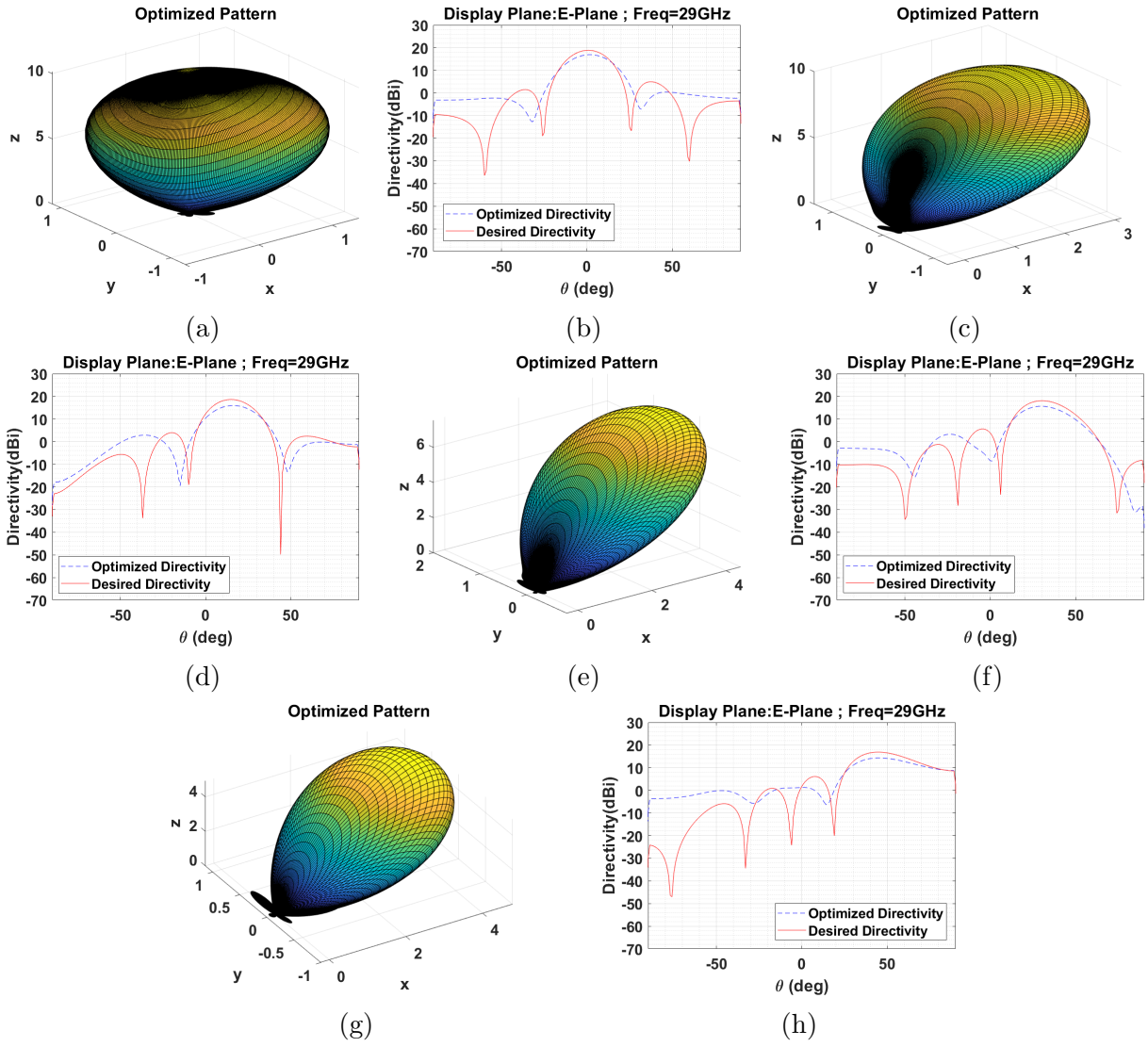


Figure 4.10: Optimization results of the thinned TCDA at 29 GHz (a) Optimized 3D pattern for broadside radiation. (b) Optimized and desired directivity in E-Plane for broadside radiation. (c) Optimized 3D pattern scanned to $\theta = 15^o$ in E-Plane. (d) Optimized and desired directivity in E-Plane scanned to $\theta = 15^o$. (e) Optimized 3D pattern scanned to $\theta = 30^o$ in E-Plane. (f) Optimized and desired directivity in E-Plane scanned to $\theta = 30^o$. (g) Optimized 3D pattern scanned to $\theta = 45^o$ in E-Plane. (h) Optimized and desired directivity in E-Plane scanned to $\theta = 45^o$.

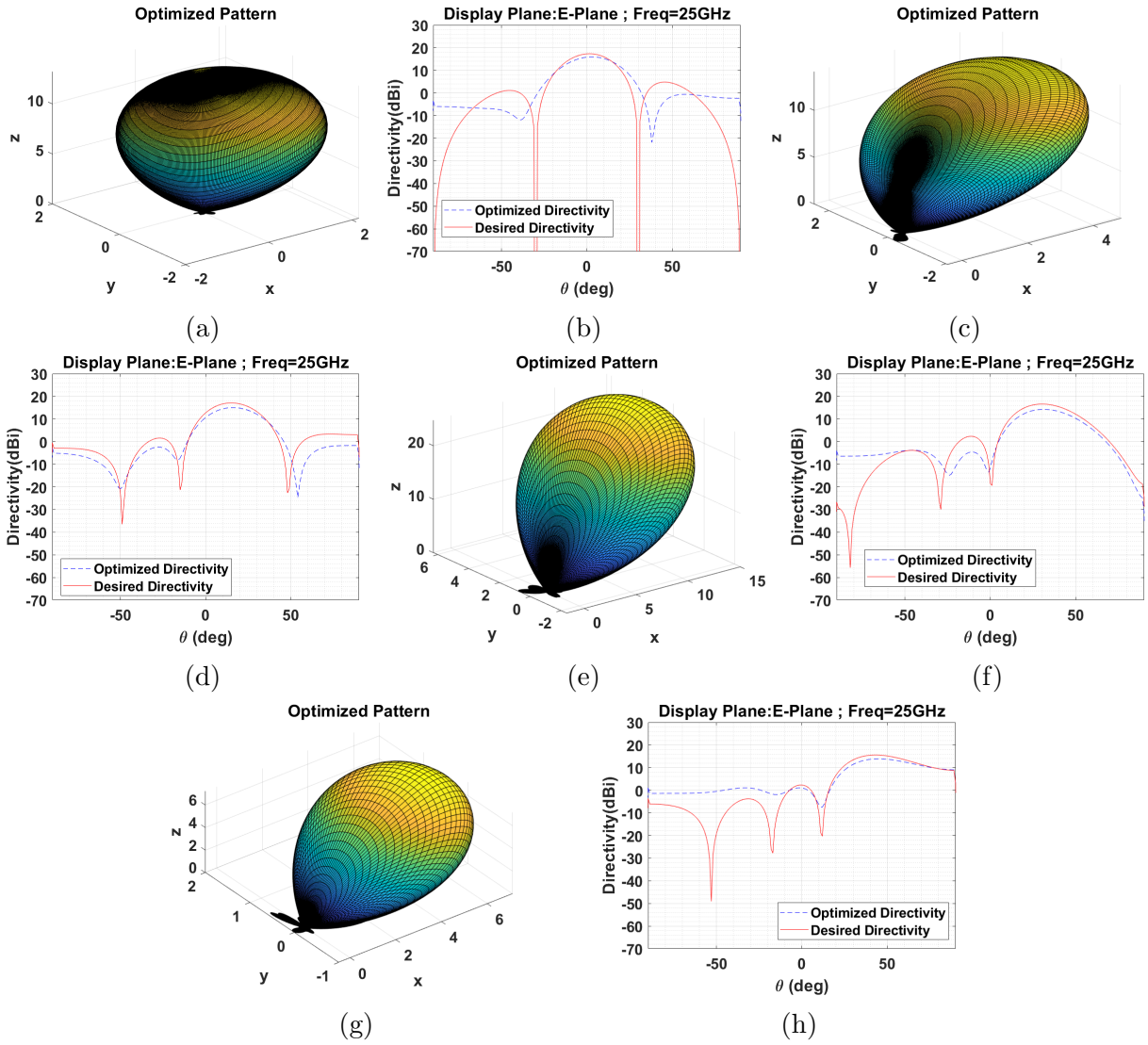


Figure 4.11: Optimization results of the thinned TCDA at 25 GHz (a) Optimized 3D pattern for broadside radiation. (b) Optimized and desired directivity in E-Plane for broadside radiation. (c) Optimized 3D pattern scanned to $\theta = 15^o$ in E-Plane. (d) Optimized and desired directivity in E-Plane scanned to $\theta = 15^o$. (e) Optimized 3D pattern scanned to $\theta = 30^o$ in E-Plane. (f) Optimized and desired directivity in E-Plane scanned to $\theta = 30^o$. (g) Optimized 3D pattern scanned to $\theta = 45^o$ in E-Plane. (h) Optimized and desired directivity in E-Plane scanned to $\theta = 45^o$.

4.7 Thinned Array Stackup

The stackup of the thinned 8×8 array comprising 6 metal layers is shown in Fig. 4.12. The substrate used is RO4350B with dielectric constant $\epsilon_r = 3.6$ and loss tangent 0.0037. The thickness of the substrates are chosen based on the RO4350B standard thicknesses. From the top to bottom, the first and second layers include the antenna balun's open stub and the antenna patch respectively, the third layer is the antenna ground layer, the forth layer includes the 20 terminating impedances, the fifth layer is the ground and the sixth layer includes the GCPW feeding lines and matching networks.

The stackup shown in Fig. 4.12 includes two antenna elements, the one on the right is representative of a terminated element and, as can be seen, the feeding via connecting the top layer to the third layer is going down to the forth layer where the terminating impedances are located. Also, the element on the left represents an excited element; so, the feeding via is going down to the bottom layer where the matching networks and GCPW feeding lines are placed. All the resistances are assembled on the bottom layer. So, a via is required to connect all the required resistances, that are part of the circuit realizing the terminating impedances on fourth layer, down to the last bottom layer.

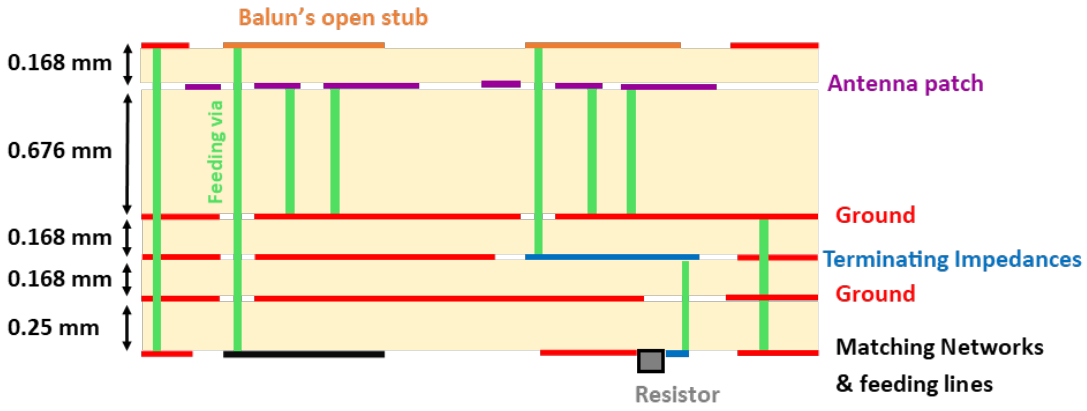


Figure 4.12: The stack up of the optimized thinned 8×8 tightly coupled bowtie array

4.8 Realization of Terminating Impedances

Fig. 4.13 shows an example of how the optimized terminating impedances behave versus frequency for randomly chosen terminated ports.

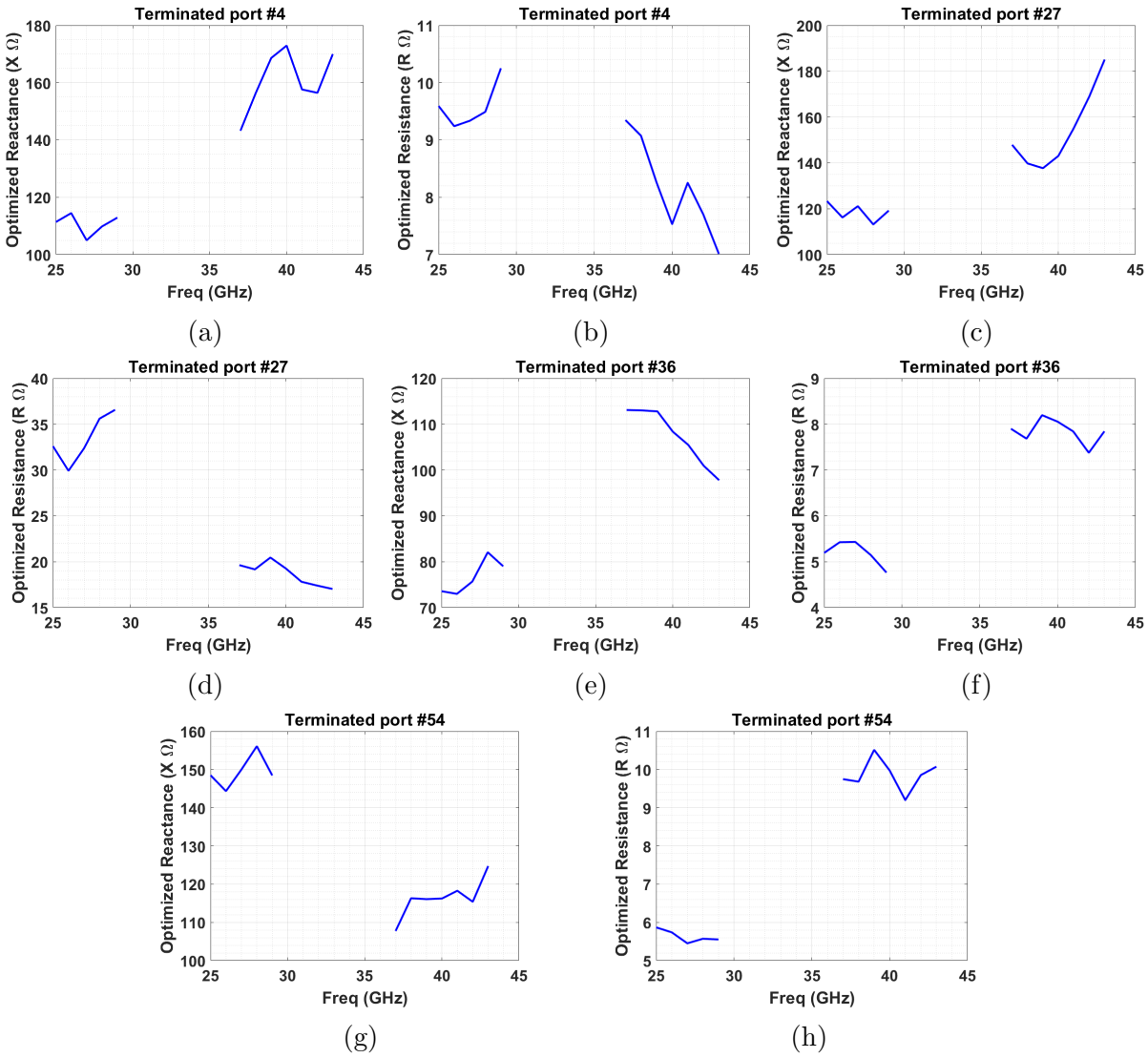


Figure 4.13: Optimized Terminating impedances at port numbers (a) 4, Imaginary part ($X\Omega$). (b) 4, real part ($R\Omega$). (c) 27, Imaginary part ($X\Omega$). (d) 27, real part ($R\Omega$). (e) 36, Imaginary part ($X\Omega$). (f) 36, real part ($R\Omega$). (g) 54, Imaginary part ($X\Omega$). (h) 54, real part ($R\Omega$).

As can be seen in these figures, by choosing the proper initial population and applying limiting conditions on the variables, the optimization has forced the optimized impedances (both real and imaginary parts) to vary fairly smoothly versus frequency and there are no

sharp variations or jumps in the two desired frequency bands where the optimization was carried out. This makes the realization of the terminating impedances a lot easier. Since the optimization is done at two separated frequency bands there is no data point between 29 GHz to 37 GHz in all those figures.

One approach in realizing the optimized loading impedances with passive RLC circuits is to first approximate the frequency behavior of the impedances with a rational function and then synthesize that rational function with passive circuit elements for which there are many available techniques such as LC ladder, Cauer, or Foster realization methods. One method used in approximating frequency response data with a rational function is the vector fitting method [55]. In this method the rational function is considered to have the following form:

$$f(s) \approx \sum_{n=1}^{N} \frac{c_n}{s - a_n} + d + sh \tag{4.9}$$

where residues c_n and poles a_n are either real quantities or come in complex conjugate pairs while d and h are real. Appendix B explains how to fit data with the rational function $f(s)$ using vector fitting method. Assuming that the optimized terminating impedances can be approximated by the rational function shown in equation 4.9, the optimized data will be realized by the circuit shown in Fig. 4.14. In this figure, n is the number of complex conjugate pairs of poles (as like N in the series shown in equation 4.9). Each parallel RLC block shown in Fig. 4.14 represents the sum of two complex conjugate terms ($\frac{c_n}{s-p} + \frac{c_n^*}{s-p^*}$). The series inductance in Fig. 4.14 represents the term sh and the series resistor R represents the constant term d in equation 4.9.

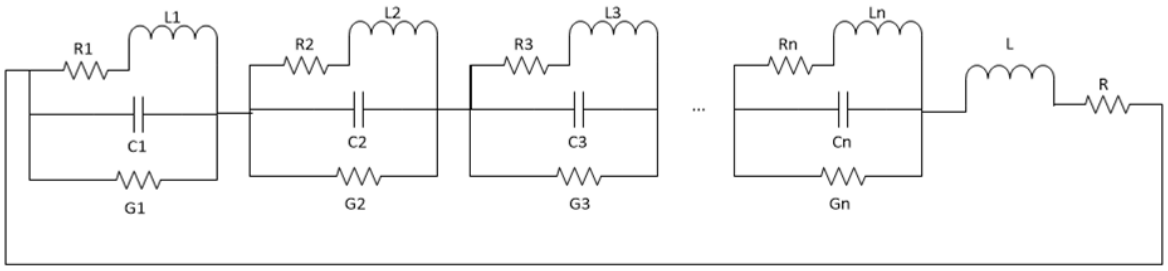


Figure 4.14: The RLC circuit synthesizing the rational function in equation (4.9)

Although it would be much easier to fit a rational function to the optimized impedances and synthesize the circuit realizing the function, we might end up obtaining poles in the

right hand side of the S-Plane because the real and imaginary parts of optimized terminating impedances are not necessarily satisfying the Hilbert Transformation. Basically, in order to have a specific reactance behaviour, a unique frequency behaviour is expected from the real part as shown by Hilbert transformation in equation 4.10.

$$\begin{aligned} Z(j\omega) &= R(\omega) + jX(\omega) \\ X(\omega) &= -\frac{1}{\pi}\int_{-\infty}^{+\infty}\frac{R(\tau)}{\omega-\tau}d_\tau \\ R(\omega) &= \frac{1}{\pi}\int_{-\infty}^{+\infty}\frac{X(\tau)}{\omega-\tau}d_\tau + R(\infty) \end{aligned} \tag{4.10}$$

However, the resistances obtained from the GA optimization are generally small values whose frequency behavior is a smooth function and has no specific relation to the reactance part. Therefore, acceptable results could not be obtained by using the theoretical vector fitting method unless we use real parts with those calculated based on the optimized reactances by using the Hilbert transformation. This can be a subject for a future work. However, at the end, realizing the series resonators shown in Fig. 4.14 with a distributed circuit would also be challenging even if we assume that the calculated component values are realizable with distributed circuits.

Basically, for a passive, lossy, one port circuit, the reactance strictly increases by frequency except at the location of poles. So, for the frequency ranges at which the reactance decreases, a pole or a series of close poles must exist. These poles generate resonances in the real part of the input impedance of the circuit as well. The peak of the resonances in the real part of input impedance can be very high for some of the ports depending on the slope of the descending curve in reactance diagram. As the (negative) slope of the reactance curve increases, the peak of the real part's resonance grows larger but its bandwidth becomes narrower.

As can be seen in Fig. 4.13a,4.13c,4.13e, the optimized reactances are mostly ascending with frequency except at the location of poles where a smooth descending behaviour is observed. There are a few ports with descending frequency behaviour from 29 GHz to 37 GHz as shown in Fig. 4.13g. For those cases with a sharp decreasing behaviour between the two frequency bands, a large quality factor resonance between 29 GHz and 37 GHz is required which results in a large peak resonance in resistive part as well. However, this would be out of our desired frequency range or near the edge of the bands, thus, it will be acceptable.

Based on the frequency bahaviour of the optimized impedances seen in Fig. 4.13, they can be realized by an inductor in series with a couple of parallel lossy resonators with

appropriate quality factors and resonance frequencies that must be optimized. The parallel lossy resonators can be realized with transmission line resonators (striplines in this case) terminated with a resistance. This circuit shown in Fig. 4.16a is optimized for all terminating ports in Keysight Advanced Design System (ADS) using Simulated Anealing Method. The substrate is defined based on the stackup shown in Fig. 4.12 and the width and length of each stripline plus the value of the series inductance make up the optimization variables. The error function is defined as the difference between the input reactance of the circuit and the GA optimized terminating reactances in the two desired frequency bands (25 GHz-29 GHz, 37 GHz-43 GHz). The optimization results show that the optimized impedances could be realized by this circuit with one to three parallel resonators. The series inductance optimized to vary between 0.2nH-0.7nH for different terminating ports.

As shown in Fig. 4.16b,4.17b,4.18b,4.19b, the input reactance of the optimized circuits fits very well with the required reactances optimized by GA algorithm at the two required frequency bands 25GHz-29GHz, 37GHz-43GHz. The input resistance of the optimized circuits are below 200Ω for the whole frequency ranges and for all terminating ports. The simulation results in section 5.7 will show that the antenna pattern is not too sensitive to the gap in resistive parts. As mentioned earlier, the resistive part of the input impedance is dictated by its reactive part using the Hilbert transformation function. As it's clear in Fig. 4.16c,4.17c,4.18c,4.19c, at frequencies where there is a sharp descending behaviour in reactance, there is a sharp peak resonance in resistance as well.

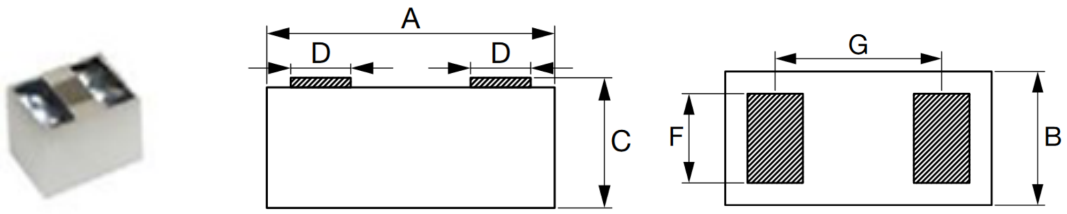
Since the last bottom layer of the stackup must be reserved for the GCPW feed lines to be accessible by the connectors on the edge of the board, the terminating impedances must be realized by striplines located on forth layer between the two ground layers on third and fifth layers as shown in Fig. 4.12. Hence, the via connecting the antenna ports on layer 3 to the layer where the terminating impedances are located can fully or partially realize the series inductance shown in Fig. 4.16a. Also, as shown in Fig. 4.16a a very thin, and short transmission line with large characteristic impedance which is in series with the via (inductor) is in charge of making the rest of the required inductance. The parallel lossy resonators can be realized by parallel striplines terminated to a resistance. Since the resistances must be assembled on the most external layer, a via coming from the impedance layer (forth layer) to the very bottom layer is also required to connect the resistance at the end of the striplines to the ground on bottom layer. This via can also compensate for the required series inductance shown in Fig. 4.16a. The resistor used is a high frequency, thin film, flip chip resistor from Vishay (CH02016). The physical dimensions and the resistor values that are used in full wave simulations were chosen based on the resistor properties given in the following section.

The optimized circuits by ADS are simulated in Ansys HFSS design tool by replacing

the series inductor with the via connecting the third layer to the forth layer. Since the available space to accommodate all 20 terminating impedances with three transmission lines in three directions on the forth layer is limited, it is preferred to have the circuit drawn along one single direction; The final design shown in Fig. 4.20 comprising cascaded striplines terminated to a resistance is optimized using Ansys HFSS for all terminating ports and the results for terminated port numbers 4,22,47,61 are shown in Figs. 4.21,4.22,4.23,4.24. As shown in these figures, the input reactance of the optimized design fits well with the required reactances; however, the input resistances becomes large at the location of resonances. The simulation results in section 5.7 will show that the pattern is not too sensitive specially to the resistive parts and the degradation of the pattern due to difference between the actual and realized impedance values is not significant. The next challenging step in this project is to design a wideband matching network matching the input impedance of 22 excited ports to 50Ω in the two far frequency bands 25-29 GHz and 37-43 GHz and for the whole required steering range. In the next chapter, a modified real frequency technique is used to design this wideband matching network for the 22 excited ports.

Resistor Characteristics

The high frequency, thin film resistor CH02016 can be used to up to 70 GHz. Fig. 4.15 shows the resistor. The dimensions and the electrical specifications of the resistor can be seen in Table 4.1 and Table 4.2, respectively. The resistor is only available in a few standard values including $10\Omega, 18\Omega, 25\Omega, 50\Omega, 75\Omega, 100\Omega, 150\Omega, 180\Omega, 200\Omega, 250\Omega, 330\Omega, 500\Omega$.



(a) (b) (c)

Figure 4.15: Resistor CH02016 from VISHAY company. (a) 3D view. (b) Side view. (c) Top view.

Table 4.1: Dimensions (mm) of the resistor shown in Fig. 4.15

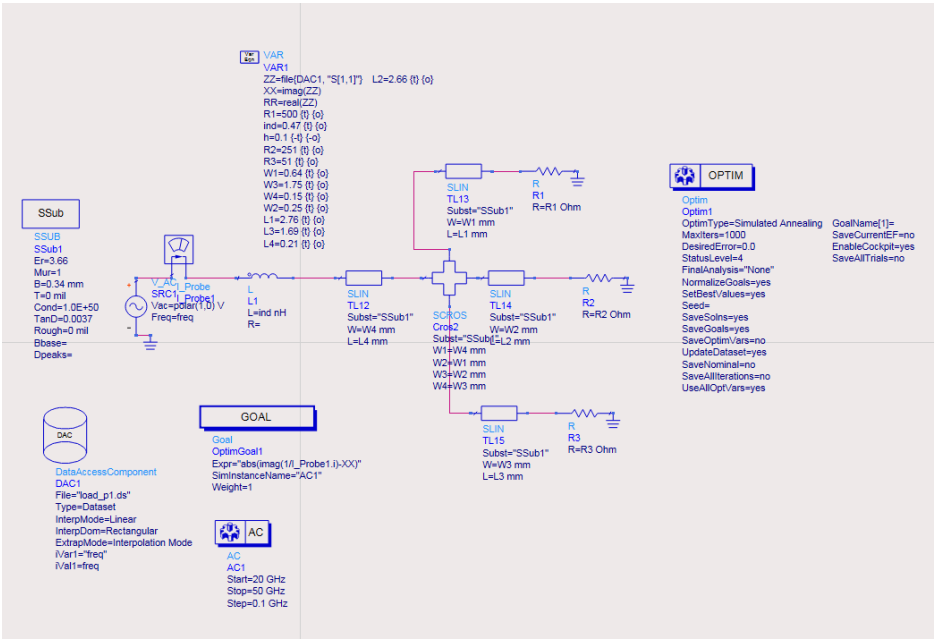
Parameter	Value	Parameter	Value
A	0.48	G	0.3
D	0.11-0.15	F	0.26
C	0.42	B	0.39

Table 4.2: Electrical specification of the resistor shown in Fig. 4.15

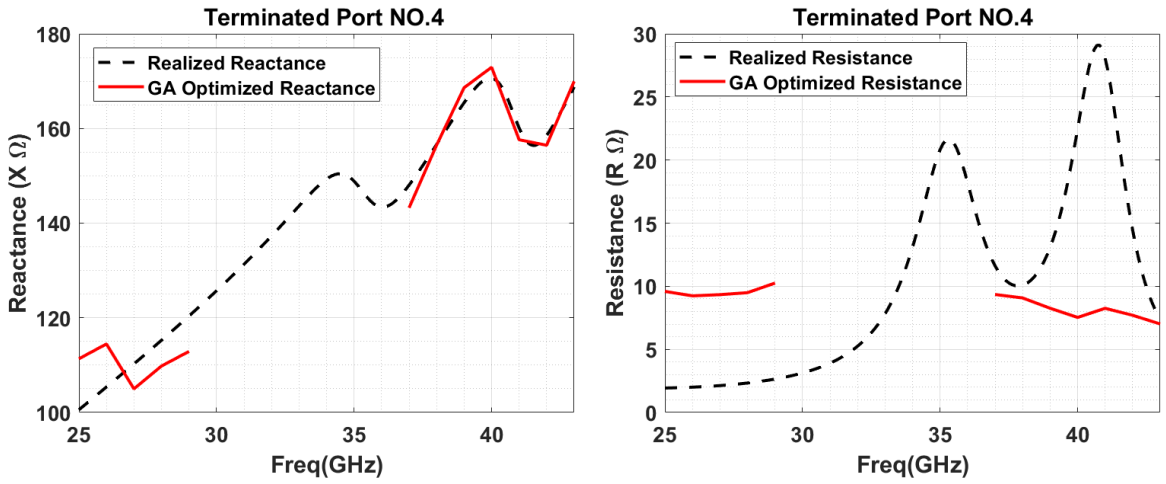
Rated Power P_n (W)	Limiting Element Voltage (V)	Tolerance	Temperature Coefficient $\pm$ppm/^{o}C
0.03	30	1% for 50Ω&100Ω,2%, 5%	100

4.9 Conclusion

In this chapter, the GA optimization results showed that by exciting only 34% of the array elements and by optimizing all the excitation voltages and terminating impedances, acceptable pattern with satisfying gain and SLL could be obtained which is close to the radiation characteristics of a fully excited array. Also, an innovative, low profile distributed circuit design is optimized by full wave simulation to realize the optimized terminating impedances for all the 20 terminated ports. In the next chapter, a matching network distributed circuit design is optimized to match the 22 excited ports to 50Ω loads and the 22 GCPW feedlines required for the lab test measurement is designed to connect the matching networks to the connectors mounted on edge of the board. Also, the whole thinned array structure including all the circuits designed for matching networks, terminating impedances, and feedlines are simulated by full wave simulation.

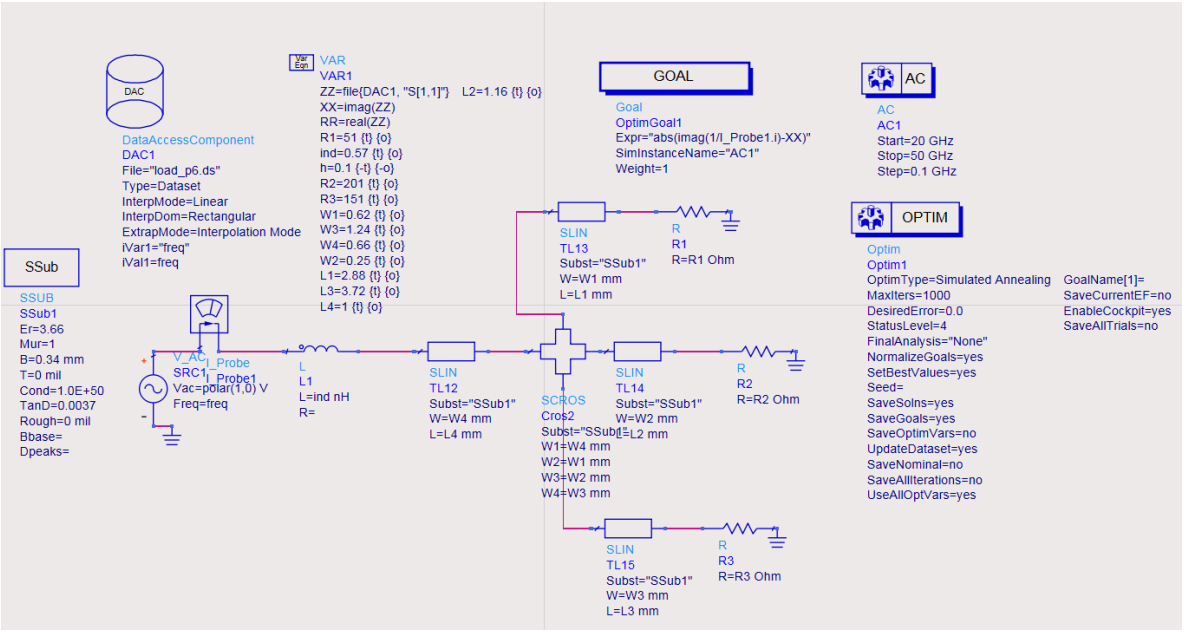


(a)

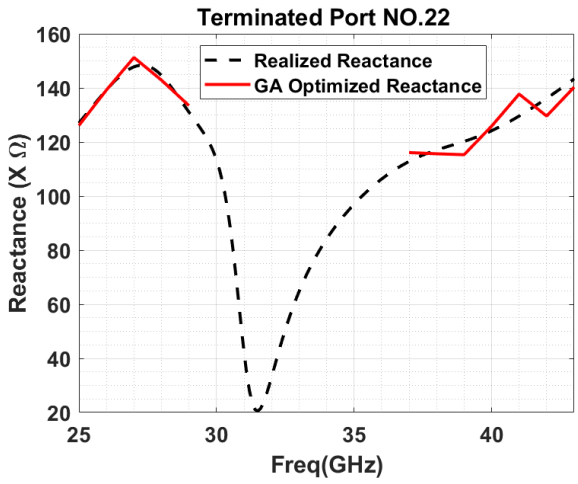


(b) (c)

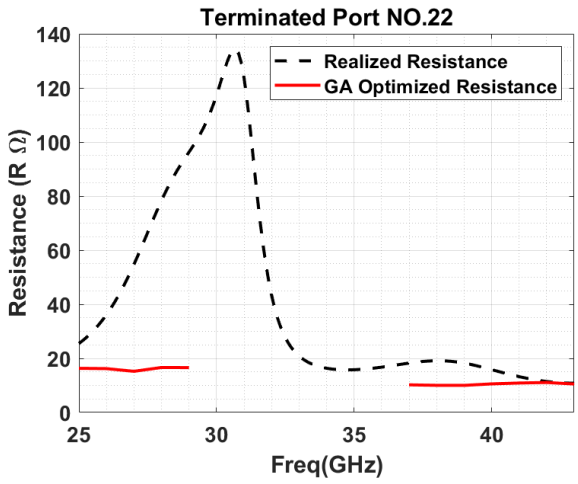
Figure 4.16: The ADS optimization result for realization of the terminating impedance at port NO. 4 (a) The optimized circuit. (b) The reactive part of the optimized circuit's input impedance in compare with the required GA optimized reactance. (c) The resistive part of the optimized circuit's input impedance in compare with the required GA optimized resistance.



(a)

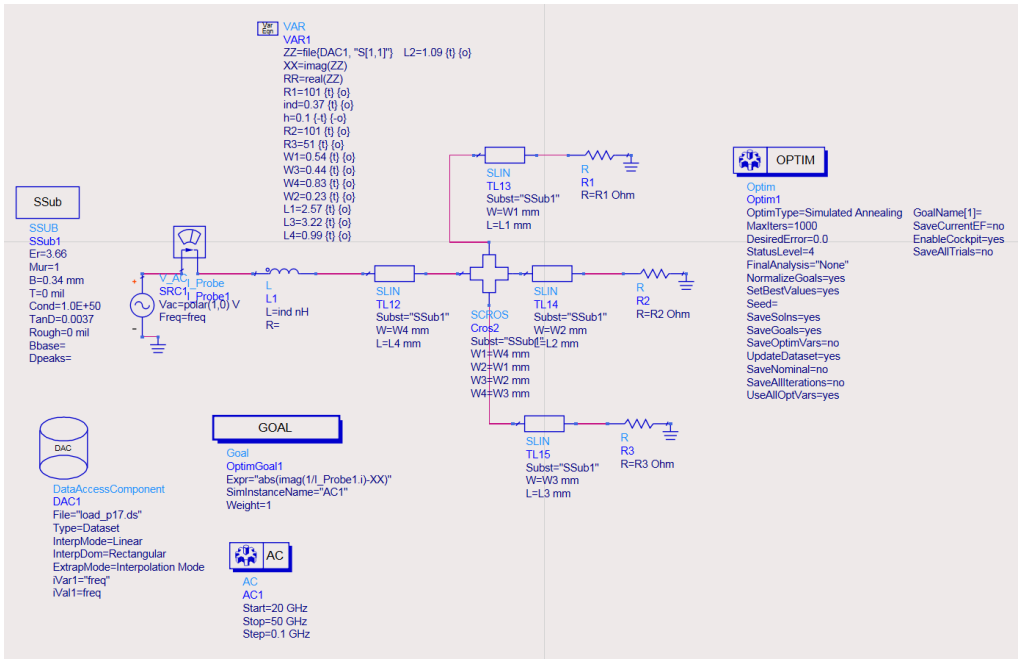


(b)

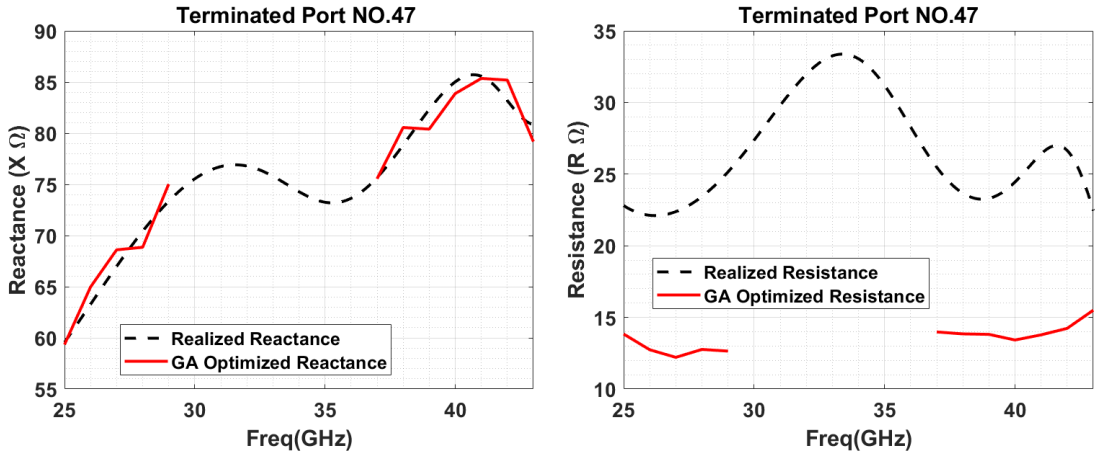


(c)

Figure 4.17: The ADS optimization result for realization of the terminating impedance at port NO. 22 (a) The optimized circuit. (b) The reactive part of the optimized circuit's input impedance in compare with the required GA optimized reactance. (c) The resistive part of the optimized circuit's input impedance in compare with the required GA optimized resistance.

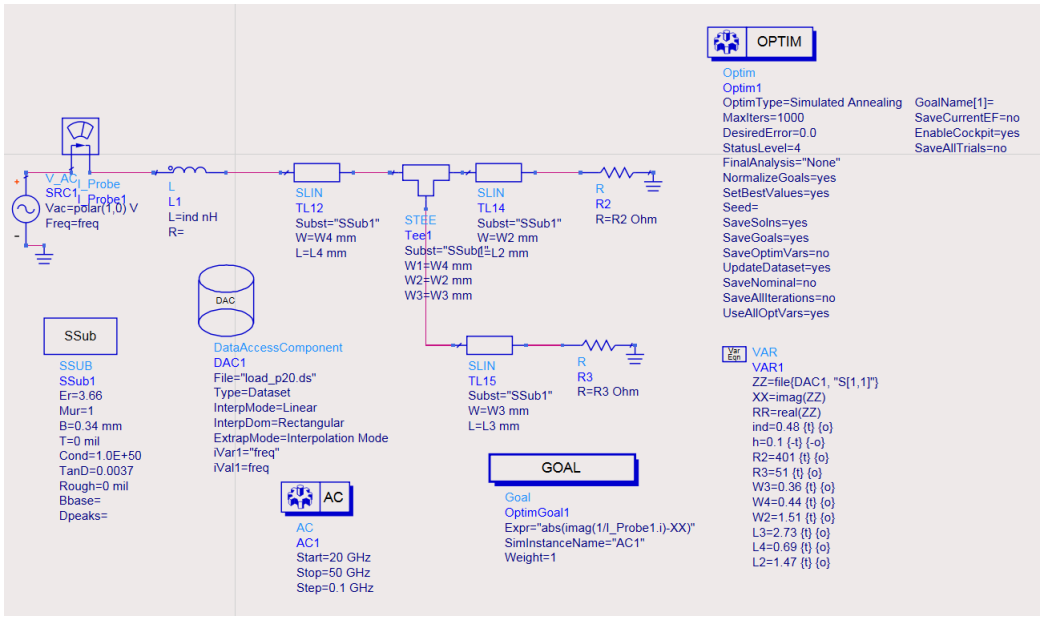


(a)

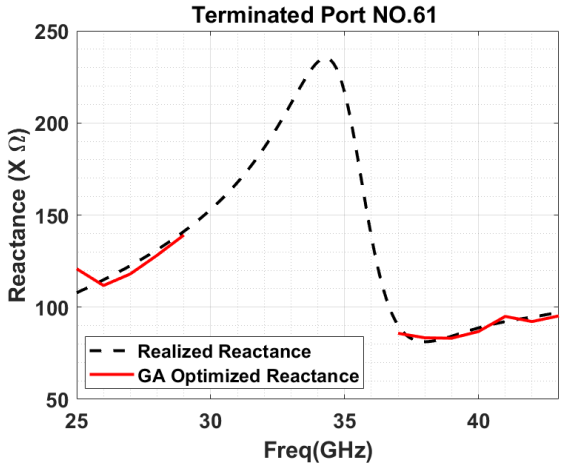


(b) (c)

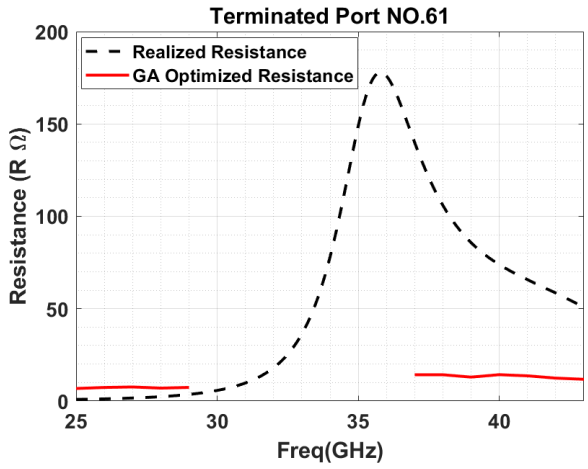
Figure 4.18: The ADS optimization result for realization of the terminating impedance at port NO. 47 (a) The optimized circuit. (b) The reactive part of the optimized circuit's input impedance compared with the required GA optimized reactance. (c) The resistive part of the optimized circuit's input impedance in compare with the required GA optimized resistance.



(a)

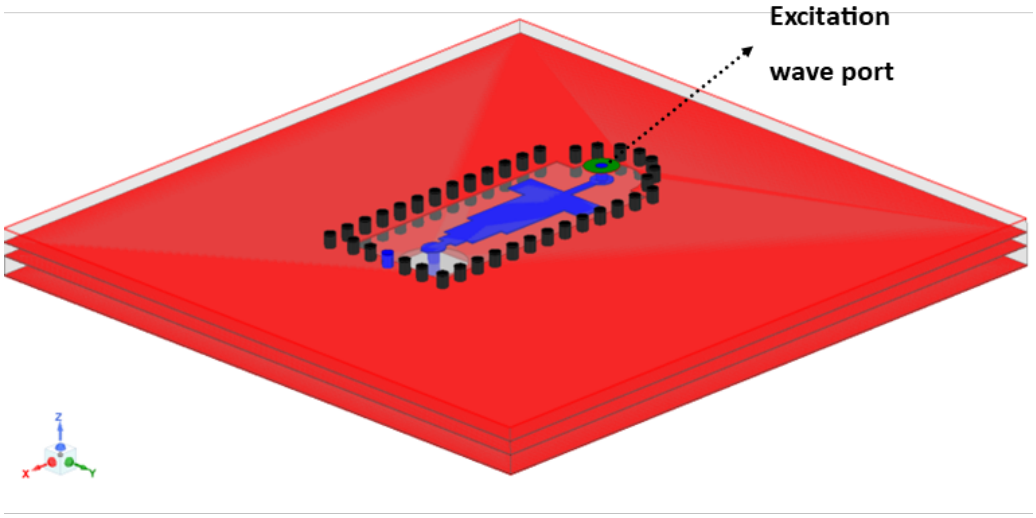


(b)

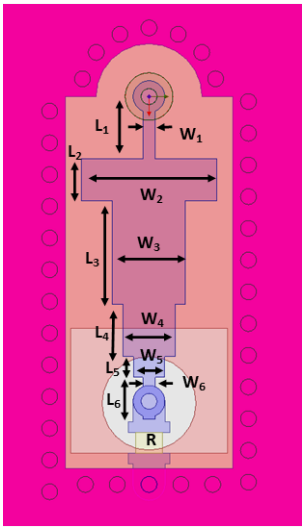


(c)

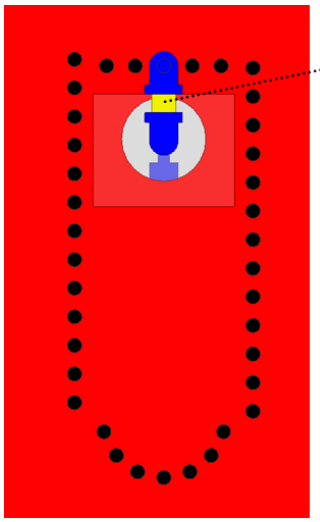
Figure 4.19: The ADS optimization result for realization of the terminating impedance at port NO. 61 (a) The optimized circuit. (b) The reactive part of the optimized circuit's input impedance in compare with the required GA optimized reactance. (c) The resistive part of the optimized circuit's input impedance in compare with the required GA optimized resistance.



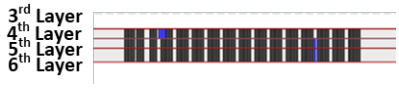
(a)



(b)

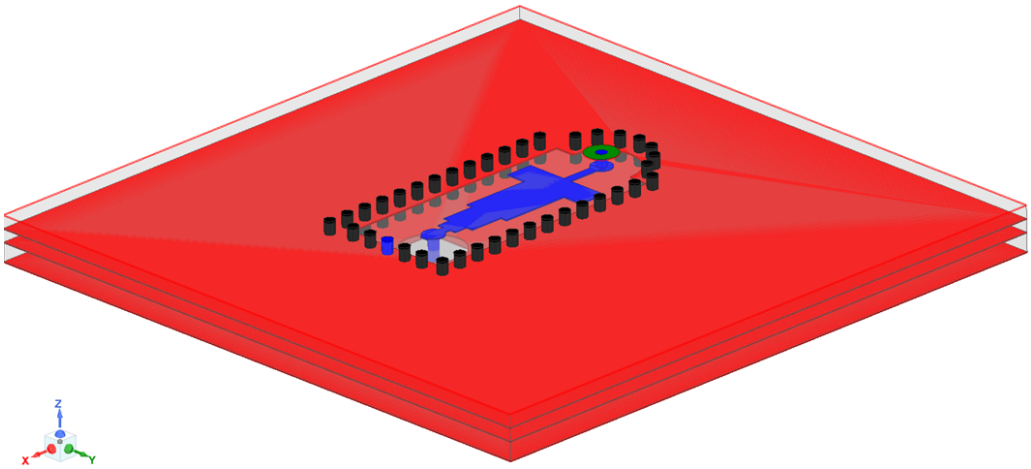


(c)

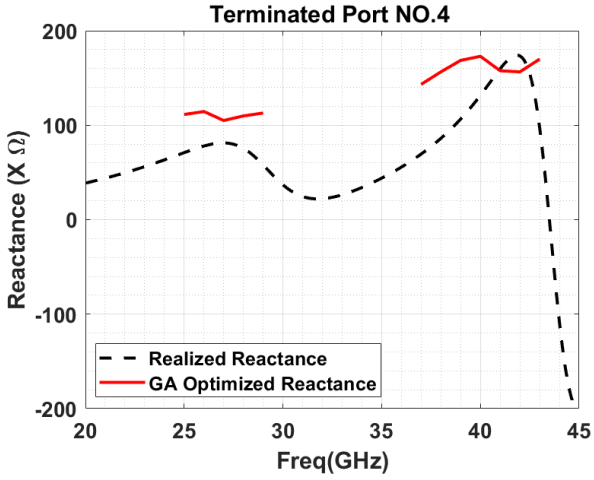


(d)

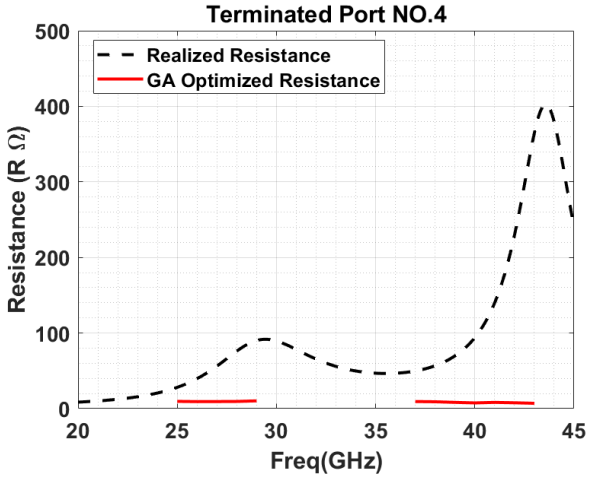
Figure 4.20: Distributed circuit optimized using Ansys HFSS to realize the required terminating impedances at all 20 terminated ports. (a) 3D view. (b) Top view showing the optimized variables of the design. (c) Bottom view. (d) Side view.



(a)

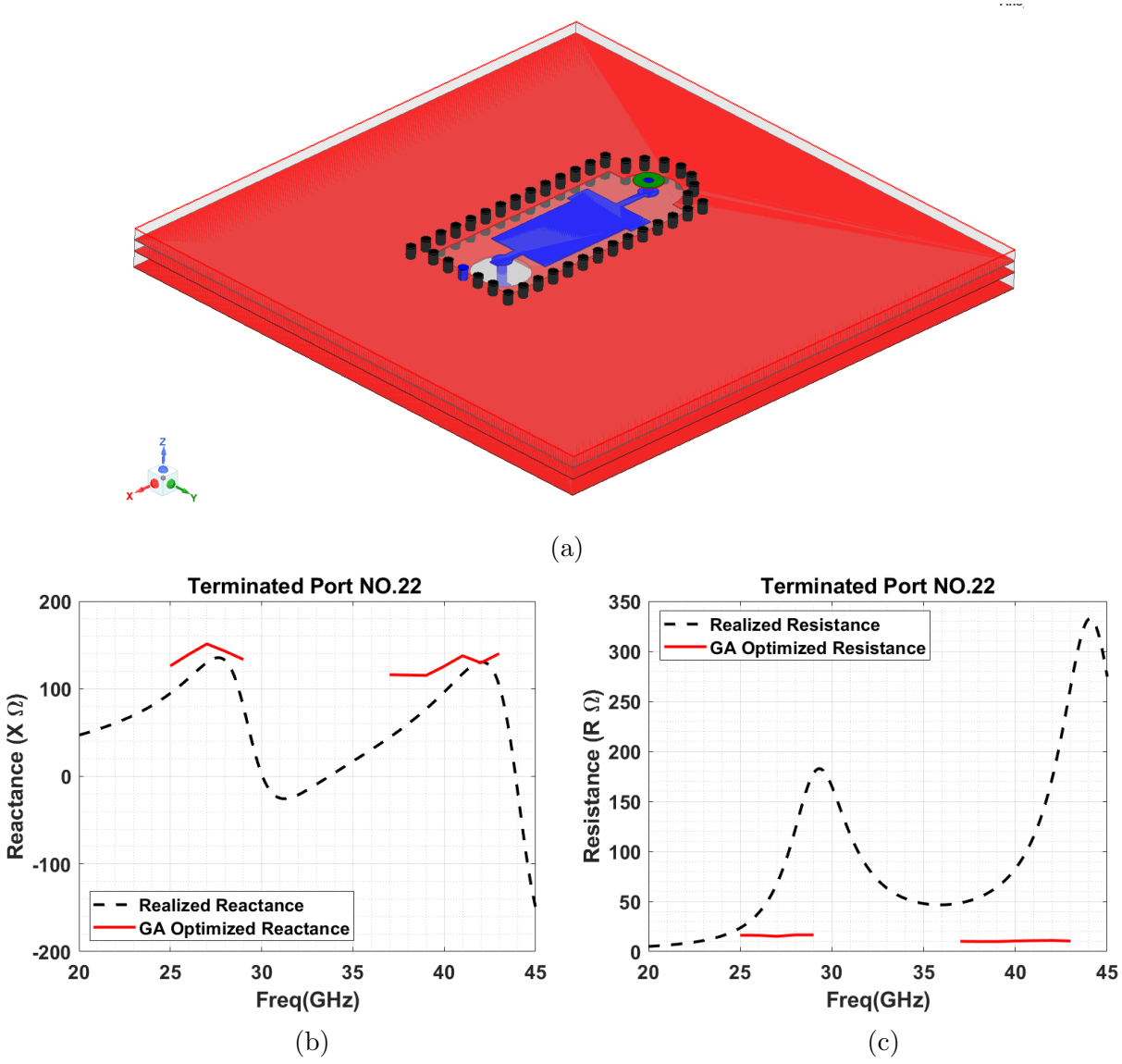


(b)



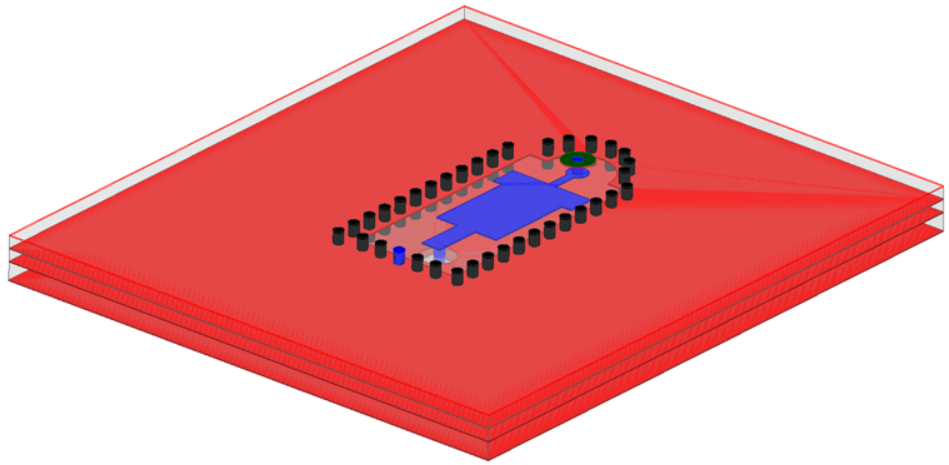
(c)

Figure 4.21: Full wave optimization result for the realization of the required terminating impedance at port NO. 4 (a) The optimized distributed circuit with $w_1 = 0.12mm, w_2 = 1.3mm, w_3 = 0.7mm, w_4 = 0.5mm, w_5 = 0.3mm, w_6 = 0.12mm, l_1 = 0.6mm, l_2 = 0.4mm, l_3 = 1mm, l_4 = 0.5mm, l_5 = 0.2mm, l_6 = 0.4mm, R = 75\Omega$. (b) The reactive part of the optimized circuit's input impedance in compare with the required GA optimized reactance. (c) The resistive part of the optimized circuit's input impedance in compare with the required GA optimized resistance.

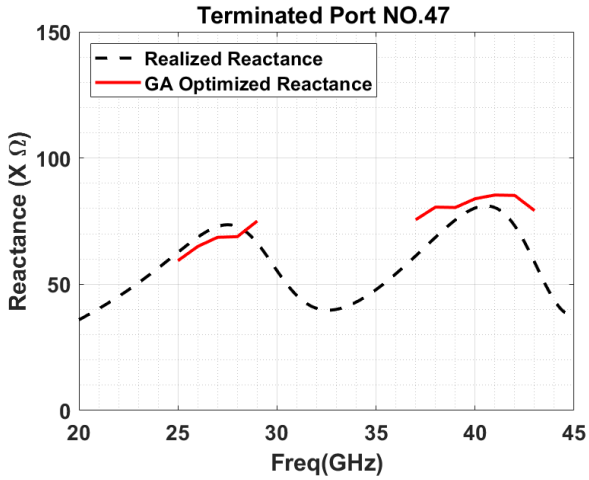


(a) (b) (c)

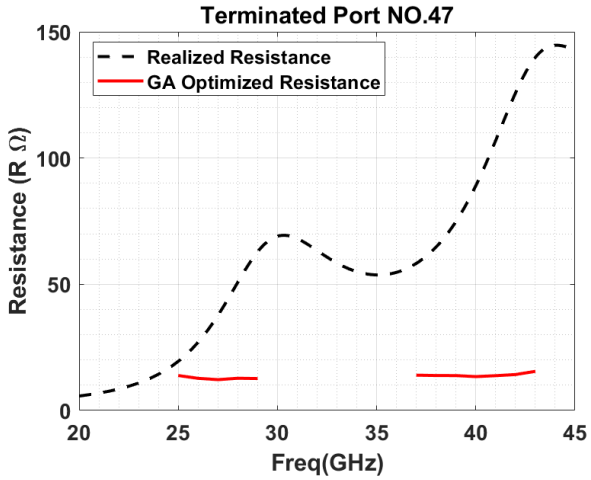
Figure 4.22: Full wave optimization result for the realization of the required terminating impedance at port NO. 22 (a) The optimized distributed circuit with $w_1 = 0.12mm, w_2 = 1.3mm, w_3 = w_4 = w_5 = 1.1mm, w_6 = 0.16mm, l_1 = 0.6mm, l_2 = 0.4mm, l_3 = 0.95mm, l_4 = 0.5mm, l_5 = 0.2mm, l_6 = 0.5mm, R = 100\Omega$. (b) The reactive part of the optimized circuit's input impedance in compare with the required GA optimized reactance. (c) The resistive part of the optimized circuit's input impedance in compare with the required GA optimized resistance.



(a)

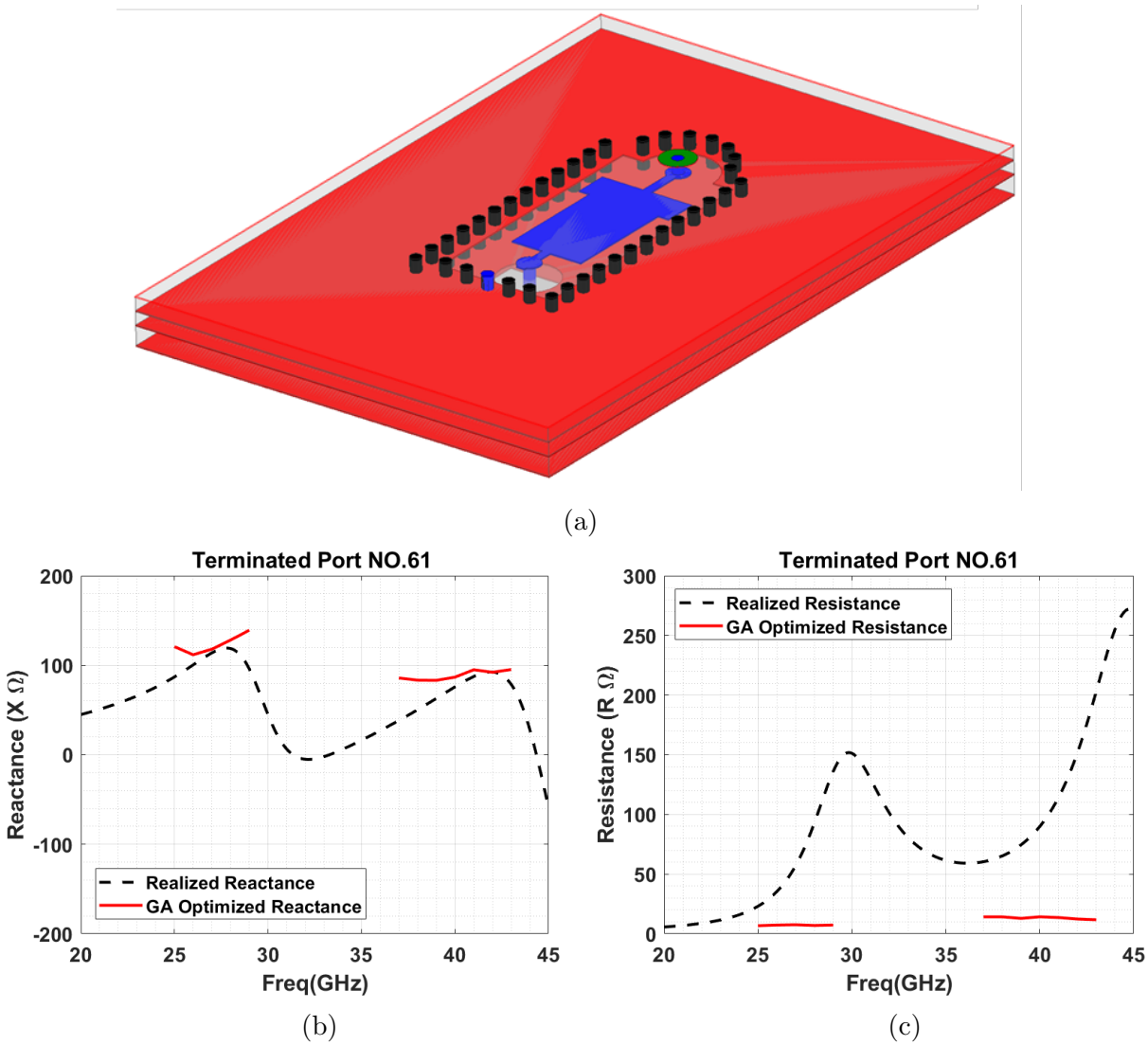


(b)



(c)

Figure 4.23: Full wave optimization result for the realization of the required terminating impedance at port NO. 47 (a) The optimized distributed circuit with $w_1 = 0.12mm, w_2 = 1.3mm, w_3 = w_4 = 1mm, w_5 = 0.3mm, w_6 = 0.3mm, l_1 = 0.5mm, l_2 = 0.4mm, l_3 = 0.8mm, l_4 = 0.5mm, l_5 = 0.3mm, l_6 = 0.4mm, R = 100\Omega$. (b) The reactive part of the optimized circuit's input impedance in compare with the required GA optimized reactance. (c) The resistive part of the optimized circuit's input impedance in compare with the required GA optimized resistance.



(a)

(b)

(c)

Figure 4.24: Full wave optimization result for the realization of the required terminating impedance at port NO. 61 (a) The optimized distributed circuit with $w_1 = 0.12mm, w_2 = 1.3mm, w_3 = w_4 = w_5 = 1mm, w_6 = 0.12mm, l_1 = 0.6mm, l_2 = 0.45mm, l_3 = 0.8mm, l_4 = 0.5mm, l_5 = 0.2mm, l_6 = 0.5mm, R = 100\Omega$. (b) The reactive part of the optimized circuit's input impedance in compare with the required GA optimized reactance. (c) The resistive part of the optimized circuit's input impedance in compare with the required GA optimized resistance.

Chapter 5

Design of a Wideband Antenna Matching Network

So far we have an inherently wideband phased array antenna but a wideband matching network is also required at each of the 22 excited ports to match the antenna input impedances to the 50Ω source impedances in the two widely separated frequency bands (25-29 GHz, 37-43 GHz) and for the whole desired range of steering angles (up to 45^o). The goal of using the matching network is to minimize the reflected power going back to the source which is a beam former in the case of this phased array and also to maximize the transmitted power going into the antenna to increase the antenna realized gain.

A lossless matching network providing acceptable return loss for the whole frequency range is ideal for this purpose; however, based on the Fano-Bode theory:

$$\frac{BW}{\omega_o}\ln(\frac{1}{\Gamma_{avg}}) < \frac{\pi}{Q} \tag{5.1}$$

the bandwidth of a lossless matching network is limited by the energy stored in the load (the antenna is this case) and the required reflection coefficient. In equation (5.1), Q is the quality factor of the load, Γ_{avg} is the average value of the reflection coefficient in the entire range of frequency, ω_o is the radian center frequency and BW represents the bandwidth. One solution to achieve broader bandwidths is adding lossy elements to the matching network [56]. However, this creates a trade off between the matching network bandwidth and antenna efficiency.

Over the last 40 years, the numerical optimization method known as the Real Frequency Technique (RFT), initiated by Prof. H.J. Carlin of Cornell University, has provided excellent solutions to construct power transfer networks for many applications [57].

Furthermore, the Simplified Real Frequency Technique (SRFT) has been verified as the most suitable one to design matching networks and microwave amplifiers [57]. Compared to analytic theory of broadband matching, SRFT neither requires a model for the load network, nor it requires the selection of transfer function. Therefore, one does not need to satisfy complicated gain-bandwidth restrictions imposed by the antenna. As opposed to brute force techniques, in SRFT, lossless equalizer is described by means of its bounded real input reflection coefficient. Thus, at the beginning of the design process, one does not need to select a circuit topology for the matching network. Furthermore, the degree of the non-linearity of the objective function is almost quadratic. Hence, the end results are not sensitive to the initial values and the convergence is almost guaranteed [57]. Moreover, the SRFT algorithm presents excellent numerical stability since all computations are made on the bounded real scattering parameters of the equalizer and on the reflection coefficient of the antenna [57].

The SRFT for lossless distributed circuits with and without lossy junctions are thoroughly explained in Appendix C to help us in the design of the wideband matching networks.

5.1 Matching Network Optimization Using Real Frequency Technique

The matching networks for the 22 excited ports are optimized using the modified real frequency technique described in section C.2 for the targeted frequency bands (25 GHz-29 GHz, 37 GHz-43 GHz) and for the four steering angles including broadside, $15^o, 30^o, 45^o$ in E-Plane. The two stage cascaded transmission lines with three lossy junctions shown in Fig. 5.1 is used as the topology of the equalizer. The required bandwidth was impossible to achieve using lossless distributed equalizers even with a large number of stages. Fig. 5.2 shows the result of the optimization using 4 and 8 stages of lossless distributed matching networks at excited port number 53. As can be seen in this figure, the input reflection coefficient is not low enough (below -10 dB) in the entire range of frequency and for all the steering angles even with using a large number of cascaded transmission lines. So, lossy junctions are added to the structure to match the ports over the two required frequency bands; however, the loss will reduce the transmitted power to the antenna and the efficiency of the system will suffer as a result. As shown in equation 5.2, the error vector is defined to maximize the transmitted power to the antenna (minimize the loss) and minimize the reflected power back to the source. For this purpose, the transmission and reflection coefficients T and R defined in equation C.1 are both compared with a given

level T_o and R_o. Note that in a lossy system T is not simply related to R by $T = 1 - R$ anymore. So, If T is smaller than T_o, the absolute difference $|T - T_o|$ times a weighting factor w_T would be added to the error vector. Similarly, if R is larger than R_o, the absolute difference $|R - R_o|$ times a weighting factor w_R would be added to the error vector. For the aim of optimization, Levenberg-Marquardt algorithm with maximum 50000 iterations and 2000 function evaluations is used. In order to start the optimization process taking $\alpha_i = \pm 1$ and $\beta_i = \pm 0.5$ was found to work well.

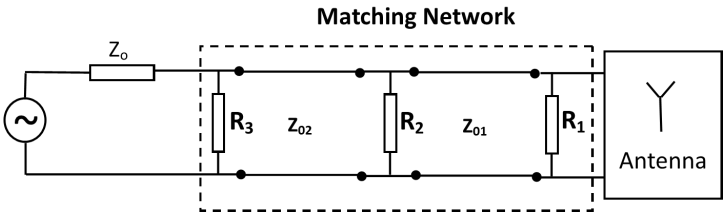


Figure 5.1: The structure of the optimized matching network using modified real frequency technique

$$error = \begin{cases} [w_R \ |R - R_o|, 0] & R \geq R_o \ \& \ T \geq T_o \\ [0, w_T \ |T - T_o|] & R \leq R_o \ \& \ T \leq T_o \\ [w_R \ |R - R_o|, w_T \ |T - T_o|] & R \geq R_o \ \& \ T \leq T_o \\ [0, 0] & \text{otherwise} \end{cases} \tag{5.2}$$

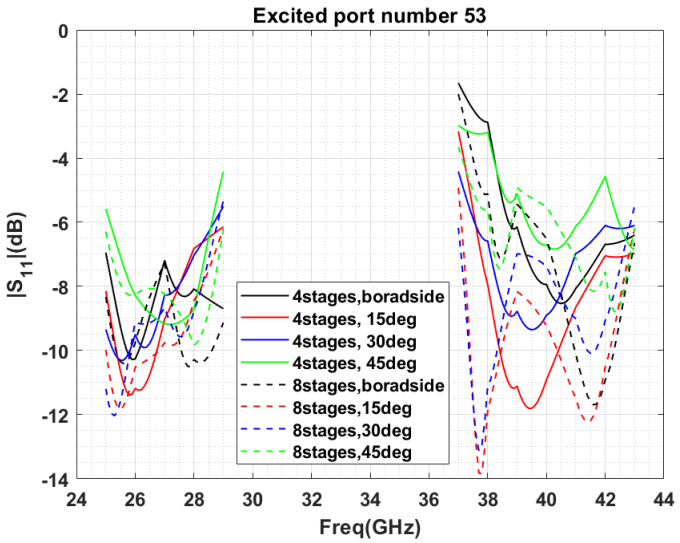


Figure 5.2: The optimized input reflection coefficient of 4 and 8 stage lossless distributed equalizers at excited port number 53 using real frequency technique.

Optimization Result

The results of RFT optimization for lossy matching networks for excited port numbers 3,28,44 are shown in Fig. 5.3,5.4,5.5. The first and second subfigures show the reflection (S_{11}) and the transmission coefficient (T) of the matching network when connected to the antenna port and the third figure compares the input reflection coefficient of the antenna on Smith Chart before (L_{11}) and after connecting to the matching network (S_{11}). The constant parameters of the optimization, T_o, R_o, w_o, w_R, w_T described in section 5.1 are set to 0.45, 10^{-4}, and $2\pi \times 38e9$, 1, 1 respectively. Since the pattern optimization is done with 1 GHz step size, the data for the input reflection coefficient of the antenna (L_{11}) is linearly interpolated in Matlab to provide data for the two frequency bands with 0.1 GHz step size.

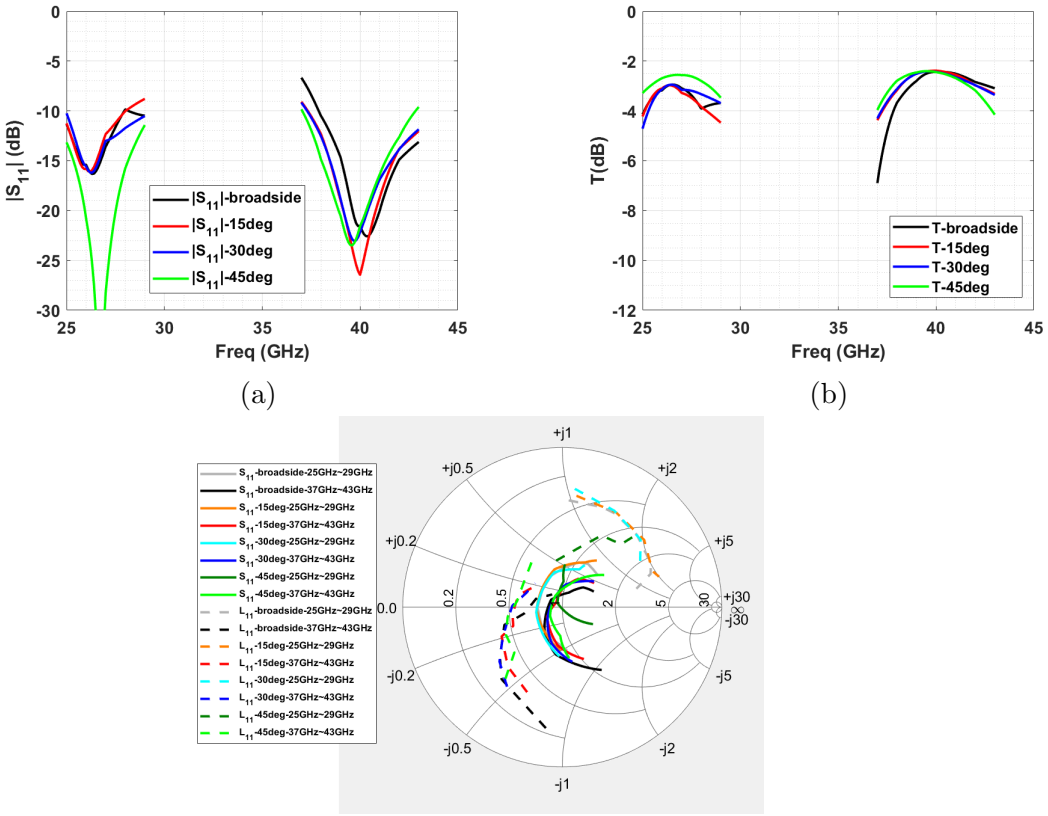


Figure 5.3: The optimization result of the 3 stages distributed matching network with lossy junctions using Real Frequency Technique at excited port number 3 with optimized parameters: $R_1 = 956.28\Omega, R_2 = 791.89\Omega, R_3 = 205.25\Omega, Z_{o1} = 76.64\Omega, Z_{o2} = 103.09\Omega$ shown in Fig. 5.1 (a) The input reflection coefficient (dB). (b) The transmission coefficient (dB). (c) The smith chart comparing the input reflection coefficient of the antenna (L_{11}) with the input reflection coefficient of the matched network (S_{11}) for different steering angles.

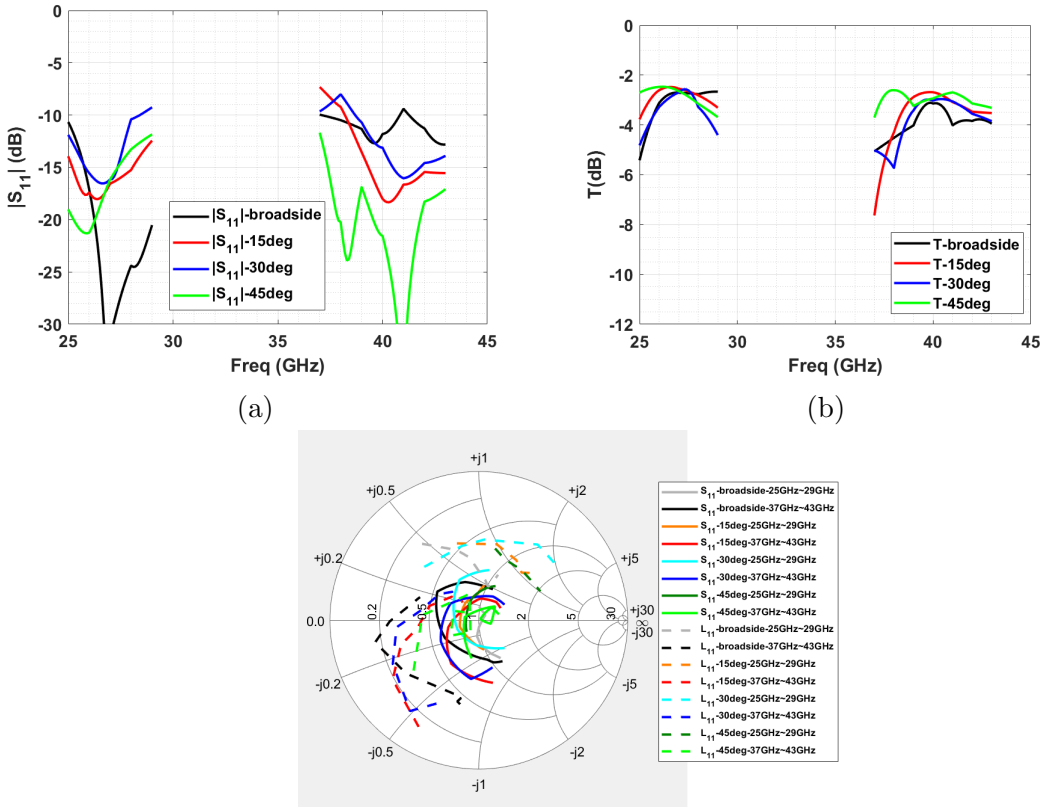
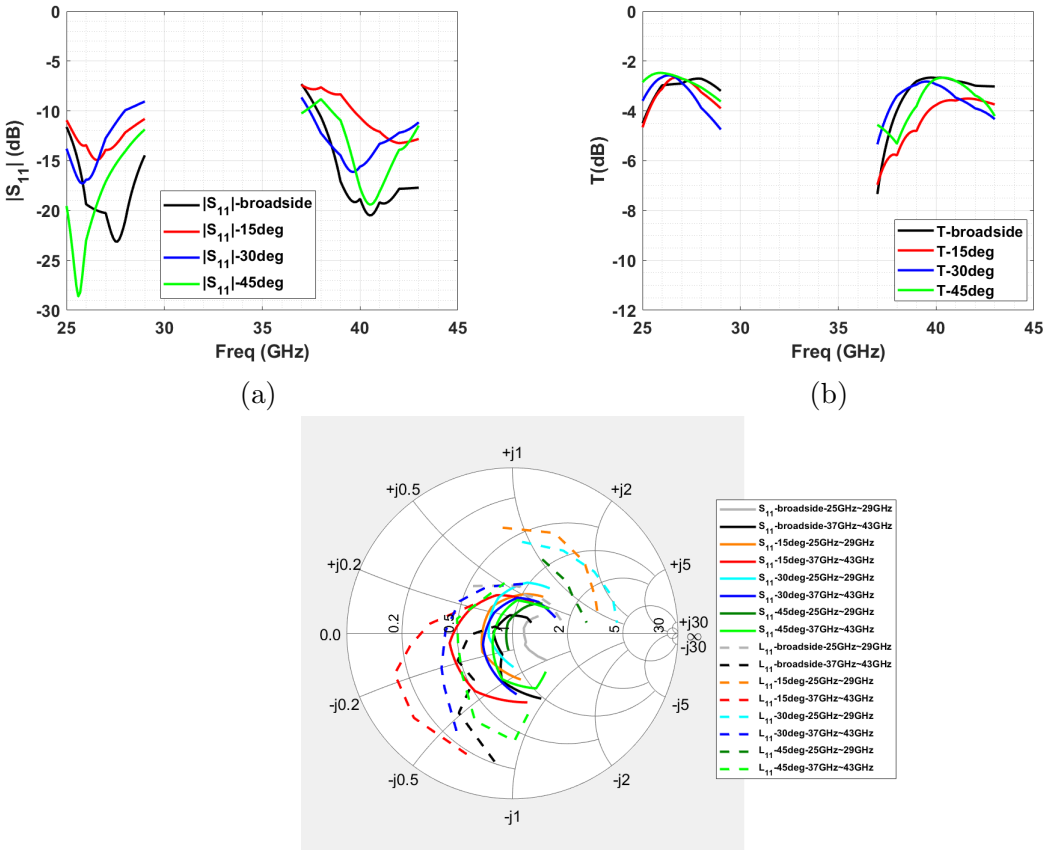


Figure 5.4: The optimization result of the 3 stages distributed matching network with lossy junctions using Real Frequency Technique at excited port number 28 with optimized parameters: $R_1 = 4392\Omega, R_2 = 730.7\Omega, R_3 = 143.8\Omega, Z_{o1} = 67.14\Omega, Z_{o2} = 95.12\Omega$ shown in Fig. 5.1 (a) The input reflection coefficient (dB). (b) The transmission coefficient (dB). (c) The smith chart comparing the input reflection coefficient of the antenna (L_{11}) with the input reflection coefficient of the matched network (S_{11}) for different steering angles.



(a) (b) (c)

Figure 5.5: The optimization result of the 3 stages distributed matching network with lossy junctions using Real Frequency Technique at excited port number 44 with optimized parameters: $R_1 = 3586\Omega, R_2 = 725\Omega, R_3 = 161.3\Omega, Z_{o1} = 78.86\Omega, Z_{o2} = 100.44\Omega$ shown in Fig. 5.1 (a) The input reflection coefficient (dB). (b) The transmission coefficient (dB). (c) The smith chart comparing the input reflection coefficient of the antenna (L_{11}) with the input reflection coefficient of the matched network (S_{11}) for different steering angles.

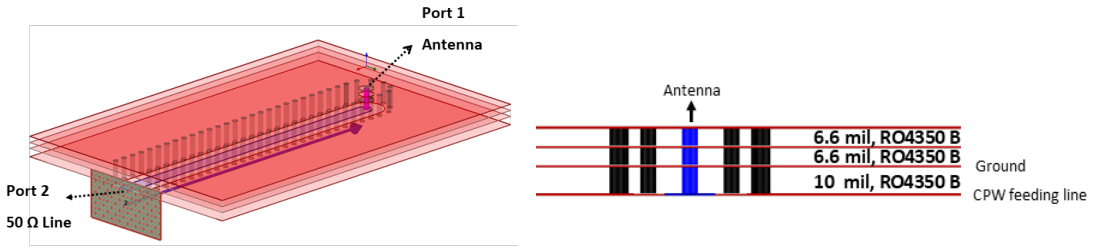
5.2 Circuit Level Optimization of the Matching Network

Before starting the full wave simulation of the optimized matching network, we need to add the effect of the via connecting the antenna port to the last bottom layer where the matching networks and the feed lines are placed. This via is connected to a long 50Ω transmission line in a separate design in HFSS and the full wave simulation is done to extract its scattering parameters. Once the simulation is done the effect of the attached transmission line is de-embeded. Fig. 5.6 shows the structure of the design. The via hole size and the pad dimensions are selected considering the limitations of PCB fabrication method. In the circuit level, the via can be treated as a two port network with known scattering parameters. Also, the transmission lines' S-parameter models are provided in the circuit design of the HFSS and the input reflection coefficient of the antenna is also imported in the design as a one port network with known input reflection coefficient (L_{11}). Fig. 5.7 shows the circuit design of the matching network including two cascaded GCPW transmission lines with three resistant junctions, connected to the antenna when the beam is on broadside.

In this optimization, the transmission lines are implemented by grounded Coplanar Waveguide (CPW) line in order to minimize the radiation from the feedlines with their close proximity to the ground, and provide better isolation between the lines. Furthermore, another advantage of using GCPW lines for the matching network structure with lossy junctions is that the resistors can be mounted easily in the gap between the trace and the nearby ground. So, it eliminates the need for extra via or long traces connecting the resistor to the ground. Also in general, there are two degrees of freedom in GCPW to achieve the required characteristic impedance, the trace width which is inversely proportional and the gap size which is directly proportional to the characteristic impedance. This enables us to realize a wide range of characteristic impedances with practical trace width and gap size that can be fabricated with the given substrate thickness; however, since we need to fix the gap size of the line to the length of space between the two pads of the resistor, in practice, we will not use this feature in this design. So, the substrate thickness and the gap size are kept constant as 0.25mm and 0.2mm respectively. The dimensions and characteristics of the resistor used were described in section 4.8.

The three stage matching network structure shown in Fig. 5.7 is optimized in the circuit design package of Ansys HFSS using Quadratic Lagrangian Algorithm. The cost function is defined in such a way to achieve S_{11} below $-12dB$ and transmission coefficient above $-5dB$ in the two frequency bands 25 GHz-29 GHz and 37 GHz-43 GHz and for all steering angles.

The optimization variables are the transmission lines' width (W_1, W_2), length (L_1, L_2), and the resistor values (R_1, R_2, and R_3). The initial values are set as the optimized values by real frequency technique. Fig. 5.8,5.9,5.10 shows the circuit level optimization results of the matching network for excited ports number 3, 28, 44.



(a) (b)

Figure 5.6: The Full wave simulation design extracting the scattering parameter model of the via connecting the 3rd layer to the 6th layer (a) 3D view. (b) Side view showing the layers and the via connecting the antenna port on 3rd layer to the 6th layer.

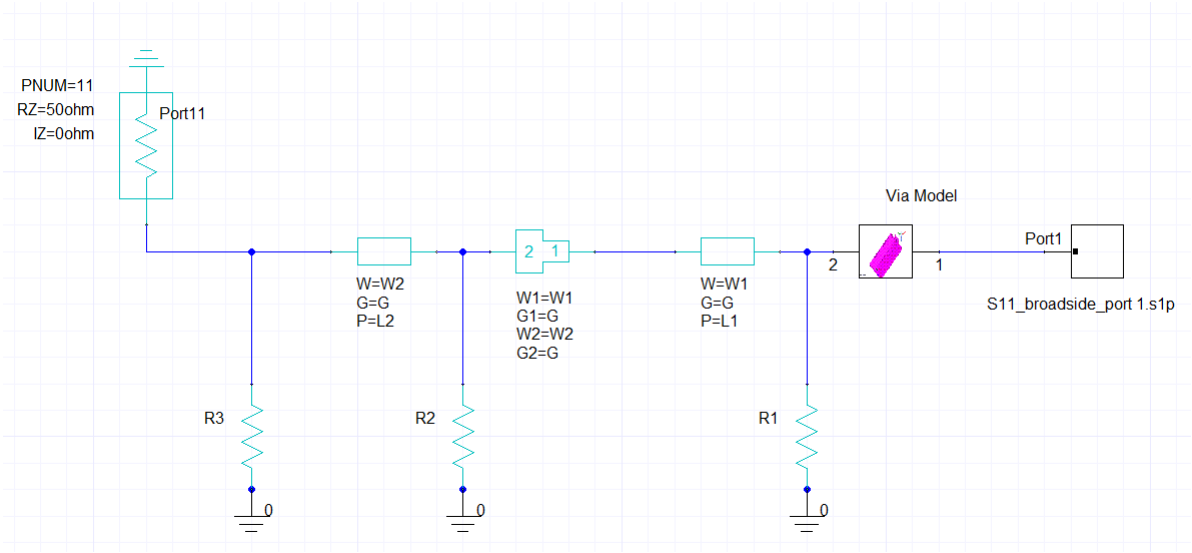


Figure 5.7: The circuit design of the three stage distributed matching network with 3 resistant junctions connected to the antenna when beam is steered to broadside

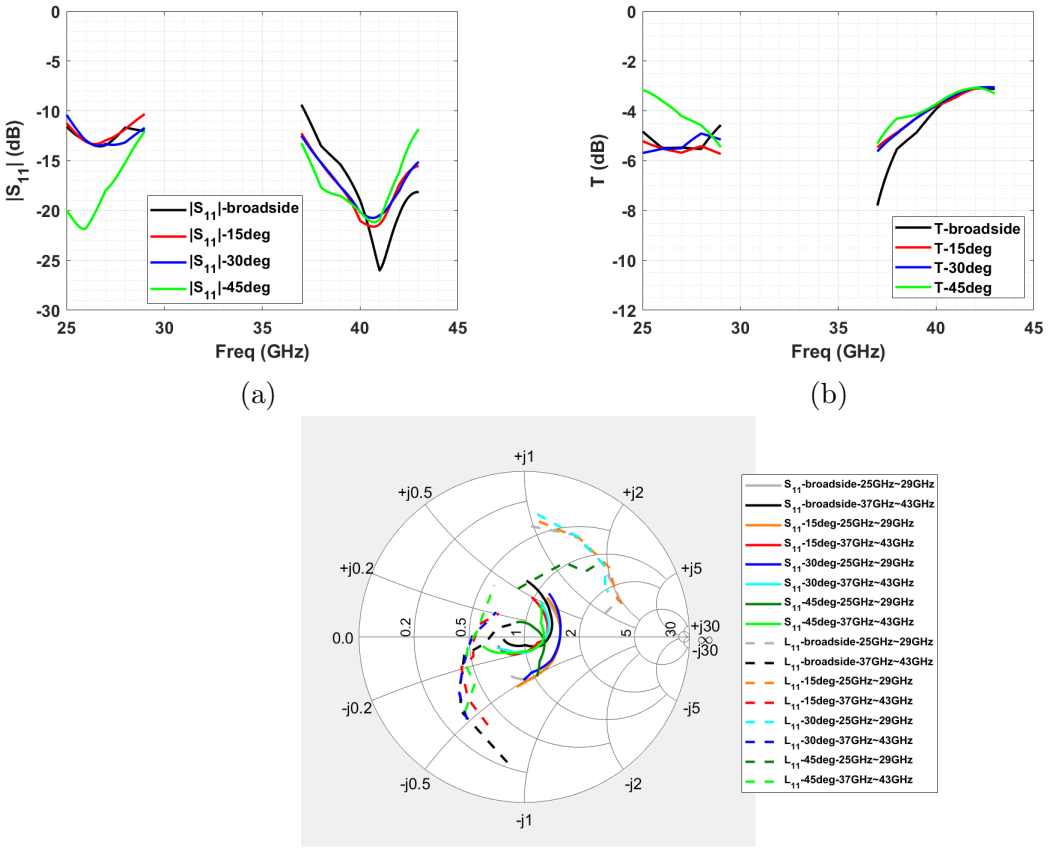


Figure 5.8: The result of the circuit level optimization of the 3 stage matching network with lossy junctions at excited port number 3 with optimized parameters: $R_1 = 2024\Omega, R_2 = 257.5\Omega, R_3 = 128\Omega, L_1 = 1.63mm, L_2 = 1.52mm, W_1 = 0.318mm, W_2 = 0.437mm, G = 0.2mm$ shown in Fig. 5.7 (a) The input reflection coefficient of the matched network. (b) The transmission coefficient of the optimized matching network defined in equation C.1. (c) The smith chart comparing the input reflection coefficient of the antenna (L_{11}) with the input reflection coefficient of the matched network (S_{11}) for different steering angles.

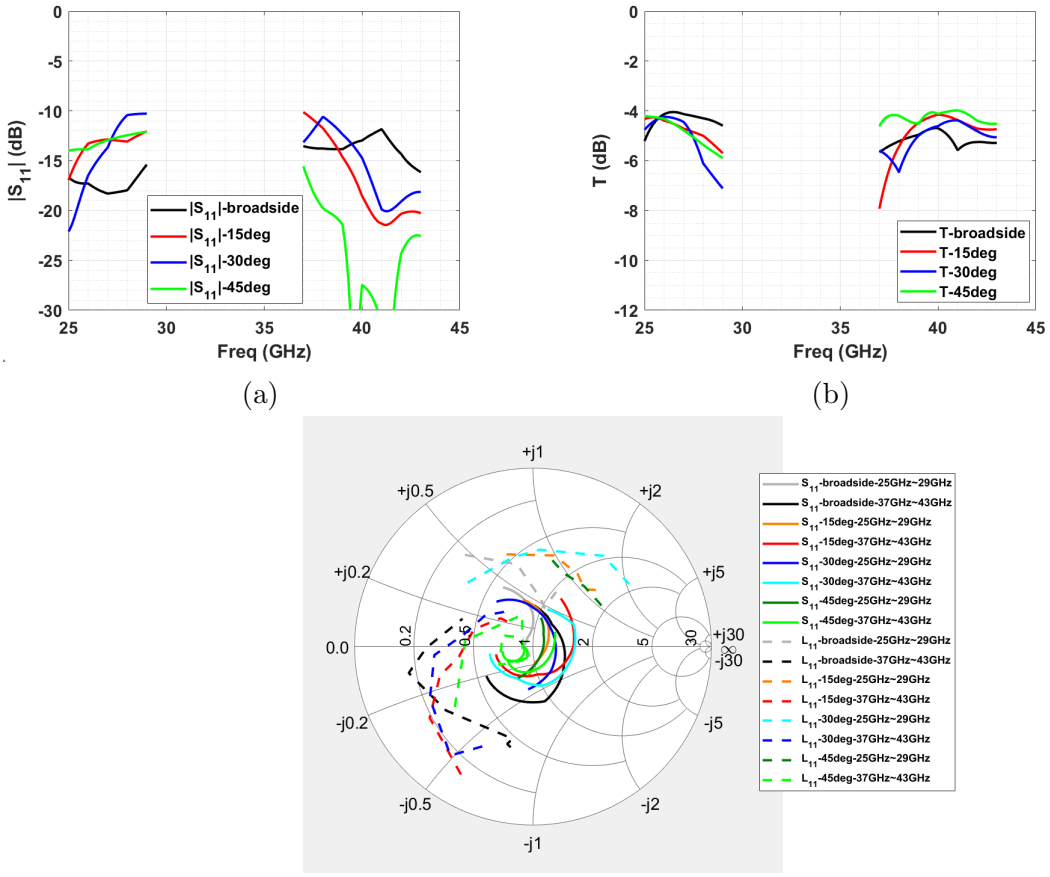
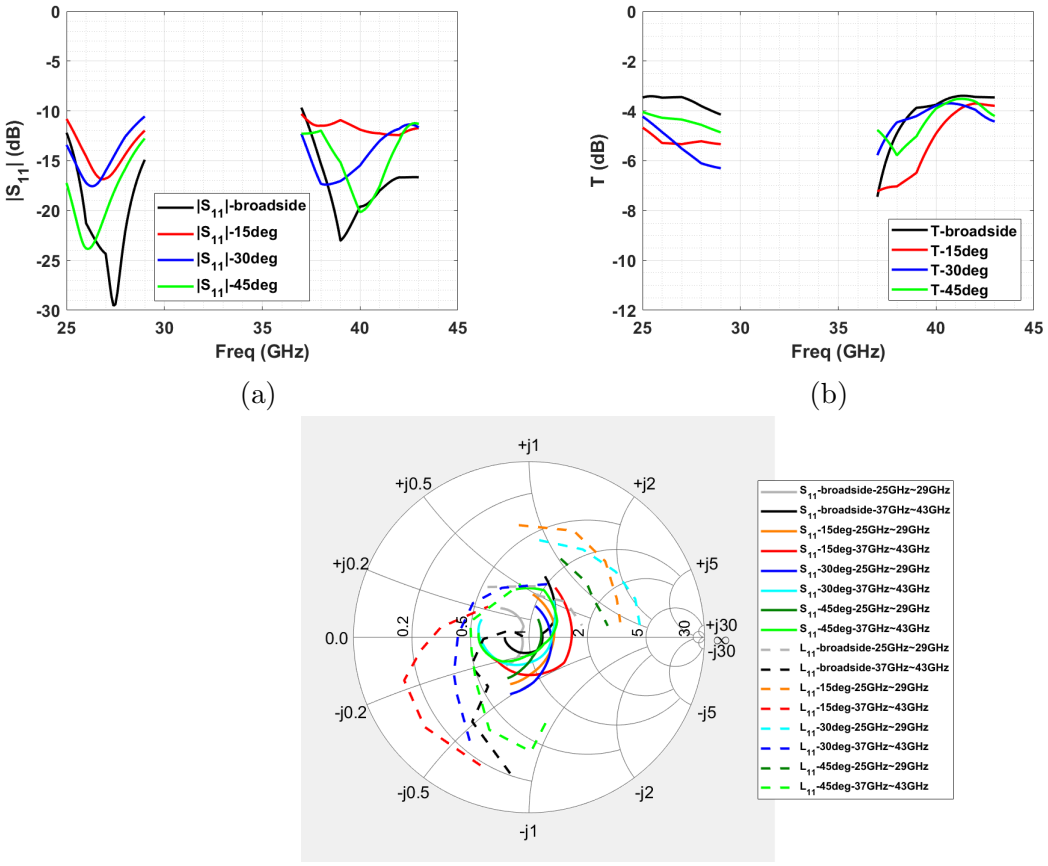


Figure 5.9: The result of the circuit level optimization of the 3 stage matching network with lossy junctions at excited port number 28 with optimized parameters: $R_1 = 396\Omega, R_2 = 453.5\Omega, R_3 = 117.5\Omega, L_1 = 0.915mm, L_2 = 0.936mm, W_1 = 0.241mm, W_2 = 0.156mm, G = 0.2mm$ shown in Fig. 5.7 (a) The input reflection coefficient of the matched network. (b) The transmission coefficient of the optimized matching network defined in equation C.1. (c) The smith chart comparing the input reflection coefficient of the antenna (L_{11}) with the input reflection coefficient of the matched network (S_{11}) for different steering angles.



(a) (b)

(c)

Figure 5.10: The result of the circuit level optimization of the 3 stage matching network with lossy junctions at excited port number 44 with optimized parameters: $R_1 = 1705.5\Omega, R_2 = 163.5\Omega, R_3 = 124.5\Omega, L_1 = 1.77mm, L_2 = 1.35mm, W_1 = 0.34mm, W_2 = 0.46mm, G = 0.2mm$ shown in Fig. 5.7 (a) The input reflection coefficient of the matched network. (b) The transmission coefficient of the optimized matching network defined in equation C.1. (c) The smith chart comparing the input reflection coefficient of the antenna (L_{11}) with the input reflection coefficient of the matched network (S_{11}) for different steering angles.

5.3 Full Wave Optimization of the Matching Network

After circuit level optimization, the optimized values are used as the starting point and the full wave optimization is done on the 3 stage matching network for all 22 excited ports using Ansys HFSS. The design parameters are swept around the circuit level optimized values in section 5.2. The resistances are only swept among the standard values of CH02016 mentioned in section 4.8 plus a high impedance value which is interpreted as open circuit. The scattering parameters of the matching network is extracted for all those sets of parameters, then the scattering parameters are used in a separate circuit design to cascade with the s parameter model of the antenna port for all steering angles. So, the input reflection coefficient (S_{11}) and transmission coefficient (T in equation C.1) of the matching network is calculated for all sets of tuned parameters and the one making smaller reflection coefficient and larger transmission coefficient is chosen as the optimized design. Fig. 5.11,5.12,5.13 shows the HFSS design and the reflection and transmission coefficient of the optimized matching network at excited ports numbers 3,28,44. The results demonstrate input reflection coefficient (S_{11}) better than -10dB at the center of both frequency bands which goes up to -6dB at the edge of the bands for some ports and for some steering angles. Also the transmission coefficient (T) is better than -6dB for large parts of the two bands and all steering angles; however, it goes down up to -10 dB at the edge of the band at some ports and for some steering angles.

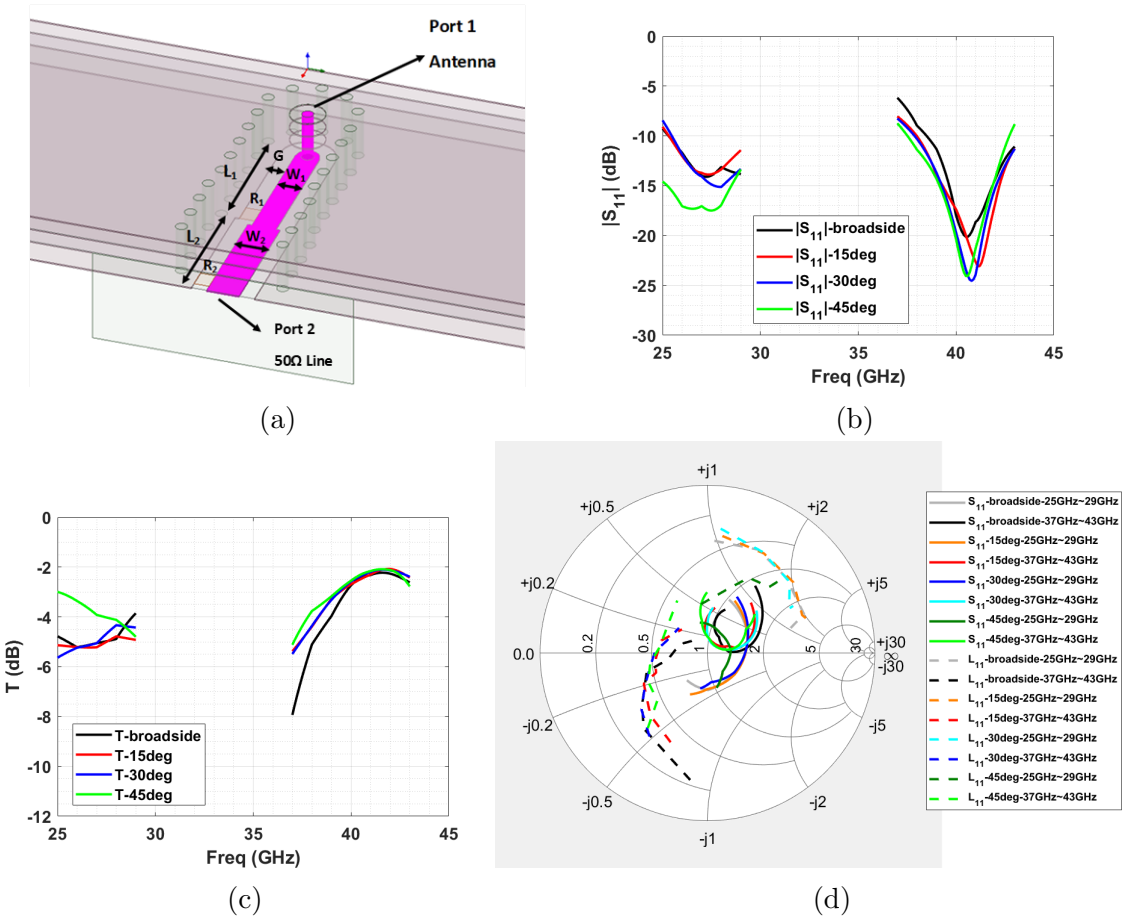


Figure 5.11: The result of the full wave optimization of the 3 stage matching network with lossy junctions at excited port number 3 with optimized parameters: $R_1 = OC, R_2 = 250\Omega, R_3 = 100\Omega, L_1 = 1.63mm, L_2 = 1.63mm, W_1 = 0.32mm, W_2 = 0.43mm, G = 0.2mm$ (a) The structure of the matching network (b) The input reflection coefficient of the matched network. (c) The transmission coefficient of the optimized matching network defined in equation C.1. (d) The smith chart comparing the input reflection coefficient of the antenna (L_{11}) with the input reflection coefficient of the matched network (S_{11}) for different steering angles.

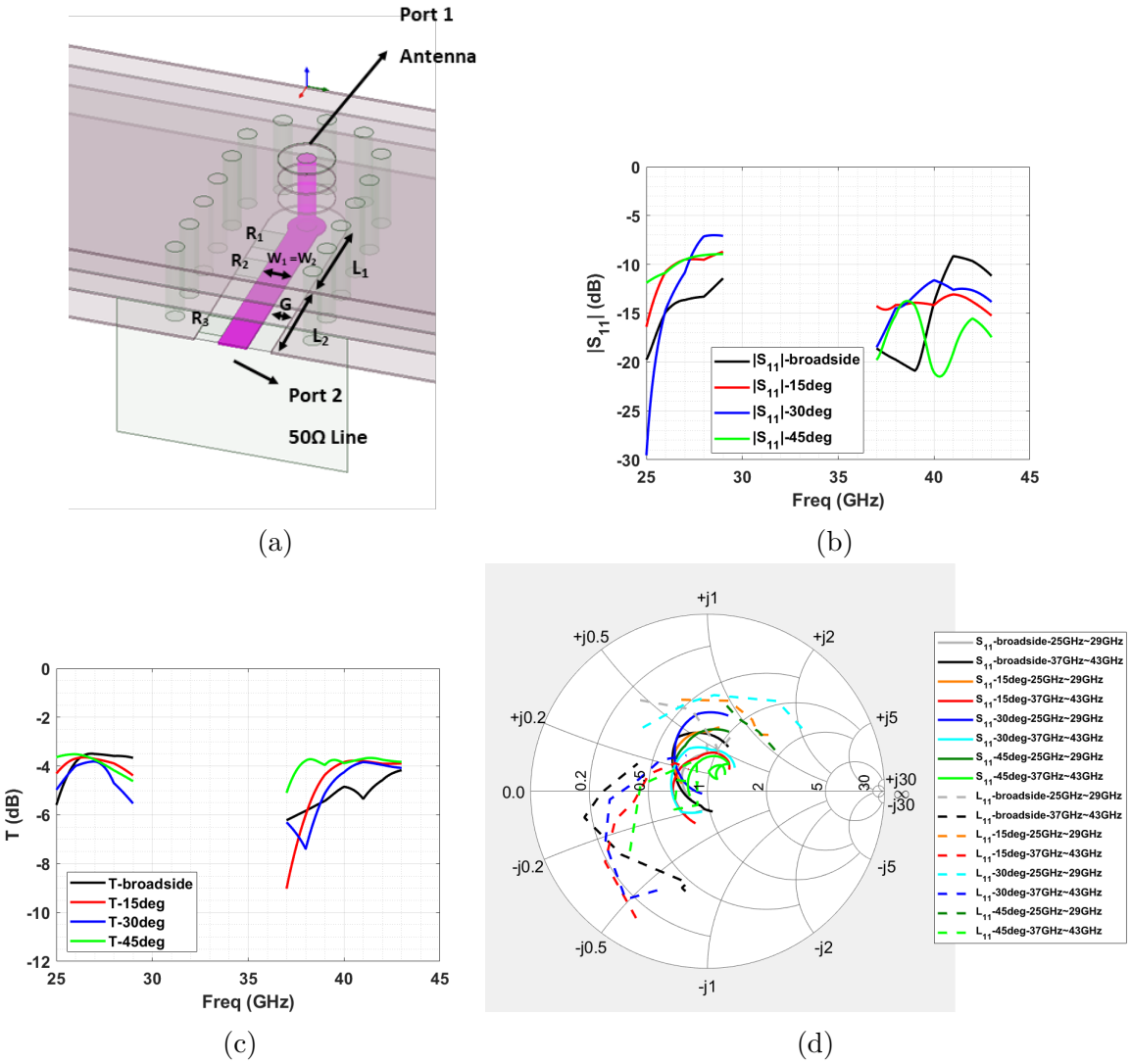


Figure 5.12: The result of the full wave optimization of the 3 stage matching network with lossy junctions at excited port number 28 with optimized parameters: $R_1 = 500\Omega, R_2 = 500\Omega, R_3 = 100\Omega, L_1 = 0.86mm, L_2 = 1mm, W_1 = 0.24mm, W_2 = 0.24mm, G = 0.2mm$ (a) The structure of the matching network (b) The input reflection coefficient of the matched network. (c) The transmission coefficient of the optimized matching network defined in equation C.1. (d) The smith chart comparing the input reflection coefficient of the antenna (L_{11}) with the input reflection coefficient of the matched network (S_{11}) for different steering angles.

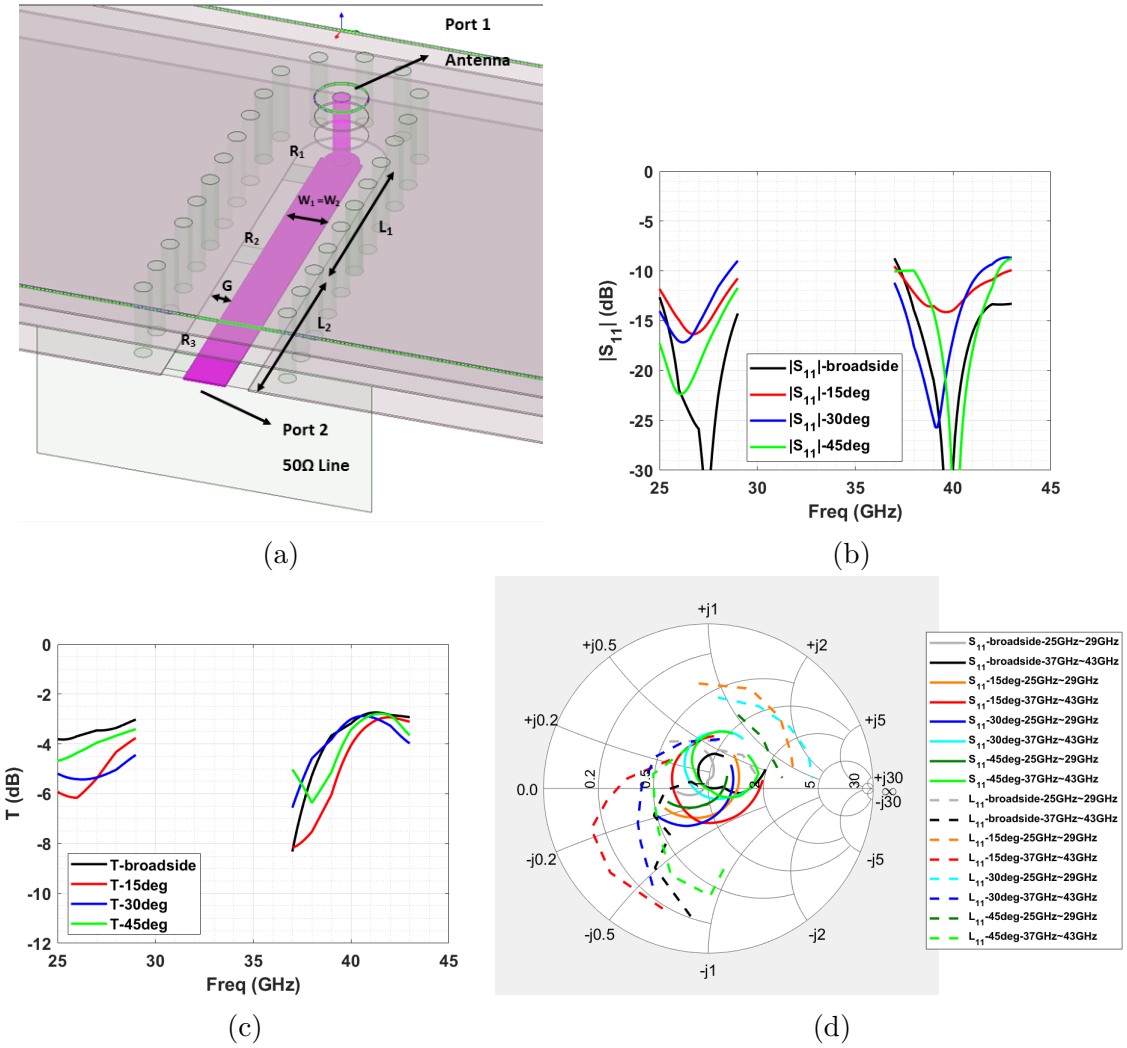


Figure 5.13: The full wave optimization results of the 3 stage distributed matching network with lossy junctions at excited port number 44 with optimized parameters: $R_1 = 500\Omega, R_2 = 500\Omega, R_3 = 100\Omega, L_1 = 1.77mm, L_2 = 1.77mm, W_1 = 0.37mm, W_2 = 0.37mm, G = 0.2mm$ (a) The structure of the matching network (b) The input reflection coefficient of the matched network. (c) The transmission coefficient of the optimized matching network defined in equation C.1. (d) The smith chart comparing the input reflection coefficient of the antenna (L_{11}) with the input reflection coefficient of the matched network (S_{11}) for different steering angles.

5.4 Design of the Feeding Network

In this section, the optimized matching networks are connected to 50Ω GCPW lines and the feeding lines are bent and drawn to the edge of the board where twenty two 50Ω, 2.4mm edge connectors are mounted. Fig. 5.14 shows how the feedlines are connected to the connercors all around the board. At first, each feedline is simulated separately in HFSS and re-optimized if the return loss is not satisfactory. Then, all 22 lines are assembled together and the design shown in Fig. 5.15 is simulated using Ansys HFSS. The impedance matrix of the 44 port structure is extracted. The 22 circular waveports shown in Fig. 5.15d are terminated to the input impedance of the antenna optimized for different frequencies and steering angles in chapter 4 and the input reflection coefficient at 22 ports shown with $\text{Exc}_1, ...\text{Exc}_{22}$ in Fig. 5.15a are calculated at the two frequency bands and for all steering angles. Fig. 5.16 shows the calculated input reflection coefficient obtained from the designed matching network. The results show S_{11} better than -10 dB at the two frequency bands (25 GHz-29 GHz, 37 GHz-43 GHz) and for all beam directions.

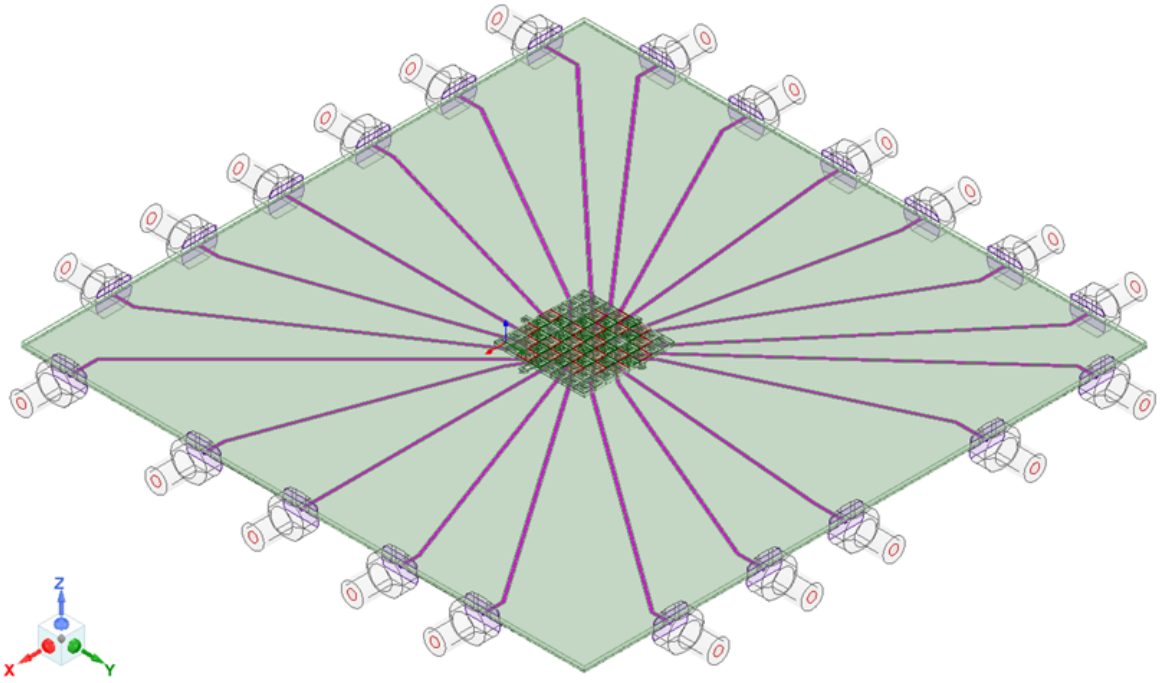


Figure 5.14: A preview of the whole thinned array structure showing the 22 feedlines connected to 22 edge connectors

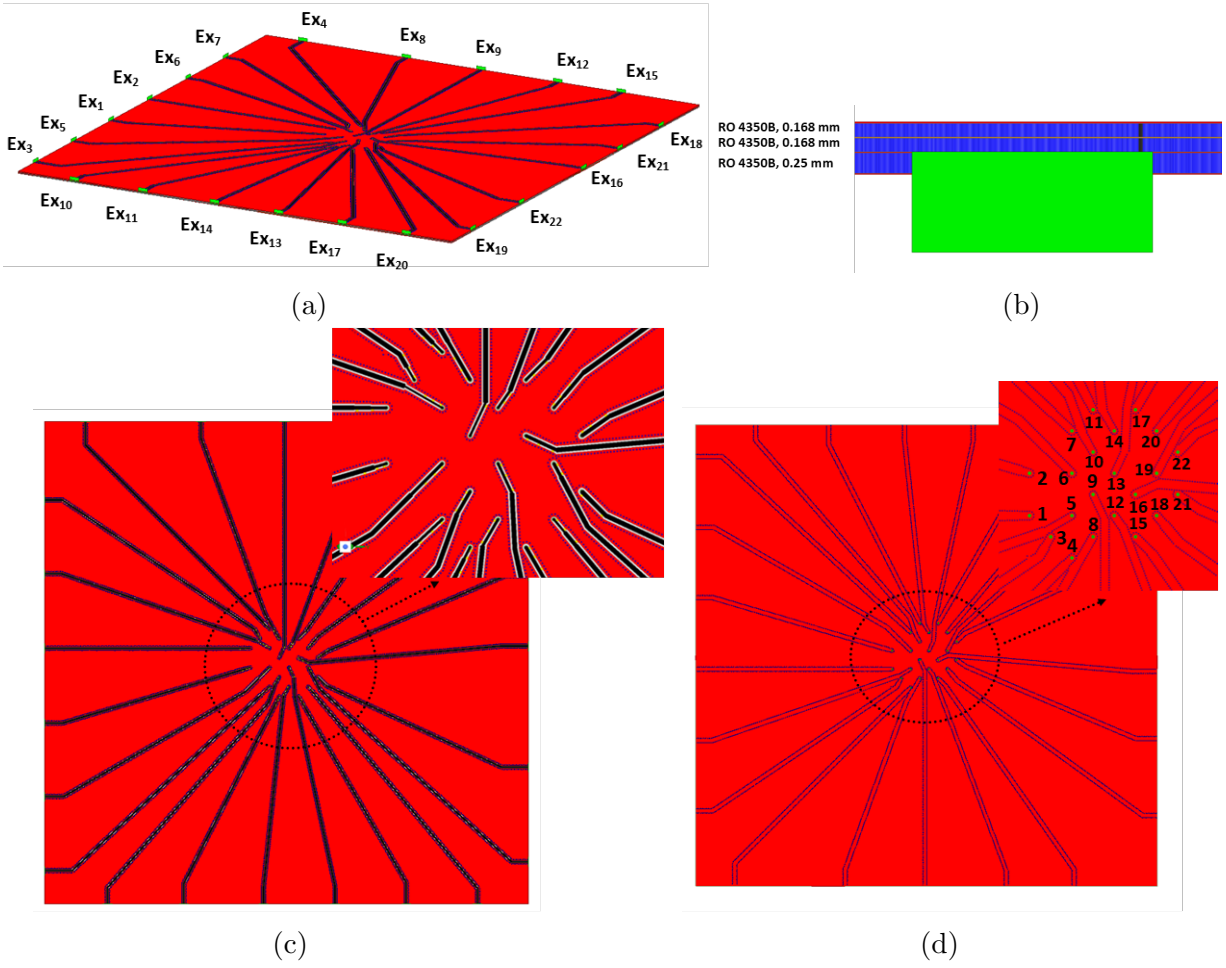


Figure 5.15: Feeding line design (a) 3D view. (b) Side view. (c) Bottomn view showing the GCPW feed lines (d) Top view showing the 22 antenna ports on 3^{rd} layer.

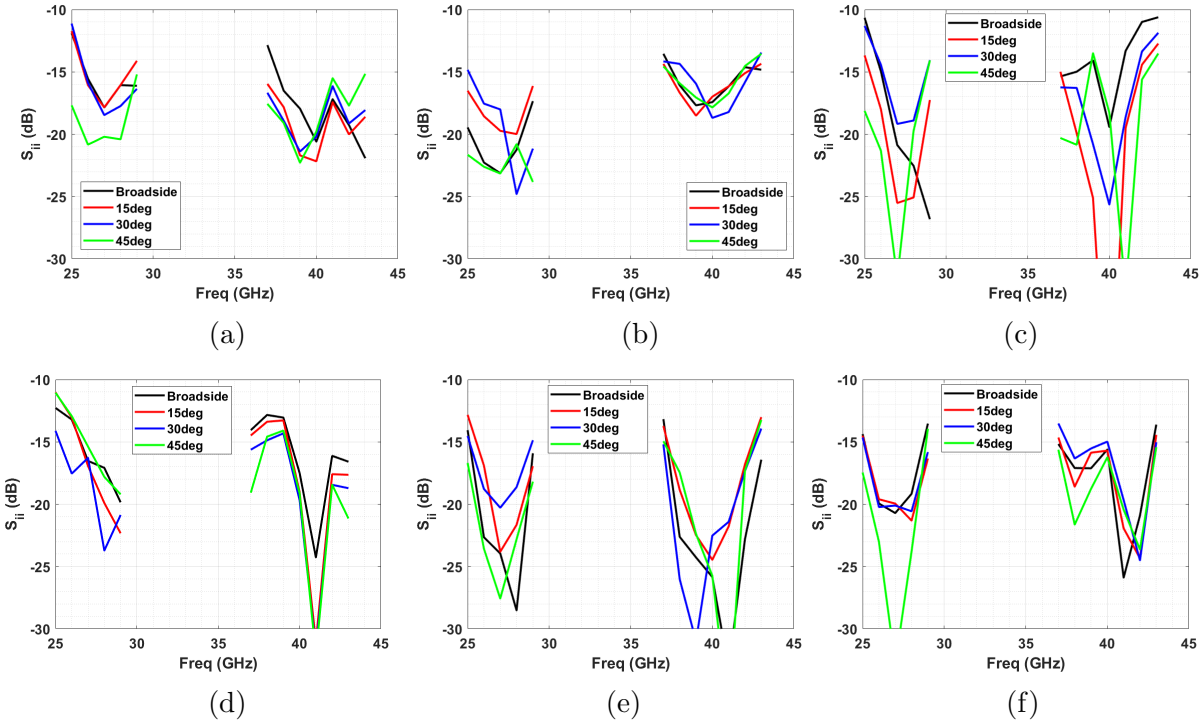


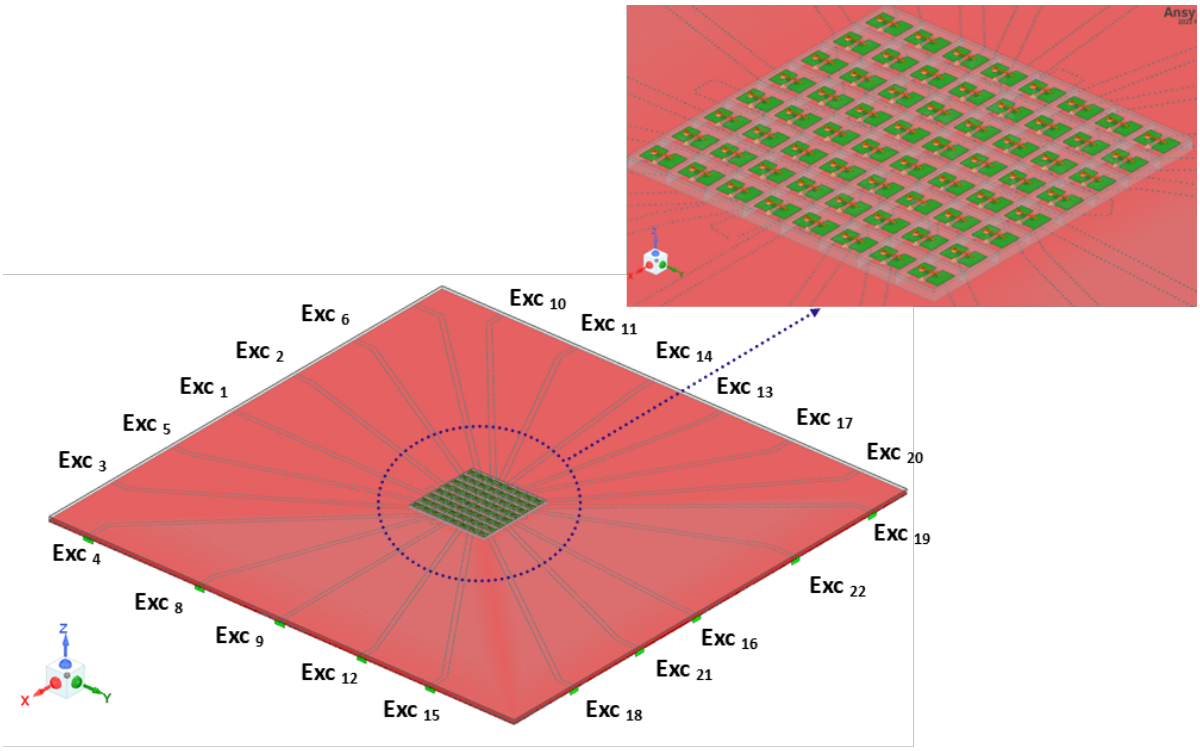
Figure 5.16: The input reflection coefficient of the feeding network design shown in Fig. 5.15 which is connected to the 8×8 thinned antenna array with known optimized voltages and currents on 22 excited ports for the whole frequency bands and steering range (a) at Exited port number 3 (Exc_3 shown in Fig. 5.15a). (b) at Exited port number 23 (Exc_7 shown in Fig. 5.15a). (c) at Exited port number 28 (Exc_9 shown in Fig. 5.15a). (d) at Exited port number 39 (Exc_{14} shown in Fig. 5.15a). (e) at Exited port number 44 (Exc_{16} shown in Fig. 5.15a). (f) at Exited port number 62 (Exc_{22} shown in Fig. 5.15a).

5.5 Thinned 8×8 Tightly Coupled Bowtie Array

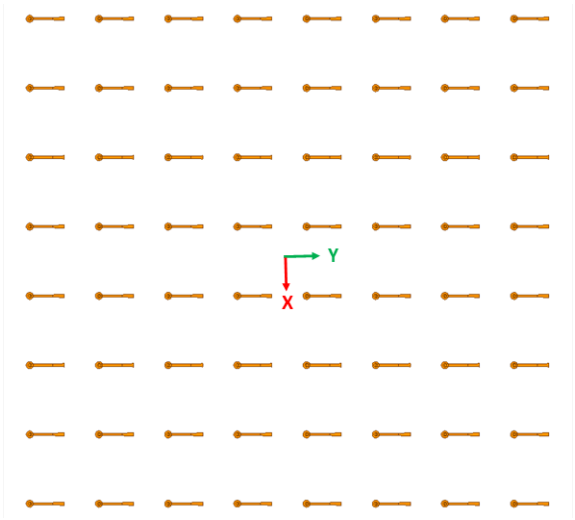
In this section, the whole antenna array structure including realized terminating impedances and feeding networks is simulated using Ansys HFSS software. Fig. 5.17 shows the structure of the thinned array. As shown in Fig. 5.17d, the 20 terminating impedances are rotated to different angles to fit in layer 4 and in order that their resistor and surrounding ground vias (blind vias connecting layer 3 to 6) don't overlap with feedlines on layer 6.

Also, the 22 feedlines are bent and tilted to be drawn to the edge of the board as shown in Fig. 5.17f. The whole antenna board is $150mm \times 150mm \times 1.43mm$. The thinned array is designed in a 6 layer stackup shown in Fig. 5.17e.

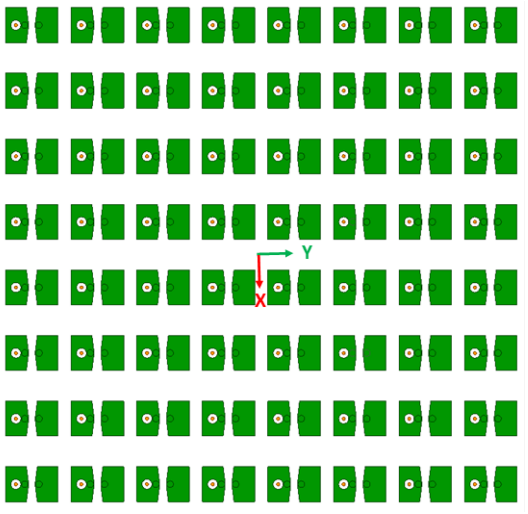
The first layer includes the antenna balun's open stubs. The bowtie antennas are located on second layer. There is a ground layer underneath the antenna on layer 3. The terminating impedances are realized by striplines located on 4th layer. The resistors at the end of the lines are located on 6th layer and are connected to the stripline by a blind via from layer 6 to 4. The 22 feedlines are implemented by GCPW lines on 6th layer. The substrate used is RO4350B with $\epsilon_r = 3.66$ and loss tangant 0.0037. There are totally 79 resistors including twenty one 100Ω, eight 75Ω, thirteen 500Ω, seventeen 150Ω, three 250Ω, eleven 200Ω, and six 330Ω that must be assembled on the last 6th layer.



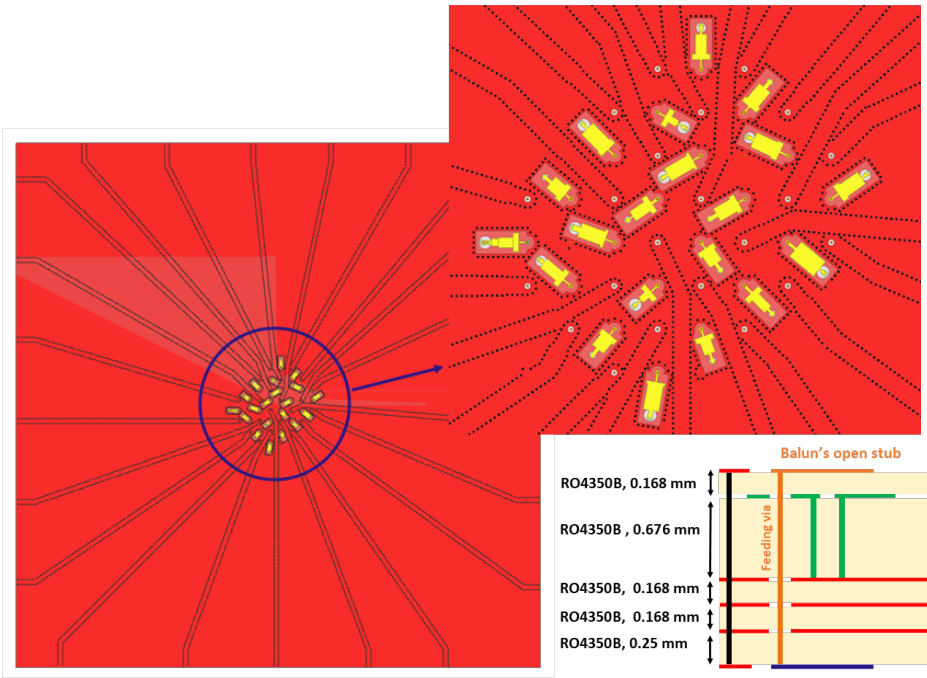
(a)


Y
X

(b)


Y
X

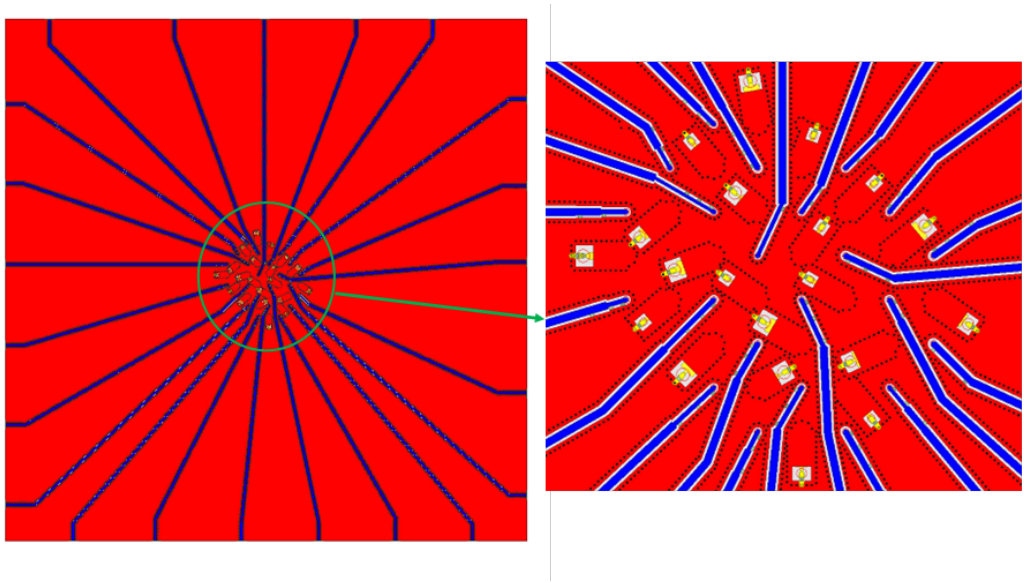
(c)



(d)

Balun's open stub
RO4350B, 0.168 mm
RO4350B , 0.676 mm
RO4350B, 0.168 mm
RO4350B, 0.168 mm
RO4350B, 0.25 mm
Feeding via
Antenna patch
Layer 1
Layer 2
Ground
Layer 4
Ground
Layer 6

(e)



(f)

Figure 5.17: Thinned tightly coupled bowtie array structure (a) 3D view. (b) Top Layer 1. (c) Layer 2. (d) Layer 4. (e) stack up showing all layers. (f) Bottom Layer 6.

5.6 Feed Network Calibration

The antenna array is excited with twenty two 50Ω waveports all around the board as shown in Fig. 5.17a. In order to find proper excitation voltages at the 22 waveports, the effects of the feedlines connecting the antenna ports on layer 3 to the 22 waveports around the board (shown in Fig.5.17a) must be calibrated. For this purpose, the 22 feedlines are simulated in a separate design as shown in Fig. 5.15 and the impedance matrix of the 44 ports structure is extracted for the whole required frequency range. The required voltages and currents on all 22 antenna ports on layer 3 is known to us from the GA optimization described in chapter 4. So, having the voltages and currents on 22 ports of the 44 port structure shown in Fig. 5.15 and by knowing the impedance matrix of this 44 port design, the required voltages and currents on 22 excitation waveports shown in Fig. 5.17a could be calculated.

However, Since the realized terminating impedances are not exactly the same as optimized values, the optimized 22 excitation voltages might not result in exactly the same current distribution on antenna array as before. However, we know that the excitation cur-

rents found on the 22 excited antenna ports produce a satisfactory array factor. Therefore, we can set the excitation currents on 22 antenna ports on layer 3 as known parameters. Please note that the current going into one system is coming out from the connected network; so, the original excitation currents must be multiplied by a -1 factor. Also, the impedance matrix of the whole structure shown in Fig. 5.17a can be extracted from the antenna array simulation ($[Z]^{\text{Thinned}}_{22\times22}$). The impedance matrix of the 44 port structure ($[Z]^{\text{feed}}_{44\times44}$) including 22 feeding lines are also known to us. So, we can find the required excitation voltages ($[V]^{\text{Calibrated}}_{22\times1}$) at the 22 waveports shown in Fig. 5.17a by using equation (5.3). The first 22 ports defined in 44 ports network shown in Fig. 5.15 are the ports excited GCPW feed lines and the second 22 ports are defined as antenna ports on layer 3. The impedance matrix of the 22 feedlines ($[Z]^{\text{feed}}_{44\times44}$) is separated into four 22×22 sub matrices named $[Z]^{\text{feed}^{11}}_{22\times22}, [Z]^{\text{feed}^{12}}_{22\times22}, [Z]^{\text{feed}^{21}}_{22\times22}, [Z]^{\text{feed}^{22}}_{22\times22}$ as seen in equation (5.3). The vectors $[V]^{\text{Exc}}, [I]^{\text{Exc}}$ represents the voltage and currents on 22 antenna ports on layer 3 and $[V]^{\text{Calibrated}}, [I]^{\text{Calibrated}}$ are the required excitation voltages and currents on the 22 waveports exciting GCPW lines on layer 6.

$$
\begin{aligned}
[Z]^{\text{feed}}_{44\times44} &= \begin{bmatrix} [Z]^{\text{feed}^{11}}_{22\times22} & [Z]^{\text{feed}^{12}}_{22\times22} \\ [Z]^{\text{feed}^{21}}_{22\times22} & [Z]^{\text{feed}^{22}}_{22\times22} \end{bmatrix} \\
[ZZ]_{44\times44} &= \begin{bmatrix} [Z]^{\text{Thinned}}_{22\times22} - [Z]^{\text{feed}^{11}}_{22\times22} & [0]_{22\times22} \\ -[Z]^{\text{feed}^{21}}_{22\times22} & \text{diag}([\text{I}])_{22\times22} \end{bmatrix} \\
[CC]_{44\times1} &= \begin{bmatrix} [Z]^{\text{feed}^{12}}_{22\times22} \\ [Z]^{\text{feed}^{22}}_{22\times22} \end{bmatrix} I^{\text{Exc}}_{22\times1} \\
\begin{bmatrix} I^{\text{Calibrated}}_{22\times1} \\ V^{\text{Exc}}_{22\times1} \end{bmatrix} &= [ZZ]^{-1}_{44\times44} [CC]_{44\times1} \\
[V]^{\text{Calibrated}}_{22\times1} &= [Z]^{\text{Thinned}}_{22\times22} [I]^{\text{Calibrated}}_{22\times1}
\end{aligned}
\tag{5.3}
$$

5.7 Simulation Results

Calculating the required excitation voltages and currents on all 22 waveports shown in Fig. 5.17a, the input impedance and the input reflection coefficient at all 22 excited ports would be calculated for all frequencies and steering angles where the GA optimization was carried out. Fig. 5.18 shows S_{11} at few excited port numbers 3,23,28,39,44,62 and for different steering angles. As can be seen, The input reflection coefficient is below -10 dB for most of the desired frequency range and steering angles except at some frequencies near the edge of the frequency bands in which S_{11} goes up to -8 dB.

The thinned antenna array shown in Fig. 5.17 is excited with calibrated excitation voltages $[V]^{\text{Calibrated}}$ at two frequency bands 25 GHz-29 GHz and 37 GHz-43 GHz with 1 GHz frequency step and for broadside radiation, steering to $15^o, 30^o, 45^o$ in E-PLane. Fig. 5.19 to Fig. 5.24, show the simulated normalized directivity in $u-v$ plane rather than in θ, ϕ variables and the directivity in E-Plane at 25 GHz, 27 GHz, 29 GHz, 37 GHz, 40 GHz, and 43 GHz for different steering angles. The $u-v$ coordinates can be derived from θ, ϕ angles by equation (5.4).

$$\begin{aligned} u &= \sin(\theta)\cos(\phi) \\ v &= \sin(\theta)\sin(\phi) \end{aligned} \tag{5.4}$$

The simulated directivity is compared with the directivity of the fully excited array in all these figures. The fully excited array directivity is calculated by having the ideal current distribution on array elements at each frequency and steering angle (obtained by equation 3.5) and the simulated element pattern of the antenna through equations 4.7,4.8. So, the fully excited array directivity shown in Fig. 5.19 to Fig. 5.24 is theoretically calculated without considering any diffraction effects due to corners and edges.

At higher frequency band (37 GHz-43 GHz), as shown in Figs. 5.19,5.20,5.21, the SLL is lower than -13 dB for broadside radiation and it goes up to -8.6 dB when the beam is steered to 45^o in E-Plane. Also, the maximum directivity is dropped by 2 dB-3.5 dB in compare with the the fully excited array. At the lower frequency band (25 GHz-29 GHz), as shown in Figs. 5.22,5.23,5.24 the maximum directivity is dropped by 2.5 dB-5 dB and the SLL is increased to -10.5 dB for broadside and 6dB when the beam is steered to 45^o in E-PLane.

Fig. 5.25a shows the simulated radiation efficiency and the simulated total efficiency including the VSWR mismatch at 22 input ports. As can be seen, the simulated total efficiency is between 0.06-0.21 in the desired frequency bands and steering angles. We will see shortly that the low antenna efficiency is predominantly due to the losses in the wideband matching networks. The simulated total and radiation efficiency are pretty much close which shows there is good antenna matching to 50Ω at 22 input ports. Also, the input reflection coefficients shown in Fig. 5.18 confirms that the VSWR mismatch is satisfactory.

By having the excitation voltages and currents at 22 waveports exciting GCPW lines ($[V]^{\text{Calibrated}}, [I]^{\text{Calibrated}}$), the total incident power exciting the antenna can be calculated as the summation of the real part of complex power provided at each port (shown in equation (5.5)). Also, by having the excitation voltages ($[V]^{\text{Exc}}$) at 22 antenna ports on layer 3 and the realized terminating impedances obtained in section 4.8 by full wave simulation, the current distribution on array elements can be re-calculated by using equations 4.4,4.5,4.6. This new calculated current vector is designated by $[I]^{\text{Realized}}_{64\times 1}$. The power delivered to the

thinned antenna array (with realized terminating impedances) can be calculated by having the voltages and currents on all 22 antenna ports on layer 3 ($P_{\text{delivered}}$ shown in equation (5.5)). Also, the power lost in all resistors used in terminating impedances ($P_{\text{Loss}_{\text{Term}}}$) can be calculated by having the currents on unexcited ports and also their realized resistances as shown in equation (5.5). So, the total efficiency and the efficiency of the matching network excluding the loss in terminating impedances can be calculated separately as below:

$$
\begin{aligned}
P_{\text{inc}} &= \Sigma_{i=1}^{i=22} Re\{\frac{1}{2} V_{\text{Calibrated}}(i) I^{*}_{\text{Calibrated}}(i)\} \\
P_{\text{delivered}} &= \Sigma_{i=1}^{i=22} Re\{\frac{1}{2} V^{\text{Exc}}(i) I^{*\text{Exc}}_{\text{Realized}}(i)\} \\
P_{\text{Loss}_{\text{Term}}} &= \Sigma_{i=1}^{i=20} \frac{1}{2} R(i) |I^{\text{Term}}_{\text{Realized}}(i)|^2 \\
\text{Total efficiency} &= \frac{P_{\text{delivered}} - P_{\text{Loss}_{\text{Term}}}}{P_{\text{inc}}} \\
\text{Matching Network efficiency} &= \frac{P_{\text{delivered}}}{P_{\text{inc}}}
\end{aligned}
\tag{5.5}
$$

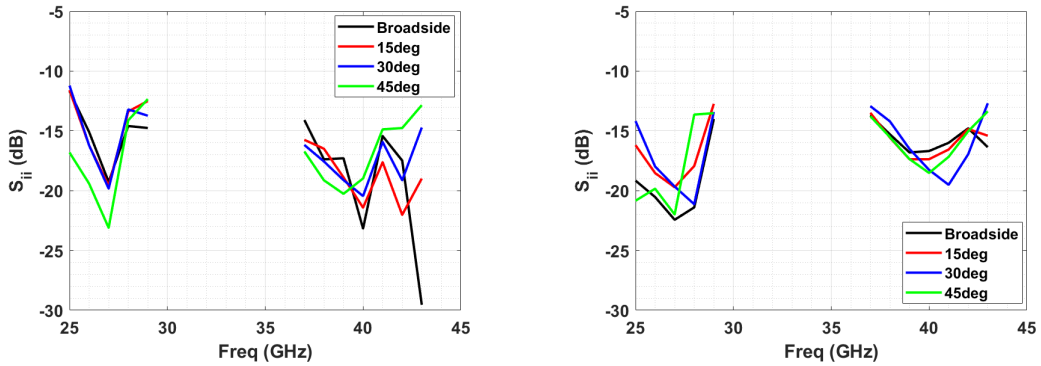
where $I^{\text{Exc}}_{\text{Realized}}(i), I^{\text{Term}}_{\text{Realized}}(i)$ represent the new calculated current vector ($[I]^{\text{Realized}}_{64\times 1}$) at i'th excited and terminated ports respectively. In this current calculation the terminated ports are loaded with realized terminating impedances not the desired terminating impedances obtained by optimization.

The calculated total efficiency agrees well with the simulation results as shown in Fig. 5.25b. However, the calculated values are a bit larger than the simulation results which makes sense because only the losses in matching networks, terminating impedances, and the reflected power due to mismatch are considered in the calculation. However, the dielectric and metal losses are not considered in this calculation which were included in the *simulated* total efficiency in HFSS. Fig. 5.25c compares the total calculated efficiency with the matching network efficiency in which the lost power in terminating impedances are not included. As can be seen, the two efficiencies are pretty much similar which shows that the low efficiency is mainly due to the losses in matching networks. Hence, the lossy terminating impedances has only a minor effect on lowering the efficiency.

5.8 Conclusion

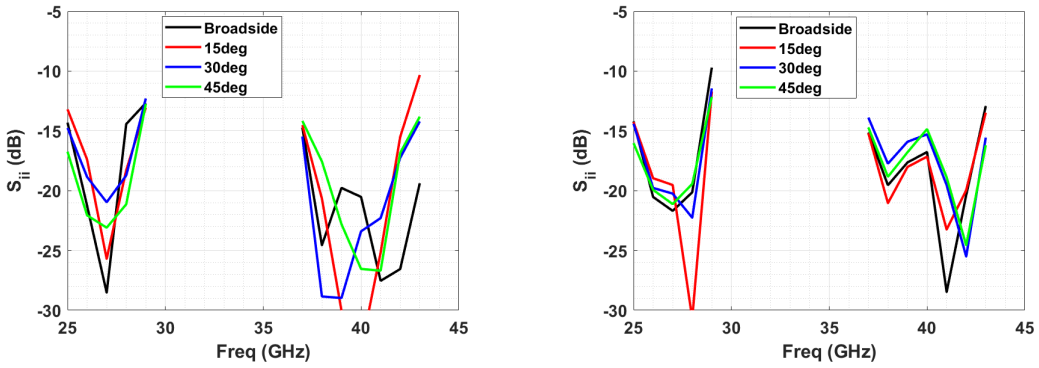
In this chapter, the distributed matching circuit design is optimized through the RFT numerical method, circuit level and full wave simulation. The 22 GCPW feedlines are

designed to connect the matching networks to the input signals all around the board. The designed thinned tightly coupled array is simulated by full wave simulation. The insertion loss of the matching networks and feedlines are calibrated to find the required 22 input excitation voltages. The simulation results show that the circuits realizing the terminating impedances and the designed matching network circuits are providing satisfying pattern, directivity, SLL, and input reflection coefficients in the whole frequency of operation (25-29 GHz, 37-43 GHz) and steering range (up to $\pm 45^o$). However, the antenna efficiency is dropping due to the resistors used in the matching network. In the next chapter, a solution idea to design an efficient, wideband matching circuit will be proposed as the future work.



(a) (b)

(c) (d)



(e) (f)

Figure 5.18: The input reflection coefficient of the simulated 8×8 thinned array shown in Fig. 5.17 at two frequency bands (25-29 GHz, 37-43 GHz) and for steering angles broadside, $15^o, 30^o, 45^o$ in E-Plane at exited port numbers (a) 3. (b) 23. (c) 28. (d) 39. (e) 44. (f) 62.

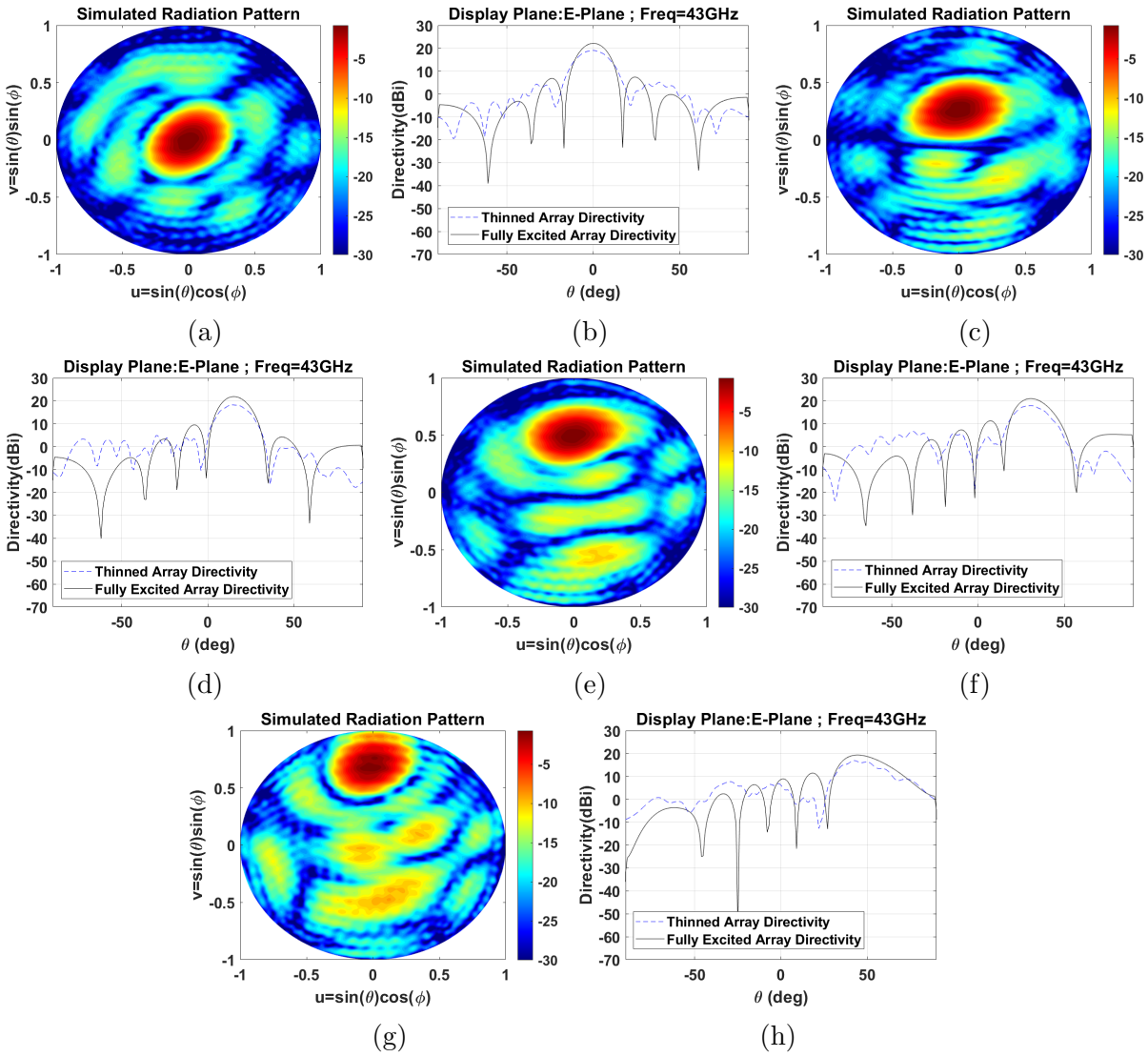


Figure 5.19: Simulated radiation pattern of the thinned array at 43 GHz for (a) broadside radiation. (c) scanned to $\theta = 15^o$ in E-Plane. (e) scanned to $\theta = 30^o$ in E-Plane. (g) scanned to $\theta = 45^o$ in E-Plane. Simulated Directivity of the thinned and fully excited array at 43 GHz for (b) broadside radiation. (d) scanned to $\theta = 15^o$ in E-Plane. (f) scanned to $\theta = 30^o$ in E-Plane. (h) scanned to $\theta = 45^o$ in E-Plane.

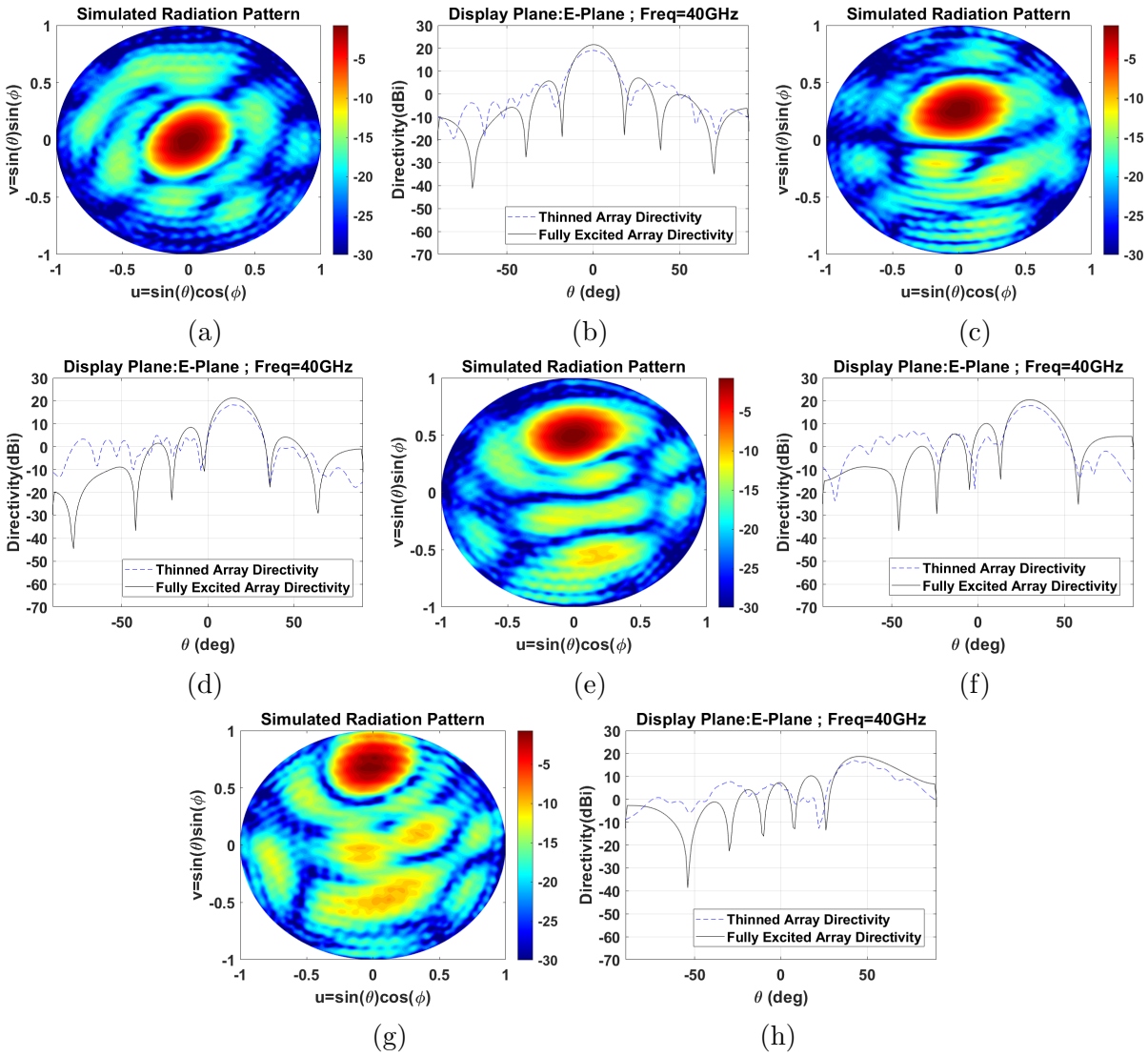


Figure 5.20: Simulated radiation pattern of the thinned array at 40 GHz for (a) broadside radiation. (c) scanned to $\theta = 15^o$ in E-Plane. (e) scanned to $\theta = 30^o$ in E-Plane. (g) scanned to $\theta = 45^o$ in E-Plane. Simulated Directivity of the thinned and fully excited array at 40 GHz for (b) broadside radiation. (d) scanned to $\theta = 15^o$ in E-Plane. (f) scanned to $\theta = 30^o$ in E-Plane. (h) scanned to $\theta = 45^o$ in E-Plane.

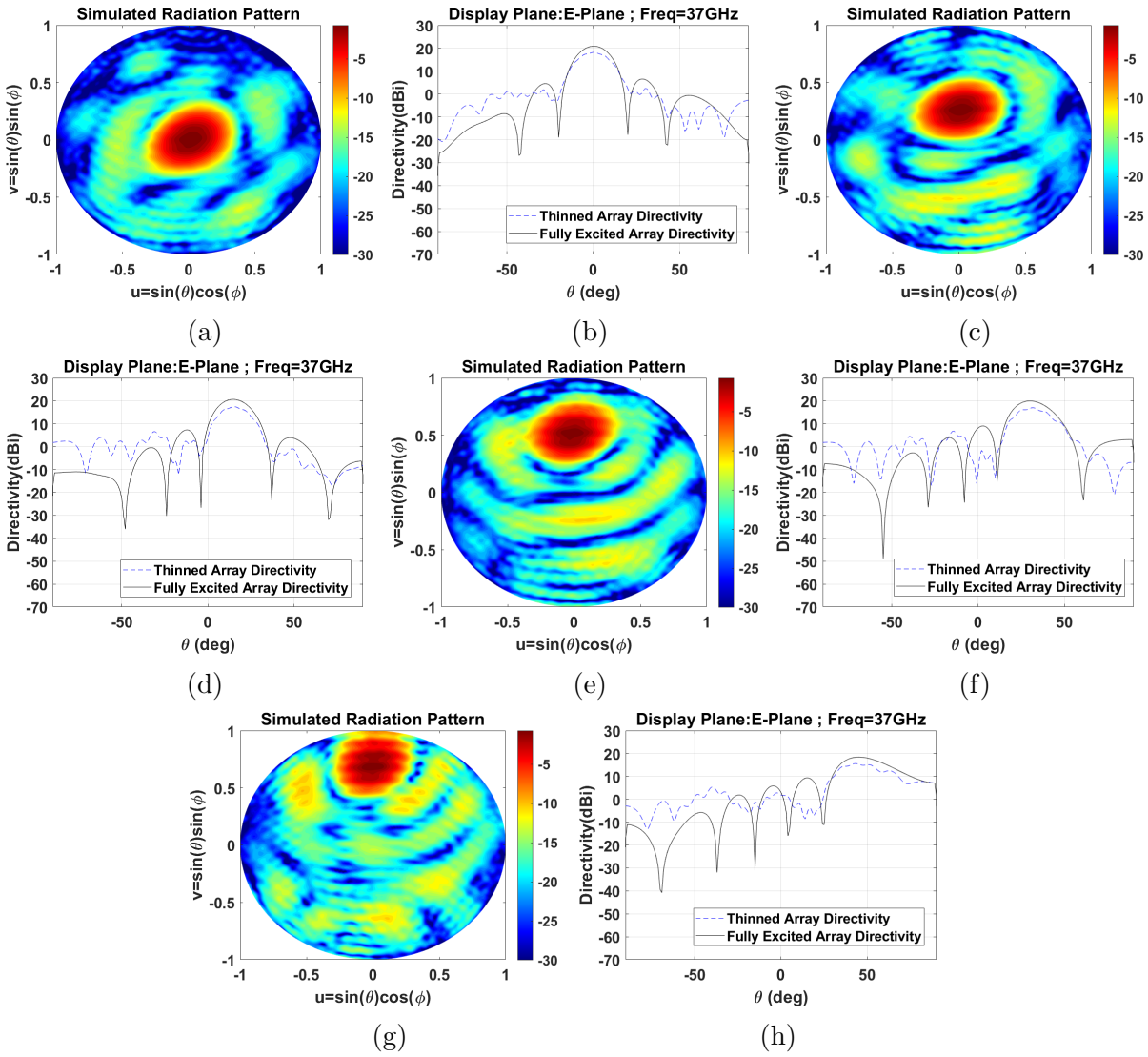


Figure 5.21: Simulated radiation pattern of the thinned array at 37 GHz for (a) broadside radiation. (c) scanned to $\theta = 15^o$ in E-Plane. (e) scanned to $\theta = 30^o$ in E-Plane. (g) scanned to $\theta = 45^o$ in E-Plane. Simulated Directivity of the thinned and fully excited array at 37 GHz for (b) broadside radiation. (d) scanned to $\theta = 15^o$ in E-Plane. (f) scanned to $\theta = 30^o$ in E-Plane. (h) scanned to $\theta = 45^o$ in E-Plane.

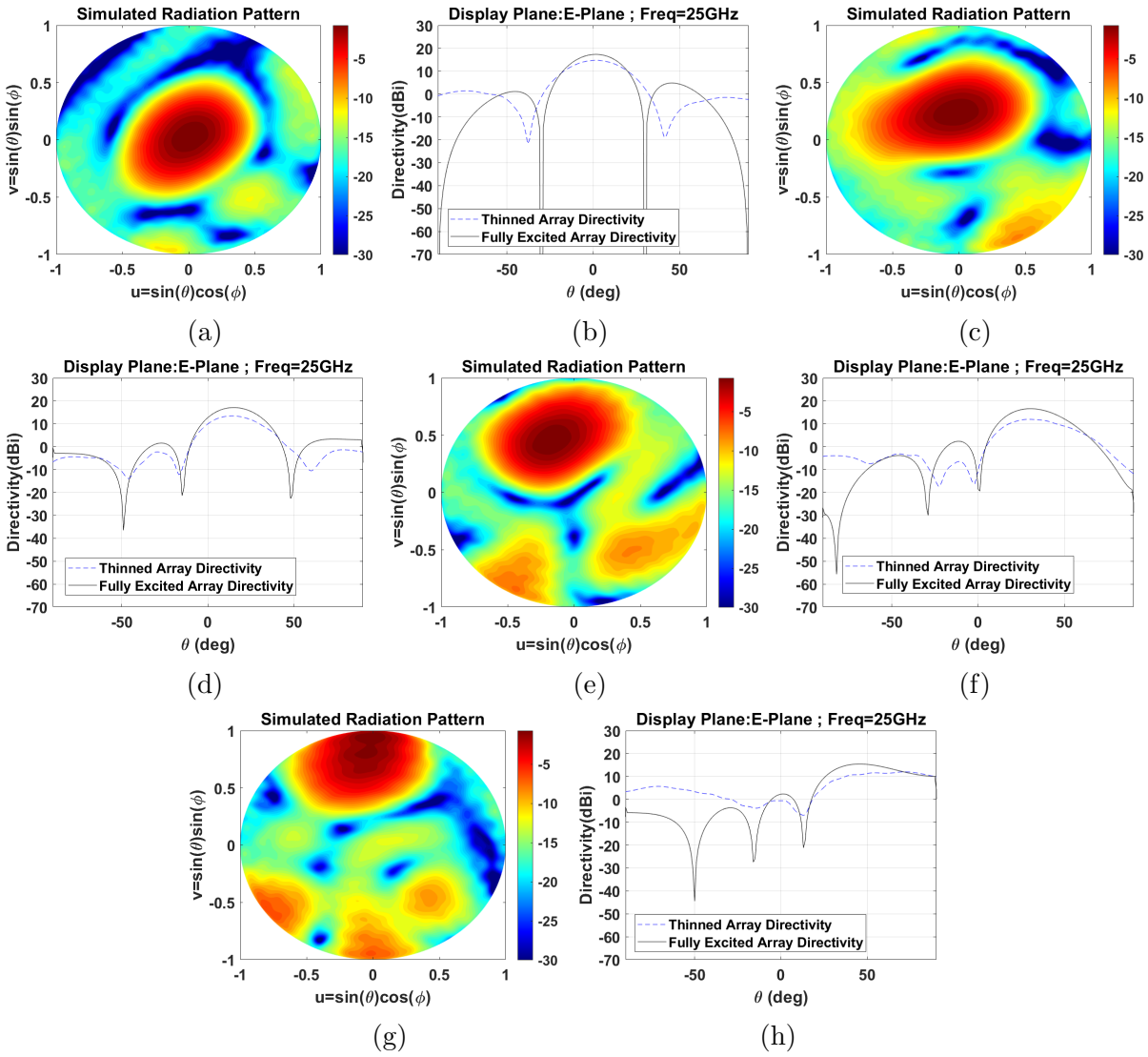


Figure 5.22: Simulated radiation pattern of the thinned array at 25 GHz for (a) broadside radiation. (c) scanned to $\theta = 15^o$ in E-Plane. (e) scanned to $\theta = 30^o$ in E-Plane. (g) scanned to $\theta = 45^o$ in E-Plane. Simulated Directivity of the thinned and fully excited array at 25 GHz for (b) broadside radiation. (d) scanned to $\theta = 15^o$ in E-Plane. (f) scanned to $\theta = 30^o$ in E-Plane. (h) scanned to $\theta = 45^o$ in E-Plane.

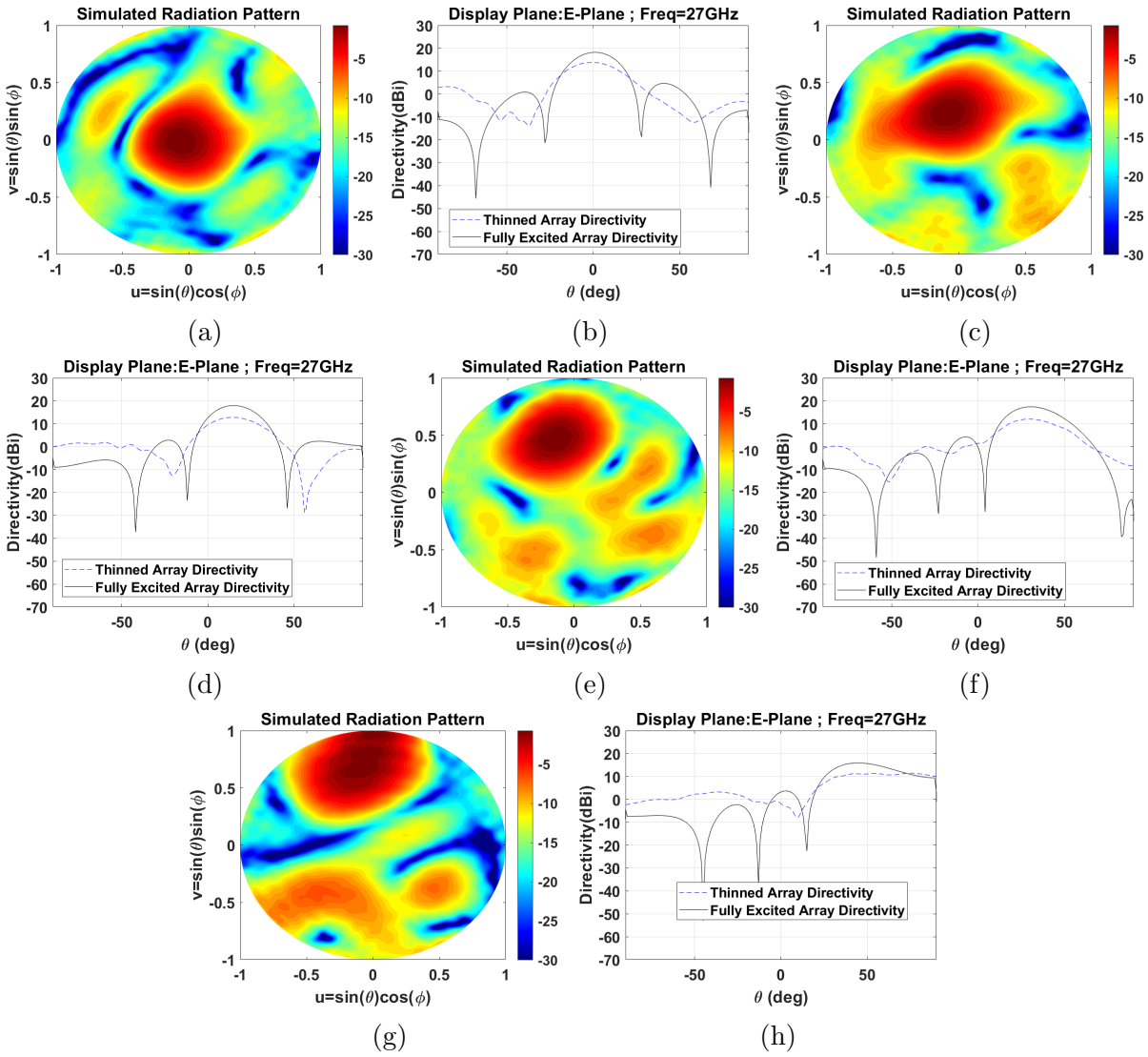


Figure 5.23: Simulated radiation pattern of the thinned array at 27 GHz for (a) broadside radiation. (c) scanned to $\theta = 15^o$ in E-Plane. (e) scanned to $\theta = 30^o$ in E-Plane. (g) scanned to $\theta = 45^o$ in E-Plane. Simulated Directivity of the thinned and fully excited array at 27 GHz for (b) broadside radiation. (d) scanned to $\theta = 15^o$ in E-Plane. (f) scanned to $\theta = 30^o$ in E-Plane. (h) scanned to $\theta = 45^o$ in E-Plane.

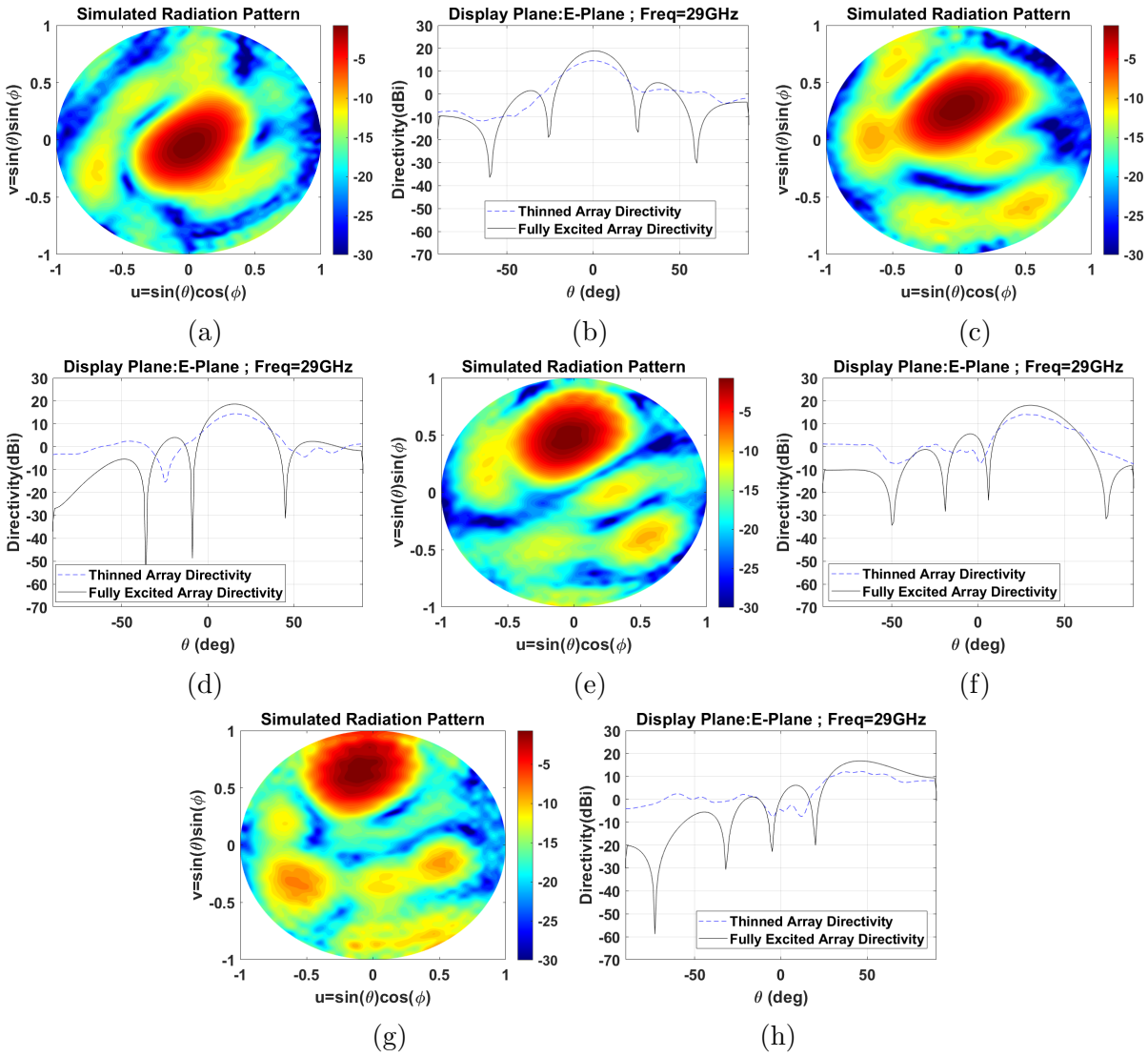


Figure 5.24: Simulated radiation pattern of the thinned array at 29 GHz for (a) broadside radiation. (c) scanned to $\theta = 15^o$ in E-Plane. (e) scanned to $\theta = 30^o$ in E-Plane. (g) scanned to $\theta = 45^o$ in E-Plane. Simulated Directivity of the thinned and fully excited array at 29 GHz for (b) broadside radiation. (d) scanned to $\theta = 15^o$ in E-Plane. (f) scanned to $\theta = 30^o$ in E-Plane. (h) scanned to $\theta = 45^o$ in E-Plane.

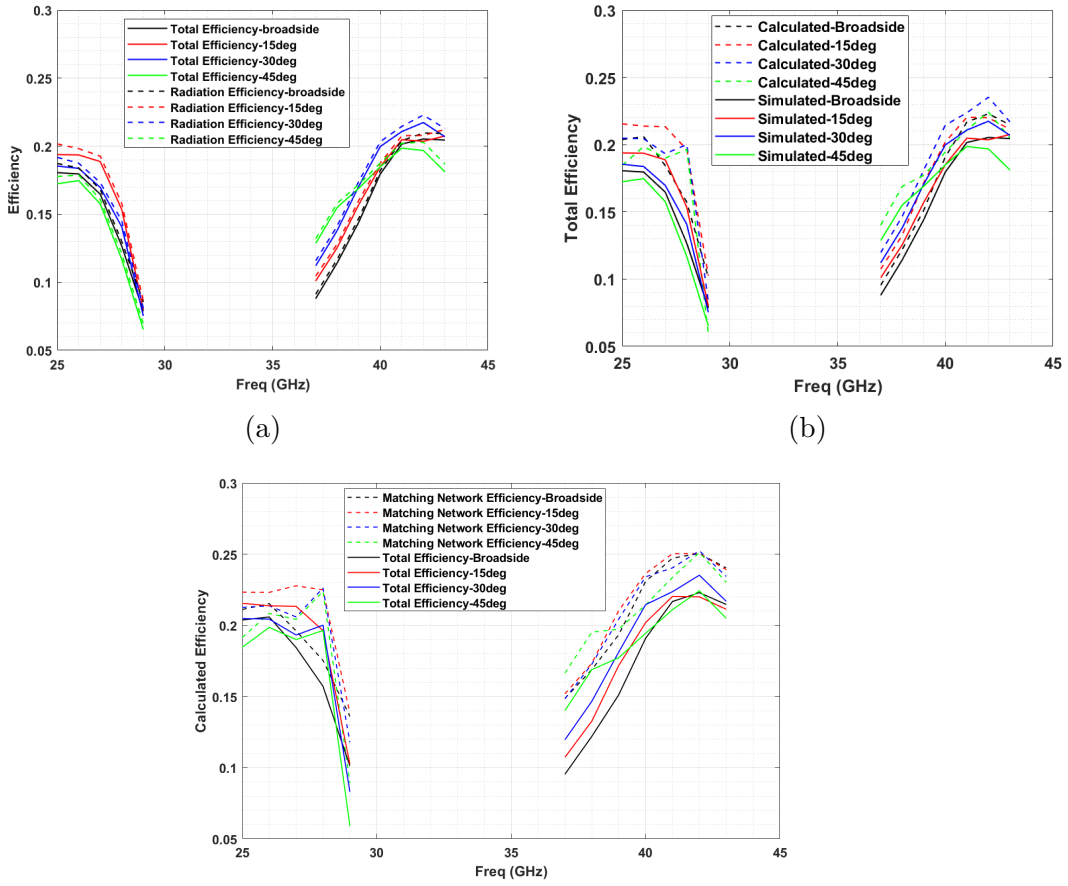


Figure 5.25: The efficiency of the designed thinned array shown in Fig. 5.17 (a) The simulated radiation efficiency and the simulated total efficiency including VSWR mismatch. (b) Simulated and calculated total efficiency. (C) Calculated total efficiency in compare with calculated matching network efficiency.

Chapter 6

Concluding Remarks and Future Works

6.1 Summary and Contribution

The evolution of mobile wireless technology towards the fifth and sixth generations has driven the demand for multi-band antenna arrays that cover the wideband frequency ranges necessary for these systems. Tightly Coupled Antennas (TCAs) are promising candidates for Ultra-Wideband (UWB) applications, particularly where low profile and beam-steering capabilities are crucial. Wheeler demonstrated that an ideal continuous Current Sheet Antenna (CSA) without a ground plane theoretically offers infinite Voltage Standing Wave Ratio (VSWR) bandwidth. The ideal CSA represents a limiting case of many small, closely spaced dipole elements. However, any practical antenna array requires a ground plane to eliminate backward radiation, which inherently limits the bandwidth. In Tightly Coupled Dipole Arrays (TCDAs), strong capacitive coupling among elements compensates for the inductive effects of the nearby ground plane, thereby enhancing the VSWR bandwidth.

While TCDAs can achieve wide input matching, the complexity of the feeding network presents a significant challenge, particularly for small, closely spaced arrays. Each dipole element necessitates a balun to provide balanced feed lines and prevent common mode resonance, which could otherwise restrict the TCDA's wide VSWR bandwidth. Common mode resonance occurs when unbalanced net currents exist on vertical feedlines, necessitating a wideband, low-profile balun for each dipole—especially critical at millimeter-wave frequencies. Wideband Marchand baluns, which use short and open-circuited transmission lines, can offer balanced feeding across a broad frequency range. However, their vertical

through-plane assembly results in a large feeding network beneath the array, which could defeat the low-profile characteristic of TCDAs. A planar wideband Marchand balun was employed in a TCA, though the antenna thickness remained too large for use in most handheld devices like 5G smartphones. As a contribution of this thesis, the planar wideband balun was modified by realizing the balun's open stub with a Grounded Coplanar Waveguide (GCPW) line with lower characteristic impedance [2].

The planar Marchand balun was utilized to design and fabricate a low-profile (6mm×6 mm×1.2mm), wideband, 2×2 tightly coupled bowtie array operating from 25 GHz to 45 GHz, covering the two 5G millimeter-wave frequency bands (24-29 GHz and 37-43 GHz) [4]. In this 2×2 array, half of the elements were designed with different parameters from the others to compensate for the asymmetric excitation port locations, achieving a return loss better than 10 dB at all four ports. The array's maximum gain ranged between 3-6.7 dBi in the targeted frequency range for broadside radiation. The array was fabricated using conventional Printed Circuit Board (PCB) manufacturing methods, and the measurement results correlated well with the simulations.

One of the main challenges in TCDA design is the feeding network and the difficulty of accommodating a large, wideband balun within each small unit cell area. To address this challenge and reduce costs by minimizing the number of required Transceiver (T/R) modules, this thesis explored an approach where only a subset of array elements is excited. The strong mutual coupling in TCAs was leveraged to induce proper currents on unexcited elements, resulting in an antenna pattern that closely resembles a fully excited array's with acceptable radiation characteristics, such as directivity and sidelobe levels (SLL) [6]. By optimizing the excitation voltages and terminating impedances of the unexcited elements, the current distribution on the antenna elements was engineered to achieve satisfactory radiation characteristics.

As a proof of concept, a thinned 8×8 tightly coupled bowtie array was designed with only 22 elements excited, 20 terminated with optimized complex impedances, and the remainder left open-circuited. The excitation voltages and terminating impedances were optimized across the two 5G millimeter-wave frequency bands (25 GHz-29 GHz and 37 GHz-43 GHz) with 1 GHz frequency steps, and for broadside radiation, steering at 15^o, 30^o, and 45^o in the E-plane. The results confirmed that in a thinned TCDA where only a subset of elements is excited, the mutual coupling among elements can maintain satisfactory radiation characteristics across a wide frequency range and steering angles by optimizing all excitation voltages and terminating impedances.

A modified real frequency technique was employed to design a wideband, lossy matching network that matched the input impedance of the thinned array across the two millimeter-

wave 5G frequency bands and the full steering range. Additionally, a distributed circuit consisting of cascaded strip transmission lines terminated with resistors was used to realize the optimized terminating impedances for all 20 ports. The 20 designed terminating impedances, 22 feeding networks, and the 8×8 antenna array were integrated into a 6-layer stack up and simulated using Ansys HFSS software. The simulation results showed that all 20 excited ports were well-matched to 50Ω, with S_{11} below -8 dB across the frequency range and steering angles. However, the losses associated with the wideband matching networks significantly affected the antenna's total efficiency. The maximum directivity dropped by 2 to 3.5 dBi compared to the fully excited array at the 37 GHz-43 GHz frequency band across all steering angles. At the lower frequency band (25 GHz-29 GHz), the maximum directivity drop was between 2.5 to 5 dBi compared to the fully excited array, likely due to deviations from the optimized terminating impedance values at those lower frequencies. The SLL was below -13 dB for broadside radiation and below -8.6 dB when the beam was steered to 45^o in the E-plane at the higher frequency band. At the lower frequency band, these values were -10.5 dB and -6 dB for broadside radiation and a 45^o beam angle, respectively. The final array design, including all dimensions and substrate thicknesses, meets PCB manufacturing tolerances and is ready for fabrication.

6.2 Future Work

The fabrication and measurement of the designed thinned TCA are currently underway. The final stackup, including the bondply layers, is illustrated in Fig. 6.1. For bonding the layers, RO4450T bondply material is used, with a dielectric constant (ϵ_r) of 3.3 and a loss tangent of 0.004. The S-parameter measurement will require twenty-two 2.4mm connectors and twenty-one 50 Ω loads. Additionally, a beamformer or a cascade of beamformers with 22 transmitting ports across two frequency bands will be necessary to apply the optimized excitation voltages to all ports.

For this purpose, the Analog Devices beamformer evaluation boards ADMV4928 (covering 37-43.5 GHz) and ADMV4828 (covering 24-29.5 GHz) are suitable, as they each support 16 dual-polarized (8 vertical, 8 horizontal) T/R channels. To achieve the required number of channels, two boards can be cascaded by employing a 1:4 splitter, with the splitter's outputs connected to the RFV and RFH input ports on each evaluation board, as depicted in Fig. 6.2. However, due to potential discrepancies between the two boards, they must be calibrated individually before cascading.

Each transmit and receive channel on these boards includes a Vector Modulator (VM) for phase control and two Digital Variable Gain Amplifier (DVGA) for amplitude control.

The VM allows for a full 360° phase adjustment in both transmit and receive modes, providing 6-bit resolution with 5.625° phase steps. The total DVGA dynamic range in transmit mode is 34.5 dB, sufficient for our requirements (the required dynamic range for the designed thinned array is calculated to be 30.48 dB). The DVGA also offers 6-bit resolution for 0.5 dB amplitude steps and 5-bit resolution for 1 dB amplitude steps. The block diagram of the ADMV4928 beamformer is shown in Fig. 6.2.

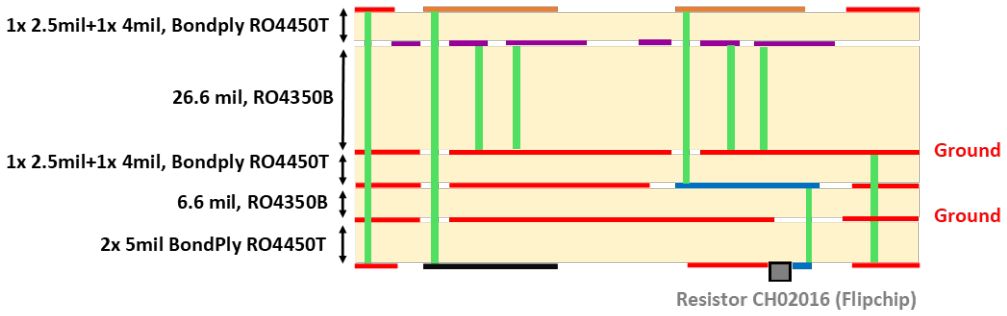


Figure 6.1: The stackup of the structure including 4450T bondply layers.

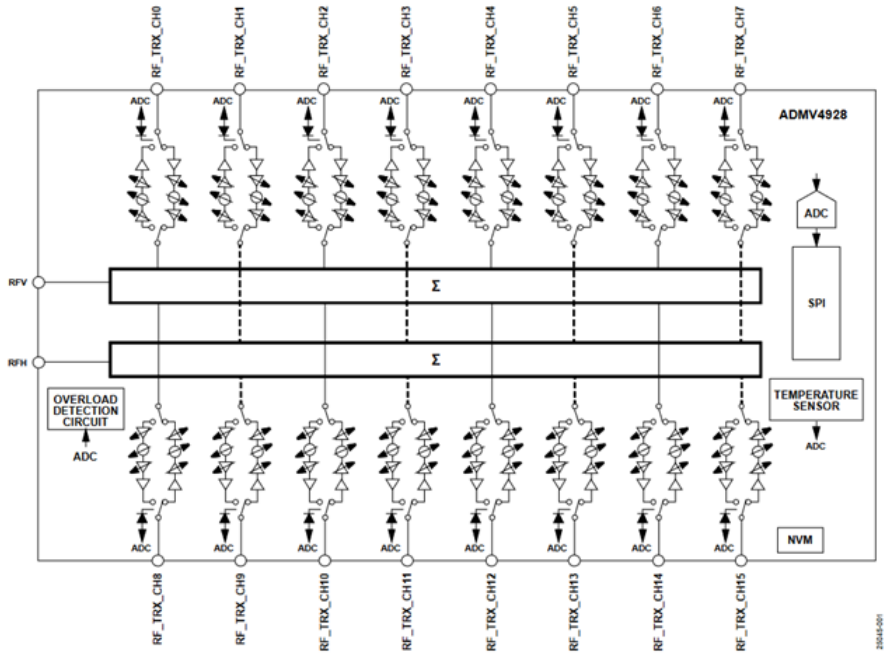


Figure 6.2: The building block of beamformer Eval board ADMV4928 from Analog Device.

Another aspect that needs more work is to minimize the loss of the system and increase the antenna efficiency as a result. In section 5.7, it was shown that the low efficiency is mostly due to the loss in matching networks. The loss in terminating impedances has only a very small effect in lowering the efficiency as shown in Fig. 5.25c. So, a low loss, multiband matching network would significantly increase the thinned array efficiency. One solution for this could be reconfigurable matching networks based on RF-Micro Electronic Mechanical Systems (MEMS) technology [58],[59],[60]. By this technique we can switch between two switched capacitors' states for matching the two frequency bands separately; so, we don't need a wideband matching network at each band and we can design each frequency bands with a low loss or even lossless network.

The phase velocity and impedance of a transmission line can be changed by capacitive loading [59]. This loaded-line technique in which a transmission line is loaded with N-switched MEMS capacitors can be used in the design of reconfigurable matching networks [59],[61],[62],[63]. The impedance of the transmission line can be controlled by switching the MEMS capacitors between two states C_U (up state) and C_D (down state). When all switched capacitors are in up states, the line impedance is 50Ω; however, by increasing

the loading capacitance in down state, the line impedance can be transformed to a very low impedance and its effective dielectric constant will be increased [59]. Basically, as the number of loaded switched capacitors increases, the more wideband matching and better smith chart coverage would be achieved. On the other side, the size and loss of the structure would be increased by increasing the number of loading capacitors. so, an optimized number of switches must be selected [59]. One of the challenges with this MEMS switches is that they have to be mounted on the last bottom layer of the stackup where all feedlines are located; so, fitting all these components and their integration with the rest of the circuit might be challenging.

Another area that is interesting to be addressed in future is making the antenna array dual-polarized (Vertical and Horizontal) and extending the frequency range to a third band by covering the third 5G mm-Wave frequency band (57 GHz-71 GHz). As part of this research, a combination of slot creation and stacking approach was employed to design a dual-polarized, triple band antenna element [6] (shown in Fig. 6.3) covering the three 5G mm-Wave frequency bands (25-29 GHz, 37-43 GHz, 57-71 GHz); however, this design still requires more optimization. The slots used on the patch prolong the current path and create some resonances at lower frequencies. Also, a resonant patch is stacked on top of the antenna element at distance 0.12mm from the antenna to produce resonances at another frequency band. Note that only the antenna element on layer 1 is excited and the one on layer 2 is only a parasitic element. Also, the UWB antenna element designed in section 3.1.2 can be easily made dual-polarized. Another layer will be required for the balun's open stub and/or the antenna patch for adding another polarization. Adding more layers to the stackup will results in more blind and burried vias which may complicate the fabrication process. In the case of dual-polarized array, the thinned array optimization must be done for each polarization separately.

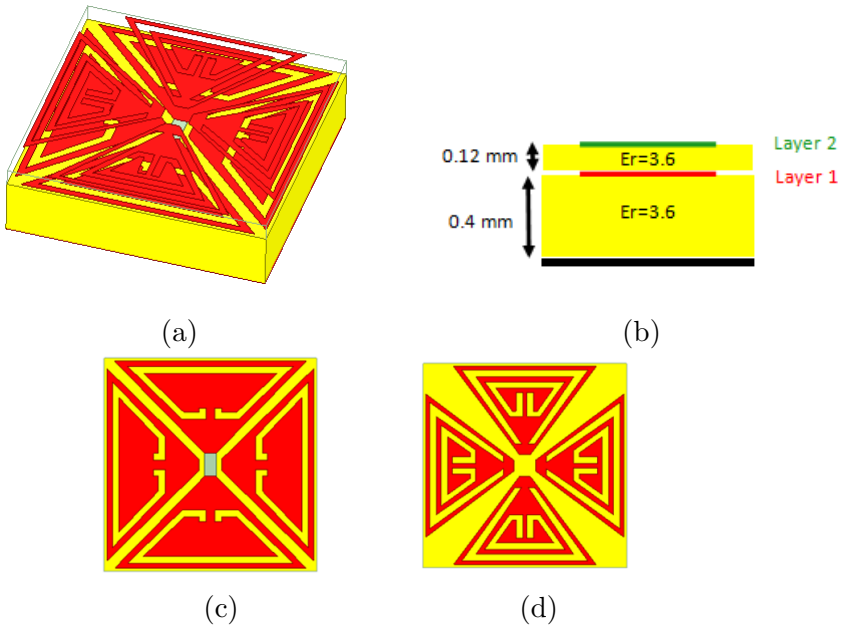


Figure 6.3: The dual-polarized, triple-band antenna element [6]. (a) 3D view (b) side view (c) layer 1 showing the antenna element (d) layer 2 showing the resonant patch

Another area that could be investigated more is optimization of of the thinned array. So far, the 8×8 antenna array is simulated separately to extract the impedance matrix, then the impedance matrix of the antenna is used in calculating the current distribution on the array and optimizing the excitation voltages and terminating impedances. Now, that the terminating loads are optimized and realized with a practical circuit. The 8×8 array can be simulated again while the *realized* loads attached to the terminated ports and a new impedance matrix could be extracted. The new $[Z]$ matrix could be used to re-optimize the excitation voltages. This iteration can further close the gap between the ideal (fully excited array) and the thinned array performance in terms of directivity and SLL.

Another area for further research is to have a new wideband antenna element design or another array design that can increase the mutual coupling among elements. For example, the coupling between two neighbouring bowtie elements in E-Plane could be increased by making the interdigital capacitors on bowtie ends. The thinned tightly coupled idea is based on the strong couplings and it's been shown in Appendix A, as stronger couplings are provided, the more surprising results would be achieved. Also, making a larger array with more degrees of freedom can help to get better optimization results. Additionally, the

scheme of excitation plays a huge role in the final array performance. A global optimization method like GA or Simulated Annealing might help to find a better scheme of excitation.

References

[1] M. H. Novak, J. L. Volakis, and F. A. Miranda, "24–71 ghz pcb array for 5g/ism," in *2017 IEEE International Symposium on Antennas and Propagation USNC/URSI National Radio Science Meeting*, pp. 1465–1466, 2017.

[2] N. Rahmati, A. Borji, and S. Safavi-Naeini, "A thin planar ultra-wideband antenna element for tightly coupled mm-wave phased arrays," in *2022 IEEE International Symposium on Antennas and Propagation and USNC-URSI Radio Science Meeting (AP-S/URSI)*, pp. 1902–1903, 2022.

[3] M. H. Novak, F. A. Miranda, and J. L. Volakis, "Ultra-wideband phased array for millimeter-wave ism and 5g bands, realized in pcb," *IEEE Transactions on Antennas and Propagation*, vol. 66, no. 12, pp. 6930–6938, 2018.

[4] N. Rahmati and A. Borji, "A wideband, low profile antenna array for mm-wave 5g applications," in *2024 IEEE International Symposium on Antennas and Propagation and USNC-URSI Radio Science Meeting (AP-S/URSI)*, 2024.

[5] C. Wang, Y. He, and C. Qi, "Analysis of grating lobe effects on geo dsc distributed antennas," *Applied Sciences*, vol. 13, no. 19, 2023.

[6] A. Borji, N. Rahmati, P. Chun, P. Chen, L. Liu, X. Wang, and S. Safavi-Naeini, "Tightly-coupled antenna array and methods thereof," World Intellectual Property Organization (WIPO) WO2023245274, Dec. 28 2023.

[7] R. Kindt and R. Pickles, "12-to-1 bandwidth all-metal vivaldi array element," in *2009 IEEE Antennas and Propagation Society International Symposium*, pp. 1–4, 2009.

[8] D. Schaubert and T. Chio, "Wideband vivaldi arrays for large aperture antennas," vol. -1, p. 49, 01 2000.

[9] D. H. Schaubert, A. Boryssenko, M. N. Vouvakis, G. Paraschos, W. Elsallal, and S. Kasturi, "Wide bandwidth arrays of vivaldi antennas," in *2008 Institution of Engineering and Technology Seminar on Wideband, Multiband Antennas and Arrays for Defence or Civil Applications*, pp. 1–20, 2008.

[10] H. Holter, "Dual-polarized broadband array antenna with bor-elements, mechanical design and measurements," *IEEE Transactions on Antennas and Propagation*, vol. 55, no. 2, pp. 305–312, 2007.

[11] J. Lee, S. Livingston, and R. Koenig, "A low-profile wide-band (5:1) dual-pol array," *IEEE Antennas and Wireless Propagation Letters*, vol. 2, pp. 46–49, 2003.

[12] J. Langley, P. Hall, and P. Newham, "Balanced antipodal vivaldi antenna for wide bandwidth phased arrays," 1996.

[13] M. Elsallal and D. Schaubert, "Electronically scanned arrays of dual-polarized, doubly-mirrored balanced antipodal vivaldi antennas (dmbava) based on modular elements," in *2006 IEEE Antennas and Propagation Society International Symposium*, pp. 887–890, 2006.

[14] S. S. Holland and M. N. Vouvakis, "The banyan tree antenna array," *IEEE Transactions on Antennas and Propagation*, vol. 59, no. 11, pp. 4060–4070, 2011.

[15] M. W. Elsallal, "Doubly-mirrored balanced antipodal vivaldi antenna (dmbava) for high performance arrays of electrically short, modular elements," 2008.

[16] W. F. Moulder, K. Sertel, and J. L. Volakis, "Superstrate-enhanced ultrawideband tightly coupled array with resistive fss," *IEEE Transactions on Antennas and Propagation*, vol. 60, pp. 4166–4172, Sep. 2012.

[17] J. A. Kasemodel, C. Chen, and J. L. Volakis, "Wideband planar array with integrated feed and matching network for wide-angle scanning," *IEEE Transactions on Antennas and Propagation*, pp. 4528–4537, Sep. 2013.

[18] J. Shim, J. Go, and J. Chung, "A 1-d tightly coupled dipole array for broadband mmwave communication," *IEEE Access*, vol. 7, pp. 8258–8265, 2019.

[19] M. H. Novak, F. A. Miranda, and J. L. Volakis, "Ultra-wideband phased array for small satellite communications," *IET Microwaves, Antennas Propagation*, vol. 11, no. 9, pp. 1234–1240, 2017.

[20] M. H. Novak, F. A. Miranda, and J. L. Volakis, "An ultra-wideband millimeter-wave phased array," in *2016 10th European Conference on Antennas and Propagation (EuCAP)*, pp. 1–3, April 2016.

[21] H. Wheeler, "Simple relations derived fom a phased-array antenna made of an infinite current sheet," *IEEE Transactions on Antennas and Propagation*, vol. 13, pp. 506–514, July 1965.

[22] L. Stark, "Radiation impedance of a dipole in an infinite planar phased array," *Radio Science*, vol. 1, no. 3, pp. 361–377, 1966.

[23] B. A. Munk, *Frequency selective surfaces: theory and design.* John Wiley & Sons, 2005.

[24] B. A. Munk, *Broadband Wire Arrays*, pp. 181–213. 2003.

[25] M. Jones and J. Rawnick, "A new approach to broadband array design using tightly coupled elements," in *MILCOM 2007 - IEEE Military Communications Conference*, pp. 1–7, 2007.

[26] Y. Zhou, F. Zhu, S. Gao, Q. Luo, L. Wen, Q. Wang, X. Yang, Y. Geng, and Z. Cheng, "Tightly coupled array antennas for ultra-wideband wireless systems," *IEEE Access*, vol. 6, pp. 61851–61866, 2018.

[27] B. Munk, R. Taylor, T. Durharn, W. Croswell, B. Pigon, R. Boozer, S. Brown, M. Jones, J. Pryor, S. Ortiz, J. Rawnick, K. Krebs, M. Vanstrum, G. Gothard, and D. Wiebelt, "A low-profile broadband phased array antenna," in *IEEE Antennas and Propagation Society International Symposium. Digest. Held in conjunction with: USNC/CNC/URSI North American Radio Sci. Meeting (Cat. No.03CH37450)*, vol. 2, pp. 448–451 vol.2, June 2003.

[28] S. S. Holland and M. N. Vouvakis, "The planar ultrawideband modular antenna (puma) array," *IEEE Transactions on Antennas and Propagation*, vol. 60, pp. 130–140, Jan 2012.

[29] J. P. Doane, K. Sertel, and J. L. Volakis, "A wideband, wide scanning tightly coupled dipole array with integrated balun (tcda-ib)," *IEEE Transactions on Antennas and Propagation*, vol. 61, pp. 4538–4548, Sep. 2013.

[30] N. Marchand, "Transmission-line conversion transformers," *Electronics*, vol. 17, pp. 142–145, Dec 1944.

[31] W. R. Pickles, "Double balun dipole," U.S. Patent US 8,350,774 B2, Jan 2013.

[32] D. Cavallo, A. Neto, and G. Gerini, "Pcb slot based transformers to avoid common-mode resonances in connected arrays of dipoles," *IEEE Transactions on Antennas and Propagation*, vol. 58, no. 8, pp. 2767–2771, 2010.

[33] E. Yetisir, N. Ghalichechian, and J. L. Volakis, "Ultrawideband array with 70° scanning using fss superstrate," *IEEE Transactions on Antennas and Propagation*, vol. 64, no. 10, pp. 4256–4265, 2016.

[34] I. Tzanidis, K. Sertel, and J. L. Volakis, "Interwoven spiral array (ispa) with a 10:1 bandwidth on a ground plane," *IEEE Antennas and Wireless Propagation Letters*, vol. 10, pp. 115–118, 2011.

[35] M. A. Elmansouri, G. R. Friedrichs, L. B. Boskovic, and D. S. Filipovic, "An x-band through ka-band thinned all-metal vivaldi phased array," *IEEE Transactions on Antennas and Propagation*, vol. 69, no. 11, pp. 7613–7623, 2021.

[36] G. S.K.Gayatri Devi, G. Raju, and P. Sridevi, "Application of genetic algorithm for reduction of sidelobes from thinned arrays," *Advances in Modelling and Analysis B*, vol. 58, pp. 35–52, 01 2015.

[37] P. Das and J. Roy, "Thinning of elliptical antenna arrays using genetic algorithm," *Int. Journal of Engineering Research and Applications (IJERA),*, vol. 4, pp. 225–229, 04 2014.

[38] M. Ortiz, M. N. Uddin, M. R. Guerra, and E. A. Alwan, "Enhancing gain through optimal antenna element distribution in a thinned array configuration," *IEEE Open Journal of Antennas and Propagation*, vol. 4, pp. 1176–1186, 2023.

[39] E. Sharp, "A triangular arrangement of planar-array elements that reduces the number needed," *IRE Transactions on Antennas and Propagation*, vol. 9, no. 2, pp. 126–129, 1961.

[40] S. Karademir, O. Prokopyev, and R. Mailloux, "Irregular polyomino tiling via integer programming with application in phased array antenna design," *Journal of Global Optimization*, vol. 65, 09 2015.

[41] T. G. Spence and D. H. Werner, "Design of broadband planar arrays based on the optimization of aperiodic tilings," *IEEE Transactions on Antennas and Propagation*, vol. 56, no. 1, pp. 76–86, 2008.

[42] Y. Ma, S. Yang, Y. Chen, S.-W. Qu, and J. Hu, "Sparsely excited tightly coupled dipole arrays based on irregular array techniques," *IEEE Transactions on Antennas and Propagation*, vol. 68, no. 8, pp. 6098–6108, 2020.

[43] N. Anselmi, P. Rocca, M. Salucci, and A. Massa, "Irregular phased array tiling by means of analytic schemata-driven optimization," *IEEE Transactions on Antennas and Propagation*, vol. 65, no. 9, pp. 4495–4510, 2017.

[44] G. Ball, "Statistical density and amplitude tapering," in *1989 Sixth International Conference on Antennas and Propagation, ICAP 89 (Conf. Publ. No.301)*, pp. 249–253 vol.1, 1989.

[45] W. P. M. N. Keizer, "Synthesis of thinned planar circular and square arrays using density tapering," *IEEE Transactions on Antennas and Propagation*, vol. 62, no. 4, pp. 1555–1563, 2014.

[46] R. Haupt, "Thinned arrays using genetic algorithms," *IEEE Transactions on Antennas and Propagation*, vol. 42, no. 7, pp. 993–999, 1994.

[47] D. Boeringer and D. Werner, "Particle swarm optimization versus genetic algorithms for phased array synthesis," *IEEE Transactions on Antennas and Propagation*, vol. 52, no. 3, pp. 771–779, 2004.

[48] N. Jin and Y. Rahmat-Samii, "Advances in particle swarm optimization for antenna designs: Real-number, binary, single-objective and multiobjective implementations," *IEEE Transactions on Antennas and Propagation*, vol. 55, no. 3, pp. 556–567, 2007.

[49] C. Meijer, "Simulated annealing in the design of thinned arrays having low sidelobe levels," in *Proceedings of the 1998 South African Symposium on Communications and Signal Processing-COMSIG '98 (Cat. No. 98EX214)*, pp. 361–366, 1998.

[50] M. H. Novak, J. L. Volakis, and F. A. Miranda, "Low cost ultra-wideband millimeter-wave array," in *2016 IEEE International Symposium on Antennas and Propagation (APSURSI)*, pp. 1841–1842, 2016.

[51] J. T. Logan and M. N. Vouvakis, "Planar ultrawideband modular antenna (puma) arrays scalable to mm-waves," in *2013 IEEE Antennas and Propagation Society International Symposium (APSURSI)*, pp. 624–625, 2013.

[52] G. Rankin, A. Tirkel, and A. Leukhin, "Millimeter wave array for uav imaging mimo radar," in *2015 16th International Radar Symposium (IRS)*, pp. 499–504, 2015.

[53] T. E. Durham, K. J. Vanhille, C. R. Trent, K. M. Lambert, and F. A. Miranda, "Design of an 8–40 ghz antenna for the wideband instrument for snow measurements (wism)," in *2015 IEEE International Symposium on Antennas and Propagation USNC/URSI National Radio Science Meeting*, pp. 1999–2000, 2015.

[54] https://www.candorind.com/capabilities/design-limits/.

[55] B. Gustavsen and A. Semlyen, "Rational approximation of frequency domain responses by vector fitting," *IEEE Transactions on Power Delivery*, vol. 14, pp. 1052–1061, 1999.

[56] P. Jarry and J. N. Beneat, *Multistage Lossy Distributed Amplifiers*, pp. 121–149. 2016.

[57] B. S. Yarman, "Design of ultra-wideband antenna matching networks," in *2007 IEEE Applied Electromagnetics Conference (AEMC)*, pp. 1–4, 2007.

[58] Fouladi Azarnaminy, Siamak, *Reconfigurable Impedance Matching Networks Based on RF-MEMS and CMOS-MEMS Technologies*. PhD thesis, 2010.

[59] G. Rebeiz, "A 4-18ghz reconfigurable rf mems matching network for power amplifier applications," *International Journal of Rf and Microwave Computer-aided Engineering - INT J RF MICROW COMPUT-AID EN*, vol. 14, pp. 356–372, 07 2004.

[60] X. Shi, H. Chen, L. Zhu, and Y. Wan, "A novel design methodology for multi-band power amplifier matching network," in *2018 International Conference on Microwave and Millimeter Wave Technology (ICMMT)*, pp. 1–3, 2018.

[61] R. Whatley, Z. Zhou, and K. Melde, "Reconfigurable rf impedance tuner for match control in broadband wireless devices," *IEEE Transactions on Antennas and Propagation*, vol. 54, no. 2, pp. 470–478, 2006.

[62] T. Vaha-Heikkila and G. Rebeiz, "A 20-50 ghz reconfigurable matching network for power amplifier applications," in *2004 IEEE MTT-S International Microwave Symposium Digest (IEEE Cat. No.04CH37535)*, vol. 2, pp. 717–720 Vol.2, 2004.

[63] Q. Shen and N. Barker, "Distributed mems tunable matching network using minimal-contact rf-mems varactors," *IEEE Transactions on Microwave Theory and Techniques*, vol. 54, no. 6, pp. 2646–2658, 2006.

[64] P. Jarry and J. N. Beneat, *Multistage Distributed Amplifier Design*, pp. 67–100. 2016.

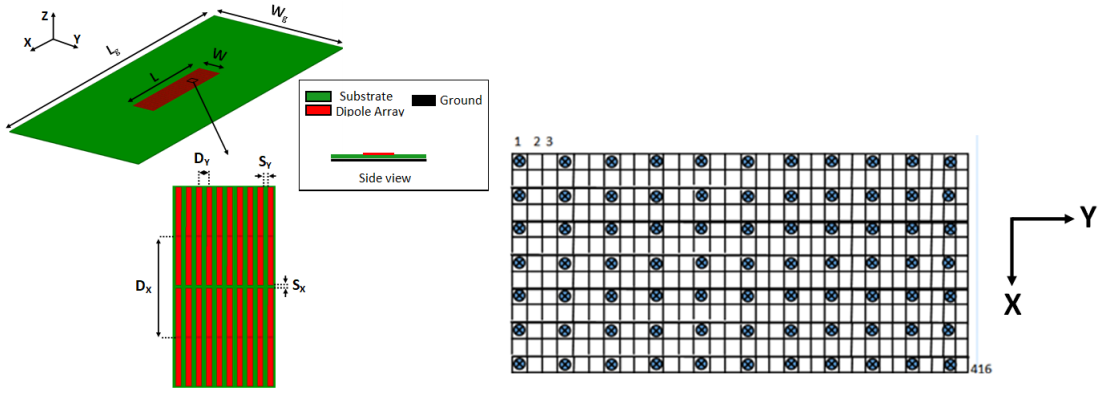
APPENDICES

Appendix A

A Thinned 32×13 Tightly Coupled Dipole Array

A.1 Thinned 32×13 TCDA Design

An array of 32×13 closely spaced dipole antenna is designed as shown in Fig. A.1a. The rectangular unit cell of the array is $0.43\lambda_H \times 0.043\lambda_H$ where λ_H is the wavelength at 70 GHz. The edge-to-edge distance between two adjacent dipoles in width (S_Y) and length directions (S_X) is $0.0207\lambda_H, 0.0129\lambda_H$, respectively. So, there are strong mutual couplings among elements specially at lower frequencies around 20 GHz. The substrate used is a BT-material with a thickness of 0.2mm, a relative permittivity of 3.6 and a loss tangent of 0.005. The overall size of the array (W, L) is $6.08mm \times 24.375mm$. The ground plane dimension (W_g, L_g) is $37.5mm \times 75mm$ which is placed $0.2mm$ underneath the array. The described antenna array is thinned with the excitation scheme shown in Fig. A.1b. In this thinned array only 77 elements shown crossed in Fig. 4.2 are excited and the rest are terminated to proper terminating impedances. Since the larger cell dimension (D_X) is chosen 0.43 of the wavelength at 70 GHz, no grating lobe would appear for frequencies below 70 GHz if all elements were excited. However, by thinning the array, the distance between the two adjacent excited elements are increased to $2D_x$ in x direction which results in grating lobe appearance at frequencies above 40 GHz at some steering angles if the unexcited elements are left open and there is no current induced on them. The grating lobe would appear at 70 GHz, 50 GHz for steering to more than 9^o, and 37^o in E-Plane respectively if the unexcited elements were left open and the excited ports were exciting with the same amplitude and phase as in a fully excited array.



(a) (b)

Figure A.1: (a) 13×32 tightly coupled dipole array. (b) Thinned array configuration.

A.2 Thinned TCDA Optimization

In this thinned array the grating lobe can be removed and the antenna radiation characteristics such as gain and SLL can closely resemble the radiation characteristics of a fully excited array by optimizing the terminating loads on unexcited or passive elements as well as the excitation voltages of the active ports. The optimization procedure of the array is the same as the methodology we used for 8×8 array which is fully described in chapter 4. Fig. A.2 shows the optimized directivity in E-Plane and compares it with the directivity of a fully excited array at 20 GHz, 50 GHz, and 70 GHz for different steering angles.

As shown in Fig. A.2, the optimized directivity and the desired directivity of the fully excited array have good agreement; however, the optimization becomes more difficult at high frequencies where the mutual couplings are less and specifically for high steering angles. As it's shown in Fig. A.2l, the maximum directivity is dropped by 3.3 dB and the SLL is reduced to 6.3 dB at 70GHz when the beam is steered to 45^o in E-Plane. However, at lower frequencies such as 50 GHz and 20 GHz the maximum directivity is only reduced by less than 0.4 dB and the SLL is better than 10 dB when the beam is steered to 45^o as shown in Fig. A.2h, A.2d. Also, at 50 GHz for broadside radiation, as shown in Fig. A.2e, the maximum directivity is reduced by 1 dB and the SLL is 13.65 dB.

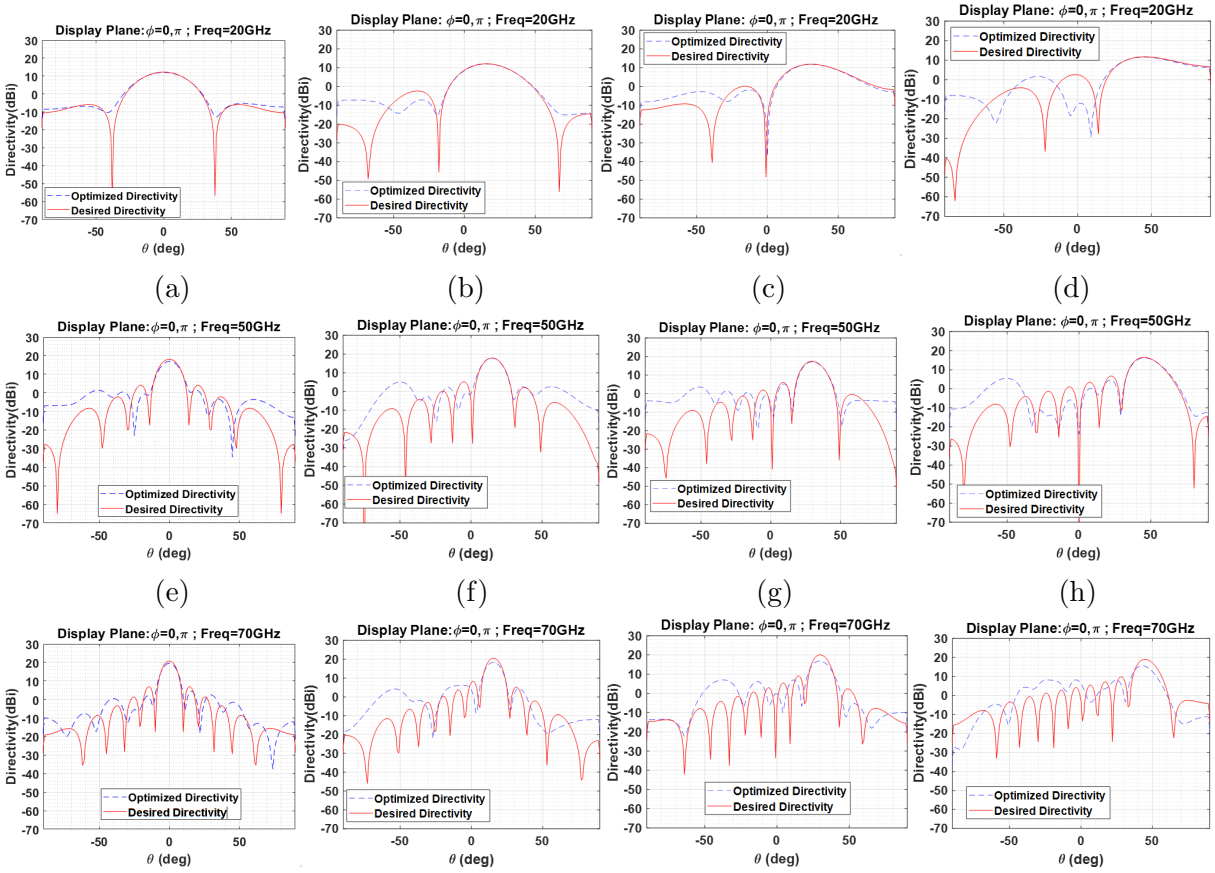


Figure A.2: optimized directivity in E-Plane when unexcited ports are terminated to complex impedances (R+jX) and the beam is steered up to broadside, 15^o, 30^o, 45^o at 20 GHz, 50 GHz, and 70 GHz (a) at 20 GHz, broadside (b) at 20 GHz steering to $\theta = 15^o$, $\phi = 0^o$. (c) at 20 GHz steering to $\theta = 30^o$, $\phi = 0^o$. (d) at 20 GHz steering to $\theta = 45^o$, $\phi = 0^o$. (e) at 50 GHz for broadside (f) at 50 GHz steering to $\theta = 15^o$, $\phi = 0^o$. (g) at 50 GHz steering to $\theta = 30^o$, $\phi = 0^o$. (h) at 50 GHz steering to $\theta = 45^o$, $\phi = 0^o$. (i) at 70GHz for broadside. (j) at 70 GHz steering to $\theta = 15^o$, $\phi = 0^o$. (k) at 70 GHz steering to $\theta = 30^o$, $\phi = 0^o$. (l) at 70 GHz steering to $\theta = 45^o$, $\phi = 0^o$.

Appendix B

Vector Fitting Method

Based on what explained in section 4.8, the problem is to find all coefficients in equation (4.9) in order to obtain the least square approximation of $f(s)$ for the whole frequency range. This is a nonlinear optimization problem since the unknown poles a_n are in the denominator. Vector fitting solves this problem iteratively as a linear problem in two stages, both times with known poles. The first stage is the pole identification. In this stage $f(s)$ is multiplied by a function $\delta(s)$ as below:

$$\begin{aligned} \delta(s) &= \sum_{n=1}^{N} \frac{\tilde{c_n}}{s - \tilde{a_n}} + 1 \\ f(s)\delta(s) &= \sum_{n=1}^{N} \frac{c_n}{s - \tilde{a_n}} + d + sh \end{aligned} \tag{B.1}$$

note that in equation (B.1) the rational approximation for $\delta(s)$ has the same poles as the approximation for $f(s)\delta(s)$. Rephrasing the equation (B.1):

$$\sum_{n=1}^{N} \frac{c_n}{s - \tilde{a_n}} + d + sh - f(s)[\sum_{n=1}^{N} \frac{\tilde{c_n}}{s - \tilde{a_n}}] = f(s) \tag{B.2}$$

The equation B.2 must be satisfied at each frequency point in our desired range. specifying a set of starting poles $\tilde{a_n}$ and writing (B.2) for several frequency points gives an over determined linear least square problem in the form of $Ax = b$ where x vector includes all the unknowns $c_n, \tilde{c_n}, d, h$. The starting poles $\tilde{a_n}$ are recommended by the author to be complex conjugate with imaginary parts linearly distributed over the desired frequency

range and the real part to be a small fraction of the imaginary part as in equation (B.3) to avoid ill-conditioning problem [55].

$$\begin{aligned} \tilde{a_n} = -\alpha + j\beta \qquad \tilde{a_{n+1}} = -\alpha - j\beta \\ \alpha = \frac{\beta}{100} \end{aligned} \tag{B.3}$$

For a given frequency point s_k we get: $A_k x = b_k$ where:

$$A_k = [\frac{1}{s_k - \tilde{a_1}} \ \ldots \ \frac{1}{s_k - \tilde{a_N}} \ \ 1 \ \ s_k \ \ \frac{-f(s_k)}{s_k - \tilde{a_1}} \ \ldots \ \frac{-f(s_k)}{s_k - \tilde{a_N}}] \tag{B.4}$$

$$x = [c_1 \ \ldots \ c_N \ \ d \ \ h \ \ \tilde{c_1} \ \ldots \ \tilde{c_N}]^T, b_k = f(s_k) \tag{B.5}$$

In the case of complex poles, a modification is introduced to ensure that the residues come in perfect conjugate pairs. Assume that the partial fractions i and i+l constitute a complex pair, i.e.,

$$a_i = a' + ja'' \ , a_{i+1} = a' - ja'' \ , c_i = c' + jc'' \ , c_{i+1} = c' - jc'' \tag{B.6}$$

The two corresponding elements $A_{k,i}$, $A_{k,i+1}$ are modified as follows:

$$A_{k,i} = \frac{1}{s_k - a_i} + \frac{1}{s_k - {a_i}^*} \ ; \ A_{k,i+1} = \frac{j}{s_k - a_i} - \frac{j}{s_k - {a_i}^*} \tag{B.7}$$

This has the effect that the corresponding residues in the solution vector x become equal to c' and c'' , respectively. Writing Ax=b for different frequency points gives an overdetermined linear matrix equation. In order to preserve the conjugacy property we have to formulate Ax=b in terms of real quantities and separating the real and imaginary part of equation as below:

$$\begin{bmatrix} A' \\ A'' \end{bmatrix} x = \begin{bmatrix} b' \\ b'' \end{bmatrix} \tag{B.8}$$

The over determined linear least square problem in the form of $Ax = b$ must be solve to find all the unknowns $c_n, \tilde{c_n}, d, h$. The equation (B.1) can also be written as follows:

$$\begin{aligned} f(s)\delta(s) = \frac{\prod_{n=1}^{N+1}(s - z_n)}{\prod_{n=1}^{N}(s - \tilde{a_n})} \qquad \delta(s) = \frac{\prod_{n=1}^{N}(s - \tilde{z_n})}{\prod_{n=1}^{N}(s - \tilde{a_n})} \\ f(s) = \frac{f(s)\delta(s)}{\delta(s)} = \frac{\prod_{n=1}^{N+1}(s - z_n)}{\prod_{n=1}^{N}(s - \tilde{z_n})} \end{aligned} \tag{B.9}$$

since the same starting poles are chosen for $f(s)\delta(s)$ and $\delta(s)$, the poles cancel in the division process and the poles of $f(s)$ become equal to the zeros of $\delta(s)$. So, by calculating the zeros of $\delta(s)$ a good set of poles for fitting the original function $f(s)$ is obtained.

Once the over determined least square equation is solved, the zeros of the function $\delta(s)$ can be found using residues $\tilde{c_n}$ and the starting poles in next section.

B.1 Calculation of Zeros

The zeros of function $\delta(s)$ are calculated as the eigenvalues of the matrix

$$H = A - b\tilde{c}^T \tag{B.10}$$

where A is a diagonal matrix containing the starting poles and b is a column vector of ones. $\tilde{c}^T$ is a row-vector containing the residues for $\delta(s)$ function . In the case of a complex pair of poles, the corresponding sub matrices in equation (B.10) are modified (via a similarity transformation) as follows:

$$\hat{A} = \begin{bmatrix} a' & a'' \\ -a'' & a' \end{bmatrix} \quad \hat{b} = \begin{bmatrix} 2 \\ 0 \end{bmatrix} \quad \hat{c} = \begin{bmatrix} \tilde{c}' & \tilde{c}'' \end{bmatrix} \tag{B.11}$$

In the next stage, the starting poles are replaced with zeros of $\delta(s)$ and the iteration continues until the error in the poles is negligible.

Appendix C

Real Frequency Technique

C.1 Designing a Lossless Distributed Matching Network

In all numerical optimization algorithms, the user must define an objective function in terms of the unknown parameters of the problem. In the case of the antenna matching network design problem, the user provides the measured or optimized (in our case) antenna input impedance to the program. Then, a reasonable circuit topology for the equalizer is selected. Let these elements be $Z_{01}, Z_{02}, ..., Z_{0n}$. For the optimization, one must maximize the Transducer Power Gain (TPG) or minimize the reflection coefficient as a function of these unknown parameters in the circuit topology together with the antenna data which could be provided as an impedance $Z_L(j\omega) = R_L(\omega) + jX_L(\omega)$, or an admittance $Y_L = \frac{1}{Z_L}$ or a reflectance $L_{11} = \frac{Z_L - 1}{Z_L + 1}$ data. In this section, since the circuit is lossless $|R|^2 = 1 - |T|^2$; so, by maximizing T, the reflection coefficient R would be minimized and vice versa. In this case, the error function is defined by either maximizing transmission coefficient T or minimizing the reflection coefficient R. In mathematical terms, we say that Transmission coefficient $T(\omega)$ and the reflection coefficient ($R = |\Gamma|^2$) are the functions of the real frequency variable ω, measured antenna data (let it be Z_L), and the unknown matching circuit elements $Z_{01}, Z_{02}, ..., Z_{0n}$ and we write $T = T(\omega, Z_L, Z_{01}, Z_{02}, ..., Z_{0n})$ and $R = R(\omega, Z_L, Z_{01}, Z_{02}, ..., Z_{0n})$. The target for the optimization is to have the T larger than a certain level T_o or the R must be lower than a prefixed level R_o. So, the error which must be minimized is the difference between measured T and defined T_o if T is smaller than T_o or the difference between R and R_o if R is larger than R_o. As shown in Fig. C.1, the antenna which is described by means of its impedance data $Z_L(j\omega)$, is targeted to be matched to a

resistive generator with $R_s = 50\Omega$ impedance over a wide frequency band. In this case the transmission (T) and reflection (R) coefficients of the matched system is given by:

$$\begin{aligned} T(s) &= \frac{|e_{21}|^2(1-|L_{11}|^2)}{|1-e_{22}.L_{11}|^2} \\ R(s) = |\Gamma|^2 &= |e_{11} + \frac{|e_{12}|^2 L_{11}}{1-L_{11}e_{22}}|^2 \end{aligned} \tag{C.1}$$

where $e_{11}, e_{12}, e_{21}, e_{22}$ are the scattering parameters of the equalizer. by the lossless condition of $[S_e]$, $|e_{21}|^2 = 1 - |e_{22}|^2$ in equation C.1.

Basically, the SRFT describes the lossless, reciprocal equalizer $[S_e]$ shown in Fig. C.1 in terms of its unit normalized reflection coefficients in Belevich form as below [64]:

$$S_E = \begin{bmatrix} e_{11}(s) = \frac{h(s)}{g(s)} & e_{12}(s) = \frac{f(s)}{g(s)} \\ e_{21}(s) = \frac{f(s)}{g(s)} & e_{22}(s) = \frac{-\epsilon h(-s)}{g(s)} \end{bmatrix} \tag{C.2}$$

where f(s) could be an even or odd function. If $f(s)$ is even then $\epsilon = 1$, and if $f(s)$ is odd then $\epsilon = -1$. In addition, the lossless condition leads to:

$$g(s)g(-s) = h(s)h(-s) + f(s)f(-s) \tag{C.3}$$

$h(s)$ and $g(s)$ are polynomials of order n with real-valued coefficients as below:

$$\begin{aligned} h(s) &= h_o + h_1 s + ... + h_{n-1}s^{n-1} + h_n s^n \\ g(s) &= g_o + g_1 s + ... + g_{n-1}s^{n-1} + g_n s^n \end{aligned} \tag{C.4}$$

The selection of transmission zeros of $f(s)$ depends on the practical implementation of the matching network for example if the matching network is a low pass LC ladder, the $f(s)$ and ϵ can be as below in general form [64]:

$$\begin{aligned} f(s) &= \pm s^k \\ \epsilon &= (-1)^k \end{aligned} \tag{C.5}$$

where k is the number of transmission zeros at $\omega = 0$; However, if the equalizer circuit consists of cascaded lossless distributed transmission lines as shown in Fig. C.2 with same lengths as $\lambda/4$ at a selected frequency w_o, the scattering matrix of the equalizer and $f(s)$ could be written as below [64]:

$$S_E = \begin{bmatrix} e_{11}(t) = \frac{h(t)}{g(t)} & e_{12}(t) = \frac{f(t)}{g(t)} \\ e_{21}(t) = \frac{f(t)}{g(t)} & e_{22}(t) = \frac{-h(-t)}{g(t)} \end{bmatrix} \tag{C.6}$$

where $t = j\Omega = jtan(\frac{\pi\omega}{2\omega_o})$ is the Rechard's variable and:

$$f(t) = t^r(1-t)^{\frac{(n-q)}{2}} \tag{C.7}$$

q and r are known to us and represents the number of low pass and high pass stubs in the matching circuit respectively. In this case, the lossless condition leads to:

$$g(t)g(-t) = h(t)h(-t) + t^{2r}(1-t)^{n-q} \tag{C.8}$$

The problem consists of defining the unknown polynomial coefficients $h_0, h_1, h_2, \ldots, h_n$ that optimize the response of the system. Once $h(t)$ is known, $G(t) = g(t)g(-t)$ can be computed using equation C.8. The left-half roots of $G(t) = g(t)g(-t)$ are computed to form a Hurwitz polynomial g(t). Having $h(t), g(t)$, and $f(t)$, The equalizer scattering parameters $e_{11}(t), e_{12}(t), e_{21}(t)$, and $e_{22}(t)$ can be computed to calculate the error function during the optimization. Once the error is optimized using levenberg-marquardt algorithm, $e_{22}(t)$ can be used to realize the equalizer using the synthesis procedures described below.

C.1.1 Synthesis Procedure

The first step in synthesis procedure is to compute the input impedance from the equalizer output reflection coefficient $e_{22}(t)$.

$$Z(t) = \frac{1 + e_{22}(t)}{1 - e_{22}(t)} \tag{C.9}$$

Having Z(t), it is possible to extract a unit element (E_1 shown in Fig. C.2) whose characteristic impedance $Z_{01} = Z(1)$ and the remaining network will have a new input impedance called $Z_1(t)$ as below [64]:

$$\begin{aligned} Z_{01} &= Z(1) \\ Z_1(t) &= Z(1)\frac{Z(t) - tZ(1)}{Z(1) - tZ(t)} \end{aligned} \tag{C.10}$$

The process is then repeated to define the characteristic impedances $Z_{02}, Z_{03}, \ldots Z_{0n}$ of the remaining units $E_2, E_3, \ldots E_n$.

C.2 Modified Real Frequency Technique for Lossy Circuits

As mentioned earlier, the bandwidth of a lossless matching network is limited by the quality factor of the load based on the equation 5.1; So, to achieve broader bandwidths,

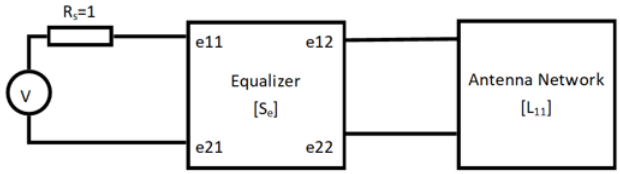


Figure C.1: the building block of the lossless, reciprocal equalizer connected to the antenna load

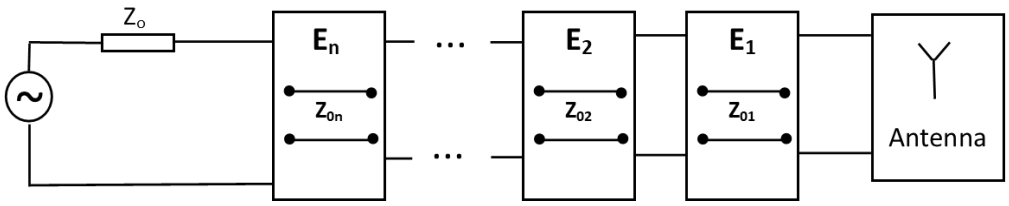


Figure C.2: Multistage lossless distributed equalizer

the equalizer network topology is being modified to introduce lossy junctions in the cascade of distributed networks described in section C.1. This structure consists of a cascade of lossless,equi-length distributed units with characteristic impedances Z_{0i} which are all $\lambda/4$ at the selected frequency w_o. Each unit of equalizer (UE) has a parallel resistor R_i on its input and a parallel resistor R_{i+1} on its output. Fig. C.3 shows the structure of the described lossy matching circuit. The image network $\overline{N}$ is formed by the same lossless transmission lines with normalized characteristic impedances z_{0i} but replacing all normalized resistances $r_i = \frac{R_i}{z_o}$ with negative normalized parallel resistors -r_i as shown in Fig. C.4. Connecting the real network N (shown in Fig. C.3) and the image network $\overline{N}$ (shown in Fig. C.4) in parallel, will result in a lossless two port network [56]. Also, if the real network N is characterized by its scattering matrix S and the image network $\overline{N}$ is characterized by its scattering matrix $\overline{S}$, then the relation below is satisfied between their scattering parameters [56].

$$\begin{aligned} I - S\overline{S}^* &= 0 \\ S_{11}\overline{S_{11}}^* + S_{21}\overline{S_{21}}^* &= 1 \end{aligned} \tag{C.11}$$

so, the scattering parameters of a lossy distributed network are described as below [56]:

$$\begin{aligned} S_{11}(t) &= \frac{h(t)}{g(t)} \\ S_{12}(t) = S_{21}(t) &= \frac{(1-t^2)^{\frac{n}{2}}}{g(t)} \\ S_{22}(t) &= -\frac{\overline{h(-t)}}{g(t)} \end{aligned} \tag{C.12}$$

where $\overline{h(-t)}$ is obtained by replacing t by -t and by replacing all the normalized resistors r_i by -r_i in the expression of h(t). if we decompose $h(t)$ into even part α(t) and odd part $\beta(t)$ with respect to $u_i = \frac{1}{r_i}$, in this case we would have:

$$\begin{aligned} h(t) &= \alpha(t) + \beta(t) \\ \overline{h(-t)} &= \alpha(-t) - \beta(-t) \end{aligned} \tag{C.13}$$

so, now, having the polynomial coefficients $\alpha_0, \alpha_1, ..., \alpha_n$ and $\beta_0, \beta_1, ..., \beta_n$ we can find $h(t)$ and then calculate $g(t)\overline{g(-t)}$ by using the equation C.11 which becomes as below [56]:

$$g(t)\overline{g(-t)} = h(t)\overline{h(-t)} + (1-t^2)^n \tag{C.14}$$

The Hurwitz polynomial $g(t)$ can be formed by the left hand roots of the calculated polynomial $G(t) = g(t)\overline{g(-t)}$. Having the roots of g(t), still a coefficient is required completely obtain the polynomial $g(t)$. This coefficient could be found by replacing $t = 0$. When t is zero, the frequency w becomes zero which means the transmission lines' lengths are very small in compare with the wavelength at w=0; so, the equalizer's circuit shown in Fig. C.3 becomes like a parallel normalized admittance equal to the sum of all parallel normalized admittances $u_1 + u_2 + ...u_{n+1}$. In this case the scattering parameters of the equalizers becomes:

$$\begin{aligned} S_{11}(0) = S_{22}(0) &= \frac{h(0)}{g(0)} = \frac{-\Sigma_{i=1}^{n+1} u_i}{2 + \Sigma_{i=1}^{n+1} u_i} \\ S_{12}(0) = S_{21}(0) &= \frac{1}{g(0)} = \frac{2}{2 + \Sigma_{i=1}^{n+1} u_i} \end{aligned} \tag{C.15}$$

so, the coefficient required to find the polynomial $g(t)$ is obtained using the equations C.15 such that:

$$g(0) = 1 - h(0) \tag{C.16}$$

Then, having h(t),f(t) and g(t) we can find the scattering parameters of the equalizer and calculate the error function during the optimization procedure. Once the optimization

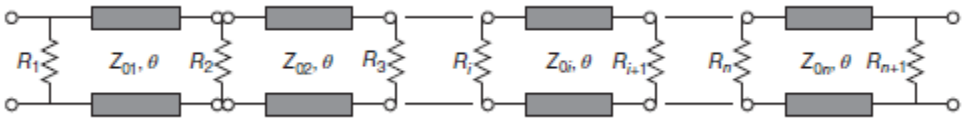


Figure C.3: The real network (N) of the multistage distributed equalizer with lossy junctions [56]

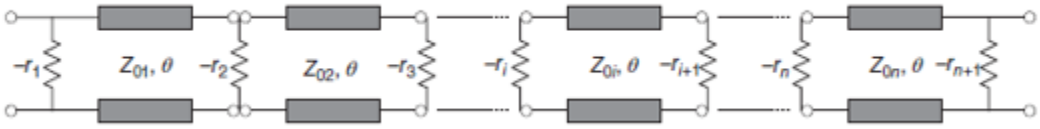


Figure C.4: The image network ($\overline{N}$) of the multistage distributed equalizer with lossy junctions [56]

is done, we can find the scattering parameters of the equalizer having the optimized coefficients α_i and β_i and synthesize the circuit by using the output reflection coefficient $e_{22}(t) = -\frac{\overline{h(-t)}}{g(t)}$. The synthesis procedure is going to be described in the following section.

C.2.1 Synthesis Procedure

In order to synthesize the multistage distributed equalizer with lossy junctions, the first step after finding the input impedance $Z(t) = \frac{1+e_{22}(t)}{1-e_{22}(t)}$ is to extract the normal resistance r_1, the normal characteristic impedance z_{01} and the remaining impedance $Z_2(t)$ using Richard's theorem as below [56]:

$$\begin{aligned} r_1 &= \frac{2Z(1)Z(-1)}{Z(1)+Z(-1)} \\ z_{01} &= \frac{2Z(1)Z(-1)}{Z(-1)-Z(1)} \\ Z_2(t) &= z_{01}\frac{(R_1+tz_{01})Z(t)-tz_{01}R_1}{z_{01}R_1-(tR_1+z_{01})Z(t)} \end{aligned} \tag{C.17}$$

Then, this process should be repeated untill all characteristic impedances $z_{01}, z_{02}, ...z_{0n}$ and impedances $r_1, r_2, ...r_{n+1}$ are calculated.